Title
Simplified Models for Dark Matter Model Building

Author
DiFranzo, Anthony

Publication Date
2016

Peer reviewed|Thesis/dissertation

UNIVERSITY OF CALIFORNIA,
IRVINE

Simplified Models for Dark Matter Model Building

DISSERTATION

submitted in partial satisfaction of the requirements
for the degree of

DOCTOR OF PHILOSOPHY

in Physics

by

Anthony Paul DiFranzo

Dissertation Committee:
Professor Tim M.P. Tait, Chair
Professor Arvind Rajaraman
Professor Yuri Shirman

2016

DEDICATION

To my parents, Guy and Susie DiFranzo

TABLE OF CONTENTS

LIST OF FIGURES

LIST OF TABLES

ACKNOWLEDGMENTS

There are countless people to whom I owe thanks for my successful graduate career. First and foremost, I am very thankful to my advisor, Tim Tait. His guidance, patience, and encouragement has helped to foster my passion for physics. He has opened up so many doors for me which have been crucial to my developing as a scientist. I have also been fortunate to have several others act as mentors to me, including Paddy Fox, Dan Hooper, Arvind Rajaraman, Yuri Shirman, Flip Tanedo, and Daniel Whiteson.

During my graduate career, I have enjoyed many useful collaborations. Including those already listed, I would like to thank Mohammad Abdullah, Prateek Agrawal, Asher Berlin, Linda Carpenter, Gopolang Mohlabeng, Michael Mulhearn, Keiko Nagao, Chase Shimmin, Sean Tulin, and Alex Wijangco.

The Theory Groups at UC Irvine and Fermilab have been a tremendous source of education, encouragement, and financial support. I owe my gratitude to all their members. These institutes will forever be my academic homes.

I am further grateful to my fellow classmates, officemates, colleagues, and friends. Over the last few years of our camaraderie, we have shared life and the joy of physics. Our time together has been fruitful on many fronts and I look forward to our future fellowship.

I owe a special thanks to my family. My parents have instilled me with a love for science and a curiosity for nature, which drew me towards physics in the first place. I owe my success and life to their love, encouragement, and support; without which this would not have been possible. My brother, Dominic, has been my friend and a huge source of support for me. I am so thankful for his presence in my life. My grandmother, Mari, has always lovingly supported us and whose home has been an escape from the usual academic stress these past years.

My research has been funded in part by the NSF grants PHY-1316792 and PHY-0970171, the Fermilab Graduate Student Research Program in Theoretical Physics, and the URA Visiting Scholars Program at the Fermi National Accelerator Laboratory.

Portions of this work were published in Physical Review D and the Journal of High Energy Physics.

CURRICULUM VITAE

Anthony Paul DiFranzo

EDUCATION

Doctor of Philosophy in Physics **2016**
University California, Irvine *Irvine, California*

Advisor: Prof. Tim M.P. Tait
Bachelor of Science in Physics **2011**
Rensselaer Polytechnic Institute *Troy, New York*

Graduated with honors, Magna Cum Laude

RESEARCH EXPERIENCE

Graduate Research Assistant **2012–2016**
University of California, Irvine *Irvine, California*
Visiting Graduate Fellow **2014–2015**

Fermilab Theory Group *Batavia, Illinois*

TEACHING EXPERIENCE

Teaching Assistant **2011–2016**
University of California, Irvine *Irvine, California*

SELECTED HONORS AND AWARDS

AGS Travel Grant **Spring 2016**
Pheno16 Travel Award **Spring 2016**
URA Visiting Scholars Program at Fermilab **Winter 2016**
Fermilab Graduate Student Research Program in Theoretical Physics **2014-2015**
UC Regents Fellowship **2011-2013**

REFEREED JOURNAL PUBLICATIONS

Vector Dark Matter through a Radiative Higgs Portal **2016**
with Patrick J. Fox and Tim M.P. Tait, JHEP04 (2016) 135, arXiv:1512.06853

Searching for MeV-Scale Gauge Bosons with IceCube **2015**
with Dan Hooper, Phys. Rev. D 92, 095007, arXiv:1507.03015

Dark Matter Benchmark Models for Early LHC Run-2 Searches: Report of the ATLAS/CMS Dark Matter Forum **2015**
with LHC Dark Matter Forum, arXiv:1507.00966

A 3.55 keV Line from Exciting Dark Matter without a Hidden Sector **2015**
with Asher Berlin and Dan Hooper, Phys. Rev. D 91, 075018 (2015), arXiv:1501.03496

Hidden On-Shell Mediators for the Galactic Center Gamma-Ray Excess **2014**
with Mohammad Abdullah, Arvind Rajaraman, Tim M. P. Tait, Philip Tanedo, and Alexander M. Wijangco, Phys. Rev. D 90, 035004 (2014), arXiv:1404.6528

Systematically Searching for New Resonances at the Energy Frontier using Topological Models **2014**
with Mohammad Abdullah, Eric Albin, Meghan Frate, Craig Pitcher, Chase Shimmin, Suneet Upadhyay, James Walker, Pierce Weatherly, Patrick J. Fox, and Daniel Whiteson, Phys. Rev. D 89, 095002 (2014), arXiv:1401.1462

Mono-Higgs: a new collider probe of dark matter **2013**
with Linda M. Carpenter, Michael Mulhearn, Chase Shimmin, Sean Tulin, and Daniel Whiteson, Phys. Rev. D 89, 075017 (2014), arXiv:1312.2592

Simplified Models for Dark Matter Interacting with Quarks **2013**
with Keiko I. Nagao, Arvind Rajaraman, and Tim M.P. Tait, JHEP 1311 (2013) 014, arXiv:1308.2679

PRESENTATIONS

Phenomenology 2016 Symposium **May 2016**
Future sensitivity to dark matter from the Z boson width

Fermilab Theory Group Journal Club **February 2016**
Composite Solutions to the Strong CP Problem

UC San Diego Theory Seminar **November 2015**
Vector Dark Matter through a Radiative Higgs Portal

UCI Journal Club **October 2015**
Vector Dark Matter through a Radiative Higgs Portal and Searching for New Gauge Bosons at IceCube

Fermilab Theory Seminar **September 2015**
Vector Dark Matter through the Higgs Portal

SUSY 2015 **August 2015**
Vector Dark Matter via Higgs Portal

Phenomenology 2015 Symposium **May 2015**
Vector Dark Matter via Higgs Portal

Fermilab Astrophysics Theory Chalk Talk **January 2015**
Dark Matter-Neutrino Interactions

UChicago KIPC Group Meeting **November 2014**
Light Mediators for the Galactic Center GeV Excess

TASI Student Talk **June 2014**
Dark Matter and the Galactic Center GeV Excess

TeV Particle Astrophysics **August 2013**
Implementing Simplified Models in the Search for Dark Matter

SCHOOLS

Pre-SUSY, UC Davis **August 2015**
Invisibles15 School, Universidad Autónoma de Madrid **June 2015**
TASI 2014, CU Boulder **June 2014**

ABSTRACT OF THE DISSERTATION

Simplified Models for Dark Matter Model Building

By

Anthony Paul DiFranzo

Doctor of Philosophy in Physics

University of California, Irvine, 2016

Professor Tim M.P. Tait, Chair

The largest mass component of the universe is a longstanding mystery to the physics community. As a glaring source of new physics beyond the Standard Model, there is a large effort to uncover the quantum nature of dark matter. Many probes have been formed to search for this elusive matter; cultivating a rich environment for a phenomenologist. In addition to the primary probes – colliders, direct detection, and indirect detection – each with their own complexities, there is a plethora of prospects to illuminate our unanswered questions. In this work, phenomenological techniques for studying dark matter and other possible hints of new physics will be discussed. This work primarily focuses on the use of Simplified Models, which are intended to be a compromise between generality and validity of the theoretical description. They are often used to parameterize a particular search, develop a well-defined sense of complementarity between searches, or motivate new search strategies. Explicit examples of such models and how they may be used will be the highlight of each chapter.

Chapter 1

Introduction

The progenitor of dark matter research is often credited to Fritz Zwicky, based on his work in 1933 [7]. He found that the mass within the Coma cluster, based its velocity dispersion, was far greater than that which could be inferred from the light produced by the bodies composing the cluster. He concluded that the remaining mass was some non-luminous matter, which he termed "*dunkle Materie*", literally *dark matter* in English.

After several hints over the next 40 years, the first robust evidence for dark matter comes from the work of Vera Rubin and Kent Ford [8]. They compiled the rotation curve of M31 out to large radial distances. For small distances, they found the rotation speeds of objects to increase sharply with increasing distance, as expected. At larger distances where the visible matter becomes much less dense, the rotation speeds are expected to decrease markedly. Instead, they found rotation speeds which were nearly constant with distance. This was suggestive of a non-luminous matter halo extending throughout M31.

This was further verified with gravitational lensing techniques, whereby the mass of an object is inferred based on how it distorts the light from a background source [9]. This technique led to one of the most convincing pieces of evidence for dark matter: the Bullet Cluster, which contains two colliding galaxy clusters [10]. Using a combination of gravitational lensing and X-ray observations, one finds that the most dense regions have significantly separated from the hot baryonic gas observable in X-rays and have moved further from the collision point than the hot gas. This suggests that dark matter is due to some non-luminous matter and not an incomplete understanding of gravity. Further, one may infer that dark matter is weakly interacting compared to the baryonic matter, as it flowed more freely through the collision.

These measurements are all telling of dark matter on galactic scales. While it motivates the existence of dark matter, it is insufficient to makes statements on the dark matter density throughout the universe. With the advent Cosmic Microwave Background observations, cosmologists could begin to probe the structure of the universe at the time of recombination. These measurements indicate the presence of a non-relativistic density of matter which is much greater than what can be attributed to baryonic matter [11]. Current measurements, fit to ΛCDM, lead to a dark matter abundance of $\Omega_\chi h^2 \approx 0.11$, approximately five times more abundant than baryons [12].

Evidence for this phenomena grew slowly over time, where today the dark matter problem is a major focus of the physics community. Yet despite over 80 years of effort, a concrete, quantum description of dark matter is still absent. Great strides have been made in developing a theory of nature at the smallest known scales. This has led to the discovery of a host of particles, described by the Standard Model (SM) of Particle Physics. While this model has been incredibly successful, none of its constituents may be dominant contributors to dark matter. Therefore, the SM is surely incomplete, leaving dark matter as a clear avenue for new physics.

Today we have many tools to constrain possibilities for dark matter, each playing a complementary role. The primary assumption of these probes is that dark matter has a coupling, albeit small, to particles in the Standard Model. The first primary probe of dark matter is

Direct Detection. If dark matter does exist as a halo throughout the Milky Way, then dark matter may be passing through the Earth. Searches of this kind rely on carefully studying large quantities of matter for signs of dark matter colliding with atomic nuclei. One drawback here is that while dark matter densities are well known on very large scales, they are not known at the small scales which are relevant for these experiments. Further, the local dark matter density is expected to be small compared to that of the Galactic Center making these experiments further sensitive to small fluctuations in the local dark matter density.

We can point telescopes in a direction where dark matter is known to have a high density, such as the Galactic Center or dwarf spheroidal galaxies. If dark matter couples to the Standard Model, visible particles may be produced during dark matter collisions or decays. This probe is referred to as Indirect Detection. Searches of this kind are complicated by poorly understood backgrounds, however this may be mitigated by well-founded expectations for the morphology of the backgrounds and dark matter signal.

The third is the bread and butter of modern particles physics: Colliders. If dark matter can scatter to produce visible matter or scatter off of visible matter, it must also be possible to make dark matter from visible matter. Here dark matter particles may be created during high energy events at particle colliders. These particles will not be directly observable in the detector, but from momentum conservation we can infer the production of an invisible particle. This is very analogous to observations which led to the postulation of the neutrino.

The probes discussed so far primarily deal with dark matter in the late universe. One may also attempt to probe how dark matter interactions affect cosmology. The most prominent being the dark matter relic abundance. Given our understanding of cosmology, we can calculate the expected abundance of dark matter today for a particular candidate. For example, if dark matter was in thermal equilibrium with the visible sector in the early universe, the relic abundance is determined by the freeze-out mechanism. As the universe cools and expands, dark matter will eventually exit thermal equilibrium, at which point its abundance will decrease through annihilation into Standard Model fields. If the annihilation rate is too small, the candidate will exceed the known amount of dark matter. Otherwise, one can determine what fraction of the abundance may be composed of such a candidate. Here we see that the freeze-out mechanism is closely tied to Indirect Detection.

As long as the coupling between the visible and dark sectors is sufficiently strong, thermal equilibrium will be reached and the freeze-out mechanism will take place. This largely washes out dark matter physics at temperatures above freeze-out. However, this still leaves a large uncertainty due to unknown physics between the freeze-out temperature and recombination, where the universe can not easily be experimentally probed. Models with this form of thermal production are often classified as Weakly Interacting Massive Particles (WIMPs).

There are many alternatives to such a thermal history. For example, the coupling between the dark and visible sector may be too weak to allow for thermal equilibrium. In this case, the dark matter density will slowly increase towards the equilibrium value until the universe is too cold to kinematically allow production of dark matter. In this case, the relic abundance is set by a "freeze-in" process. Such models are referred to as Feebly Interacting Massive Particles (FIMPs) [13]. There are also dark matter candidates which do not rely on thermal production; the two most popular examples being sterile neutrinos and axions. Each of which have motivated unique search strategies.

Note that no one probe can concretely discover dark matter. Multiple different experiments are needed to paint a complete picture. However, to make concrete relations between different measurements, a model describing the specific quantum properties of dark matter is necessary. A phenomenologist typically has two primary paths to push our scientific understanding of nature. The first is to combine these astrophysical, cosmological, and particle physics inputs to determine possibilities models for dark matter. The second is to motivate new experiments and novel search strategies which may explore unknown facets of new physics, such as in Ch. 3 or for a non-dark matter related example in Ch. 7.

There is a continuum of model building strategies. The extremes of which I'll refer to as "Complete Theories" and "Effective Theories". A Complete Theory is a top-down approach where a model is developed which, either accidentally or with minor adjustments, includes a dark matter candidate. Such models are often intended to solve other problems in physics. They tend to be UV complete, or at least valid up to very large scales. Famous examples of this class include the Minimal Supersymmetric Standard Model (MSSM) and Extra Dimensions [14, 15], whose R-parity and KK-parity respectively allow for dark matter candidates. This method has the benefit that it is highly predictive, allowing full complementarity between experiments. However, such theories often contain a large number of free parameters which may be difficult to efficiently explore.

On the other extreme sits Effective Field Theories (EFTs). In this bottom-up approach, the typical concerns for validity at all scales is ignored. Instead the focus is to write effective operators involving a dark matter field and fields in the Standard Model. Such models benefit from having few parameters, greatly simplifying search strategies. However, this is balanced by the lose of predictiveness. Since the model is not expected to be valid at all energy scales, making credible translations between experiments not guaranteed.

In the continuum between these two extremes exist Simplified Models, where one maintains predictiveness and a manageable number of parameters without completely sacrificing generality. Constructing a Simplified Model can be seen from two perspectives. From the top-down mindset, the most important degrees of freedom from a Complete Theory can be extracted to form a Simplified Model, as discussed in Ch. 2. One often finds that many different Complete Theories can map onto the same Simplified Model in certain regimes. Allowing one to make general statements about a larger class of models.

From the bottom-up mindset, one fills in the physics that an EFT may be ignoring. This most often expresses itself as introducing new fields; allowing phenomena to arise which were not expressed by the EFT as in as in Ch. 4 and Ch. 6. Simplified Models contain interactions that are mass dim-4, causing them to be UV complete or easily completable with further extensions. Further, upon making a UV completion one commonly finds new fields or interactions which are necessarily present. One may also then search for these secondary fields, independently of dark matter, as a probe of the dark sector.

Simplified Models also serve as a platform for future model building. When a model meets tight experimental constraints or conflicting data, one can disregard that model as excluded. Or one may interpret this as a clue on how to extend the model. At some point, we want a complete picture, which we should not expect to be overly simple. See Ch. 5 for such an example. Simplified Models should be seen as a stepping stone in developing a fundamental extension of the Standard Model.

The remainder of this thesis will detail the following. Ch. 2 will look at a Simplified Model where dark matter interacts with quarks via a colored scalar. This is similar to regimes of parameter space in the MSSM, where dark matter is a neutralino and interactions with the SM are mediated via squarks.

Ch. 3 proposes a new search channel called the *mono-Higgs* signature at colliders, where dark matter is produced in association with a Higgs boson. This chapter also develops a collection of Simplified and Effective Models which produce such a signature.

Ch. 4 motivates an alternate annihilation topology for dark matter in the Galactic Center, whereby multiple light mediators are produced in the final state and subsequently decay to SM fields. Viable topologies and their effect on photon spectra are discussed with various motivations for constructing simplified models in the context of the Galactic Center Excess.

Ch. 5 develops a model to resolve conflicts between the observation of a 3.55 keV photon line or lack thereof from various astrophysical bodies, assuming the excess is due to dark matter. The model also makes accommodations for producing the GeV Excess from the Galactic Center. This model is an example of making a Simplified Model more complex so as to simultaneously fit different observations.

Ch. 6 postulates a spin-1 dark matter candidate whose coupling to the SM is generated by radiative interactions with the Higgs. This model requires several other fields for UV-completeness, allowing for a rich phenomenology involving searches for these secondary fields.

Ch. 7 explores an application of a Simplified Model outside of dark matter searches. Here a light vector boson which interacts with neutrinos is postulated. Such a boson with the correct mass would cause resonant scattering between the Cosmic Neutrino Background and high energy astrophysical neutrinos, the spectral effects of which may be observable by IceCube.

Chapter 2

Simplified Models for Dark Matter Interacting with Quarks

Based on arXiv:1308.2679 [16]

2.1 Introduction

The largest mass component of the universe is a longstanding mystery to the physics community. Dark Matter has been probed using particle colliders, direct detection experiments, and indirect detection in telescopes. Despite these intensive searches it has proven elusive. It is clear we must be thorough and creative as we continue the important mission to search for it.

From a particle physics perspective, it is essential to have a theoretical description of dark matter. Such a description allows one to contrast various searches [17], and fit the dark matter into the broader context of the Standard Model (SM). There are two common approaches to dark matter model building. The first is to find a complete theory (which typically addresses some other problem such as the gauge hierarchy), and also contains a potential dark matter candidate. The prototypical example of this approach is the Minimal Supersymmetric Standard Model (MSSM). One can work with the complete theory with every detail included. Often there are many free parameters, which on the one hand leads to a rich range of phenomena, but on the other makes it difficult to draw general conclusions (see, e.g. [18]). An alternative is to look at Simplified models [19] where only the particles and parameters most relevant to the search are included. The simplified model can be understood as a phenomenological sketch of a complete model; for example, in the MSSM this might include only looking at the two lightest supersymmetric particles.

The most model-independent theory of dark matter is to adopt an Effective Field Theory (EFT) which includes only the SM plus the dark matter itself as states in the theory. This approach has led to a fruitful program, in which one enumerates the possible operators describing dark matter interaction and places bounds on each of them (or in combination) from the null results of collider [4, 20–34] and/or astro-particle [35–48] searches. This method's greatest power is that it is very generic. However it suffers from its UV incompleteness and breaks down at energies comparable to the mass of the underlying mediator particle, which can call its applicability into question, particularly at high energy colliders.

The strategy which we employ in this chapter attempts to mediate these issues. A UV complete theory can be formed which is not necessarily a simplification of a particular complete theory, but instead captures features of classes of models. The Simplified models we construct are broad enough to capture features of a certain class of models, while remaining valid at higher energies. Thus, it facilitates relating processes at varying energies, in particular results from collider and direct detection experiments. Specifically, we will examine models involving fermionic dark matter and scalar mediators. For other constructions in similar directions, see Refs. [49–60].

2.2 Simplified Models

Our simplified models contain a fermionic dark matter particle denoted by χ, which is a SM singlet and can be either a Dirac or a Majorana fermion. In addition, our theory contains scalar mediator particles which interact with the dark matter and SM quarks. Given our choice of dark matter which is a SM singlet, this leads to three choices for gauge representations of the mediators under the SM $(SU(3), SU(2))_Y$:

$$(3,1)_{2/3}, \qquad (3,1)_{-1/3}, \qquad (3,2)_{-1/6}. \tag{2.1}$$

We refer to these three choices as the u_R model (with mediators labeled as $\tilde{u}$), the d_R model (with mediators $\tilde{d}$), and the q_L model (with mediators $\tilde{q}$). For each model, the Lagangrian density consists of kinetic terms for χ and the scalar mediators (including their gauge interactions), and a trilinear interaction between χ, the scalar mediator, and the corresponding SM quark. For example, in the u_R model with Dirac DM the Lagrangian density is:

$$\mathcal{L} = i\bar{\chi}\partial\!\!\!/\chi - M_\chi\bar{\chi}\chi + (D_\mu\tilde{u})^*(D^\mu\tilde{u}) - M_{\tilde{u}}^2\tilde{u}^*\tilde{u} + (g_{_{DM}}\tilde{u}^*\bar{\chi}P_R u + h.c.) \tag{2.2}$$

where,

$$D_\mu \equiv \partial_\mu - ig_s G_\mu^a T^a - i\frac{2}{3}eA_\mu, u \equiv \begin{pmatrix} u \\ c \\ t \end{pmatrix}, \qquad \tilde{u} \equiv \begin{pmatrix} \tilde{u} \\ \tilde{c} \\ \tilde{t} \end{pmatrix}, \tag{2.3}$$

such that D_μ defines the appropriate covariant derivative for the scalars, u is the flavor vector of up-type quarks, and $\tilde{u}$ a flavor vector of scalars. Similar actions may be simply written down for the d_R and q_L models, and the kinetic terms for χ may be appropriately modified for the Majorana cases.

Each of our models is constructed with three scalar mediators, in order to implement Minimal Flavor Violation (MFV) [61], with the mediators transforming as triplets under the appropriate factors of the flavor group. This insures that in moving from the gauge to mass basis, the deviations from flavor-universality will be proportional to SM Yukawa interactions, and thus small for the first two generations. In particular, this implies that the leading term (in an expansion in the SM Yukawa matrices Y^u and Y^d) g_{DM} will be equal for all flavors, and that the masses $M_{\tilde{u}}^2$ will be degenerate. We can further rephase χ such that g_{DM} is a real parameter.

While we will not move beyond these leading terms in our analysis, one can easily determine the next terms one would find (continuing to illustrate with the u_R model):

$$\mathcal{L}_{FV} = \left(\delta g_{_{DM}}\ \tilde{u}^* Y^{u\dagger} Y^u \bar{\chi} P_R u + h.c.\right) + \delta m^2\ \tilde{u}^* Y^{u\dagger} Y^u \tilde{u} + \mathcal{O}(Y^4)\ . \tag{2.4}$$

The effect of non-zero $\delta g_{_{DM}}$ and/or δm^2 would be to split apart the couplings and masses of the third generation mediators apart from the still largely degenerate first and second generations. We defer consideration of non-zero $\delta g_{_{DM}}$ and δm^2 to future work.

2.3 Experimental Constraints

2.3.1 Collider Bounds

We derive bounds from CMS results which studied the simplfied model T2 [62], which assumes that the dominant production mode produces two squark-like objects each of which subsequently decays into a jet and a neutralino. They place an upper limit on the production cross section of that process as a function of the masses of the squark and neutralino. For our corresponding process, two scalars are produced and, similarly, each decay into a jet and dark matter particle. The CMS study was conducted at $\sqrt{s} = 8$ TeV with 11.7 fb^{-1} of data. The selection for this study requires 2-4 jets with $p_T > 50$ GeV and $|\eta| < 3.0$, where the two most energetic jets have $p_T > 100$ GeV and $|\eta| < 2.5$. Events with an isolated electron or muon with $p_T > 10$ GeV and events with an isolated photon with $p_T > 25$ GeV are vetoed. Events are also required to have $H_T > 275$ GeV and $\alpha_T > 0.55$. See [62] for more detailed information.

We simulate production cross sections (including the decays) with used MadGraph 1.5.9 [63] with model files implemented in FeynRules 1.7 [64]. We simulate at $\sqrt{s} = 8$ TeV and using the CTEQ6L pdf set. We have verified that we can reproduce the CMS limits for QCD production of light squarks, up to the fact that CMS uses NLO cross sections from Prospino [65] whereas we use leading order cross sections. To convert cross section limits into limits on our parameter, g_{DM}, we use a bisection method, choosing the interval $g_{DM} = 0$ to 4π. Larger values correspond to non-perturbative coupling, which would call into question the validity of the simplified model as an effective field theory.

We leave for future work consideration of other processes, such as the mono-jet process, $pp \to \chi\overline{\chi}j$ and associated production such as $pp \to \chi\widetilde{u}$. These processes lead to a distinct signature and may help fill in the regime where the dark matter and the mediator are quasi-degenerate in mass, but otherwise tend to provide weaker bounds than mediator pair production for $g_{DM} \lesssim g_s$. It would be worthwhile to include these processes in a full collider analysis. In addition, the q_L model could lead to leptonic signals due to transitions between the $\widetilde{u}$ and $\widetilde{d}$ states resulting in W bosons, once one includes the mass splitting effects from the terms analogous to Equation (2.4).

The derived limits are shown for all three Dirac models in Figure 2.1 and for the Majorana models in Figure 2.2. In both figures, the white regions correspond to regions not considered by CMS, because the mediator and dark matter are too degenerate in mass to efficiently pass the analysis cuts (and in addition, much of this parameter space is theoretically inaccessible because the scalar mediators are lighter than the χ), whereas the black regions are simply excluded by the CMS bounds for all values of g_{DM}. The excluded regions are largely similar for both the Majorana and Dirac cases, where the limit is driven by gluon fusion into a scalar mediator and its anti-particle. However, in some regions the bounds are stronger for Majorana dark matter, which has the additional production process of two scalar mediators from a qq initial state by exchanging the Majorana χ in the t-channel.

2.3.2 Direct Detection Bounds

Elastic scattering of χ involves momentum transfers far below any mediator mass of interest, and the contributions to spin-independent (SI) and spin-dependent (SD) scattering are most easily extracted by computing the contact interaction between two χ's and two quarks. Using the u_R model as an example, the matrix element for $\chi u \to \chi u$ is:

$$\mathcal{M} = (-ig_{DM})^2(\bar{\chi}P_R u)\frac{i}{p^2 - M_{\tilde{u}}^2}(\bar{u}P_L\chi) \tag{2.5}$$

$$\approx (-ig_{DM})^2(\bar{\chi}P_R u)\frac{-i}{M_{\tilde{u}}^2 - M_\chi^2}(\bar{u}P_L\chi) \tag{2.6}$$

Where in the second line we take the limit of small momentum transfer. Applying a generalized Fierz transformation [66] yields,

$$\mathcal{M} = \frac{ig_{DM}^2}{M_{\tilde{u}}^2 - M_\chi^2}\frac{1}{2}(\bar{\chi}\gamma^\mu P_L\chi)(\bar{u}\gamma_\mu P_R u) \tag{2.7}$$

$$\begin{aligned} = \frac{ig_{DM}^2}{M_{\tilde{u}}^2 - M_\chi^2}\frac{1}{8}[&(\bar{\chi}\gamma^\mu\chi)(\bar{u}\gamma_\mu u) - (\bar{\chi}\gamma^\mu\gamma^5\chi)(\bar{u}\gamma_\mu\gamma_5 u) \\ &+(\bar{\chi}\gamma^\mu\gamma^5\chi)(\bar{u}\gamma_\mu u) - (\bar{\chi}\gamma^\mu\chi)(\bar{u}\gamma_\mu\gamma_5 u)] \end{aligned} \tag{2.8}$$

$$\approx \frac{ig_{DM}^2}{M_{\tilde{u}}^2 - M_\chi^2}\frac{1}{8}[(\bar{\chi}\gamma^\mu\chi)(\bar{u}\gamma_\mu u) - (\bar{\chi}\gamma^\mu\gamma^5\chi)(\bar{u}\gamma_\mu\gamma_5 u)] \tag{2.9}$$

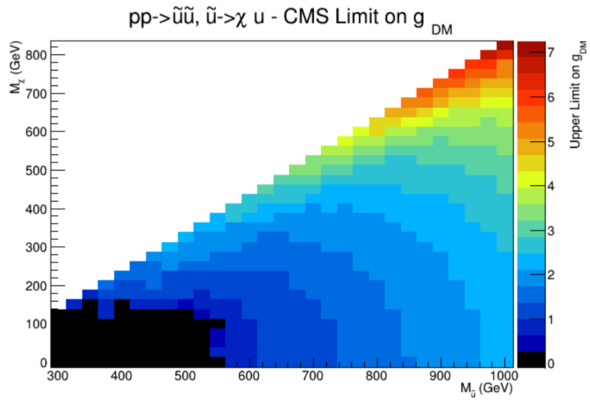

(a)

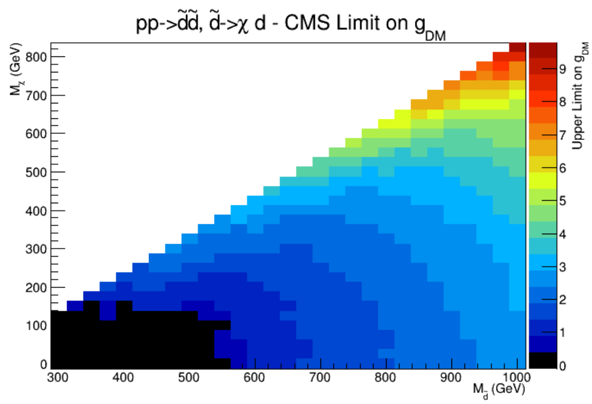

(b)

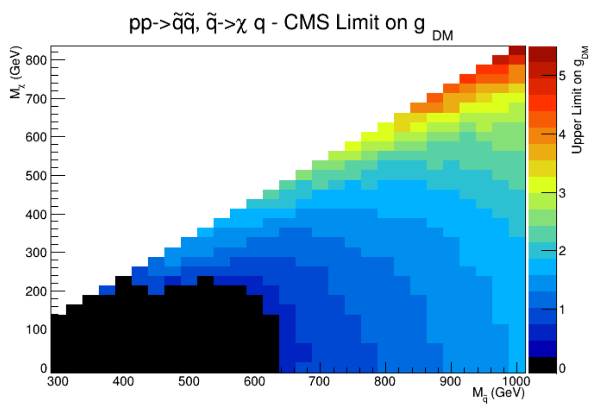

(c)

Figure 2.1: Bounds on the the coupling g_{DM} for each of the three simplified models with Dirac Dark Matter, from the CMS collider bounds. (a) is the u_R model, (b) the d_R model, and (c) is the q_L model.

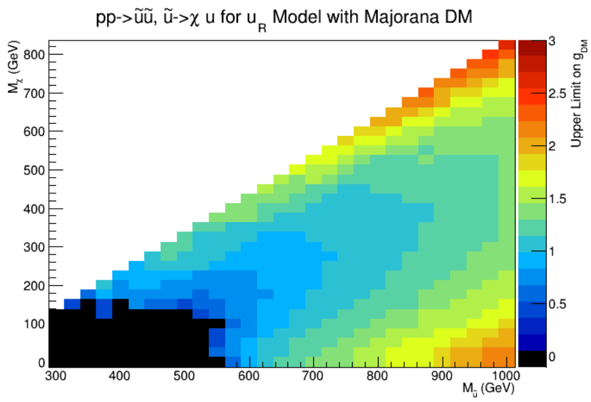

(a)

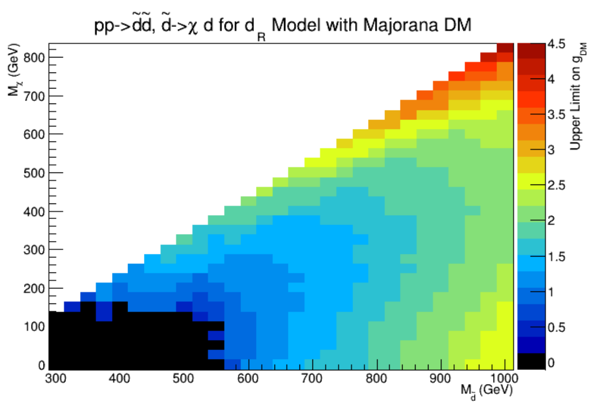

(b)

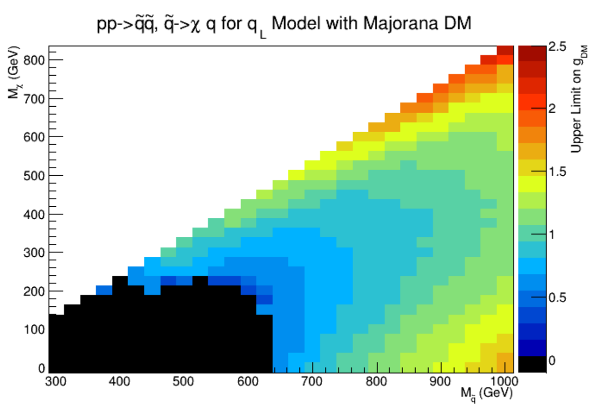

(c)

Figure 2.2: Bounds on the the coupling g_{DM} for all three models with Majorana Dark Matter, from the CMS collider bounds.

where (as discussed in, e.g. [67]) we have dropped terms suppressed by the dark matter velocity. The two remaining terms result in spin-independent and spin-dependent scattering, respectively. In the u_R model, this results in cross sections for SI and SD scattering with a nucleon:

$$\sigma_{SI}^{u_R} = \frac{1}{64\pi}\frac{M_N^2 M_\chi^2}{(M_N + M_\chi)^2}\frac{g_{DM}^4}{(M_{\tilde{u}}^2 - M_\chi^2)^2}\left(1 + \frac{Z}{A}\right)^2 \quad (2.10)$$

$$\sigma_{SD}^{u_R} = \frac{3}{64\pi}\frac{M_N^2 M_\chi^2}{(M_N + M_\chi)^2}\frac{g_{DM}^4}{(M_{\tilde{u}}^2 - M_\chi^2)^2}(\Delta u^N)^2 \quad (2.11)$$

where Z, A, and $N = p, n$ specifies the nucleon of interest and the structure functions Δu^N can be found, for example, in Refs. [67, 68]. Note that this theory has different SI cross sections for protons and neutrons.

A similar calculation for the d_R and q_L Dirac models yields:

$$\sigma_{SI}^{d_R} = \frac{1}{64\pi}\frac{M_N^2 M_\chi^2}{(M_N + M_\chi)^2}\frac{g_{DM}^4}{(M_{\tilde{d}}^2 - M_\chi^2)^2}\left(2 - \frac{Z}{A}\right)^2 \quad (2.12)$$

$$\sigma_{SD}^{d_R} = \frac{3}{64\pi}\frac{M_N^2 M_\chi^2}{(M_N + M_\chi)^2}\frac{g_{DM}^4}{(M_{\tilde{d}}^2 - M_\chi^2)^2}(\Delta d^N + \Delta s^N)^2 \quad (2.13)$$

$$\sigma_{SI}^{q_L} = \frac{9}{64\pi}\frac{M_N^2 M_\chi^2}{(M_N + M_\chi)^2}\frac{g_{DM}^4}{(M_{\tilde{q}}^2 - M_\chi^2)^2} \quad (2.14)$$

$$\sigma_{SD}^{q_L} = \frac{3}{64\pi}\frac{M_N^2 M_\chi^2}{(M_N + M_\chi)^2}\frac{g_{DM}^4}{(M_{\tilde{q}}^2 - M_\chi^2)^2}(\Delta u^N + \Delta d^N + \Delta s^N)^2 \quad (2.15)$$

And likewise the cross sections for Majorana DM are also computed for each model:

$$\sigma_{SD}^{u_R} = \frac{3}{16\pi}\frac{M_N^2 M_\chi^2}{(M_N + M_\chi)^2}\frac{g_{DM}^4}{(M_{\tilde{d}}^2 - M_\chi^2)^2}(\Delta u^N)^2 \quad (2.16)$$

$$\sigma_{SD}^{d_R} = \frac{3}{16\pi}\frac{M_N^2 M_\chi^2}{(M_N + M_\chi)^2}\frac{g_{DM}^4}{(M_{\tilde{d}}^2 - M_\chi^2)^2}(\Delta d^N + \Delta s^N)^2 \quad (2.17)$$

$$\sigma_{SD}^{q_L} = \frac{3}{16\pi}\frac{M_N^2 M_\chi^2}{(M_N + M_\chi)^2}\frac{g_{DM}^4}{(M_{\tilde{d}}^2 - M_\chi^2)^2}(\Delta u^N + \Delta d^N + \Delta s^N)^2 \quad (2.18)$$

Note that since a Majorana fermion has a vanishing vector bilinear, there are only spin-dependent cross-sections for the Majorana DM cases[1].

For Dirac dark matter, this class of simplified models results in roughly comparable spin-independent and dependent cross sections. Since the SI bounds at a given dark matter mass are currently much lower than the corresponding SD ones, they dominate the constraints. We translate the limits from XENON100 [69] and XENON10 [70] into bounds on g_{DM} at every point in the plane of the dark matter and mediator masses. For Majorana dark matter, the dominant constraint is from the SD interaction, with the best experimental limits for neutrons and protons arising from XENON100 [71] and PICASSO [72], respectively. It turned out in all cases that the PICASSO limit was weaker than the CMS limit corresponding to that point of parameter space.

Applying these limits, the results for Dirac dark matter are shown in Figure 2.3 (with a zoomed in view of the small dark matter mass region in Figure 2.4 from Xenon10 limits), and for Majorana dark matter in 2.5. In these plots, the white regions indicate theoretically inaccessible regions with colored mediators lighter than the dark matter itself. For large M_χ, the XENON limits are slowly varying and nearly linear. In this regime, the elastic scattering cross section is approximately independent of M_χ and we observe the expected behavior where the curves of constant g_{DM} go like $(M_\chi^2 - M_{\tilde{q}}^2)^{-2}$, similar to the dependence of the direct detection cross section on the two masses. For $M_\chi \lesssim 10$ GeV, the limit on g_{DM} from XENON weakens very rapidly as the experiments approach their threshold for observable scattering. In turn, this allows g_{DM} to be much larger as M_χ decreases. This feature is illustrated in 2.4 where we have zoomed into a much smaller scale of M_χ to more clearly show the behavior in this regime.

[1]It would be interesting to compute the induced SI cross section at one-loop for this class of simplified model.

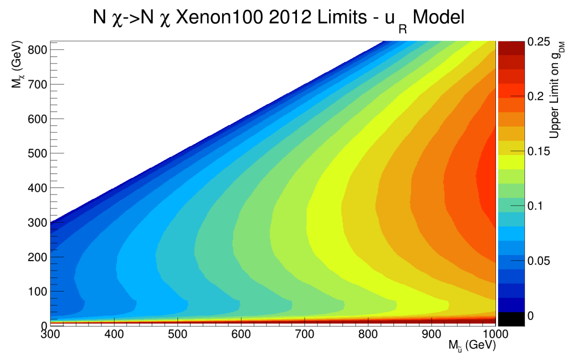

(a)

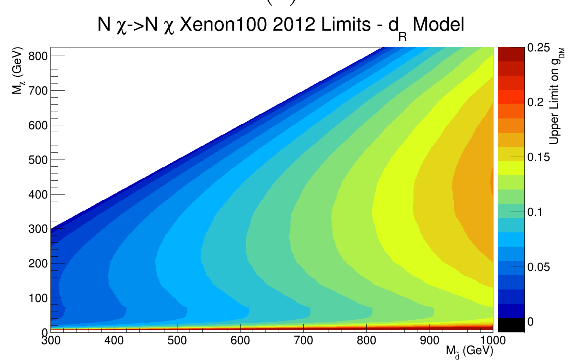

(b)

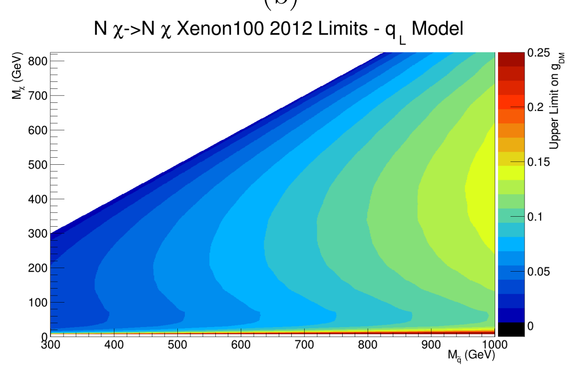

(c)

Figure 2.3: Bounds on the the coupling g_{DM} for all three models with Dirac Dark Matter, from the spin-independent XENON100 Limits.

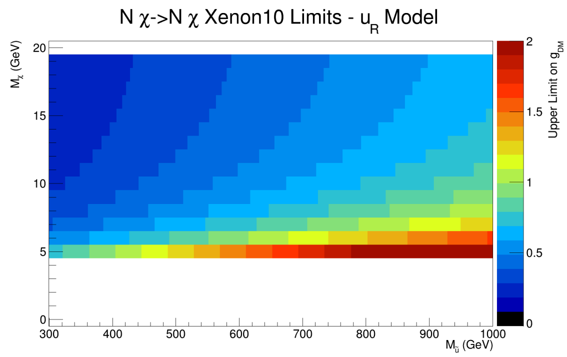

(a)

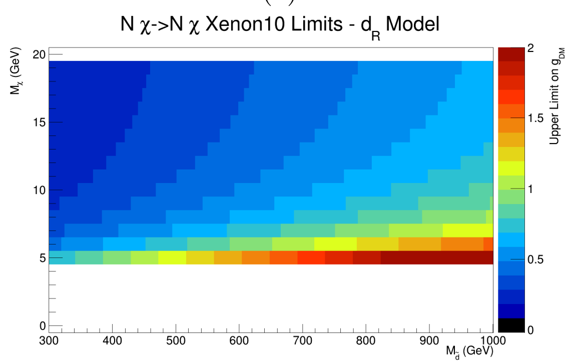

(b)

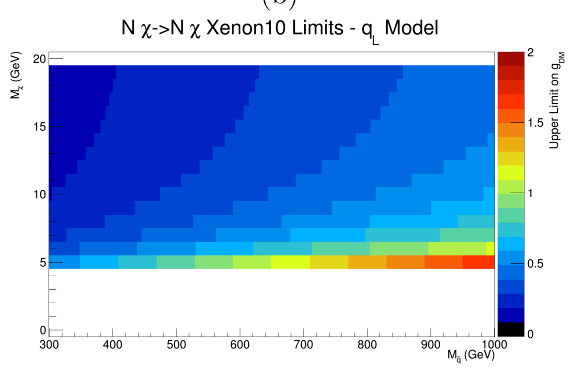

(c)

Figure 2.4: Dirac Dark Matter bounds on g_{DM} from the spin-indepedent XENON10 Limits.

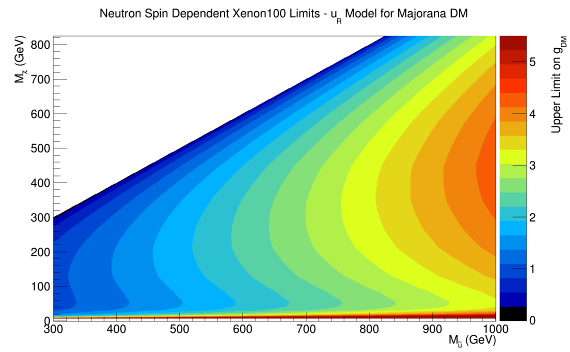

(a)

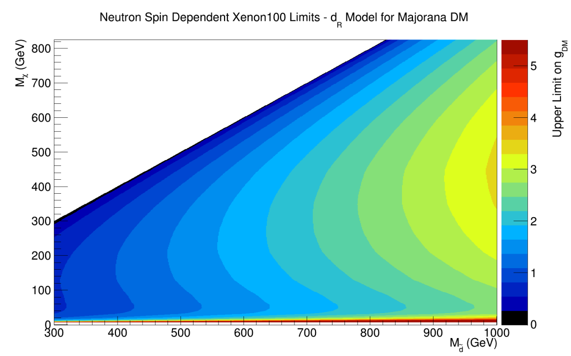

(b)

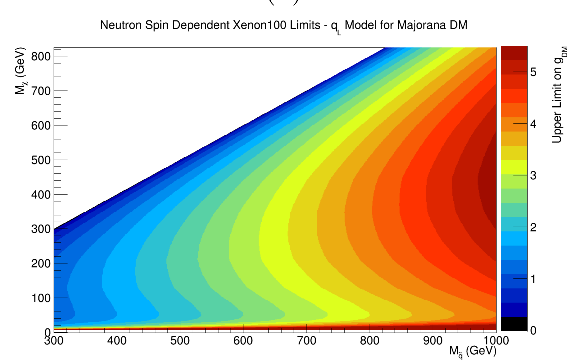

(c)

Figure 2.5: Bounds on g_{DM} from neutron-WIMP spin-dependent XENON100 Limits on Majorana Dark Matter.

2.4 Results

We determine combined limits by first applying the CMS bounds, and overlaying those from direct detection, replacing the existing limit on g_{DM} only when the direct detection limit is stronger than the collider one. The resulting limits are shown in Figure 2.6 for Dirac dark matter, and in Figure 2.7 for Majorana dark matter. Generically, the most tightly bounded case is the q_L model, due to its larger number of colored states which can either be produced at the collider or mediate elastic scattering. However, the contribution to the SD elastic scattering in the Majorana model exhibits destructive interference between up-quarks and down-quarks, which allows for weaker constraints in that case.

These results illustrate an important complementarity between experimental probes of dark matter. In addition to the well-known cases where colliders dominate direct detection bounds for very light dark matter and/or dark matter with predominantly spin-dependent interactions, we also see a different kind of complementarity. Because colliders can access the mediators directly through QCD production, they can rule out cases where the mediator mass is light enough. Instead, direct detection cannot rule out a model, but generically places the strongest limits on g_{DM} for Dirac dark matter which has SI interactions. For the Majorana cases, the SD limits are typically weak enough so as to be subdominant to the collider bounds, except for very degenerate spectra.

2.4.1 Forecasts for Future Experiments

Based on the combined bounds of Figures 2.6 and 2.7, we can make forecasts for what other types of experiments might hope to see in this class of simplified model. For example, for the Dirac dark matter, there SD interactions which correspond to the maximum values of g_{DM} at each mass point. In Figures 2.8 and 2.9, we show the maximum allowed spin-dependent

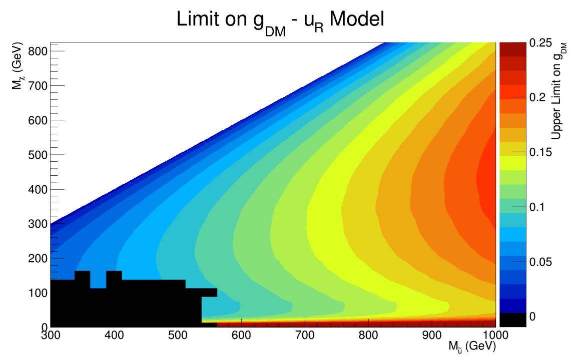

(a)

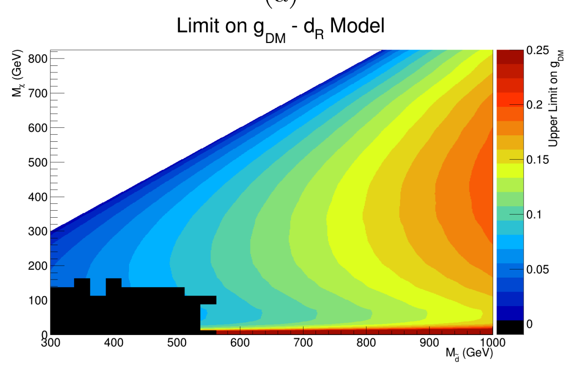

(b)

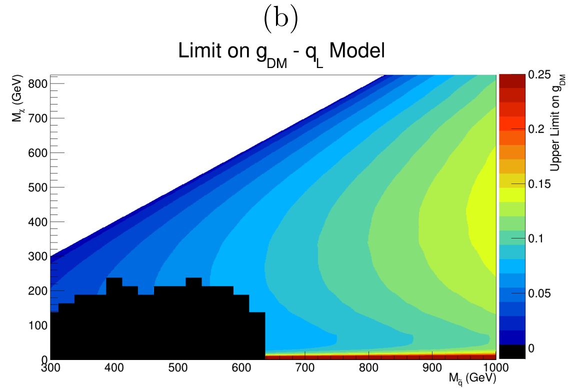

(c)

Figure 2.6: The combined lowest bounds on g_{DM} from CMS, XENON100, and XENON10 for Dirac Dark Matter.

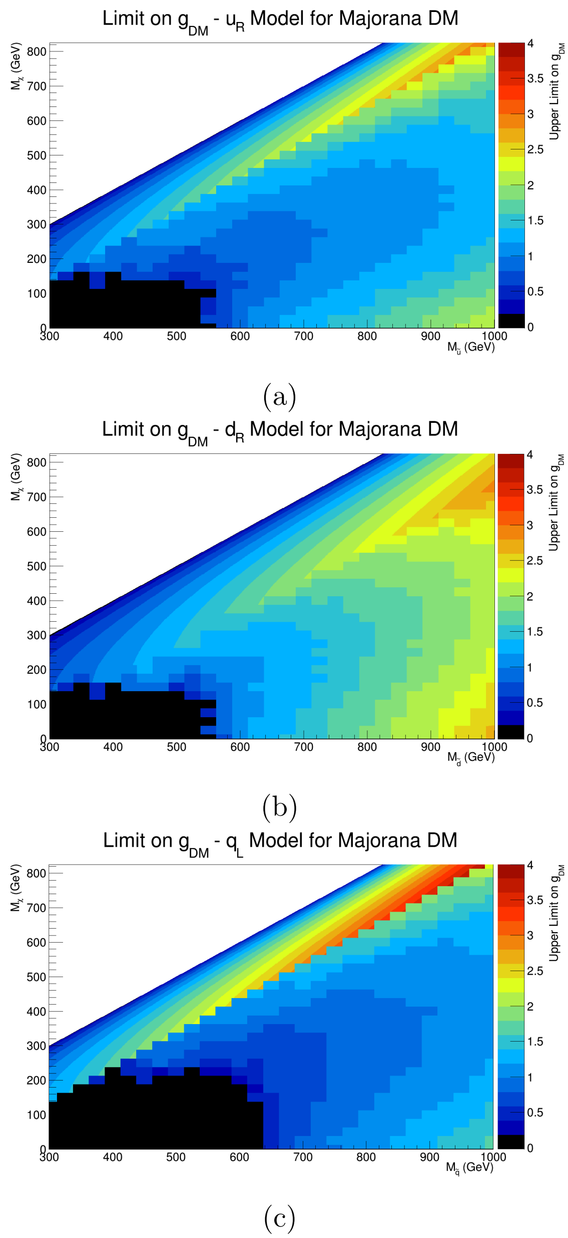

Figure 2.7: The combined lowest limit on g_{DM} from CMS and XENON100 for Majorana Dark Matter.

cross section on neutrons and protons (respectively), given the constraints from colliders and XENON. Based on these results, the outlook for SD searches is such that large improvements over the current generations of experiments will be necessary if a Dirac simplified model of the type considered here accurately represents the low energy physics of dark matter. In contrast, the forecast for SD searches for Majorana dark matter, shown in Figures 2.10 and 2.11, show that there is hope in the near-future for these searches to make a discovery.

Another very important observable is the annihilation cross section. We compute the thermally averaged annihilation cross section to all possible quark pairs $\langle \sigma v \rangle$ at the time of freeze-out using micrOMEGAS [73] and the results are shown in Figures 2.12 and 2.13. These figures indicate that for this class of simplified model, the bounds from colliders and direct detection are already strong enough that additional annihilation channels would be required to allow for the dark matter to be a thermal relic with a standard cosmology if it is Dirac. Instead, if it is Majorana, there are accessible regions where it could be a standard thermal relic.

2.5 Outlook

We have considered simplified models where the dark matter is either a Dirac or Majorana fermion, and interacts with a quark as well as a colored mediator. We found that the demands of gauge invariance suggest that when the dark matter is an electroweak singlet, only three classes of mediator are possible. Minimal flavor violation further suggests that the couplings and masses of the mediators are flavor-universal, with some freedom with respect to the third generation that we chose not to explore here. It is worth emphasizing that we have been pushed toward a simplified model that essentially already existed to interpret searches for squark-like states. We have found that by trading the LHC production cross section as one of its defining parameters for the strength of the coupling of the dark matter to a quark

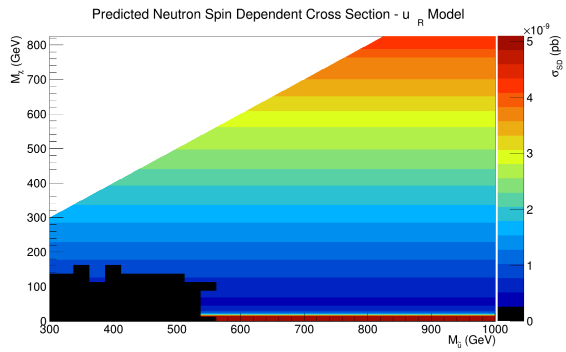

(a)

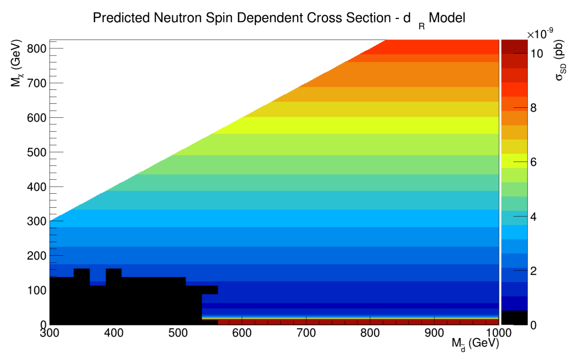

(b)

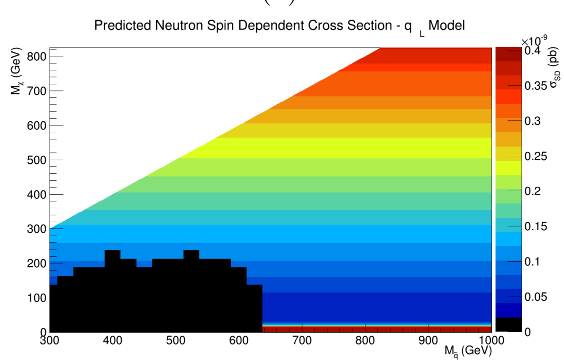

(c)

Figure 2.8: The predicted maximum spin-dependent neutron-DM cross section from the combined Collider and Direct Detection bounds for Dirac Dark Matter.

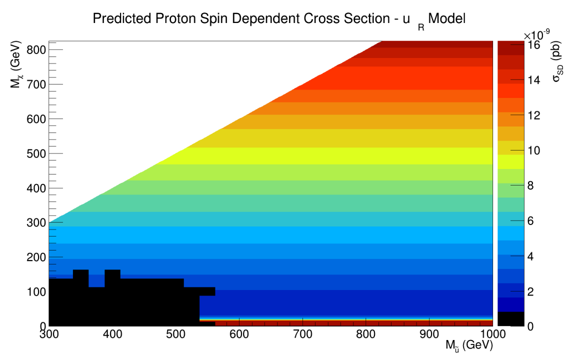

(a)

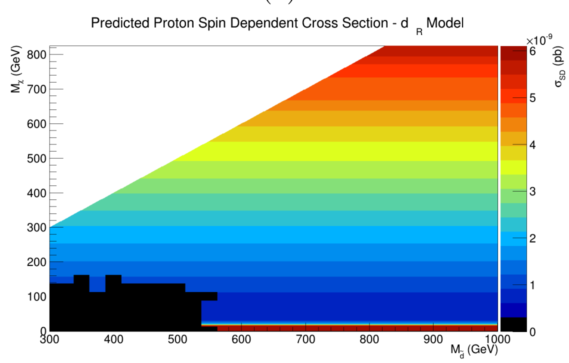

(b)

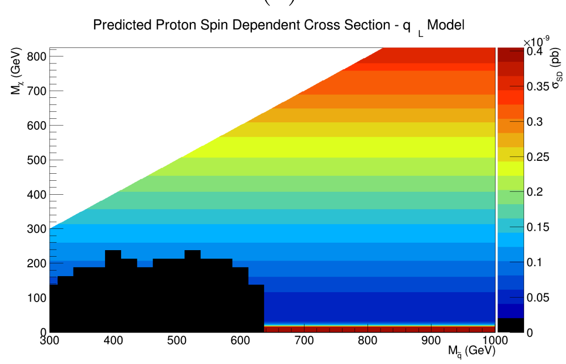

(c)

Figure 2.9: The predicted maximum spin-dependent proton-DM cross section from the combined Collider and Direct Detection bounds for Dirac Dark Matter

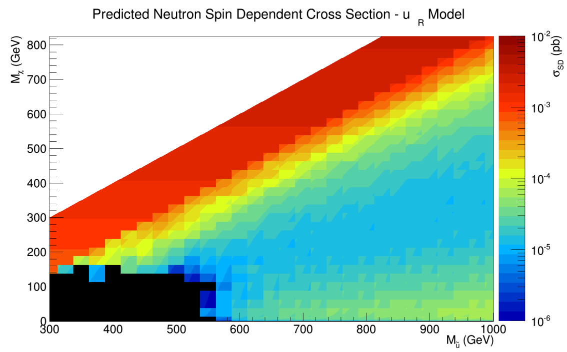

(a)

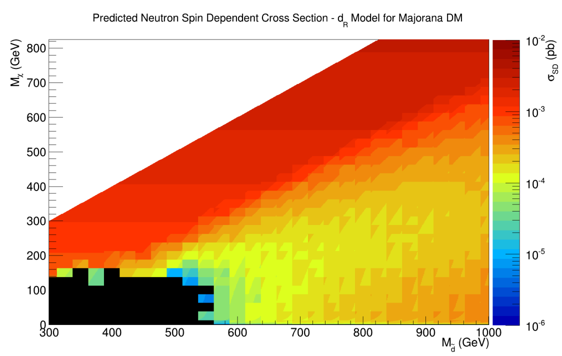

(b)

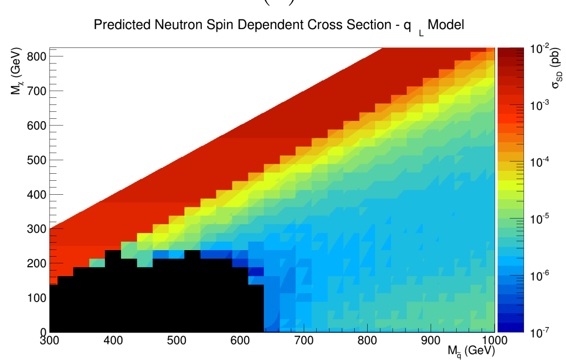

(c)

Figure 2.10: The predicted maximum spin-dependent neutron-DM cross section from the combined Collider and Direct Detection bounds for Majorana Dark Matter

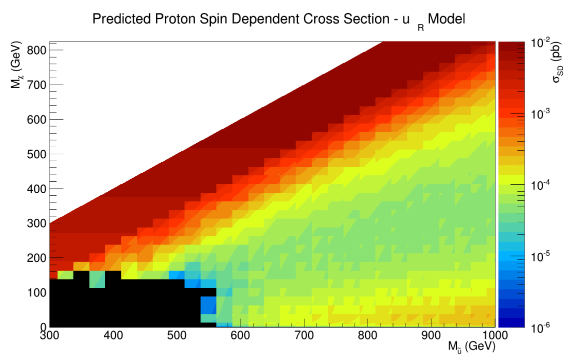

(a)

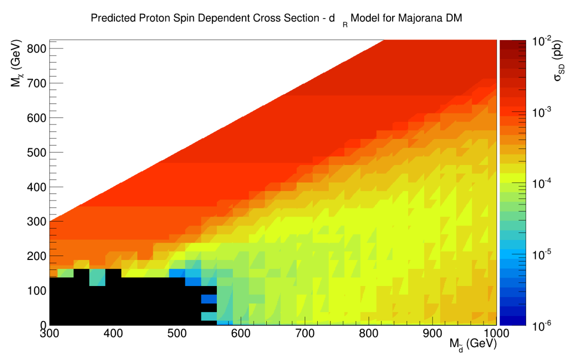

(b)

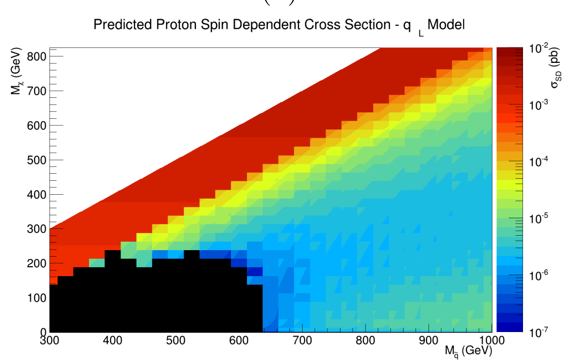

(c)

Figure 2.11: The predicted maximum spin-dependent proton-DM cross section from the combined Collider and Direct Detection bounds for Majorana Dark Matter

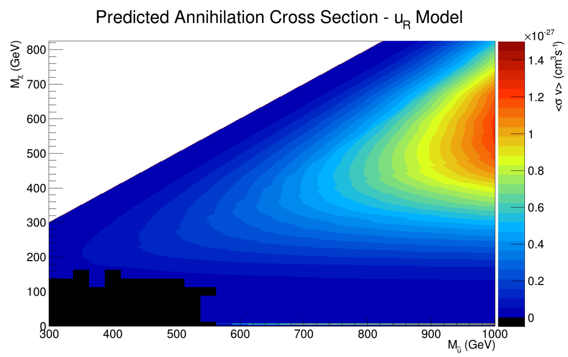

(a)

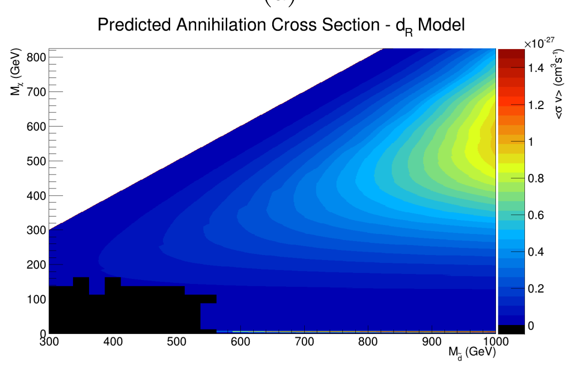

(b)

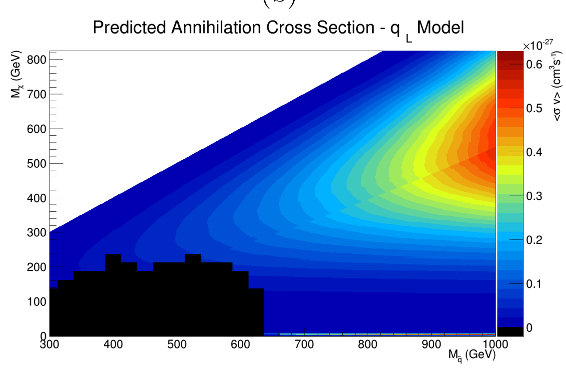

(c)

Figure 2.12: The predicted maximum annihilation cross section from the combined Collider and Direct Detection bounds for Dirac Dark Matter

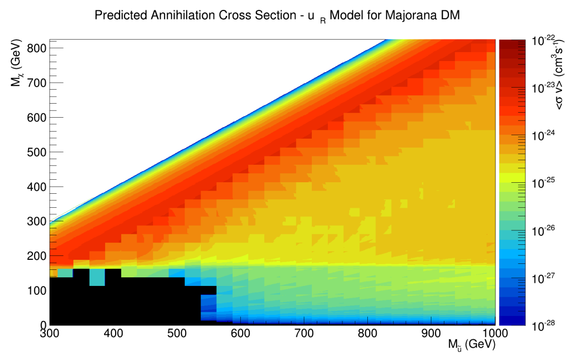

(a)

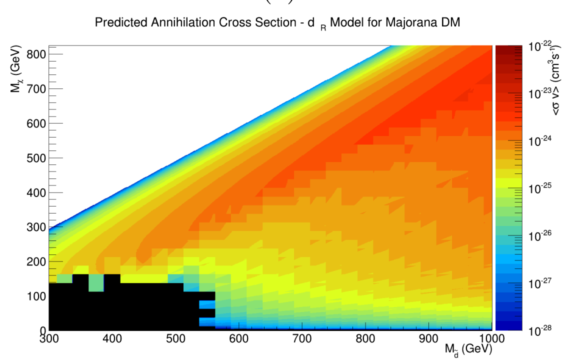

(b)

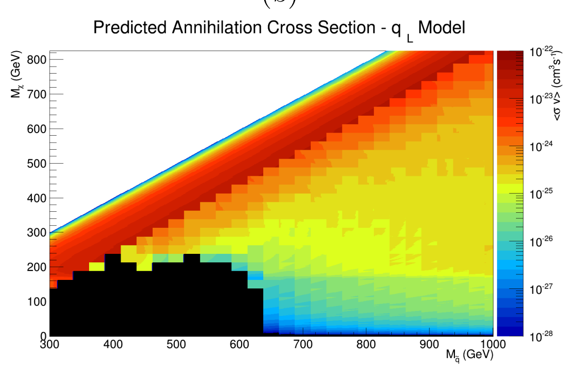

(c)

Figure 2.13: The predicted maximum annihilation cross section from the combined Collider and Direct Detection bounds for Majorana Dark Matter

and a scalar mediator, we arrive at a full effective field theory with the same number of parameters, but capable of describing the physics of dark matter even outside of the context of colliders.

We have derived the bounds from collider searches and elastic scattering of the dark matter from nuclei via either spin-independent or spin-dependent interactions. We find that the two probes are complementary to one another, and provide different kinds of information. The summarized bounds for Dirac and Majorana dark matter are shown in Figures 2.6 and 2.7, which represent our best knowledge to date of such constructions. These simplified models are potentially UV-complete sketches of dark matter, and can realistically capture some of its most important features. If a robust detection of dark matter lies in the near future, the first step to establishing it as dark matter and putting it into the context of particle physics will be to explore these models and their close cousins, to determine which ones seem to most accurately explain the experimental data. Ultimately, the hope is to connect with a complete theory of dark matter which will extend the SM into a more fundamental theory.

Note that Refs. [74–76] have conducted a similar study with a substantial overlap with the ideas presented here, though assumptions and presentation have small variations.

Chapter 3

Mono-Higgs: a new collider probe of dark matter

Based on arXiv:1312.2592 [77]

3.1 Introduction

Although most of the matter in the Universe is dark matter (DM), its underlying particle nature remains unknown and cannot be explained within the Standard Model (SM). Many DM candidates have been proposed, largely motivated in connection with new physics at the electroweak symmetry breaking scale [78, 79]. Weak-scale DM also naturally accounts for the observed relic density via thermal freeze-out [80]. With the discovery of the Higgs boson [81, 82], a new window to DM has opened. If DM is indeed associated with the scale of electroweak symmetry breaking, Higgs-boson-related signatures in colliders are a natural place to search for it.

Invisible Higgs boson decays provide one well-known avenue for exploring possible DM-Higgs-boson couplings, provided such decays are kinematically allowed. Null results from searches at the Large Hadron Collider (LHC) for an invisibly decaying Higgs boson produced in association with a Z boson, combined with current Higgs boson data, already provide a model-independent constraint on the Higgs invisible branching ratio of $\mathcal{B}_{\text{inv}} < 38\%$ at 95% CL [83]; see Ref. [84] for results in Wh. On the other hand, invisible Higgs boson decays are not sensitive to DM with mass above $m_h/2 \approx 60$ GeV. Therefore, it is clearly worthwhile to investigate other Higgs-boson-related collider observables.

DM production at colliders is characterized by missing transverse energy ($\not{E}_T$) from DM particles escaping the detector and recoiling against a visible final state X. Recent mono-X studies at the LHC have searched for a variety of different $X + \not{E}_T$ signals, such as where X is a hadronic jet (j) [85, 86], photon (γ) [87, 88], or W/Z boson [33, 84]. The discovery of the Higgs boson opens a new collider probe of dark matter. This chapter explores the theoretical and experimental aspects of this new LHC signature of dark matter: DM pair production in association with a Higgs boson, $h\chi\chi$, dubbed 'mono-Higgs', giving a detector signature of $h + \not{E}_T$. We consider mono-Higgs signals in four final state channels for h: $b\bar{b}$, $\gamma\gamma$, and $ZZ^* \to 4\ell$ and $ZZ^* \to \ell\ell jj$.

There is an important difference between mono-Higgs and other mono-X searches. In proton-proton collisions, a $j/\gamma/W/Z$ can be emitted directly from a light quark as initial state radiation (ISR) through the usual SM gauge interactions, or it may be emitted as part of the new effective vertex coupling DM to the SM. In contrast, since Higgs boson ISR is highly suppressed due to the small coupling of the Higgs boson to quarks, a mono-Higgs is preferentially emitted as part of the effective vertex itself. In a sense, a positive mono-Higgs signal would probe directly the structure of the effective DM-SM coupling.

Mono-X studies have largely followed two general paths. In the effective field theory (EFT) approach, one introduces different non-renormalizable operators that generate $X+\not{E}_T$ without specifying the underlying ultraviolet (UV) physics. Since the operators are non-renormalizable, they are suppressed by powers of $1/\Lambda$, where Λ is the effective mass scale of

UV particles that are integrated out. Alternatively, in the simplified models approach, one considers an explicit model where the UV particles are kept as degrees of freedom in the theory. Although the EFT approach is more model-independent, it cannot be used reliably when the typical parton energies in the events are comparable to Λ [89], and additionally it is blind to possible constraints on the UV physics generating its operators (e.g., dijet resonance searches). Simplified models avoid these short-comings, but at the expense of being more model-dependent. The two approaches are therefore quite complementary and in the present chapter, we consider both.

The remainder of this chapter is outlined as follows. In Sec. 3.2, we construct both EFT operators and simplified models for generating mono-Higgs signatures at the LHC. Our simplified models consist of DM particles coupled to the SM through an s-channel mediator that is either a Z' vector boson or a scalar singlet S. In Sec. 3.3, we assess the sensitivity of LHC experiments to mono-Higgs signals at the 8 TeV and 14 TeV LHC, with 20 fb^{-1} and 300 fb^{-1} respectively, in four Higgs boson decay channels ($b\bar{b}$, $\gamma\gamma$, 4ℓ, $\ell\ell jj$), including both new physics and SM backgrounds. In Sec. 3.5, we conclude.

3.2 New physics operators and models

We describe new physics interactions between DM and the Higgs boson that may lead to mono-Higgs signals at the LHC. In all cases, the DM particle is denoted by χ and may be a fermion or scalar. We also assume χ is a gauge singlet under $SU(3)_C \times SU(2)_L \times U(1)_Y$.

First, we consider operators within an EFT framework where χ is the only new degree of freedom beyond the SM. Next, we consider simplified models with an s-channel mediator coupling DM to the SM. For both cases, Fig. 3.1 illustrates schematically the basic Feynman diagram for producing $h + \not\!\!E_T$ (although not *all* models considered here fit within this topol-

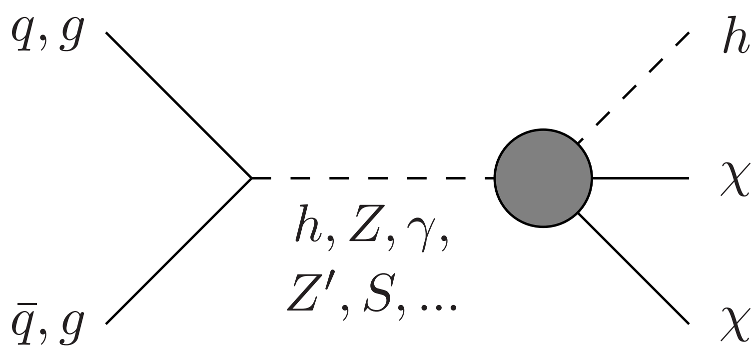

Figure 3.1: Schematic diagram for mono-Higgs production in pp collisions mediated by electroweak bosons (h, Z, γ) or new mediator particles such as a Z' or scalar singlet S. The gray circle denotes an effective interaction between DM, the Higgs boson, and other states.

ogy). Quarks or gluons from pp collisions produce an intermediate state (e.g., an electroweak boson or a new mediator particle) that couples to $h\chi\chi$.

At the end of this section, we identify several benchmark scenarios (both EFT operators and simplified models) that we consider in our mono-Higgs study, see Table 3.1.

3.2.1 Effective operator models

The simplest operators involve direct couplings between DM particles and the Higgs boson through the Higgs portal $|H|^2$ [90–96]. For scalar DM, we have a renormalizable interaction at dimension-4:

$$\lambda |H|^2 \chi^2 \,, \tag{3.1}$$

where χ is a real scalar and λ is a coupling constant. For (Dirac) fermion DM, we have two operators at dimension-5:

$$\frac{1}{\Lambda}|H|^2 \bar{\chi}\chi \,, \quad \frac{1}{\Lambda}|H|^2 \bar{\chi} i\gamma_5 \chi \,, \tag{3.2}$$

suppressed by a mass scale Λ. Mono-Higgs can arise via $gg \to h^* \to h\chi\chi$ through these operators. However, it is important to note that these interactions lead to invisible Higgs boson decay for $m_\chi < m_h/2$. Treating each operator independently, the partial widths in each case are

$$\Gamma(h \to \chi\chi) = \frac{\lambda^2 v^2}{4\pi m_h} \qquad \text{scalar } \chi \tag{3.3a}$$

$$\Gamma(h \to \chi\bar{\chi}) = \frac{v^2 m_h}{8\pi\Lambda^2} \qquad \text{fermion } \chi \tag{3.3b}$$

neglecting $\mathcal{O}(m_\chi^2/m_h^2)$ terms, where $v \approx 246$ GeV is the Higgs vacuum expectation value. If invisible decays are kinetimatically open, it is required that $\lambda \lesssim 0.016$ ($\Lambda \gtrsim 10$ TeV) for scalar (fermion) DM to satisfy $\mathcal{B}_{\rm inv} < 38\%$ obtained in Ref. [83]. In this case, since the couplings must be so suppressed, the leading mono-Higgs signals from DM are from di-Higgs production where one of the Higgs bosons decays invisibly, as we show below. On the other hand, if $m_\chi \gtrsim m_h$, invisible Higgs boson decay is kinematically blocked and the DM-Higgs couplings can be much larger.

At dimension-6, there arise several operators that give mono-Higgs signals through an effective h-Z-DM coupling. For scalar DM, we have

$$\frac{1}{\Lambda^2}\chi^\dagger i\overleftrightarrow{\partial^\mu}\chi H^\dagger i D_\mu H \tag{3.4}$$

while for fermionic DM we have

$$\frac{1}{\Lambda^2}\bar{\chi}\gamma^\mu\chi H^\dagger i D_\mu H\,, \quad \frac{1}{\Lambda^2}\bar{\chi}\gamma^\mu\gamma_5\chi H^\dagger i D_\mu H\,. \tag{3.5}$$

When the Higgs acquires its vev, the Higgs bilinear becomes

$$\frac{1}{\Lambda^2}H^\dagger i D_\mu H \;\to\; -\frac{g_2 v^2}{4c_W\Lambda^2}Z_\mu\Big(1+\frac{h}{v}\Big)^2\,, \tag{3.6}$$

where g_2 is the $SU(2)_L$ gauge coupling and $c_W \equiv \cos\theta_W$ is the cosine of the weak mixing angle. Thus, these operators generate mono-Higgs signals via $q\bar{q} \to Z^* \to h\chi\chi$. However, for $m_\chi < m_Z/2$, these operators are strongly constrained by the invisible Z width. The partial width for scalar DM is

$$\Gamma(Z \to \chi\chi^\dagger) = \frac{g_2^2 v^4 m_Z}{768\pi c_W^2 \Lambda^4} \quad \text{scalar } \chi\,, \tag{3.7}$$

neglecting $\mathcal{O}(m_\chi^2/m_Z^2)$ terms. For fermionic DM, the partial width is larger by a factor of four for either of the operators in Eq. (3.5). Requiring $\Gamma_Z^{\rm inv} \lesssim 3$ MeV [97] imposes that $\Lambda \gtrsim 400$ GeV (550 GeV) for scalar (fermion) DM if such decays are kinematically open.

At higher dimension, there are many different operators to consider for coupling $h\chi\chi$ to additional SM fields. Here we focus in particular on operators arising at dimension-8 that couple DM particles and the Higgs field with electroweak field strength tensors [98]. (Such operators have been considered recently in connection with indirect detection signals [98,99].) For fermionic DM, there are many such operators, e.g.,

$$\frac{1}{\Lambda^4}\bar\chi\gamma^\mu\chi B_{\mu\nu} H^\dagger D^\nu H\,, \qquad \frac{1}{\Lambda^4}\bar\chi\gamma^\mu\chi W^a_{\mu\nu} H^\dagger t^a D^\nu H \tag{3.8a}$$

$$\frac{1}{\Lambda^4}\bar\chi\sigma^{\mu\nu}\chi B_{\mu\nu} H^\dagger H\,, \qquad \frac{1}{\Lambda^4}\bar\chi\sigma^{\mu\nu}\chi W^a_{\mu\nu} H^\dagger t^a H \tag{3.8b}$$

where $W^a_{\mu\nu}$ and $B_{\mu\nu}$ are the $SU(2)_L$ and $U(1)_Y$ field strength tensors, respectively. Additional operators arise where $\bar\chi\gamma^\mu\chi$ can be replaced by the axial current $\bar\chi\gamma^\mu\gamma_5\chi$, or the field strength tensors are replaced with their duals. For illustrative purposes, we investigate the mono-Higgs signals from one operator

$$\frac{1}{\Lambda^4}\bar\chi\gamma^\mu\chi B_{\mu\nu} H^\dagger D^\nu H\,. \tag{3.9}$$

This operator leads to $h + \not{E}_T$ via $q\bar q \to Z^*/\gamma^* \to h\chi\chi$. It is noteworthy that the Feynman rule for this process involves derivative couplings, i.e., $\partial_\mu Z_\nu \partial^\nu h$. Consequently, compared to our other effective operators, this one leads to a harder $\not{E}_T$ spectrum and has by far the best kinematic acceptance efficiency, as we show below. We also note that the operators in (3.8) also induce mono-$W/Z/\gamma$ signals, as required by gauge invariance, when both Higgs fields H are replaced by v. For a single operator, the ratio between mono-$h/W/Z/\gamma$ is fixed, and therefore constraints on each channel are relevant. In the presence of a signal, on the other hand, all channels are complementary in disentangling the underlying operator(s).

3.2.2 Simplified models

Beyond the EFT framework, it is useful to consider simple, concrete models for how DM may couple to the visible sector. Simplified models provide a helpful bridge between bottom-up EFT studies and realistic DM models motivated by top-down physics [19]. Here, we explore a few representative scenarios where the dark and visible sectors are coupled through a new massive mediator particle. Mono-Higgs signals are a prediction of these scenarios since in general the mediator may couple to the Higgs boson.

Vector mediator models (Z')

A Z' vector boson is a well-motivated feature of many new physics scenarios, arising either as a remnant of embedding the SM gauge symmetry within a larger rank group or as part of a hidden sector that may be sequestered from the SM (see e.g. [100] and references therein). The Z' has an added appeal for DM since the corresponding $U(1)'$ gauge symmetry ensures DM stability, even if the symmetry is spontaneously broken.[1] Although how the Z' couples to SM particles is highly model-dependent, we focus here on simple scenarios that are representative of both extended gauge models and hidden sector models. For practical purposes, this distinction affects whether the Z'-quark vertex is a gauge-strength coupling or is suppressed by a small mixing angle, which in turn impacts DM production at the LHC.

[1] It is required that the $U(1)'$ is broken by $n > 1$ units, where the χ field carries $n = 1$ unit of $U(1)'$ charge. This breaks the $U(1)'$ down to a $\mathbb{Z}_n$ discrete symmetry.

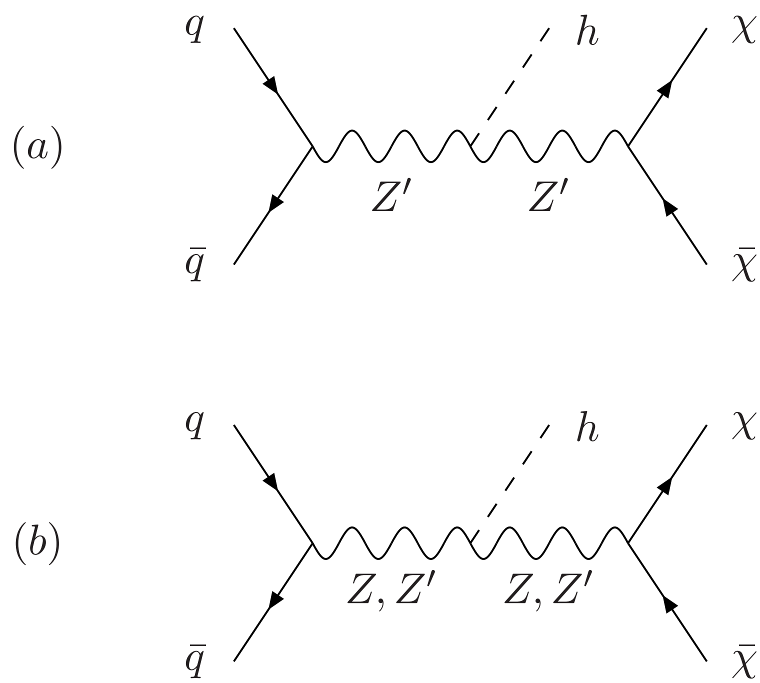

Figure 3.2: Diagram showing collider production mode in a simplified model including a Z' boson which decays to $\chi\bar{\chi}$.

One gauge extension of the SM is to suppose that baryon number (B) is gauged, with the Z' being the gauge boson of $U(1)_B$ [101]. The consistency of such theories often implies the existence of new stable baryonic states that are neutral under the SM gauge symmetry, providing excellent DM candidates [102, 103]. Taking the DM particle χ to carry baryon number B_χ, the Z'-quark-DM part of the Lagrangian is

$$\mathscr{L} \supset g_q \bar{q}\gamma^\mu q Z'_\mu + \begin{cases} i g_\chi \chi^\dagger \overleftrightarrow{\partial^\mu} \chi Z'_\mu + g_\chi^2 |\chi|^2 Z'_\mu Z'^\mu & \text{scalar} \\ g_\chi \bar{\chi}\gamma^\mu \chi Z'_\mu & \text{fermion} \end{cases} \tag{3.10}$$

depending on whether χ is a scalar or fermion. The Z' couplings to quarks and DM are related to the $U(1)_B$ gauge coupling g_B by $g_q = g_B/3$ and $g_\chi = B_\chi g_B$, respectively. This scenario is an example of a leptophobic Z' model, and many precision constraints are evaded since the Z' does not couple to leptons [104].

To investigate mono-Higgs signals, we ask whether the Z' is coupled to the Higgs boson h.

To generate the Z' mass, the minimal possibility is to introduce a "baryonic Higgs" scalar to spontaneously break $U(1)_B$. Analogous to the SM, there remains a physical baryonic Higgs particle, denoted h_B, with a coupling $h_B Z' Z'$. This coupling comes from the Z' mass term

$$\mathscr{L} \supset \frac{1}{2} m_{Z'}^2 \left(1 + \frac{h_B}{v_B}\right)^2 Z'_\mu Z'^\mu \,, \tag{3.11}$$

where v_B is the baryonic Higgs vev. Generically h_B will mix with the SM Higgs boson, giving rise to an interaction of the form

$$\mathscr{L} \supset -g_{hZ'Z'} h Z'_\mu Z'^\mu \,, \qquad g_{hZ'Z'} = \frac{m_{Z'}^2 \sin\theta}{v_B} \tag{3.12}$$

where θ is the h-h_B mixing angle. Combining Eqs. (3.10) and (3.12) allows for mono-Higgs signals at the LHC, shown in Fig. 3.2(a). At energies below $m_{Z'}$, the relevant effective operators for fermionic DM are

$$\mathscr{L}_{\text{eff}} = -\frac{g_q g_\chi}{m_{Z'}^2} \bar{q}\gamma^\mu q \bar{\chi}\gamma_\mu \chi \Big(1 + \frac{g_{hZ'Z'}}{m_{Z'}^2} h\Big) \,, \tag{3.13}$$

and similarly for scalar DM. The first term in Eq. (3.13) is relevant for mono-$j/\gamma/W/Z$ signals (through ISR), while the second term gives rise to mono-Higgs. It is clear that mono-Higgs, depending on a different combination of underlying parameters, offers a complementary handle for DM studies.

An alternate framework for the Z' is that of a hidden sector (see e.g. [105–109]). In this case, we suppose that DM remains charged under the $U(1)'$, while all SM states are neutral. The Lagrangian we consider is

$$\mathscr{L} \supset \frac{g_2}{2c_W} J^\mu_{\text{NC}} Z_\mu + g_\chi \bar{\chi}\gamma^\mu \chi Z'_\mu \,, \tag{3.14}$$

where J^μ_{NC} is the usual SM neutral current coupled to the Z, and the Z' is coupled to fermionic DM. Although the two sectors appear decoupled, small couplings can arise through mixing [109–111]. One simple possibility is that the Z' has a mass mixing term with the Z. In this case, one diagonalizes the Z, Z' system by a rotation

$$Z \to c_\theta Z - s_\theta Z', \quad Z' \to c_\theta Z' + s_\theta Z\,, \tag{3.15}$$

where θ is the Z-Z' mixing angle, and $s_\theta \equiv \sin\theta$ and $c_\theta \equiv \cos\theta$. Thus, the physical Z, Z' states are linear combinations of the gauge eigenstates, and each one inherits the couplings of the other from Eq. (3.14). We note that such mixing gives a contribution to the ρ parameter of $\delta\rho = \sin^2\theta(m_{Z'}^2/m_Z^2 - 1)$ [111]. Current precision electroweak global fits exclude $|\delta\rho| \gtrsim 10^{-3}$ [97], although any tension is also affected by new physics entering other observables in the global fit.

Mono-Higgs signals arise through diagrams shown in Fig. 3.2(b). The hZZ' vertex arises as a consequence of the fact Z-Z' mixing violates $SU(2)_L$ and is given by

$$\mathscr{L} \supset \frac{m_Z^2 s_\theta}{v} h Z'_\mu Z^\mu\,. \tag{3.16}$$

Scalar mediator models

New scalar particles may provide a portal into the dark sector [94]. The simplest possibility is to introduce a real scalar singlet, denoted S, with a Yukawa coupling to DM

$$\mathscr{L} \supset -y_\chi \bar{\chi}\chi S\,. \tag{3.17}$$

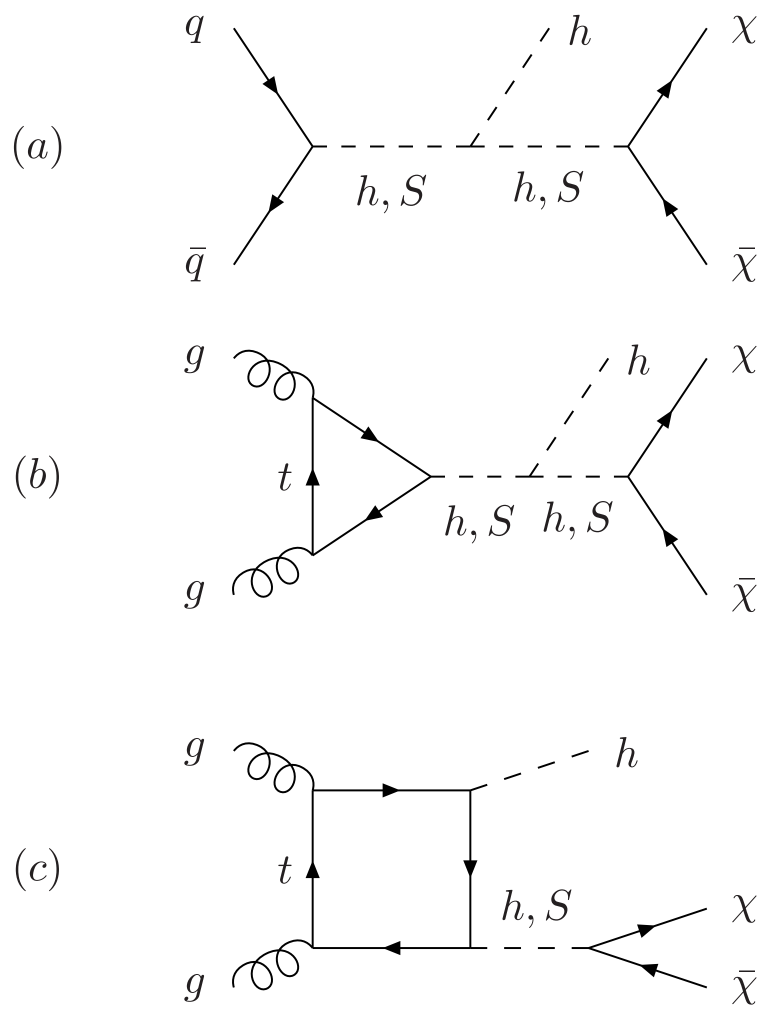

Figure 3.3: Diagram showing collider production mode in a simplified model including a Z' boson which decays to $\chi\bar{\chi}$.

By virtue of gauge invariance, S may couple to the SM (at the renormalizable level) only through the Higgs field [112]. The relevant terms in the scalar potential are

$$\begin{aligned} V &\supset a|H|^2 S + b|H|^2 S^2 + \lambda_h |H|^4 \\ &\longrightarrow \tfrac{1}{2}a(h+v)^2 S + \tfrac{1}{2}b(h+v)^2 S^2 + \frac{\lambda_h}{4}(h+v)^4, \end{aligned} \tag{3.18}$$

where a, b are new physics couplings and λ_h is the usual Higgs quartic. The second line in Eq. (3.18) follows once the Higgs field acquires a vev, thereby leading to a mixing term av in the h-S mass matrix. (Without loss of generality, the vev of S can be taken to be zero through a field shift [112].) The two scalar system is diagonalized by a field rotation

$$h \to c_\theta h + s_\theta S\,, \quad S \to c_\theta S - s_\theta h \tag{3.19}$$

where the mixing angle θ is defined by $\sin 2\theta = 2av/(m_S^2 - m_h^2)$, with $s_\theta \equiv \sin\theta$ and $c_\theta \equiv \cos\theta$. After the field rotation, the quark and DM Yukawa terms become

$$\mathscr{L} \supset -y_\chi \bar{\chi}\chi(c_\theta S - s_\theta h) - \frac{m_q}{v}\bar{q}q(c_\theta h + s_\theta S)\,. \tag{3.20}$$

The mixing angle is constrained by current Higgs data, which is consistent with $\cos\theta = 1$ within $\mathcal{O}(10\%)$ uncertainties [83, 113–116], thereby requiring $\sin\theta \lesssim 0.4$.

Mono-Higgs signals in this model arise through processes shown in Fig. 3.3(a,b). These processes depend on the $h^2 S$ and hS^2 cubic terms in Eq. (3.18). At leading order in $\sin\theta$, these terms are

$$V_{\text{cubic}} \approx \frac{\sin\theta}{v}(2m_h^2 + m_S^2)h^2 S + bvhS^2 + \ldots \tag{3.21}$$

where we have expressed a and λ_h in terms of $\sin\theta$ and m_h^2, respectively. We note that the $h^2 S$ term is fixed (at leading order in $\sin\theta$) once the mass eigenvalues m_h, m_S and mixing angle are specified. However, the hS^2 is not fixed and remains a free parameter depending

Table 3.1: Summary of benchmark models for $h + \not{E}_T$ signals.

Effective operators	
$\|\chi\|^2\|H\|^2$	$\lambda = 0.01$
	$\lambda = 1$
$\bar{\chi}\chi\|H\|^2$	$\Lambda = 100$ GeV
	$\Lambda = 10$ TeV
$\bar{\chi}i\gamma_5\chi\|H\|^2$	$\Lambda = 100$ GeV
	$\Lambda = 10$ TeV
$\chi^\dagger\partial^\mu\chi H^\dagger D_\mu H$	$\Lambda = 300$ GeV
$\bar{\chi}\gamma^\mu\chi B_{\mu\nu}H^\dagger D_\nu H$	$\Lambda = 100$ GeV
Simplified models with s-channel mediator	
Z'_B	$m_{Z'} = 100$ GeV, $g_\chi = g_B = 1$, $g_{hZ'Z'}/m_{Z'} = 0.3$
	$m_{Z'} = 1000$ GeV, $g_\chi = g_B = 1$, $g_{hZ'Z'}/m_{Z'} = 0.3$
Z'_H	$m_{Z'} = 100$ GeV, $g_\chi = 1$, $\sin\theta = 0.1$
	$m_{Z'} = 1000$ GeV, $g_\chi = 1$, $\sin\theta = 0.1$
Scalar S	$m_S = 100$ GeV, $y_\chi = 1$, $\sin\theta = 0.3$, $b = 3$
	$m_S = 1000$ GeV, $y_\chi = 1$, $\sin\theta = 0.3$, $b = 3$

on b. Alternately, a Higgs can be radiated directly from the t quark in the production loop, shown in Fig. 3.3(c). In our study, we include the $ggh S$ box contribution through an effective Lagrangian

$$\mathscr{L}_{\text{eff}} = -\frac{\alpha_s \sin 2\theta}{24\pi v^2} G^a_{\mu\nu} G^{a\mu\nu} h S \,, \tag{3.22}$$

which we have evaluated in the large m_t limit. Although this will likely overestimate our $h + \not{E}_T$ signal [117], we defer an evaluate of the true box form factor to future study.

3.2.3 Benchmark Models

For the purposes of our collider study to follow, we consider several illustrative benchmark scenarios for both EFT operators and simplified models. These models are summarized in Table 3.1. For the Z' models, we henceforth denote the Z' coupled to baryon number as Z'_B and the hidden sector Z' mixed with the Z as Z'_H. Otherwise, the parameters and interactions are as described above.

3.3 Collider Sensitivity

In this section we estimate the sensitivity of the LHC to mono-Higgs production with pp collisions at $\sqrt{s} = 8$ TeV and 14 TeV with $\mathcal{L} = 20$ fb^{-1} and $\mathcal{L} = 300$ fb^{-1}, respectively.

Signal events are generated in MADGRAPH5 [118], with showering and hadronization by PYTHIA [119] and detector simulation with DELPHES [120] assuming pileup conditions of $\mu = 20$ and $\mu = 50$ for $\sqrt{s} = 8, 14$ TeV, respectively.

The critical experimental quantity is the missing transverse energy; a comparison of the $\not{E}_T$ for a few choices of dark matter or mediator masses for the models under study can be seen in Fig. 3.4. The production cross section for $h\chi\chi$ under the various models are shown in Fig. 3.5.

In the following sub-sections, we estimate the LHC sensitivity in four Higgs boson decay modes: $\gamma\gamma, 4\ell, b\bar{b}, \ell\ell jj$.

3.3.1 Two-photon decays

The $\gamma\gamma$ decay mode has a small branching fraction, $\mathcal{B}(h \to \gamma\gamma) = 2.23 \times 10^{-3}$ [121], but smaller backgrounds than other final states and well-measured objects, which leads to well-measured $\not{E}_T$.

Significant backgrounds to the $\gamma\gamma + \not{E}_T$ final state include:

- Zh production with $Z \to \nu\bar{\nu}$, an irreducible background;
- Wh production with $W \to \ell\bar{\nu}$ where the lepton is not identified;
- $h \to \gamma\gamma$ or non-resonant $\gamma\gamma$ production, with $\not{E}_T$ from mismeasurement of photons or soft radiation;

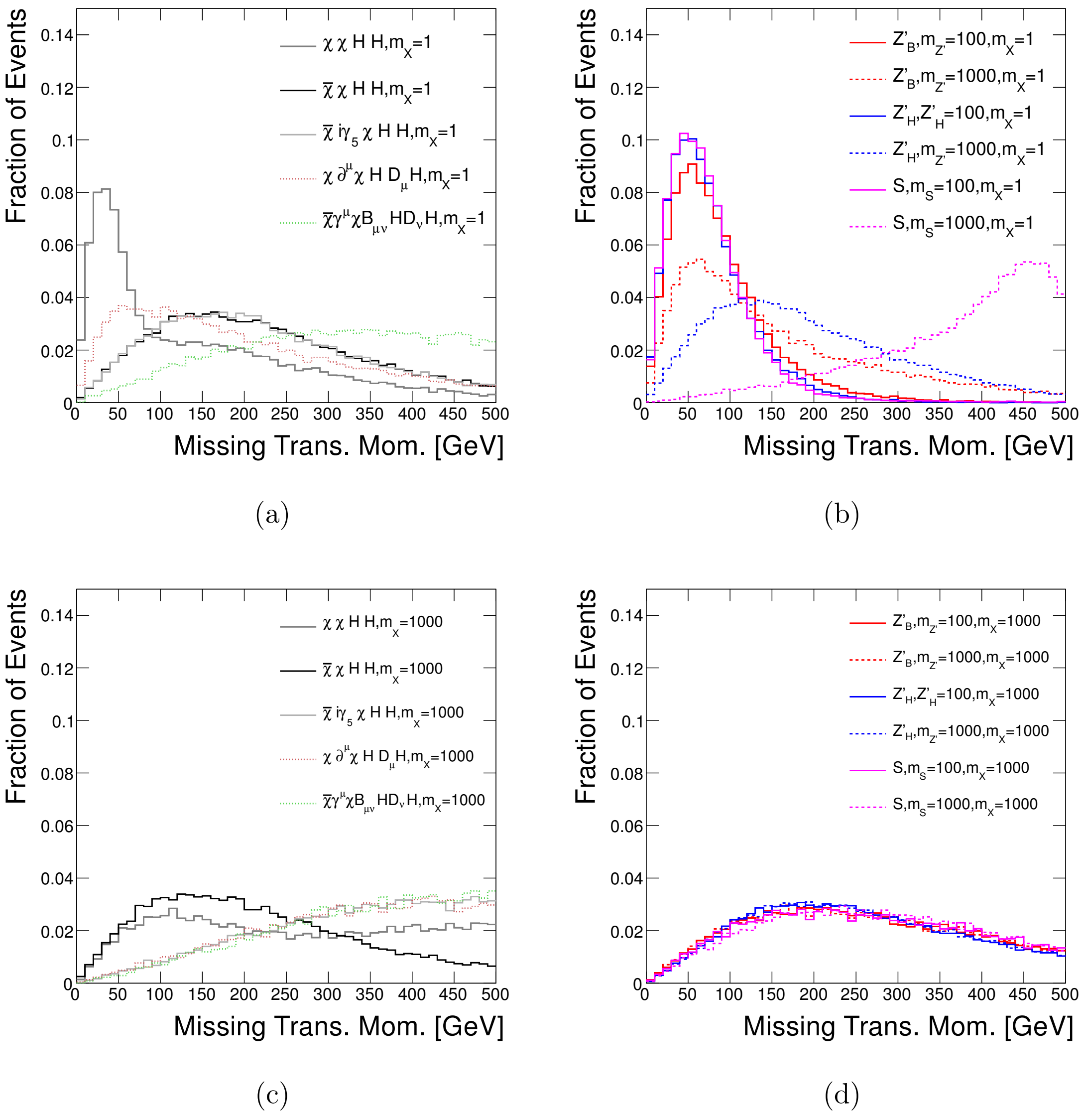

Figure 3.4: Distribution of missing transverse momentum for EFT models (top) and simplified models (bottom) for $m_\chi = 1$ GeV (left) and $m_\chi = 1000$ GeV (right).

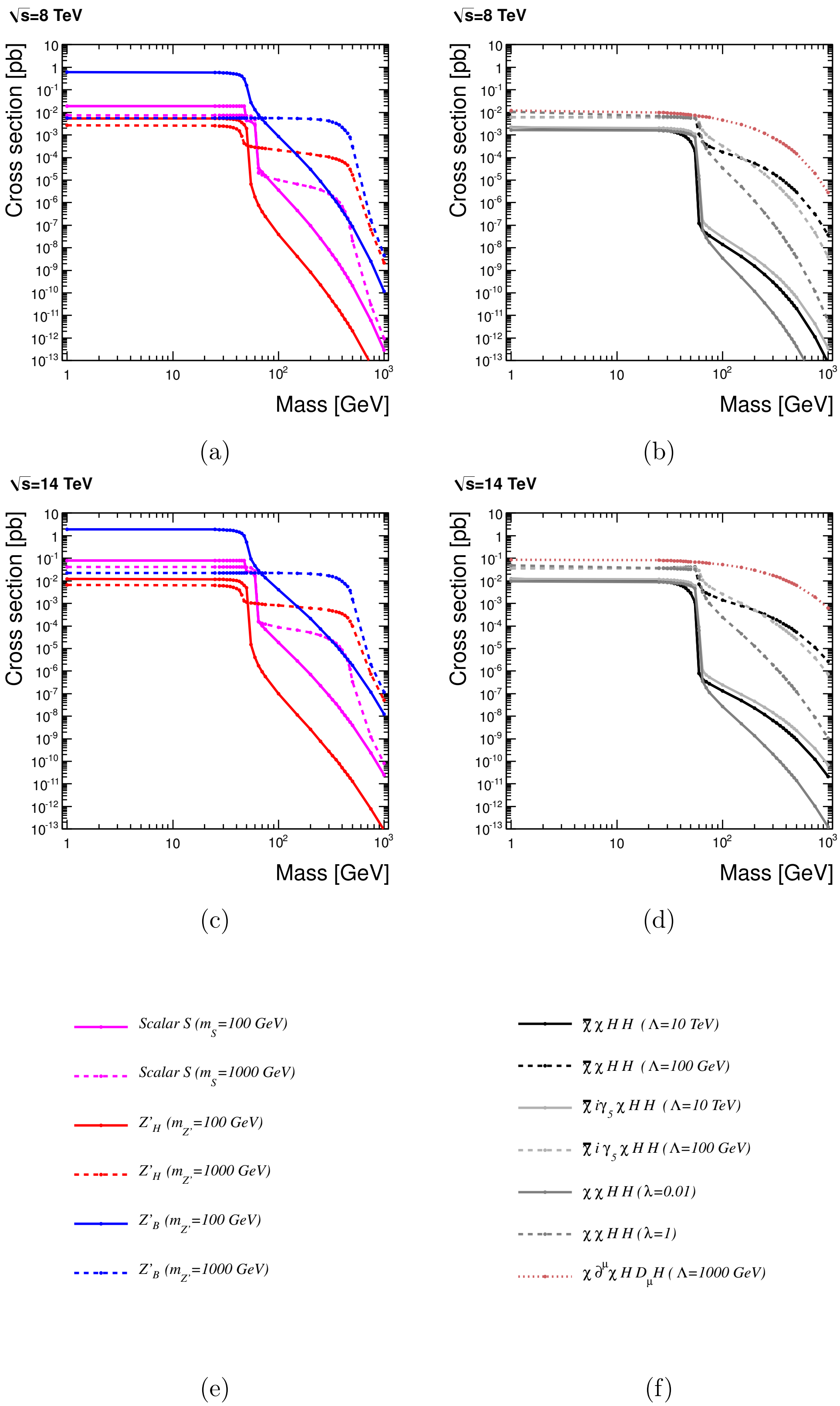

Figure 3.5: Production cross section for $h\chi\chi$ for each model at $\sqrt{s} = 8$ TeV (top) and $\sqrt{s} = 14$ TeV (bottom) using the benchmark values in Table 3.1.

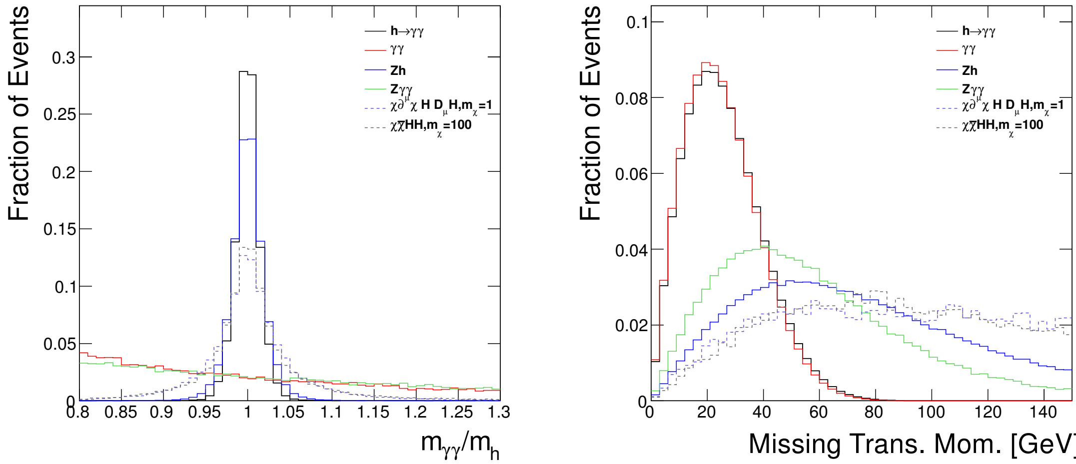

(a) (b)

Figure 3.6: Distributions of diphoton invariant mass, top, and missing transverse momentum (bottom) for simulated $\bar{\chi}\chi HH$ signal samples with two choices of m_χ, as well as the major background processes. All are for pp collisions at $\sqrt{s} = 8$ TeV.

- $Z\gamma\gamma$ with $Z \to \nu\bar{\nu}$.

Figure 3.6 shows distributions of the diphoton mass ($m_{\gamma\gamma}$) and the missing transverse momentum for two example signal cases and the background processes.

The production cross section for $gg \to h$ is taken at NNLO+NNLL in QCD plus NLO EW corrections [121] with 8% uncertainty due to renormalization and factorization scale dependence and 7% uncertainty due to parton distribution function (PDF) and α_s uncertanties. For Wh, Zh, we use the calculation of Ref. [121] which employs a zero-width approximation with NNLO QCD + NLO EW in which the dominant uncertainties are 1-3% due to scales and 4% due to PDFs and α_s. In each case, we use $\mathcal{B}(h \to \gamma\gamma) = 2.23 \times 10^{-3}$ with a 5% relative uncertainty [121].

The cross section for $Z\gamma\gamma$ is calculated at LO by MADGRAPH5, but normalized to NLO calculations using a k-factor of 1.75 ± 0.25 [122]. The cross section for $\gamma\gamma$ production is calculated at leading order by MADGRAPH5, corrected using a k-factor of 1.6 ± 0.7 extracted by comparing to the measured di-photon cross section [123].

Systematic uncertainties due to photon efficiency and resolution will be small compared to the uncertainty on the backgrounds, and are neglected. A potential significant source of systematic uncertainty is the modeling of the missing transverse momentum spectrum due to mismeasurement, as arises in the $\gamma\gamma$ and $h \to \gamma\gamma$ backgrounds. For the purposes of this sensitivity study, the thresholds in $\not{E}_T$ are designed to suppress these backgrounds to essentially negligible levels. A future experimental analysis must consider these more rigorously.

The event selection is:

- at least two photons with $p_T > 20$ and $|\eta| < 2.5$
- invariant mass $m_{\gamma\gamma} \in [110, 130]$ GeV
- no electons or muons with $p_T > 20$ and $|\eta| < 2.5$
- $\not{E}_T > 100$ or 250 GeV.

Figure 3.7 shows the distribution of expected events at $\sqrt{s} = 8$ and 14 TeV as a function of missing transverse momentum. We select a minimum $\not{E}_T$ threshold by optimizing the expected cross-section upper limit, finding $\not{E}_T > 100$ GeV and $\not{E}_T > 250$ GeV for the $\sqrt{s} = 8$ and 14 TeV cases, respectively. Note that the $\not{E}_T$ spectrum varies between the models, such that a single global optimal value of $\not{E}_T$ is not possible. We select a single $\not{E}_T$ threshold which gives the best aggregrate limits across choices of models and m_χ; further optimization is not warranted given the approximate nature of our background model and systematic uncertainties. Table 3.2 shows the expected event yields for each of these cases.

Limits are calculated using the CLs method with the asymptotic approximation [124]. Selection efficiency and upper limits on $\sigma(pp \to h\chi\bar{\chi} \to \gamma\gamma\chi\bar{\chi})$ are shown in Fig. 3.8.

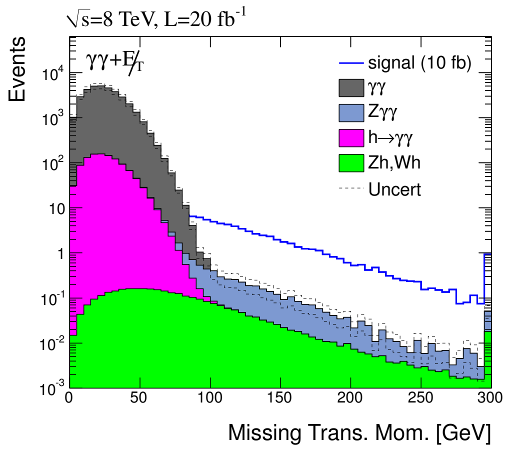

(a)

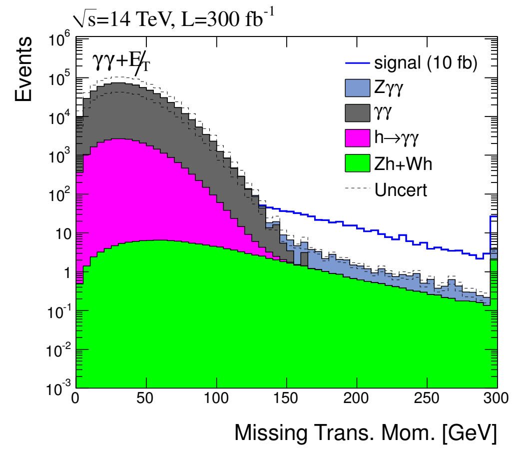

(b)

Figure 3.7: Distributions of missing transverse momentum in the $\gamma\gamma + \not{E}_T$ final state for background sources and one example signal process with after requiring $m_{\gamma\gamma} \in [110, 130]$ GeV, normalized to expected luminosity for $\sqrt{s} = 8$ TeV (top) and $\sqrt{s} = 14$ TeV (bottom).

Table 3.2: Expected background and signal yields in the $\gamma\gamma + \not{E}_T$ channel for pp collisions at $\sqrt{s} = 8$ TeV with $\mathcal{L} = 20$ fb^{-1}, left, or $\sqrt{s} = 14$ TeV with $\mathcal{L} = 300$ fb^{-1}, right. The signal case corresponds to $\sigma = 10$ fb, and $m_\chi = 1$ GeV in the $\bar{\chi}\chi HH$ model.

	$\sqrt{s} = 8$ TeV $\mathcal{L} = 20$ fb^{-1} $\not{E}_T > 100$	$\sqrt{s} = 14$ TeV $\mathcal{L} = 300$ fb^{-1} $\not{E}_T > 250$
$Z\gamma\gamma$	2.4 ± 0.3	3.4 ± 0.4
$\gamma\gamma$	$0^{+0.5}_{-0.0}$	$0^{+0.5}_{-0.0}$
$h \to \gamma\gamma$	$0^{+0.1}_{-0.0}$	$0^{+0.1}_{-0.0}$
Zh, Wh	0.7 ± 0.1	3.9 ± 0.4
Total Bkg	3.1 ± 0.6	7.3 ± 0.7
$\bar{\chi}\chi HH$	50	45

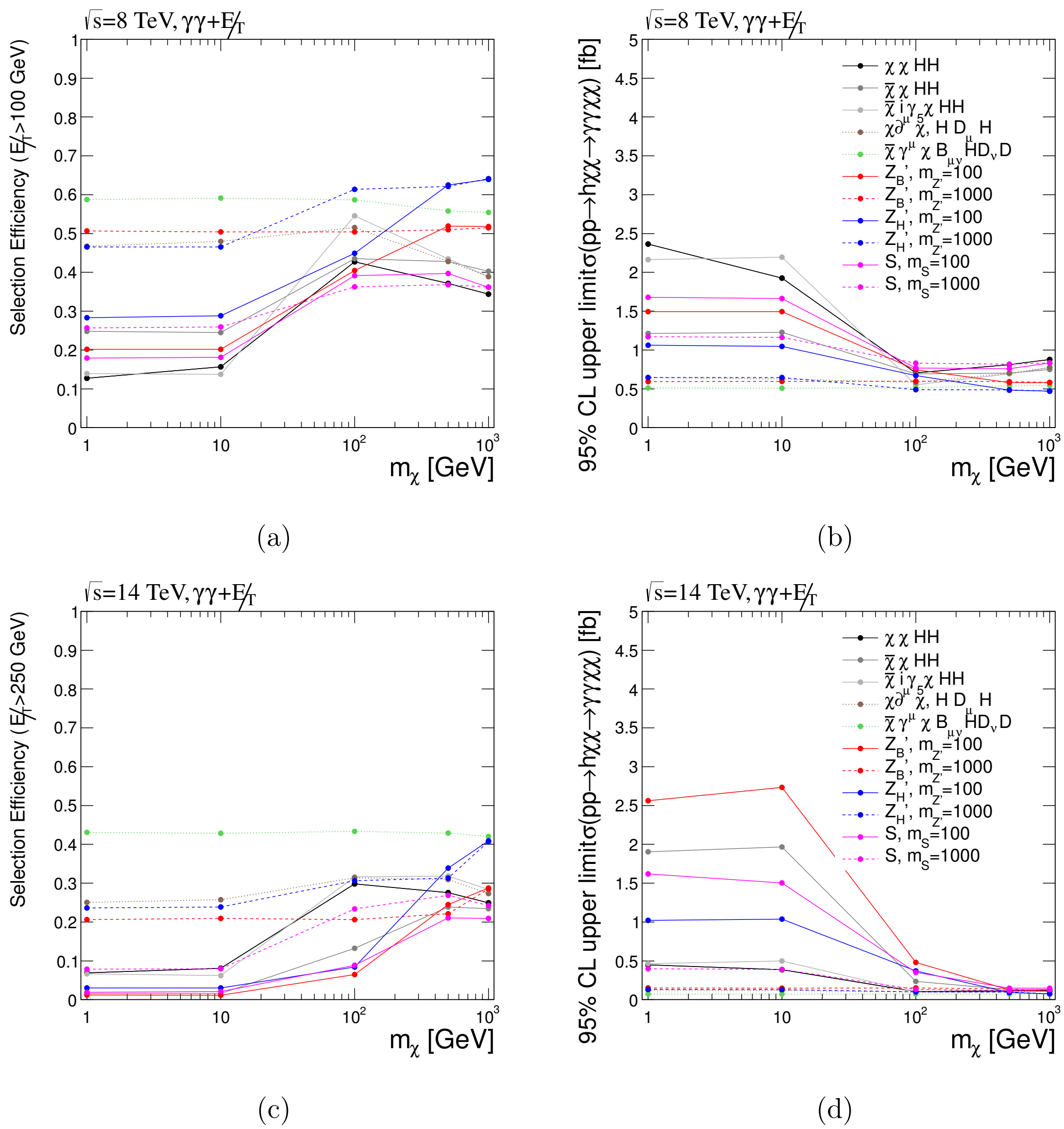

Figure 3.8: Selection efficiency in the $\gamma\gamma + \not{E}_T$ channel (left) and upper limits (right) on $\sigma(pp \to h\chi\bar{\chi} \to \gamma\gamma\chi\bar{\chi})$ for $\sqrt{s} = 8$ TeV (top) and $\sqrt{s} = 14$ TeV (bottom).

3.3.2 Four-lepton decays

The four-lepton decay mode, via $h \to ZZ^* \to 4\ell$, has the smallest branching ratio of the modes considered here, but also offers the smallest backgrounds.

Backgrounds to the $4\ell + \not{E}_T$ final state include:

- Zh production with $Z \to \nu\bar{\nu}$, an irreducible background;
- Zh production with $Z \to \ell\ell$ and $h \to \ell\ell\nu\nu$;
- Wh production with $W \to \ell\bar{\nu}$ where the lepton from the W decay is not identified;
- $h \to ZZ^* \to 4\ell$ or the continuum $(Z^{(*)}/\gamma^*)(Z^{(*)}/\gamma^*) \to 4\ell$ production, with $\not{E}_T$ from mismeasurement of leptons or soft radiation.

As in the case for two-photon decays, the cross sections and uncertainties for $gg \to h$, Wh, and Zh production, and the h branching fractions are taken from Ref. [121]. We take branching fractions $\mathcal{B}(h \to 4\ell) = 1.26 \times 10^{-4}$, and $\mathcal{B}(h \to 2\ell 2\nu) = 1.06 \times 10^{-2}$. The considerably larger branching fraction involving neutrinos results in a significant contribution from the non-resonant Zh $(Z \to \ell\ell)$ background.

Simulated samples of $(Z^{(*)}/\gamma^*)(Z^{(*)}/\gamma^*)$ events, hereafter referred to simply as ZZ^*, are generated by MADGRAPH5 at LO. The yield is compared against NLO values calculated with POWHEG and gg2ZZ in [125], and the difference is assigned as a systematic.

To improve the accuracy of the modeling of lepton reconstruction efficiency by DELPHES, we scale the per-lepton efficiencies to match those reported by ATLAS [125] in the $4e, 4\mu, 2e2\mu$ final states and apply these efficiences to all simulated samples.

We define the leading lepton pair to be the same-flavor, opposite-sign pair with invariant mass m_{12} closest to the Z-boson mass. The sub-leading pair's invariant mass, m_{34}, is the

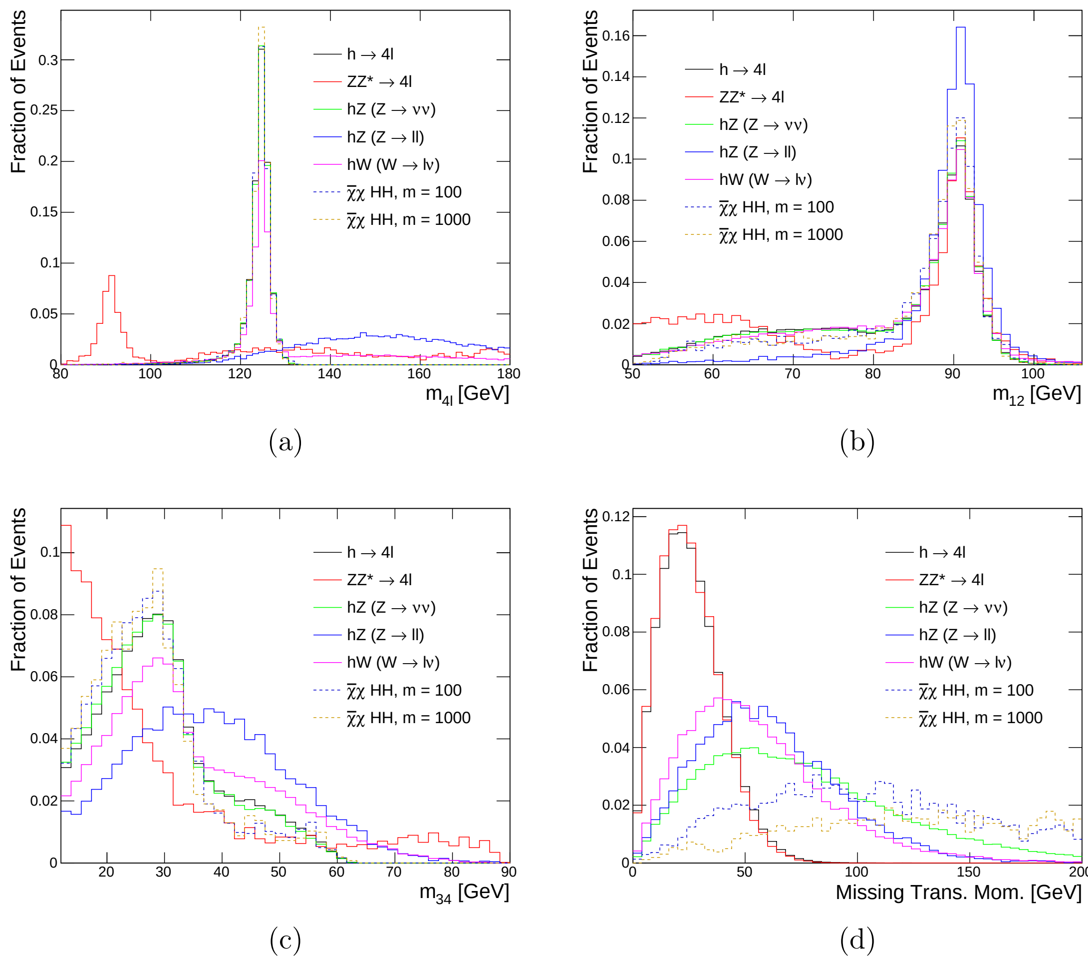

Figure 3.9: Distributions of four-lepton invariant mass $m_{4\ell}$, leading (m_{12}) and subleading (m_{34}) dilepton mass, and missing transverse momentum for simulated $h\chi\bar{\chi}$ signal samples with two choices of m_χ, as well as the major background processes. All are for pp collisions at $\sqrt{s} = 8$ TeV.

next closest to the Z-boson mass. Figure 3.9 shows distributions of the lepton pair masses, m_{12} and m_{34}, the four-lepton invariant mass, $m_{4\ell}$, and the missing transverse momentum. We also define $m_{\min}$ as a function which is a constant 12 GeV for $m_{4\ell} < 140$ GeV, then rises linearly to 50 GeV for $m_{4\ell} < 190$ GeV and remains constant. Then each event must satisfy:

- at least four leptons with each electron (muon) satisfying:
  - $p_T > 7$ GeV ($p_T > 6$ GeV)
  - $|\eta| < 2.47$ ($|\eta| < 2.7$)
- highest p_T lepton is an electron (muon) with $p_T > 20$ GeV, and the second (third) lepton satisfies $p_T > 15$ GeV ($p_T > 10$ GeV)
- 50 GeV $< m_{12} <$ 106 GeV
- $m_{\min} < m_{34} <$ 115 GeV
- 105 GeV $< m_{4\ell} <$ 145 GeV
- $\not{E}_T > 75$ or 150 GeV.

Figure 3.10 shows the distribution of expected events at $\sqrt{s} = 8$ and 14 TeV as a function of missing transverse momentum. We select a minimum $\not{E}_T$ threshold by optimizing the expected cross-section upper limit, finding $\not{E}_T > 75$ GeV and $\not{E}_T > 150$ GeV for the $\sqrt{s} = 8$ and 14 TeV cases, respectively. Table 3.3 shows the expected event yields for each of these cases.

Selection efficiency and upper limits on $\sigma(pp \to h\chi\bar{\chi} \to 4\ell\chi\bar{\chi})$ are shown in Fig. 3.11.

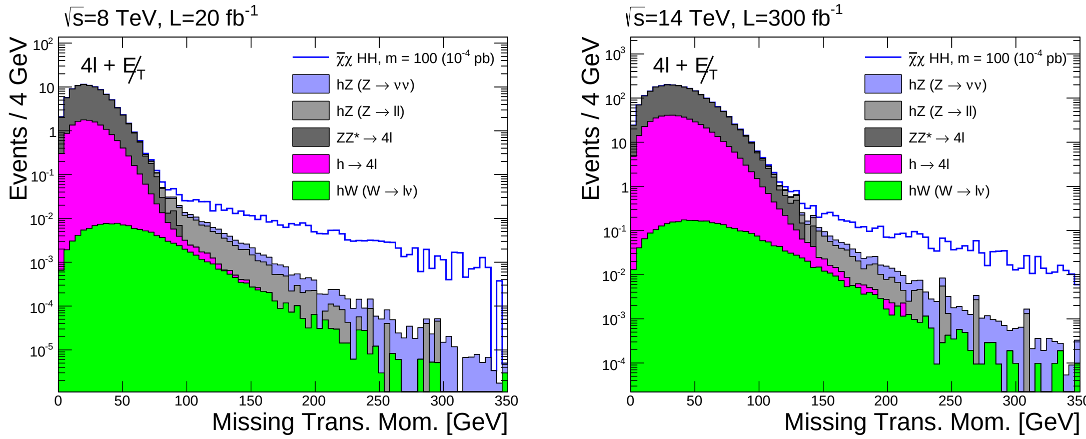

(a) (b)

Figure 3.10: Distributions of missing transverse momentum in the $4\ell + \not{E}_T$ final state for simulated signal and background samples with normalized to expected luminosity.

Table 3.3: Expected background and signal yields in the $4\ell + \not{E}_T$ channel for pp collisions at $\sqrt{s} = 8$ TeV with $\mathcal{L} = 20$ fb^{-1}, left, or $\sqrt{s} = 14$ TeV with $\mathcal{L} = 300$ fb^{-1}, right. The signal case corresponds to $\sigma = 10^{-4}$ pb, and $m_\chi = 1$ GeV.

	$\sqrt{s} = 8$ TeV $\mathcal{L} = 20$ fb^{-1} $\not{E}_T > 75$	$\sqrt{s} = 14$ TeV $\mathcal{L} = 300$ fb^{-1} $\not{E}_T > 150$
ZZ^*	$(5.21 \pm 0.05) \times 10^{-1}$	$0^{+0.45}_{-0.00} \times 10^{-1}$
$hZ(Z \to \ell\ell)$	$(2.09 \pm 0.09) \times 10^{-1}$	$(6.30 \pm 0.49) \times 10^{-1}$
$h \to 4\ell$	$(1.83 \pm 0.20) \times 10^{-1}$	$(2.33 \pm 0.57) \times 10^{-1}$
$hZ(Z \to \nu\nu)$	$(3.11 \pm 0.13) \times 10^{-2}$	$(1.89 \pm 0.13) \times 10^{-1}$
hW	$(3.29 \pm 0.09) \times 10^{-2}$	$(9.73 \pm 0.52) \times 10^{-2}$
Total Bkg	0.977 ± 0.023	1.15 ± 0.09
$\chi\bar{\chi}HH$	0.279	0.866

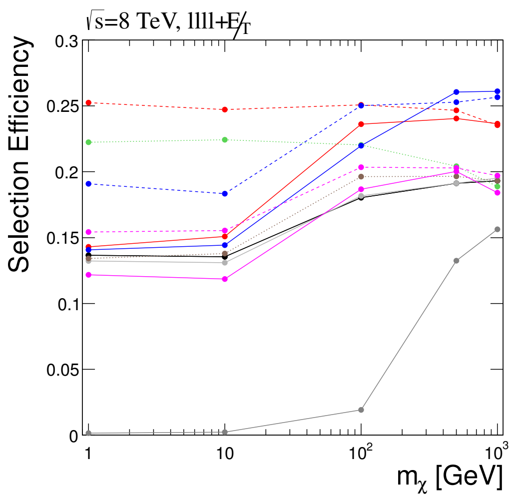

(a)

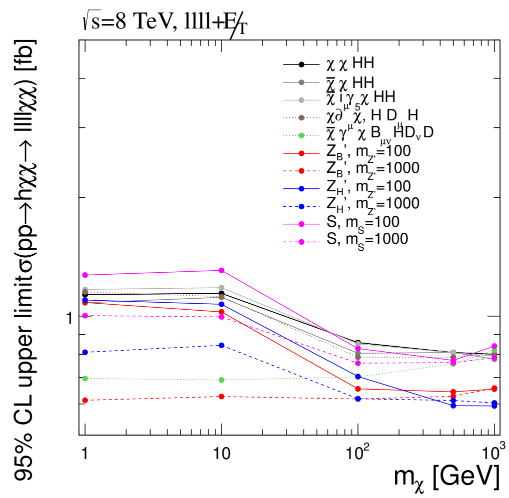

(b)

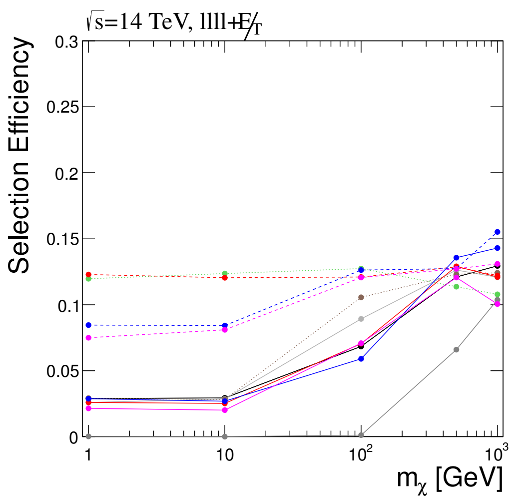

(c)

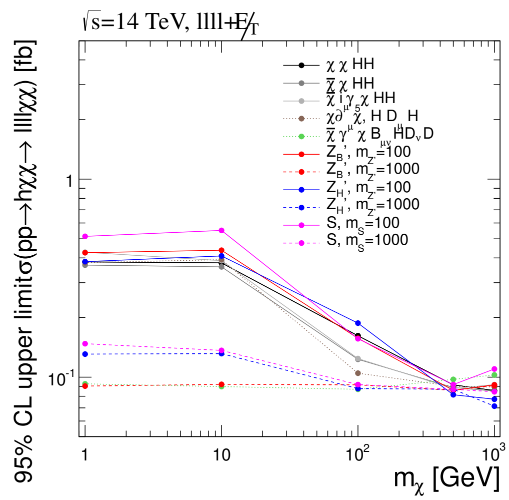

(d)

Figure 3.11: Selection efficiency in the $4\ell + \not{E}_T$ channel (left) and upper limits on $\sigma(pp \to h\chi\bar{\chi} \to 4\ell\chi\bar{\chi})$ for $\sqrt{s} = 8$ TeV (top) and $\sqrt{s} = 14$ TeV (bottom).

3.3.3 Two-b-quark decays

The two-b-quark mode is the dominant Higgs boson decay mode, but suffers from a very large background due to strong production of dijets as well as the poorest $\not\!\!E_T$ resolution.

Backgrounds to the $b\bar{b} + \not\!\!E_T$ final state include:

- Zh production with $Z \to \nu\bar{\nu}$, an irreducible background;
- Wh production with $W \to \ell\bar{\nu}$ where the lepton from the W decay is not identified;
- $Zb\bar{b}$ and $Wb\bar{b}$ production;
- $h \to b\bar{b}$ or non-resonant $b\bar{b}$ production, with $\not\!\!E_T$ from mismeasurement of leptons or soft radiation;
- top-quark pair production $t\bar{t}$

The event selection is:

- two b-tagged jets with $p_T > 50, 20$ GeV and $|\eta| < 2.5$
- invariant mass $m_{bb} \in [50, 130]$ GeV
- no electons or muons with $p_T > 20$ and $|\eta| < 2.5$
- no more than one additional jet with $p_T > 20$ GeV and $|\eta| < 2.5$
- $\Delta\phi(b\bar{b}, \not\!\!E_T) > 2.5$ and $\Delta\phi(j, \not\!\!E_T) > 1$ to suppress false $\not\!\!E_T$
- $\not\!\!E_T > 250$ GeV ($\sqrt{s} = 8$ TeV) or $\not\!\!E_T > 300$ GeV ($\sqrt{s} = 14$ TeV).

Figure 3.7 shows the distribution of expected events at $\sqrt{s} = 8$ and 14 TeV as a function of missing transverse momentum.

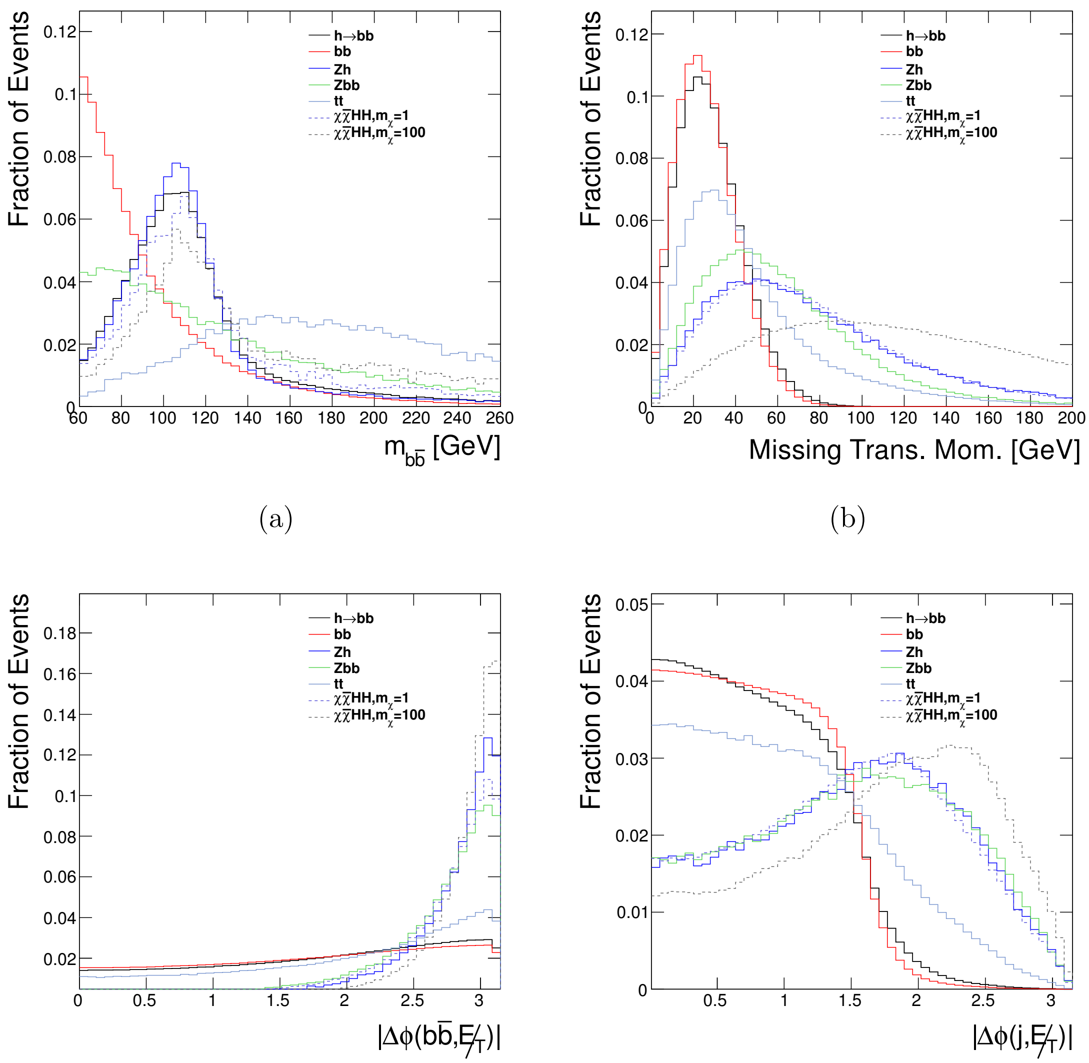

(a) (b) (c) (d)

Figure 3.12: Distributions of bb invariant mass, missing transverse momentum and the angle between the $\not{E}_T$ and the $b\bar{b}$ system and the nearest jet, for simulated $h\chi\bar{\chi}$ signal samples with two choices of m_χ, as well as the major background processes. All are for pp collisions at $\sqrt{s} = 8$ TeV.

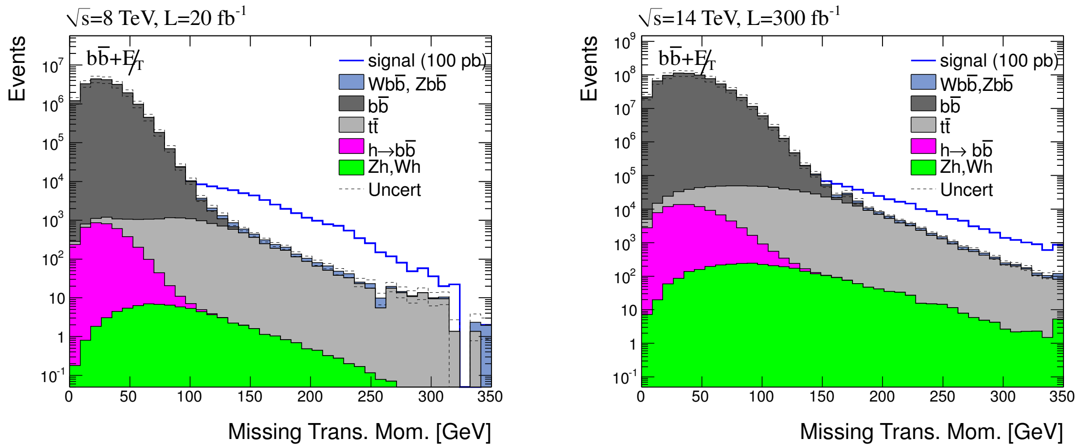

(a) (b)

Figure 3.13: Distributions of missing transverse momentum for simulated signal and background samples in the $bb + \not{E}_T$ final state with with all selection other than the $\not{E}_T$ threshold, normalized to expected luminosity.

The production cross section and uncertaintaties for $gg \to h$, Zh and Wh are calculated as above, with branching fraction $\mathcal{B}(h \to b\bar{b}) = 0.57$ with a 3% relative uncertainty [121]. The cross section for $t\bar{t}$ production is calculated at NNLO [126]. The $Z/W + b\bar{b}$ cross sections are calculated at LO with MADGRAPH5 and scaled using the inclusive Z and W boson production cross section k-factors [127, 128]. The $b\bar{b}$ cross section is calculated at leading order with MADGRAPH5 scaled to NLO using a k-factor [129].

We select a minimum $\not{E}_T$ threshold by optimizing the expected cross-section upper limit, finding $\not{E}_T > 85$ GeV and $\not{E}_T > 250$ GeV for the $\sqrt{s} = 8$ and 14 TeV cases, respectively. Table 3.2 shows the expected event yields for each of these cases.

Selection efficiency and upper limits on $\sigma(pp \to h\chi\bar{\chi} \to b\bar{b}\chi\bar{\chi})$ are shown in Fig. 3.14. Note that the small signal efficiency is largely due to the need for a high minimum threshold on $\not{E}_T$ to supress the backgrounds. Similar missing energy thresholds and efficiencies are seen in mono-jet analyses.

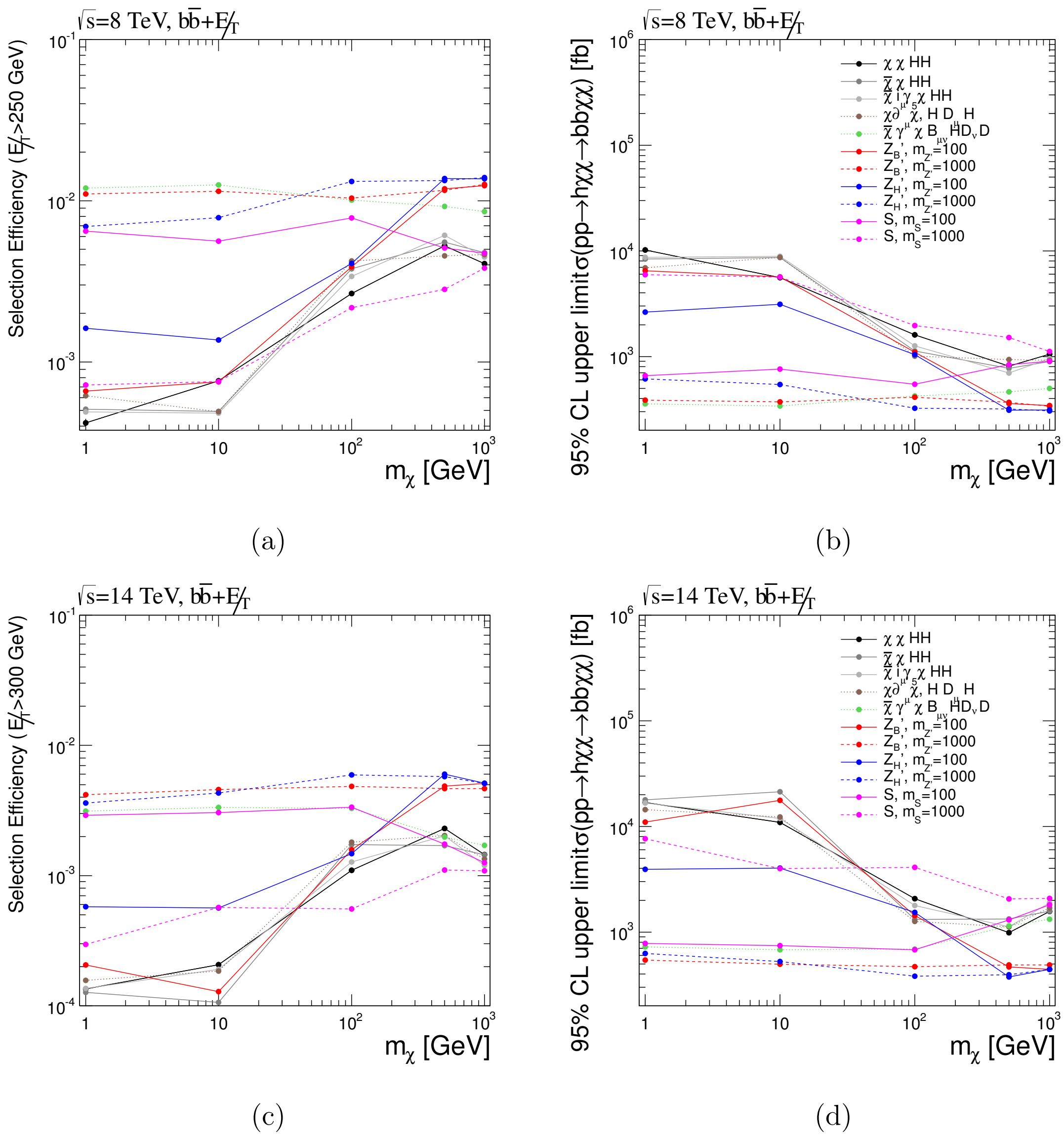

Figure 3.14: Selection efficiency in the $b\bar{b} + \not{E}_T$ channel (left) and upper limits on $\sigma(pp \to h\chi\bar{\chi} \to b\bar{b}\chi\bar{\chi})$ for $\sqrt{s} = 8$ TeV (top) and $\sqrt{s} = 14$ TeV (bottom).

Table 3.4: Expected background and signal yields in the $b\bar{b}+\not{E}_T$ channel for pp collisions at $\sqrt{s}=8$ TeV with $\mathcal{L}=8$ fb^{-1}, left, or $\sqrt{s}=14$ TeV with $\mathcal{L}=14$ fb^{-1}, right. The signal case corresponds to $\sigma=1$ pb, and $m_\chi=1$ GeV.

	$\sqrt{s}=8$ TeV $\mathcal{L}=20$ fb^{-1} $\not{E}_T>250$	$\sqrt{s}=14$ TeV $\mathcal{L}=300$ fb^{-1} $\not{E}_T>300$
$Zb\bar{b}+Wb\bar{b}$	15 ± 3	130 ± 15
$b\bar{b}$	0^{+5}_{-0}	0^{+5}_{-0}
$t\bar{t}$	90 ± 10	750 ± 75
$h\to b\bar{b}$	0^{+5}_{-0}	0^{+5}_{-0}
Zh, Wh	1 ± 0.5	15 ± 5
Total Bkg	105 ± 11	900 ± 140
$\chi\bar{\chi}HH(\sigma=10$ pb)	63	60

3.3.4 Two-lepton and two-jet decays

The branching fraction of ZZ^* to four leptons is quite small due to the small charged-lepton decay fraction relative to hadronic decay modes. To balance that, we consider the $h\to ZZ^*\to\ell\ell jj$ mode.

The backgrounds to the $\ell\ell jj+\not{E}_T$ final state include:

- Zh production with $Z\to\nu\bar{\nu}$ and $h\to\ell\ell jj$, an irreducible background;
- Additional decay modes of Zh and Wh production, all with final state $jj\ell\ell\nu\nu$;
- Higgs boson production with $h\to ZZ^*\to\ell\ell jj$;
- Diboson production: $ZZ\to\ell\ell jj$ and $ZW\to\ell\ell jj$;
- Production of WW plus additional jets, with $WW\to\ell\nu\ell\nu$;
- Z boson plus jets production, with $Z\to\ell\ell$;
- W boson plus jets production, with $W\to\ell\nu$ and one jet misreconstructed as an isolated lepton;

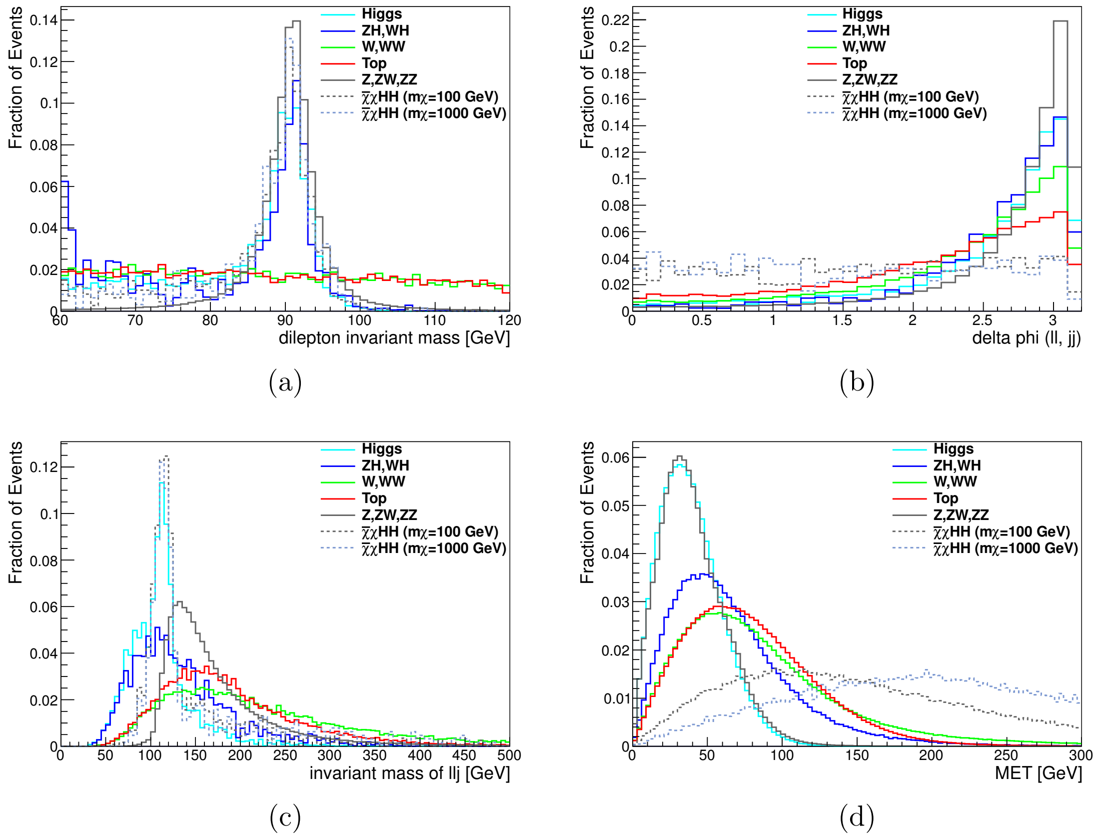

Figure 3.15: Distributions of dilepton invariant mass, $\Delta\phi$ between dilepton and the dijet system formed by the two highest-p_T jets, invariant mass of the two leptons plus the jet nearest the direction of the dilepton system, and missing transverse momentum, for simulated $h\chi\bar{\chi}$ signal samples with two choices of m_χ, as well as the major background processes. All are for pp collisions at $\sqrt{s} = 8$ TeV.

- $t\bar{t}$ production with $t \to \ell^+\nu b$ and $\bar{t} \to \ell^-\bar{\nu}\bar{b}$.

The event selection is

- Two opposite-sign leptons of the same flavor with leading lepton $p_T > 20$ GeV, second leading lepton $p_T > 15$, and $|\eta| < 2.5$.
- No additional leptons with $p_T > 10$ GeV.
- Two or more jets with $p_T > 15$ and $|\eta| < 2.5$.
- Dilepton invariant mass between 82 and 98 GeV.

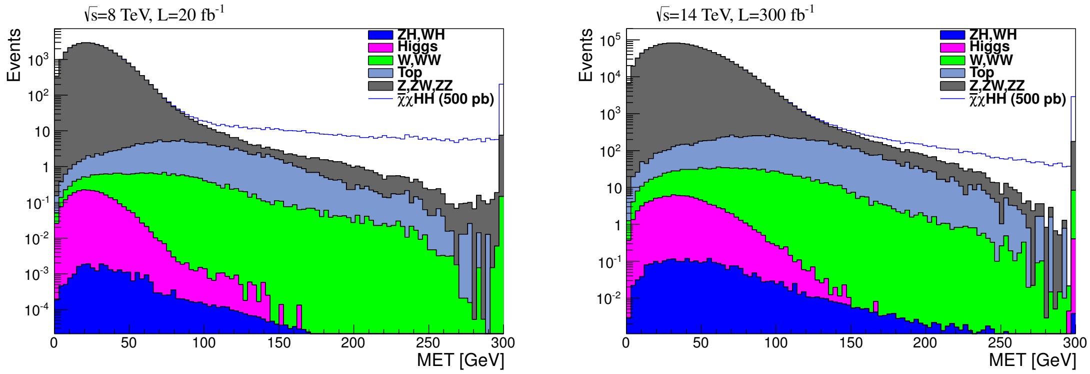

(a) (b)

Figure 3.16: Distributions of missing transverse momentum for simulated signal and background samples in the $lljj + \not\!\!E_T$ final state with with all selection other than the $\not\!\!E_T$ threshold, normalized to expected luminosity.

- $\Delta\phi$ between the dilepton system and the dijet system (formed by the two highest-p_T jets) less than 2.25 radians.
- Invariant mass of both leptons plus the jet in the direction with smallest ΔR from the dilepton system less than 124 GeV.

Figure 3.15 shows distributions of kinematic variables used in the event selection, and missing transverse momentum. Figure 3.16 shows distributions of missing transverse momentum, after event selection, for both $\sqrt{s} = 8$ and 14 TeV.

To increase the number of simulated events used to model the W-boson+jets background, where one jet is misreconstructed as a lepton, the W+jet events were weighted by a fake rate for a randomly choosen jet, to match the event yield determined from DELPHES. As this represents a small contribution to the final selection, a large uncertainty here has only a small effect on the calculated limits.

We select a minimum $\not\!\!E_T$ threshold by optimizing the expected cross-section upper limit, finding $\not\!\!E_T > 250$ GeV for both the $\sqrt{s} = 8$ and 14 TeV cases. Table 3.5 shows the expected event yields for each of these cases.

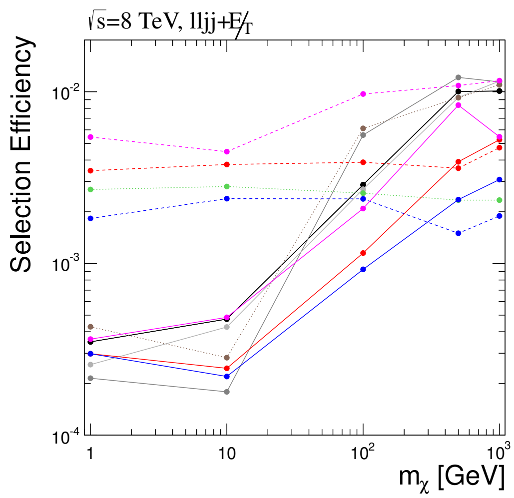

(a)

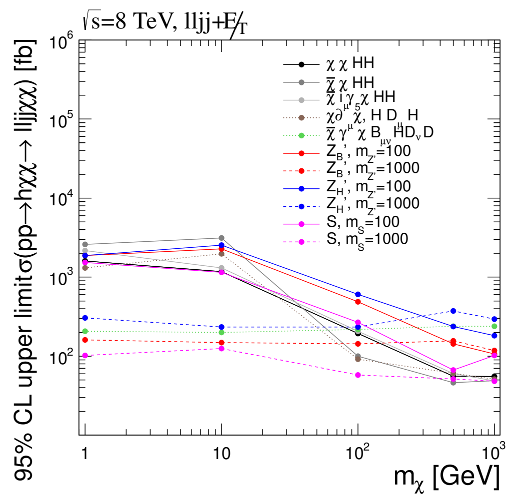

(b)

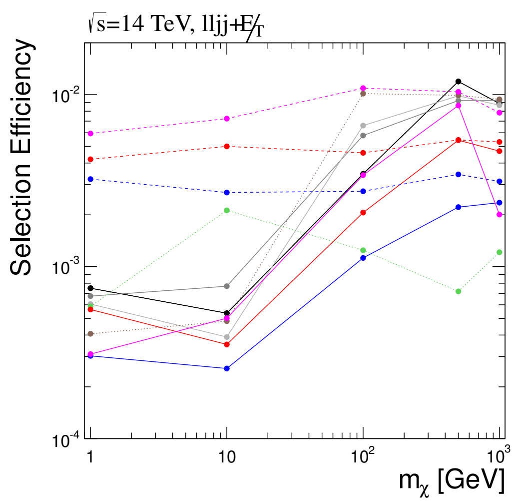

(c)

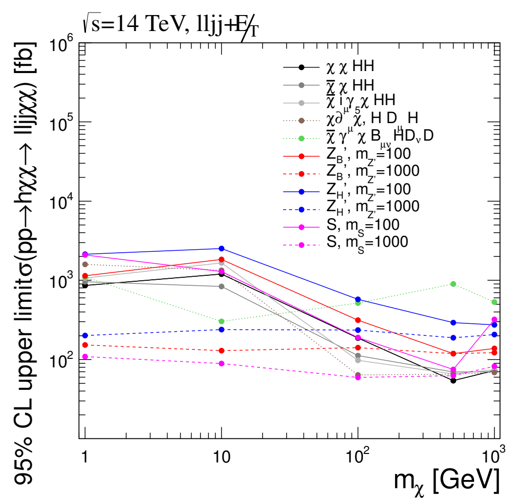

(d)

Figure 3.17: Selection efficiency in the $\ell\ell jj + \not{E}_T$ channel (left) and upper limits on $\sigma(pp \to h\chi\bar{\chi} \to \ell\ell jj\chi\bar{\chi})$ for $\sqrt{s} = 8$ TeV (top) and $\sqrt{s} = 14$ TeV (bottom).

Table 3.5: Expected background and signal yields in the $\ell\ell jj + \not{E}_T$ channel for pp collisions at $\sqrt{s} = 8$ TeV with $\mathcal{L} = 20$ fb^{-1}, left, or $\sqrt{s} = 14$ TeV with $\mathcal{L} = 300$ fb^{-1}, right. The signal case corresponds to $\sigma = 500$ pb, and $m_\chi = 500$ GeV.

	$\sqrt{s} = 8$ TeV $\mathcal{L} = 20$ fb^{-1} $\not{E}_T > 250$	$\sqrt{s} = 14$ TeV $\mathcal{L} = 300$ fb^{-1} $\not{E}_T > 250$
Z,ZW,ZZ	9.2 ± 0.2	211 ± 6
Higgs	0.17 ± 0.01	0.39 ± 0.04
WW,W+jets	0.26 ± 0.06	9.5 ± 0.9
$t\bar{t}$	0.26 ± 0.5	21 ± 4
WH,ZH	$-$	0.013 ± 0.001
Total Bkg	9.7 ± 1.0	242 ± 8
$\chi\bar{\chi}HH$	56 ± 0.5	684 ± 7

Selection efficiency and upper limits on $\sigma(pp \to h\chi\bar{\chi} \to \ell\ell jj\chi\bar{\chi})$ are shown in Fig. 3.17.

3.3.5 Comparison

A comparison of sensitivities between final states is shown in Figs. 3.18 and 3.19. The di-photon final state has the strongest sensitivity across all models and masses. The two-b-quark final state also has significant power, which may be improved by more aggressive rejection of the $t\bar{t}$ background and use of jet-substructure techniques to capture events with large Higgs boson p_T.

Note that these comparisons assume the SM Higgs boson branching fractions, which may be diluted in cases where $\mathcal{B}(h \to \chi\chi)$ is large, but the relative BFs will be unaltered, allowing a comparison of the relative power of each channel.

The systematic uncertainty on the background estimate typically controls the sensitivity of each channel. In this study, we have used simulated samples to describe the background contributions. In future experimental analyses, many of these backgrounds can be estimated by extrapolating from signal-depleted control regions, which significantly reduces the systematic error due to modeling of the $\not{E}_T$ tail. For example, in the $b\bar{b} + \not{E}_T$ final state, one can measure the rate of $Wh \to \ell\nu b\bar{b}$ and $Zh \to \ell\ell b\bar{b}$ in final states with one or two leptons, respectively.

3.4 Discussion and results

For a range of different models and DM mass m_χ, the LHC sensitivity to mono-Higgs production is approximately 100 fb − 1 pb. (More precise values are given in Figs. 3.18 and 3.19.) In this section, we compare these projected sensitivities to the predicted cross sections for our benchmark theories (Fig. 3.5) in order to constrain the parameter space of these scenarios. We also consider other important constraints, such as invisible h or Z decays, as well as the recent bound on the spin-independent (SI) direct detection cross section from the LUX experiment [3]. The SI cross section for DM scattering on a nucleus N with atomic and mass numbers (Z, A) is

$$\sigma_{\chi N}^{\mathrm{SI}} = \frac{\mu_{\chi N}^2}{\pi}\big(Zf_p + (A-Z)f_n\big)^2 \tag{3.23}$$

where $\mu_{\chi N}$ is the χ-N reduced mass and $f_{p,n}$ are the DM couplings to protons/neutrons. We emphasize, however, that direct detection constraints can be avoided if DM is inelastic [130], i.e., if the complex state χ is split into real states $\chi_{1,2}$ with an $\mathcal{O}(\mathrm{MeV})$ or larger mass splitting, with no change to the collider phenomenology provided it is much smaller than the typical parton energy.

Our results are shown in Figs. 3.20-3.22. The "$\gamma\gamma + \not{E}_T$" contours show the LHC reach on our models at $\sqrt{s} = 8$ and 14 TeV, based on 20 and 300 fb^{-1} respectively, from mono-Higgs searches with $\gamma\gamma$ final states, which provides the stronger bound compared to $b\bar{b}$ and ZZ^*. The limit contours shown exclude larger values of couplings and mixing angles, or smaller values of the effective operator mass scale Λ.

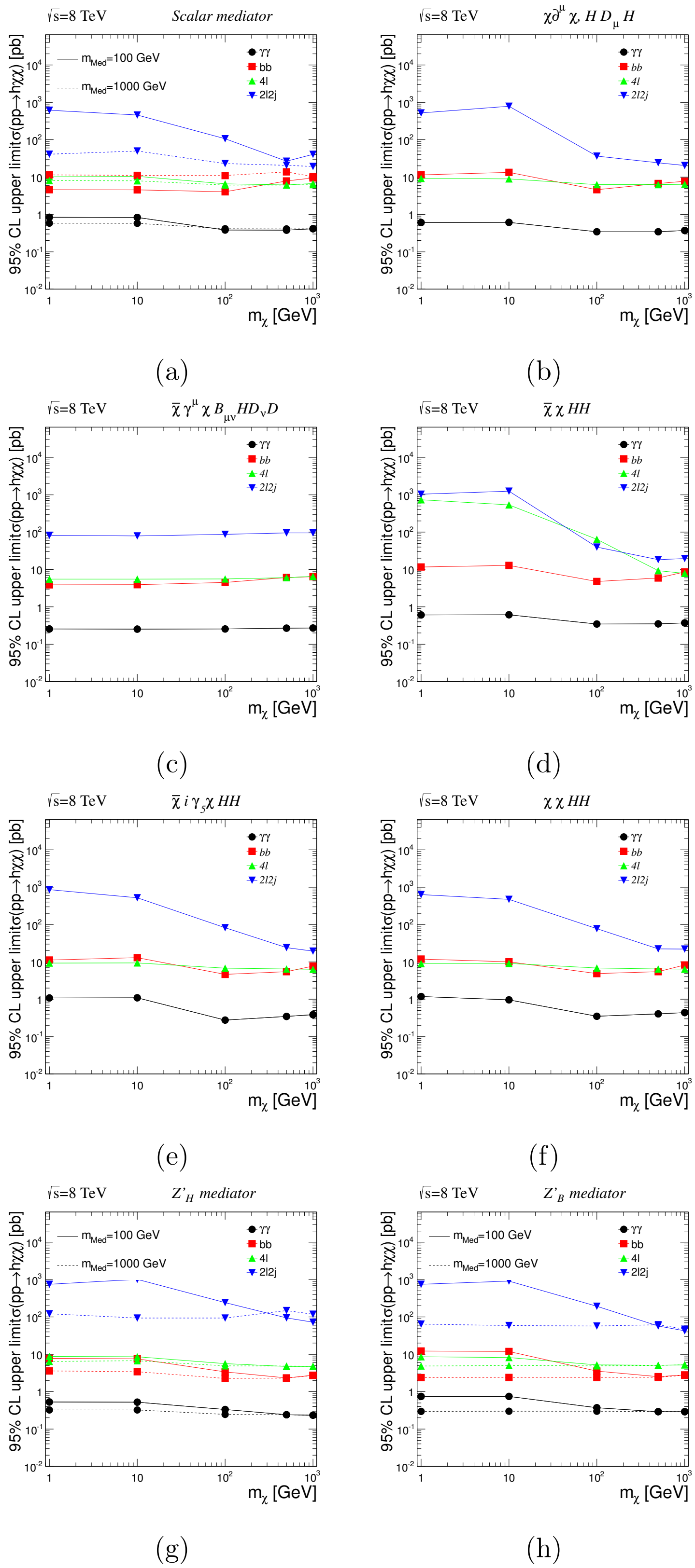

Figure 3.18: Upper limits on $\sigma(pp \to h\chi\bar{\chi})$ for $\sqrt{s} = 8$ TeV in different decay modes and different models. For simplified models with explicit mediators, solid lines are for 100 GeV mediator, and dashed for 1000 GeV.

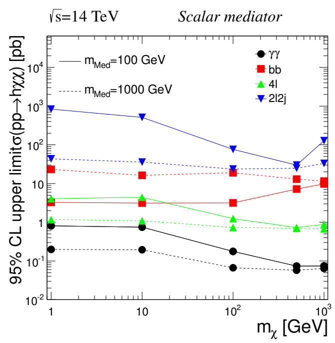

(a)

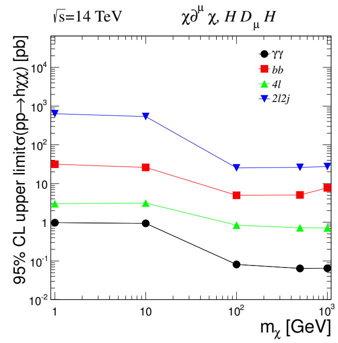

(b)

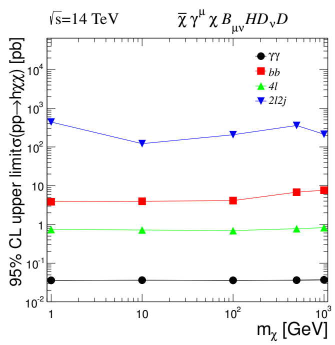

(c)

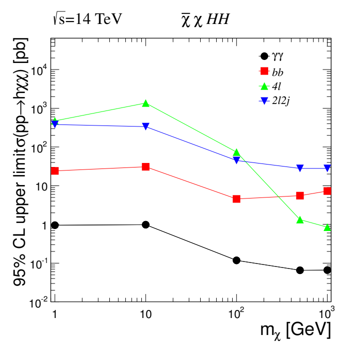

(d)

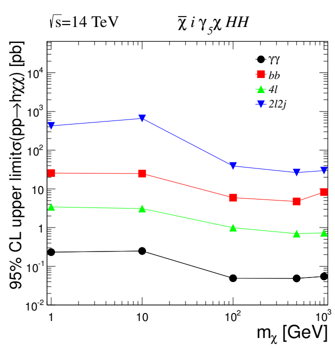

(e)

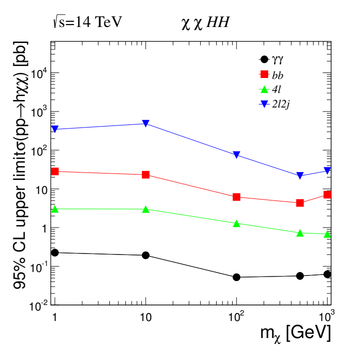

(f)

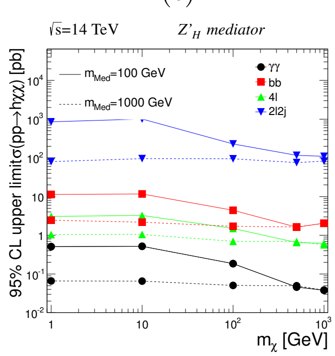

(g)

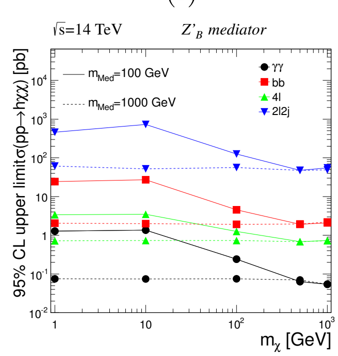

(h)

Figure 3.19: Upper limits on $\sigma(pp \to h\chi\bar{\chi})$ for $\sqrt{s} = 14$ TeV in different decay modes and different models. For simplified models with explicit mediators, solid lines are for 100 GeV mediator, and dashed for 1000 GeV.

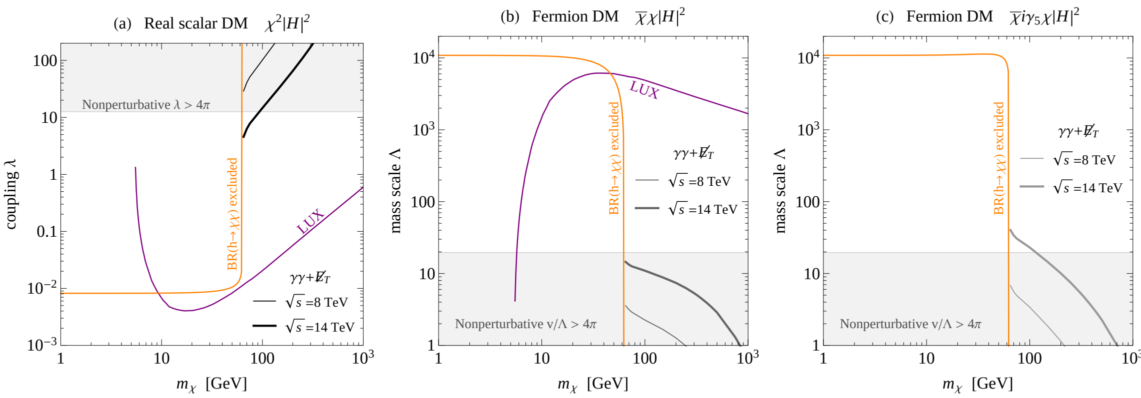

(a) (b) (c)

Figure 3.20: Projected LHC mono-Higgs sensitivities at $\sqrt{s} = 8$ TeV (20 fb^{-1}) and 14 TeV (300 fb^{-1}), with $\gamma\gamma + \not{E}_T$ final states, on Higgs portal effective operators. All constraint contours exclude larger coupling λ or smaller mass scale Λ. Shaded region is excluded based on perturbativity arguments; orange contours denote limits from invisible h decays; purple contours are exclusion limits from LUX.

3.4.1 Higgs portal effective operators

The simplest models for coupling DM and the Higgs boson are the Higgs portal effective operators (3.1) and (3.2). For real scalar DM there is one operator $\chi^2|H|^2$ with a dimensionless coupling λ, while for fermion DM there are two operators $\bar{\chi}\chi|H|^2$ and $\bar{\chi}i\gamma_5\chi|H|^2$ suppressed by a mass scale Λ. All three operators, which we consider separately, are qualitatively similar, and all three contribute to the invisible h branching ratio $\mathcal{B}_{\rm inv}$ for $m_\chi < m_h/2$. The LHC reach depends on whether m_χ is above or below $m_h/2$.

For $m_\chi < m_h/2$, mono-Higgs signals cannot be observed for these operators unless LHC sensitivities can be improved by a factor of ~ 30 over our estimates. Actually, this is true for *any* value of $\mathcal{B}_{\rm inv}$, independently of whether one imposes a constraint on $\mathcal{B}_{\rm inv}$ or not. Although $h\chi\chi$ production is enhanced as λ becomes larger (or Λ smaller), the *visible* branching ratios to $b\bar{b}$, $\gamma\gamma$, etc., become quenched as $\mathcal{B}_{\rm inv}$ becomes large, thereby suppressing the mono-Higgs signal. The most favorable trade-off is for $\mathcal{B}_{\rm inv} \sim 50\%$, close to the present bound. In this case, the dominant $h\chi\chi$ channel is resonant di-Higgs boson production (i.e. hh produced on-shell) followed by an invisible decay $h \to \chi\chi$. The $h\chi\chi$ cross section is bounded by the

hh cross section, 10 fb (34 fb) at 8 (14) TeV [131, 132], which is below the sensitivity limits we have found. For recent LHC studies of di-Higgs cross sections, see for example [133]. As $\mathcal{B}_{\text{inv}}$ becomes larger, resonant production saturates when $\mathcal{B}_{\text{inv}} \sim 100\%$, while nonresonant production continues to grow as λ^2 or $1/\Lambda^2$. However, the visible branching ratios fall as λ^{-2} or Λ^2, compensating any enhancement in production.

On the other hand, for $m_\chi > m_h/2$, there is no bound on λ or Λ from $\mathcal{B}_{\text{inv}}$. Fig. 3.5 shows that our benchmark points with $\lambda = 1$ or $\Lambda = 100$ GeV are below the LHC sensitivity reach. However, since $h\chi\chi$ is produced purely nonresonantly (h cannot decay on-shell to $\chi\chi$), the cross section grows with λ^2 or $1/\Lambda^2$ with no suppression of visible decays.

In Fig. 3.20, we show how our LHC sensitivities map onto the parameter space of these scenarios. The "$\gamma\gamma + \not{E}_T$" contours show the LHC reach from mono-Higgs searches with $\gamma\gamma$ final states. These limits should be interpretted with care since such values push the boundaries imposed by perturbativity and validity of the effective field theory. The shaded region is excluded based on perturbativity. For scalar DM we require $\lambda < 4\pi$, while for fermion DM we require that the $h\bar{\chi}\chi$ Yukawa coupling v/Λ be less than 4π. As discussed above, there is no LHC sensitivity for $m_\chi < m_h/2$. However, this region is strongly contrained by invisible Higgs decays, shown by the orange contour, taking $\mathcal{B}_{\text{inv}} < 38\%$. For direct detection, the SI cross section is given by Eq. (3.23) where

$$f_{p,n} = \frac{m_{p,n}}{m_h^2}\left(1 - \tfrac{7}{9} f_{TG}\right) \times \begin{cases} \lambda/m_\chi\,, & \chi^2|H|^2 \\ 1/\Lambda\,, & \bar{\chi}\chi|H|^2 \end{cases}, \tag{3.24}$$

taking $f_{TG} = 0.92$ [73]. The purple contour shows the exclusion limit from the LUX experiment. On the other hand, the $\bar{\chi}i\gamma_5\chi|H|^2$ operator leads to a velocity-suppressed SI cross section that is very weakly constrained.

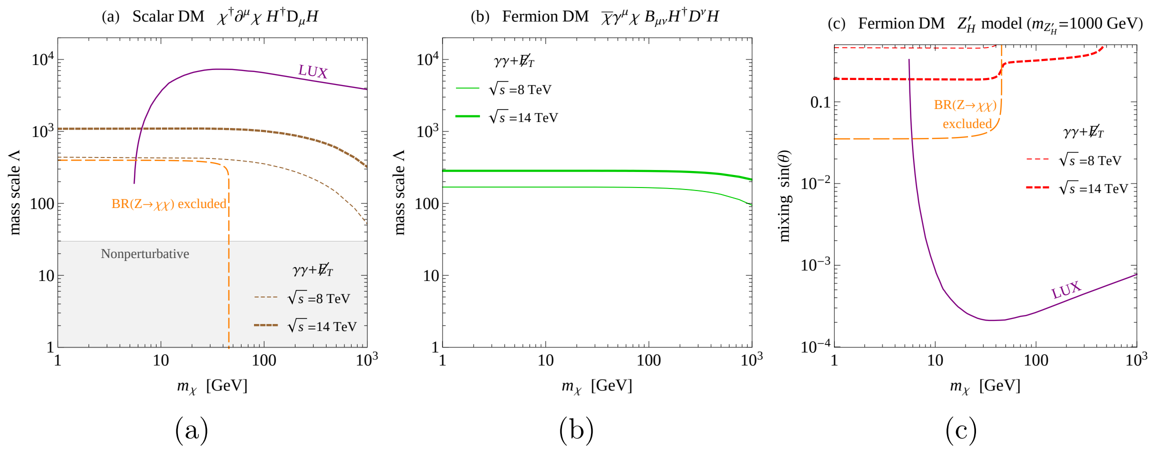

Figure 3.21: Projected LHC mono-Higgs sensitivities at $\sqrt{s} = 8$ TeV (20 fb^{-1}) and 14 TeV (300 fb^{-1}), with $\gamma\gamma + \not{E}_T$ final states, on effective operator models and simplified models. All constraint contours exclude larger mixing angles or smaller mass scales Λ. Shaded region is excluded based on perturbativity arguments or requiring $\sin\theta \leq 1$; dashed orange contours denote limits from invisible Z decays; purple contours are exclusion limits from LUX.

3.4.2 Other effective operators

Beyond the Higgs portal, we have studied mono-Higgs signals from two effective operators coupling DM to the electroweak degrees of freedom. First, at dimension six, we have a scalar DM model with interaction (3.4), which generates an effective coupling of χ to the Z boson that is $\mathcal{O}(v^2/\Lambda^2)$ as strong as a neutrino. In Fig. 3.21(a), the brown dashed contours show the LHC mono-Higgs sensitivity with $\gamma\gamma$ final states. For $m_\chi < m_Z/2$, the invisible Z width measured at LEP constrains this operator, requiring $\Lambda \lesssim 400$ GeV for $\Gamma(Z \to \chi\chi^\dagger) \lesssim 3$ MeV [97] (dashed orange contour). There is no invisible Higgs decay. It is interesting to note that mono-Higgs searches can be more powerful than the invisible Z width bound. However, the Z coupling between DM and nucleons leads to a sizable cross section for direct detection. The proton and neutron couplings are

$$f_n = \frac{1}{4\Lambda^2}, \quad f_p = -(1 - 4s_W^2)\frac{1}{4\Lambda^2}. \tag{3.25}$$

The purple contour shows the current LUX bound, rescaled by the Xenon neutron fraction of ≈ 0.6 since DM couples predominantly to neutrons only. While the LUX bound is highly constraining, it may be evaded completely if DM is inelastic. If the complex field χ is split into two real components $\chi_{1,2}$, operator (3.4) becomes a transition interaction between χ_1 and χ_2, and the energetics of direct detection may be insufficient to excite a transition. We also exclude the shaded region by perturbativity, where the effective Z coupling to DM, given in (3.6), becomes larger than 4π.

At dimension eight, there are many operators that are constrained neither by invisible decays nor direct detection. As an example, we considered here operator (3.9) with fermionic DM. The LHC sensitivities are shown in Fig. 3.21(b) by the green contours. Direct detection signals, arising at one-loop order, are expected to be suppressed, especially compared to other potential operators generated from the same UV physics as operator (3.9).

3.4.3 Simplified models

Beyond effective operators, we have described three simplified models for mono-Higgs signals with a new s-channel mediator particle that couples χ to SM particles.

Hidden sector Z'

First, we consider a hidden sector Z', denoted Z'_H, that couples to SM particles by mixing with the Z boson. The only parameters in this model are $m_{Z'_H}$ (Z'_H mass), g_χ (DM-Z'_H coupling), and $\sin\theta$ (Z-Z'_H mixing angle). Fig. 3.21(c) shows the LHC mono-Higgs sensitivity to this model, as a function of $\sin\theta$, for $m_{Z'_H} = 1000$ GeV and $g_\chi = 1$. The dashed orange contour shows the exclusion limit from the invisible Z width if $m_\chi < m_Z/2$, requiring $\sin\theta \lesssim 0.03$ for $\Gamma(Z \to \chi\bar{\chi}) \lesssim 3$ MeV [97]. The ρ-parameter provides in principle a much stronger limit, at the level of $\sin\theta \lesssim 3 \times 10^{-3}$ for any m_χ. However, the quantitative details depend on doing a global fit to precision electroweak data, which is sensitive to other sources of new physics that may affect those observables. Nevertheless, large values of $\sin\theta$ accessible to mono-Higgs searches have significant tension with precision electroweak observables.

For direct detection, the proton and neutron couplings entering Eq. (3.23) are

$$f_n = \frac{g_2 g_\chi \sin 2\theta}{8 c_W m_Z^2} \left(1 - \frac{m_Z^2}{m_{Z'_H}^2} \right) , \quad f_p = -(1 - 4 s_W^2) f_n \, . \tag{3.26}$$

The LUX exclusion limits, rescaled by the Xenon neutron fraction ≈ 0.6, are denoted by the purple contour. These limits may be evaded for a Z'_H that couples to the axial vector current $\bar{\chi}\gamma^\mu\gamma_5\chi$, instead of the vector current $\bar{\chi}\gamma^\mu\chi$ that we had assumed. In that case, although the collider phenomenology would be identical, this model would contribute to the spin-dependent direction detection cross section only (at leading order in velocity), which is less constrained. Alternately, χ may be inelastic if it has a Majorana mass term that splits the Dirac field χ into two Majorana fields $\chi_{1,2}$. Eq. (3.14) becomes a transition coupling between χ_1 and χ_2 that can be energetically forbidden in direct detection scattering.

Baryon-number Z'

Second, we consider a leptophobic Z', denoted Z'_B, that couples to both baryon number and DM. The dark blue contours in Figs. 3.22(a,b) show the LHC mono-Higgs sensitivities for our two Z'_B benchmarks ($m_{Z'_B} = 100$ GeV and $m_{Z'_B} = 1000$ GeV; see Table 3.1) except we have allowed the quark-Z'_B coupling g_q to vary. The mono-Higgs cross section scales with $g_{hZ'Z'}^2$. The light gray contours show the LHC reach if $g_{hZ'Z'}$ is pushed as large as allowed by perturbativity arguments.[2] There is no constraint from invisible h or Z decays.

[2]We impose a bound $m_{Z'_B}^2/v_B^2 < 4\pi$ based on perturbativity of the underlying $h_B^2 Z'Z'$ coupling in Eq. (3.11) before mixing, which requires $g_{hZ'Z'} < \sqrt{4\pi} m_{Z'_B} \sin\theta$.

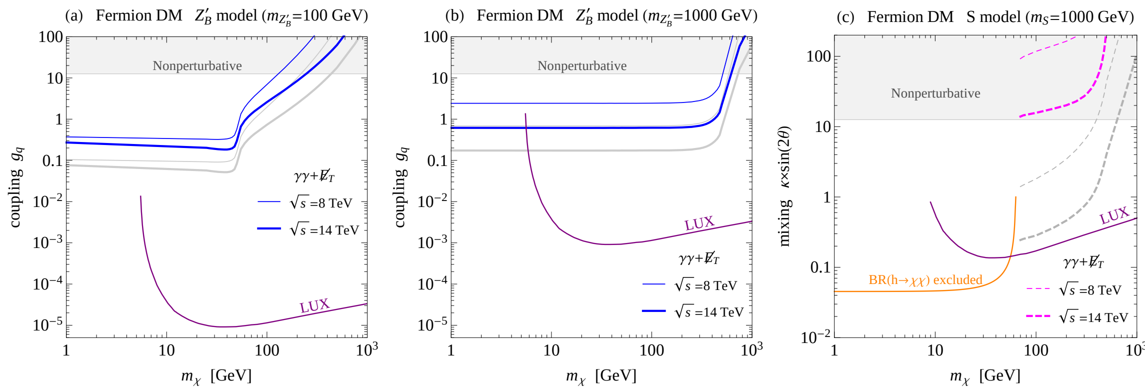

(a) (b) (c)

Figure 3.22: Projected LHC mono-Higgs sensitivities at $\sqrt{s} = 8$ TeV (20 fb^{-1}) and 14 TeV (300 fb^{-1}), with $\gamma\gamma + \not{E}_T$ final states, on simplified models. All constraint contours exclude larger couplings or mixing angles. The light gray contours show the LHC reach if $g_{hZ'Z'}$ is pushed as large as allowed by perturbativity arguments. Shaded region is excluded based on perturbativity arguments or requiring $\sin\theta \leq 1$; orange contour denotes limit from invisible h decays; purple contours are exclusion limits from LUX.

The DM-nucleon couplings for SI direct detection are

$$f_{p,n} = \frac{3 g_q g_\chi}{m_{Z'_B}^2}\,. \tag{3.27}$$

For our benchmark scenarios, LUX strongly excludes the entire parameter region above kinematic threshold, thereby requiring extremely small values of g_q. However, like the Z'_H model, this bound can be evaded by appealing to inelastic DM or an axial-vector DM interaction. Alternately, DM particles below ~ 5 GeV are below LUX thresholds and are not excluded by invisible h or Z decays.

It is clear from Figs. 3.22(a,b) that mono-Higgs searches have sensitivity only for $m_\chi < m_{Z'_B}/2$, where the Z'_B can be produced on-shell and then decays into $\chi\bar{\chi}$. However, the Z'_B has a sizable coupling to quarks and can decay back into jets instead, giving a dijet resonance. The constraints on a leptophobic Z' DM model from both mono-jet and dijet resonance searches were explored by Ref. [52] based on Tevatron and 7 TeV LHC studies with ~ 1 fb. The constraints obtained therein are stronger than the our projected $h +$

$\not{E}_T$ sensitivities. Thus, mono-Higgs searches do not give a strong probe of the Z'_B model compared to other existing analyses. (This conclusion would be strengthened by considering more recent searches compared to Ref. [52].)

Scalar singlet S model

Lastly, we consider the scalar singlet model, where S couples to SM particles by mixing with the Higgs boson. We focus on the benchmark case with $m_S = 1000$ GeV (see Table 3.1). For $m_\chi < m_h/2$, LHC sensitivities are insufficient to put any limit on this model, similar to the Higgs portal operators discussed above, due to the visible $\gamma\gamma$ signal becoming diluted by a large $h \to \chi\bar{\chi}$ branching ratio. However, this mass range is strongly constrained by the invisible h width.

For $m_\chi > m_h/2$, the dominant $h\chi\bar{\chi}$ channel is via Higgstrahlung from an intermediate S propagator, shown in Fig. 3.3(b). This process is proportional to $\sin^2(2\theta)$, where θ is the h-S mixing angle in (3.19). To present our bounds, it is useful to introduce an extra scaling parameter κ, defined by $\sin(2\theta) \to \kappa \sin(2\theta)$, such that now the $h\chi\bar{\chi}$ cross section is proportional to $\kappa^2 \sin^2(2\theta)$. The model we have discussed in Sec. 3.2 is obtained with $\kappa = 1$. However, larger values of κ may be obtained in more complicated models, e.g., with an additional Higgs doublet [55].[3] The magenta contours in Fig. 3.22(c) show the LHC sensitivities on $\kappa \times \sin(2\theta)$, with other model parameters fixed as in Table 3.1. The corresponding light gray contours show the enhanced LHC reach if we take coupling parameters $b = 4\pi$ and $y_\chi = 4\pi$ as large as perturbatively allowed. For $\kappa = 1$, since $\sin(2\theta)$ cannot be larger than unity, the LHC has sensititivity only for $\sqrt{s} = 14$ TeV and for values of b, y_χ near their

[3] Suppose we introduce an additional Higgs doublet H' coupled to quarks. The CP-even neutral scalar couplings to fermions are

$$\mathscr{L} \supset -y_\chi \bar{\chi}\chi S - \frac{m_q}{v}\bar{q}q(h + \kappa\, h')\,, \tag{3.28}$$

where h' is an additional neutral Higgs state with couplings aligned with those of the SM Higgs boson h, up to a constant κ. If S mixes with h', as opposed to h, the diagram in Fig. 3.3(b) is enhanced by a factor κ.

perturbative limits. Mono-Higgs signals may be more readily observable, however, in scalar extended models with $\kappa > 1$. The shaded region is excluded if we require $\kappa < 4\pi$ based on perturbativity of the top Yukawa coupling in Eq. (3.28). The purple contour denotes the current LUX bound for the $\kappa = 1$, with nucleon couplings

$$f_{p,n} = \frac{y_\chi m_{p,n} \sin(2\theta)}{2 v m_h^2} \left(1 - \frac{m_h^2}{m_S^2}\right) \left(1 - \tfrac{7}{9} f_{TG}\right). \tag{3.29}$$

However, these limits can be evaded if S couples to $\bar{\chi} i \gamma_5 \chi$, rather than $\bar{\chi}\chi$ as we assumed, with little impact on the collider signatures. The orange contour shows the limit from $\mathcal{B}_{\text{inv}} < 38\%$ for $\kappa = 1$, although this bound can be weakened if S mixes primarily with an additional Higgs boson, rather than h.

3.5 Conclusions

Since the particle theory of DM is as yet unknown, it is worthwhile exploring all possible avenues for discovery. In this chapter, we have studied a new DM signature to be explored at the LHC: missing energy from DM particles produced in association with a Higgs boson ($h + \not{E}_T$). Coupling between DM and the Higgs boson is a generic feature of many weak-scale DM models. While the h invisible branching fraction $\mathcal{B}_{\text{inv}}$ is a sensitive probe of Higgs boson couplings to light DM, mono-Higgs searches provide a complementary window into DM masses above $m_h/2$ or into models that otherwise do not lead to invisible h decays.

We have considered several benchmark DM models for generating mono-Higgs signals at the LHC, including both EFT operators and simplified models with new s-channel mediators. We performed a study of SM backgrounds to $h + \not{E}_T$ searches at $\sqrt{s} = 8$ TeV (20 fb^{-1}) and 14 TeV (300 fb^{-1}) for four h decay channels: $h \to b\bar{b}$, $\gamma\gamma$, and $ZZ^* \to 4\ell$, $\ell\ell jj$. The $h \to b\bar{b}$ channel, despite having the largest branching ratio, does not give the best LHC sensitivity reach due to a large $t\bar{t}$ background. The greatest reach for all our models is set by the $h \to \gamma\gamma$ channel. Future experimental analyses may achieve reduced systematic uncertainties from data-driven background extrapolation or may find avenues for more aggressive background supporession than were plausible in the context of approximations made for these sensitivity studies.

The most promising scenarios for mono-Higgs signals are models where the effective coupling of DM to SM particles requires additional insertions of the Higgs field H. One example is an effective coupling of DM to the Z boson via higher dimensional operators. We showed that, for scalar DM, LHC mono-Higgs searches at 14 TeV can set a limit $\Lambda \gtrsim$ TeV on the effective mass scale governing this coupling. For light DM ($m_\chi < m_Z/2$), this constraint would be stronger than the invisible Z width bound from LEP. Another scenario is the case of scalar mediator models. While LHC sensitivities to the minimal Higgs-mixing model we considered are insufficient to constrain this scenario, extended scalar models (e.g., [134]) offer a promising direction for mono-Higgs studies.

Ref. [135] explores similar mono-Higgs ideas within the framework of EFT operators with fermionic DM. These authors reinterpreted a recent CMS search for $Z(\nu\bar{\nu}) + h(b\bar{b})$ at 8 TeV with 19 fb^{-1} [136] in terms limits on $h\chi\chi$. The new physics sensitivity adopted in Ref. [135] is consistent with our projected 8 TeV sensitivities with 20 fb^{-1} in the $b\bar{b}$ channel, although somewhat different cuts were adopted. Ref. [135] did not consider other Higgs boson final states ZZ^* and $\gamma\gamma$ studied herein, the latter of which is significantly more sensitive than $b\bar{b}$. For EFT operators, Ref. [135] studied the dimension-5 operators given in (3.2), obtaining a lower bound $\Lambda \gtrsim$ GeV. Such limits are not physically meaningful since not only is the EFT invalid at LHC energies, but more generally any perturbative analysis would fail since the $h\bar{\chi}\chi$ Yukawa coupling would be $v/\Lambda \sim 100$. On the other hand, interesting limits were obtained for a variety of other operators. Ref. [135] considered dimension-6 operators given in (3.5) — whereas we considered a similar operator but for scalar DM, given in (3.4) —

as well as dimension-7 and -8 operators involving quarks and gluons. Although we did not consider the latter operators here, they arise in the low-energy limit of the simplified models we have studied.

Chapter 4

Hidden On-Shell Mediators for the Galactic Center γ-ray Excess

Based on arXiv:1404.6528 [137]

4.1 Introduction

The particle nature of dark matter (DM) remains one of the outstanding open questions in high energy physics. Experimental probes of the dynamics that connect the dark sector and the Standard Model (SM) fall into three complimentary classes shown schematically in Fig. 4.1 See [138] for a status report.

Recent analyses of the FERMI Space Telescope data find an excess of 1–10 GeV γ-rays from the center of the galaxy. In fact, a similar excess seems to extend away from the center to high galactic latitudes [139–141]. This may be indicative of dark matter annihilating into SM final states which later shower to produce the observed excess photon spectrum [1,142–151]; see [151–160] for recent models. While an early estimate argued that an alternate interpretation based on unidentified millisecond pulsars is unlikely [161], [1] and [162] recently

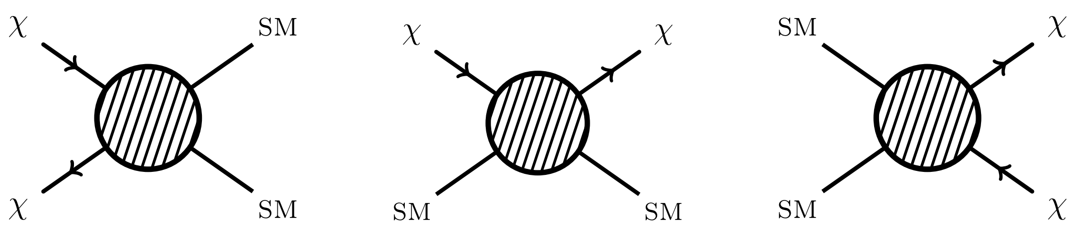

(a) (b) (c)

Figure 4.1: (a) Annihilation, (b) Direct Detection, (c) Collider. Complimentary modes of dark matter detection. Annihilation sets both the thermal relic abundance and the present-day indirect detection rate.

demonstrated the consistency of this hypothesis with the γ-ray excess. Indeed, it may be difficult to distinguish these two possibilities since the extrapolated millisecond pulsar (MSP) profile is very similar to standard DM profiles [163]. For the remainder of this chapter we assume the excess is generated by DM annihilation. The latest analyses prefer a 40 GeV dark matter candidate that annihilates into $b\bar{b}$ pairs[1] with a thermally averaged cross section $\langle\sigma v\rangle_{b\bar{b}} \approx \mathcal{O}(\text{few})\times 10^{-26}\text{cm}^3/\text{s}$ [1,150]. Further, because $\langle\sigma v\rangle_{b\bar{b}}$ is close to the value required to be a thermal relic from standard freeze-out, it is implausible that such a relic could produce such a γ-ray signal without having an s-wave annihilation mode. Combined with constraints from direct detection and collider experiments, this signal motivates a more detailed study of the physics encoded in the shaded regions of Fig. 4.1.

4.1.1 From Effective Theories to Simplified Models

A simple parameterization of the SM–DM interaction is to treat the shaded blobs as effective contact interactions between dark matter particles (χ) and SM states. For example, the

[1] Annihilation of 10 GeV DM into $\tau\bar{\tau}$ is also plausible fit, see [154,155,158,164–166] for recent models. [167] found that a universal coupling to charged leptons may be favored after bremsstrahlung and inverse Compton scattering effects are included. In this chapter we focus on the case where the γ-ray excess is generated by $b\bar{b}$ pairs; we comment on more general final states in Section 4.6.1 and Appendix A.

coupling of fermionic DM to a quark q is parameterized through nonrenormalizable operators

$$\mathcal{L} \supset \frac{1}{\Lambda^2} \left(\bar{\chi}\mathcal{O}_\chi\chi\right) \left(\bar{q}\mathcal{O}_q q\right), \tag{4.1}$$

where, for example, $\mathcal{O}_\chi \otimes \mathcal{O}_q = \gamma^\mu \otimes \gamma_\mu$ corresponds to an interaction mediated by a heavy vector mediator that has been integrated out. The coefficient Λ^{-2} can be calculated for specific DM models and allow one to apply bounds from different types of experiments in a model-independent way. This technique has been applied, for example, for collider [4, 20–26, 28–34, 37, 77, 168–171], indirect detection [35, 37–44] and direct detection [36, 67, 172–178] bounds on dark matter. The choice of pairwise dark matter interactions assumes the existence of a symmetry that also stabilizes the DM particle against decay while the pairwise SM interactions are assumed to be the leading order gauge-invariant operators. This need not be the case as has been demonstrated for annihilation [179] and direct detection [180]. In these cases, the structure in (4.1) fails to capture the physics of the mediator fields which couple to both the dark and visible (SM) sectors: the effective contact interaction description breaks down when the mediators do not decouple. The limitations of the contact interaction bounds were pointed out in [23] and highlighted in [49, 54, 181, 182].

This motivates a shift in the *lingua franca* used to compare experimental results to models: rather than contact interactions, light (nondecoupled) mediators suggest using 'simplified models' that include the renormalizable dynamics of the mediator fields [19]. This approach has been applied to colliders [16, 49, 51–56, 74, 75, 182–185] and astrophysical bounds where the physics of the mediator has been explored in DM self-interactions [45, 186–204].

4.1.2 The γ-ray Excess Suggests Light Mediators

When the galactic center signal is combined with complementary bounds from direct detection and colliders, one is generically led to the limit where the contact interaction description

Name	Operator	Constraint
D2	$(\bar{\chi}\gamma_5\chi)\,(\bar{q}q)$	Edge of EFT validity from monojet bounds
D4	$(\bar{\chi}\gamma_5\chi)\,(\bar{q}\gamma_5 q)$	Edge of EFT validity from monojet bounds
D5	$(\bar{\chi}\gamma^\mu\chi)\,(\bar{q}\gamma_\mu q)$	Spin independent direct detection
D6	$(\bar{\chi}\gamma^\mu\gamma_5\chi)\,(\bar{q}\gamma_\mu q)$	Related to D5, D8 in chiral basis
D7	$(\bar{\chi}\gamma^\mu\chi)\,(\bar{q}\gamma_\mu\gamma_5 q)$	Related to D5, D8 in chiral basis
D8	$(\bar{\chi}\gamma^\mu\gamma_5\chi)\,(\bar{q}\gamma_\mu\gamma_5 q)$	Spin dependent direct detection
D9	$(\bar{\chi}\sigma^{\mu\nu}\chi)\,(\bar{q}\sigma_{\mu\nu}q)$	Nontrivial spin-2 UV completion
D10	$(\bar{\chi}\sigma^{\mu\nu}\gamma^5\chi)\,(\bar{q}\sigma_{\mu\nu}q)$	Nontrivial spin-2 UV completion
D12	$(\bar{\chi}\gamma_5\chi)\,G_{\mu\nu}G^{\mu\nu}$	Monojet bounds
D14	$(\bar{\chi}\gamma_5\chi)\,G_{\mu\nu}\widetilde{G}^{\mu\nu}$	Monojet bounds

Table 4.1: Contact operators between Dirac DM and quarks or gluons [4] that support s-wave annihilation and the constraint for the galactic center. See [5] for a recent technical analysis.

(4.1) breaks down and a simplified model description is necessary. By 'generic' we mean no parameter tuning or additional model building is invoked.

The tension is summarized in Table 4.1, where we list the Dirac fermion dark matter contact interactions that satisfy the requirement of s-wave annihilation[2]. Because each effective operator simultaneously encodes the various DM–SM interactions in Fig. 4.1, requiring a coupling large enough to produce the γ-ray excess automatically generates signals that are constrained by null results at direct detection [3, 71] and monojet [205] experiments. These rule out operators D5, D8, D12, and D14 in Table 4.1. The operators D2 and D4 are at the edge of the validity of the effective theory [49, 54, 182]. We ignore the D9 and D10 operators since they cannot be UV completed by a renormalizable theory. Finally, the D6 and D7 operators are related to D5 and D8 by the chiral structure of the Standard Model. The fermionic $\mathrm{SU}(2)_\mathrm{L}\times\mathrm{U}(1)_\mathrm{Y}$ eigenstates are chiral so that gauge invariant interactions are naturally written in a chiral basis $\bar{q}\mathcal{O}_q P_{L,R} q$ where $P_{L,R} = \frac{1}{2}(1 \mp \gamma^5)$. Thus one generically expects that in the absence of tuning[3], the presence of vector or axial couplings implies the

[2]Majorana dark matter relaxes these bounds by forcing some of these operators to vanish identically.

[3]It is worth noting that such a 'coincidental' cancellation occurs in the Z coupling to charged leptons which is dominantly axial due to $\sin^2\theta_W \approx 1/4$.

existence of the other.

It is thus difficult to account for the γ-ray excess in the 'heavy mediator' limit where these contact interactions are valid. A more technical analysis of the contact interaction description was recently performed in [5, 40, 206] and includes the case of scalar dark matter. The γ-ray excess thus generically implies a dark sector with mediators that do not decouple and hence is more accurately described in a simplified model framework. Recent comprehensive studies of simplified models for the γ-ray excess have dark matter annihilating through off-shell mediators (s- and t-channel diagrams) [207, 208]; see [209, 210] for an earlier model.

4.1.3 Annihilation to On-shell Mediators

In this chapter we focus on a different region in the space of simplified models where mediators are light enough that they can be produced on-shell in dark matter annihilation, henceforth referred to as the on-shell mediator scenario. This annihilation mode is largely independent of the mediator's coupling to the SM so long the latter is nonzero. Lower limits on the SM coupling—that is, upper limits on the mediator lifetimes—are negligible since the mediator may propagate astrophysical distances before decaying to the $b\bar{b}$ pairs that subsequently yield the γ-ray excess. The SM coupling can be parametrically small which suppresses the off-shell s-channel annihilation mode as well as the direct detection and collider signals. This is shown in Fig. 4.2.

Because on-shell annihilation into mediators requires at least two final states[4], the resulting annihilation produces at least four b quarks, as shown in Fig. 4.2a. This, in turn, requires a heavier dark matter mass in order to eject ≈ 40 GeV b quarks from each annihilation to fit the γ-ray excess. This avoids the conventional wisdom that this excess requires $10-40$ GeV dark matter. In the limit on-shell annihilation dominates, the total excess γ-ray flux is

[4] One may also consider semi-annihilation processes $\chi_1\chi_2 \to \chi_3$(mediator) [211]. See [212] for a prototype model for the galactic center γ-ray excess.

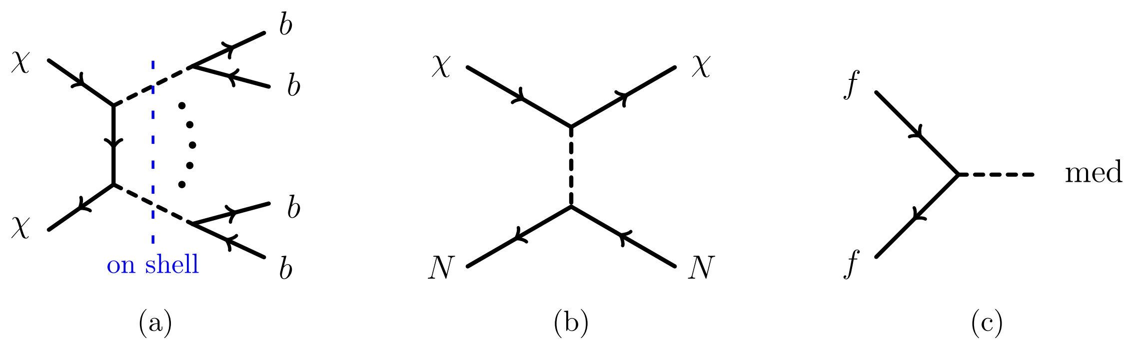

Figure 4.2: (a) Annihilation, (b) Direct Detection, (c) Collider. DM complimentarity for on-shell mediators; compare to Fig. 4.1. (a) The annihilation rate is independent of the mediator coupling to the Standard Model. (b) Direct detection remains 2-to-2, here N is a target nucleon. (c) Colliders can search for the presence of the mediator independently of its DM coupling.

fit by a single parameter, the mediator coupling to dark matter. Once fit, this parameter determines whether the DM may be a thermal relic. We remark that the spectrum is slightly boosted by the on-shell mediator; we address this below and explore possibilities where the mediator mass can be used as a handle to change the spectral features.

The on-shell mediator limit thus separates the physics of mediators SM and DM couplings. The former can be made parametrically small to hide DM from direct detection and collider experiments, while the latter can be used to independently fit indirect detection signals such as the galactic center γ-ray excess. Observe that these simplified models modify the standard picture of complementary DM searches for contact interactions shown schematically in Fig. 4.2. Annihilation now occurs through multiple mediator particles and is independent of the mediator coupling to the SM. Direct detection proceeds as usual through single mediator exchange between DM and SM. Collider bounds, on the other hand, need not depend on the DM coupling at all and can focus on detecting the mediator rather than the dark matter missing energy.

In this chapter we explore the phenomenology of on-shell mediator simplified models for the galactic center. This chapter is organized as follows. In the following two sections we present

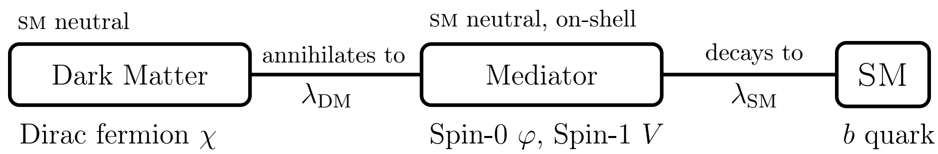

Figure 4.3: Dark matter annihilates to on-shell mediators, which in turn decay into $b\bar{b}$ pairs. Each step is controlled be a separate coupling, λ. See text for details.

the on-shell simplified models that generate the γ-ray excess and determine the range of dark sector parameters. We then assess in Section 4.4 the extent to which the on-shell mediators must be parametrically hidden from direct detection and colliders. In Section 4.5 we discuss the viability of this scenario for thermal relics. We comment on the lessons for UV models of dark matter in Section 4.6. Appendix A briefly describes plausible variants for generating γ-ray spectra with more diverse SM final states.

4.2 On-Shell Simplified Models

Fig. 4.3 schematically represents the class of simplified models that we consider. We assume the existence of a single SM neutral spin-0 or spin-1 mediator which couples to Dirac fermion DM with coupling λ_{DM} and $b\bar{b}$ pairs with coupling λ_{DM}. Majorana fermions do not differ qualitatively in this regime. We focus on the case where mediators couple to the Dirac DM fermion with coupling λ_{DM} and to $b\bar{b}$ pairs with coupling λ_{SM}.

4.2.1 Parity Versus Chirality

Before describing the mediator interactions, we remark on the utility of the parity and chirality bases for four-component fermion interactions. In the parity basis, one uses explicit factors of the γ^5 matrix to parameterize

$$\text{scalar } (\mathbb{1}), \qquad \text{pseudoscalar } (\gamma^5), \qquad \text{vector } (\gamma^\mu), \qquad \text{and axial } (\gamma^\mu\gamma^5). \tag{4.2}$$

interactions. This basis is most suited for nonrelativistic interactions. Equivalently, in the chirality basis, one inserts chiral projection operators $P_{L,R} = \frac{1}{2}\left(1 \mp \gamma^5\right)$ into fermion bilinears. This is the natural description of SM gauge invariants. The spin-0 fermion bilinears are

$$\bar{\Psi}(\mathbb{1}, \gamma^5)\Psi = \bar{\Psi}P_L\Psi \pm \bar{\Psi}P_R\Psi = \psi\chi \mp \text{h.c.} \tag{4.3}$$

where we have written the Dirac spinor in terms of two-component left-handed Weyl spinors $\Psi = (\psi, \chi^\dagger)^T$, see e.g. [213]. Similarly, the spin-1 bilinears are

$$\bar{\Psi}\gamma^\mu(\mathbb{1}, \gamma^5)\Psi = \bar{\Psi}\gamma^\mu P_L\Psi \pm \bar{\Psi}\gamma^\mu P_R\Psi = \psi^\dagger\bar{\sigma}^\mu\psi \mp \chi^\dagger\bar{\sigma}^\mu\chi. \tag{4.4}$$

The γ^5 appears as a phase in the spin-0 coupling and a relative sign in the spin-1 couplings of opposite chirality fermions.

The phenomenology of the γ-ray excess suggests the use of both descriptions. DM annihilation and direct detection occur nonrelativistically so the choice of a scalar (vector) versus a pseudoscalar (axial) can dramatically affect the rate for these processes. It is thus useful to parameterize these in the language of (4.2), whether or not the DM interactions are chiral. On the other hand, electroweak gauge invariance mandates chiral interactions for the mediator's SM coupling.

We are thus led to consider a hybrid description where the mediator's interaction with the SM is naturally described by a chiral coupling while the interaction with DM is most usefully described by a coupling of definite parity. The chiral description of the SM breaks down for direct detection; however, since chiral interactions generically include both the $\mathbb{1}$ and

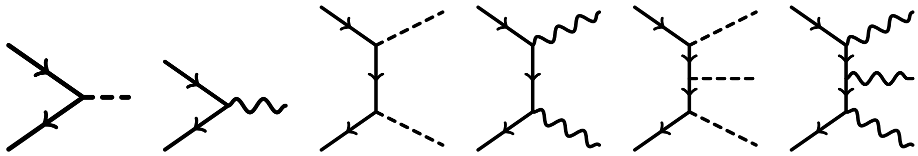

Interaction	S (P)	V (A)	S (P)	V (A)	S (P)	V (A)
Partial Wave	p (s)	s (p/s)	p (p)	s (s)	p (s)	p (p)
On/Off-Shell	Off	Off	On	On	On	On
DM Mass [GeV]	≈ 40	≈ 40	≈ 80	≈ 80	≈ 120	≈ 120

Table 4.2: Annihilation to mediators. S,P,V,A correspond to scalar, pseudoscalar, vector, and axial vector interactions with DM. Also shown: the leading velocity (partial wave) dependence, whether the process may occur on-shell, and the approximate mass for 40 GeV final state b quarks. The off-shell axial coupling is s- or p-wave for axial/vectorlike SM coupling respectively [6].

γ^5 terms, we focus on bounds from the parity-even interaction that yields stronger bounds. Dark matter searches at colliders probe relativistic energies without polarization information and are thus typically independent of parity. In this chapter we refer to the 'spin-0' or 'pseudoscalar' mediator to mean the spin-0 field which has a pseudoscalar interaction with the Dirac DM without assuming a particular parity-basis interaction to the SM.

4.2.2 Mediators Versus s-wave Annihilation

The parity basis for dark matter interactions clarifies the types of interactions that can yield s-wave annihilation for the γ-ray excess. In Table 4.2 we show annihilation modes to up to three spin-0 or spin-1 mediators for the interactions in (4.2). On-shell kinematics require at least two final states so that the leading annihilation modes in the on-shell mediator limit are two spin-1 particles (of either parity) or three pseudoscalars. The off-shell diagrams represent the s-channel simplified models in [207, 208].

Also shown in Table 4.2 are the approximate masses for the on-shell mediator scenarios. In order to eject 40 GeV b quarks from each annihilation, the two (three) body final states require that the DM mass is approximately $m_\chi = 80$ (120) GeV. Observe that this mechanism allows one to circumvent the conventional wisdom that the galactic center signal requires DM lighter than typical electroweak scale states.

Note that these masses are back-of-the-envelope estimates that do not account for the boost in the b spectrum from the mediator momentum or the spread in mediator energies for the 3-body final state. Further, we assume only couplings to b. This is a reasonable estimate and does not violate flavor bounds for spin-0 mediators since it follows approximately from minimal flavor violation (MFV) [61,214–216]. On the other hand, spin-1 mediators generically couple democratically to all three generations in the MFV ansatz, as can be seen when comparing (4.3) and (4.4). Finally, one should also account for the effect of the off-shell, s-channel annihilation modes for finite coupling to the SM, λ_{SM}. We account for these in Sec. 4.3 where we perform a fit to the γ-ray excess.

The amplitudes for annihilation to two spin-1 mediators via the vector and axial interactions are identical so in this case the choice of parity versus chirality basis is irrelevant. Of the spin-0 mediators, however, only pseudoscalars generate s-wave annihilation. If the dark sector is described by a chiral theory, one generically expects both parities to be present. However, since the scalar is p-wave, it is suppressed by $\langle v^2 \rangle \sim 10^{-6}$ and may be ignored for annihilation. On the other hand, this dramatically affects the direct detection rate, as discussed in Sec. 4.4.2.

4.2.3 Requirements for On-Shell Mediators

On-shell mediator models must satisfy the following conditions for the dark sector spectrum,

$$2m_\chi > \begin{cases} 2m_V & \text{for a spin-1 mediator} \\ 3m_\varphi & \text{for a spin-0 mediator} \end{cases} \tag{4.5a}$$

$$m_{V,\varphi} > 2m_b \tag{4.5b}$$

and the following requirements on the mediator couplings,

$$\lambda_{\text{DM}} \sim 1 \tag{4.5c}$$

$$\lambda_{\text{SM}} \ll 1. \tag{4.5d}$$

These are interpreted as follows:

(a) Nonrelativistic DM annihilation has enough energy to produce on-shell mediators.

(b) The mediator may decay into b quarks to produce the spectrum of the γ-ray excess.

(c) The additional coupling(s) in the on-shell diagrams do not suppress the amplitude nor are they so large that they are nonperturbative, $\lambda_{\text{DM}}^2 < 4\pi$.

(d) Parametrically suppress the off-shell, s-channel mediator diagrams in annihilation and simultaneously ameliorate limits from direct detection and colliders.

We now elucidate the conditions (4.5c–4.5d) more carefully by determining the coupling scaling of the on-shell versus off-shell annihilations. For a spin-1 mediator, the on-shell annihilation mode goes through two on-shell mediators which subsequently decay into $b\bar{b}$ pairs. The key observation is that unlike the case of an off-shell s-channel mediator, the annihilation to on-shell mediators is largely independent of the coupling to the SM, λ_{SM}.

We thus focus on the limit where the on-shell mode dominates over the off-shell s-channel diagram,

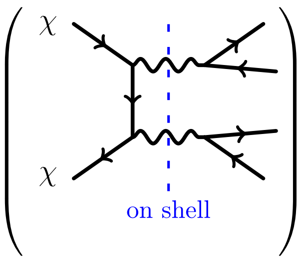

$$\sim \lambda^2_{\rm DM} \qquad \gg$$

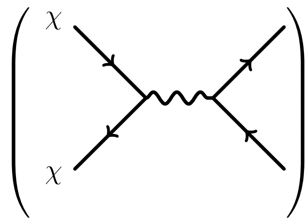

$$\sim \lambda_{\rm DM}\lambda_{\rm SM}. \tag{4.6}$$

Note that this condition is trivial if the mediator has axial couplings since the s-channel diagram is p-wave. As discussed above, in a UV model that avoids flavor bounds, a spin-1 mediator is likely to couple democratically to other SM fermion generations. The annihilation rate relevant to the galactic center γ-ray excess would be multiplied by the branching ratio to $b\bar{b}$ pairs, $\text{Br}(V \to b\bar{b})$. If one insists that the γ-ray excess is generated exclusively by the decay of b quarks, then the branching ratio is an additional $\mathcal{O}(10^{-1})$ factor that must be compensated by $\lambda_{\rm DM}$. More dangerously, one must also account for the γ-ray pollution from annihilations yielding light quarks. We address the effect of this pollution on the fit to the γ-ray spectrum in Sec. 4.6.1.

For a pseudoscalar mediator the analogous limit is

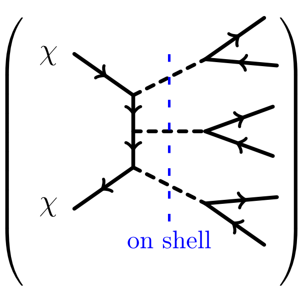

$$\sim \frac{\lambda^3_{\rm DM}}{\sqrt{4\pi}} \qquad \gg$$

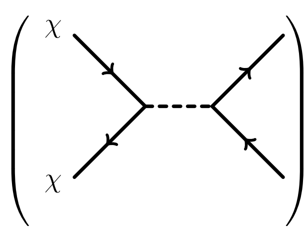

$$\sim \lambda_{\rm DM}\lambda_{\rm SM}. \tag{4.7}$$

We have also inserted an explicit factor of $\sqrt{4\pi}$ for the additional phase space suppression in the cross section of a three- versus two-body final state.

Both (4.6) and (4.7) impose the limit $\lambda_{\rm SM} \ll 1$ to suppress the s-channel off-shell mediator with $\lambda_{\rm DM}$ fixed (for given masses) to give the correct galactic center photon yield. The magnitude of '$\gg$' is addressed in Sec. 4.4. The limit of a very small coupling to the Standard Model is further motivated by the dearth of observational evidence for dark matter interactions at colliders and direct detection experiments. This limit also occurs naturally in models of dark photon kinetic mixing or compositeness. In our scenario, parametrically suppressing this coupling increases the lifetime of the mediator. This has little phenomenological consequence given the astronomical distance scales associated with the galactic center.

4.2.4 Estimates for the γ-ray Excess

Before doing a fit to the γ-ray excess, we establish a back-of-the-envelope benchmark using the DM masses in Table 4.2 and neglecting the mediator spectrum and boost. This gives a reasonable estimate while also highlighting the parametric behavior of the fit. The contact interaction fits to the galactic center γ-ray excess suggest annihilation to a pair of b quarks with a thermally averaged cross section [1],

$$\langle \sigma v \rangle_{b\bar{b}} \approx 5 \times 10^{-26} \text{ cm}^3/\text{s}. \tag{4.8}$$

Note that [150] found a slightly smaller cross section, 1.5×10^{-26} cm^3/s due to a slightly tighter DM halo (larger γ parameter in the generalized NFW profile [217–219]). The photon spectrum from this annihilation is

$$\frac{d\Phi(b,\ell)}{dE_\gamma} = \frac{\langle \sigma v \rangle_{b\bar{b}}}{2} \frac{1}{4\pi m_\chi^2} \frac{dN_\gamma}{dE_\gamma} \int_{\rm LOS} dx\, \rho^2 \left(r_{\rm gal} \left(b, \ell, x \right) \right), \tag{4.9}$$

where (b,ℓ) are Galactic coordinates, ρ is the DM profile, and $r_{\rm gal}$ is the distance from the galactic center along the line of sight (LOS).

In on-shell mediator models, the DM annihilates into 2 (3) mediators which each decay into pairs of b quarks. In order that each of these final state b quarks to carry 40 GeV, the DM mass must be approximately 80 (120) GeV as stated in Table 4.2. This reduces the DM number density by 4 (9) in order to maintain the observed mass density; this is manifested in the m_χ^{-2} factor of (4.9). This is factor is partially compensated by the multiplicity of $b\bar{b}$ pairs in the final state increases the total secondary photon flux by a factor of 2 (3). Together, these effects require that the annihilation cross section is a factor of ≈ 2 (3) times larger than $\chi\bar{\chi} \to b\bar{b}$ cross section (4.8),

$$\langle \sigma v \rangle_{\text{ann.}} \approx 2\,(3) \times \langle \sigma v \rangle_{b\bar{b}}. \tag{4.10}$$

where $\langle \sigma v \rangle_{b\bar{b}}$ is the contact interaction value (4.8). Because $\langle \sigma v \rangle_{b\bar{b}}$ is already determined to be close to the thermal relic, one may worry if the additional factor in (4.10) violates the feasibility of a thermal relic. We address this in Sec. 4.5. Considering the range of kinematically allowed mediator masses and accounting for the powers of λ_{DM} in the spin-0 and spin-1 cases, (4.10) gives the estimate

$$\lambda_{\text{DM}} \sim 1.1 - 1.4 \qquad \text{(spin-0)} \tag{4.11}$$

$$\lambda_{\text{DM}} \sim 0.27 - 0.44. \qquad \text{(spin-1)} \tag{4.12}$$

These couplings indeed agree with the estimate (4.5c) while remaining perturbative, $\lambda_{\text{DM}}^2 < 4\pi$. The scale of the spin-1 coupling implies a slight suppression on the left-hand side of (4.6) which must be compensated by a stronger upper bound on λ_{SM}. We show below that direct detection also constraints λ_{SM} strongly for the spin-1 mediator.

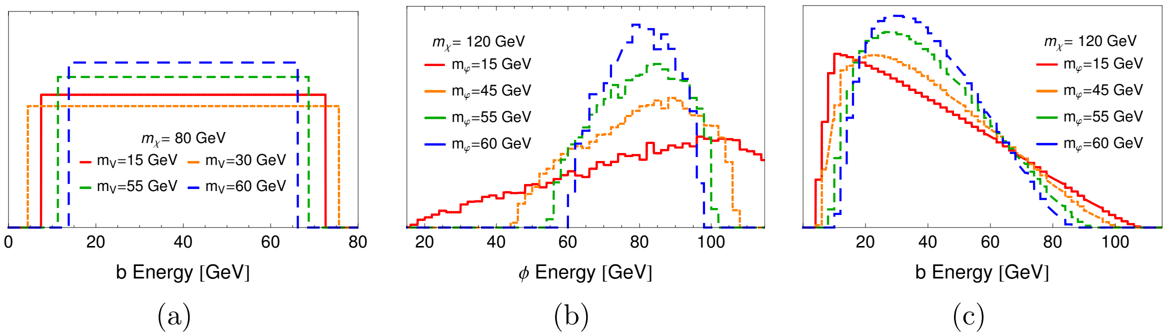

Figure 4.4: (a) $\chi\bar{\chi} \to VV \to 4b$, (b) $\chi\bar{\chi} \to 3\varphi$, (c) $\chi\bar{\chi} \to 3\varphi \to 6b$. Energy spectrum with arbitrary normalization from DM annihilation for (a) b quarks from two on-shell spin-1 mediators, (b) pseudoscalar mediators, (c) b quarks from three on-shell pseudoscalar mediators. (a) corresponds to $m_\chi = 80$ GeV while (b,c) corresponds to $m_\chi = 120$. Lines correspond to $m_V = 15, 30, 55, 60$ GeV or $m_\phi = 15, 45, 55, 60$ GeV from red (solid) to blue (most dashed). The 'box' width in (a) is not monotonically decreasing with m_V, as evidenced by the 30 GeV line (orange).

4.3 The γ-Ray Excess from On-Shell Mediators

Having established the intuition developed in Sec. 4.2.4, we examine the photon spectrum predicted from the on-shell mediator scenario and fit to the observed γ-ray excess.

4.3.1 Mediator Spectra

In 2-to-2 scattering, the final state energies is completely determined by kinematics. This is the case for $\chi\bar{\chi} \to b\bar{b}$ from effective contact interactions or simplified models with single off-shell mediators; the monochromatic spectrum of final state b quarks yield, upon showering, a spectrum of photons which fits the observed γ-ray excess well. In the case of annihilation to on-shell mediators, however, the b quark spectrum is no longer monochromatic, as shown in Figure 4.4.

For spin-1 mediators, it is well known that the final states of a $\chi\bar{\chi} \to VV \to 4b$ cascade has box-like energy spectrum over the kinematically allowed range; see, for example, [220, 221].

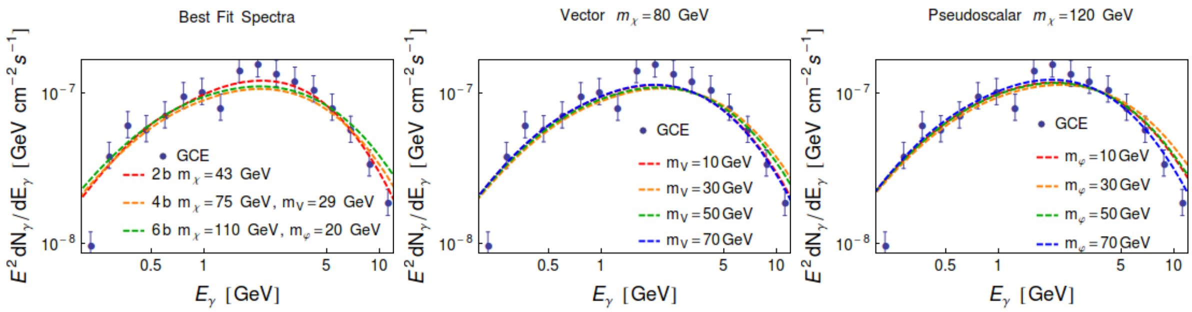

(a) (b) (c)

Figure 4.5: (a) Comparison, (b) Spin-1, (c) Spin-0. Predicted spectra for the galactic center γ-ray excess (GCE) for (a) the best fit models categorized by the number of final state b quarks, (b) a range of spin-1 mediator masses, (c) a range of spin-0 mediator masses. Overlayed is the measured γ-ray spectrum from [1], bars demonstrate an arbitrary measure of goodness-of-fit. See Sec. 4.3.3 for details.

The V spectrum is monochromatic in the lab frame and the $b\bar{b}$ spectrum is monochromatic in the V rest frame. The b energies in the lab frame depend on the angle of the $b\bar{b}$ axis relative to the direction of the V boost. Isotropy of the V boost washes out the angular dependence and gives a flat b spectrum over the kinematically allowed region. This is demonstrated in Fig. 4.4(a). The box becomes more sharply peaked as $m_V \to m_\chi = 40$ GeV. The case of annihilation into three spin-0 mediators is more complicated since the mediators have a nontrivial energy spectrum and it is no longer simple to derive the b spectrum from kinematics alone. Monte Carlo energy spectra for $\chi\bar{\chi} \to 3\varphi$ and the subsequent decay in to $6b$ are shown in Fig. 4.4(b,c) using MadGraph 5 [63].

4.3.2 Generating γ-Ray Spectra

γ-ray spectra for our simplified models are generated using PPPC 4 DM ID (henceforth PPPC) [222–224], a *Mathematica* [225] package that generates indirect detection spectra based on data extracted from PYTHIA 8 [226]. Presently, PPPC only generates signals for DM annihilation into pairs of SM particles. In order to include the effects of the on-shell mediators,

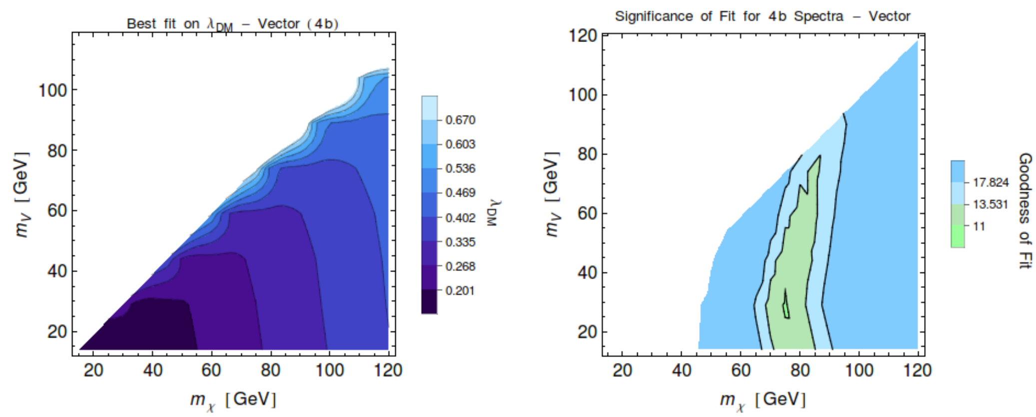

Figure 4.6: Fits for on-shell annihilation through spin-1 mediators. LEFT: best fit values of λ_{DM}. RIGHT: fit significance highlighting the best $(m_\chi, m_{\text{med.}})$ values. See text for details.

one must account for the boost by convolving the PPPC photon spectrum $dN_\gamma(E_b)/dE_\gamma$ with a distribution of b energies E_b which may be taken as a box for the case of two on-shell mediators or interpolated from Monte Carlo simulations such as Fig. 4.4(c).

For on-shell annihilation into spin-0 and spin-1 mediators, the shape of the photon spectrum is completely determined by the masses of the DM particle m_χ and the mediator $m_{\varphi,V}$ while the overall normalization is fit to the necessary cross section by fixing λ_{DM}, as estimated in (4.11 – 4.12). The effect of the mediator mass is fairly modest, as demonstrated in the $E_\gamma^2\, dN_\gamma/dE_\gamma$ spectra in Fig. 4.5. The reason for this is that the requirement that the mediator is massive enough to decay into $b\bar{b}$ pairs (4.5d) limits the extent to which the mediators are boosted.

4.3.3 Fitting the γ-Ray Excess

We use the $\chi\bar{\chi} \to b\bar{b}$ γ-ray excess spectrum assuming a $\chi\bar{\chi} \to b\bar{b}$ template from Figure 8 of [1]. We note, however, that this is an approximation since the on-shell mediator scenario predicts a different spectral shape that, in principle, should be modeled and included in the fit for the γ-ray excess. The comparison of the best fit $\chi\bar{\chi} \to 2b$ spectrum versus the on-shell mediator spectra in Fig. 4.5(a) qualitatively demonstrates the degree of approximation.

Indeed, [1] showed how the spectrum of the excess (though not its existence) can depend on both the background subtraction and the choice of DM template assumed in the fit. This highlights a second caveat when building DM models for the γ-ray excess. As is standard in astrophysics literature, [1] and [150] only quote statistical errors on their fits since the systematic errors associated with fitting and subtracting background is nontrivial and intractable to quantify. Both [1] and [150] make this clear in their text. Model builders from the particle physics community, however, should be careful not to interpret these statistical uncertainties in the same way as quoted uncertainties from collider data, where both statistical and systematic errors are included. [1] demonstrated some of the systematic uncertainties by exploring the differences in the spectral fits from different background subtraction. Further still, both [1] and [150] use the FERMI collaboration's 2FGL point sources and recommended diffuse emission model `gal_2yearp7v6_v0`. These assumptions also carry an implicit systematic uncertainty that are difficult to quantify without further input from the FERMI collaboration.

That being said, one can see from the $1\sigma_{\text{stat.}}$ error bars in Fig. 5 of [150] that even just the statistical errors on the γ-ray excess can accommodate modified spectra. Combined with the estimated systematic errors in Figure 8 of [1] and additional systematic errors from the FERMI background, this suggests that more general final states beyond the standard $b\bar{b}$ and $\tau\bar{\tau}$ should be considered for the γ-ray excess. In Appendix A we present simple explorations for the range of spectra that can be generated in the on-shell mediator scenario.

Because of the unquantified systematic error associated with these spectra, we do not parameterize the statistical significance of our fits in terms of confidence intervals. Instead, we measure the goodness of fit using the χ^2 value with an arbitrarily chosen 20% error,

$$\text{goodness of fit} = \sum_i \left(\frac{\log D_i - \log\left(\lambda_{\text{DM}}^{2n} S_i\right)}{\log(0.2 D_i)} \right)^2 . \tag{4.13}$$

Smaller values are better fits. The index i runs over the bins in the extended source data set, D and S are the $E_\gamma^2 \frac{dN_\gamma}{dE_\gamma}$ values for the extended source data and the model spectra (assuming $\lambda_{\text{DM}} = 1$) respectively, and λ_{DM}^{2n} is the overall normalization of our input spectra, where $n = 2, 3$ is the number of on-shell mediators produced in each annihilation. The denominator reflects the assumed 20% error: we emphasize that this is not a statement about the total error, but rather a standard candle for quantifying the goodness-of-fit. This is shown as a bar on the data in Fig. 4.5.

In Figs. 4.6 and 4.7 we fit the spectral shape over the region of DM and mediator masses, m_χ and $m_{\text{med.}}$, estimated in Table 4.2 and (4.5a – 4.5b). The DM coupling λ_{DM} parameterizes the overall normalization and is fixed to minimize (4.13) for each value of m_χ and $m_{\text{med.}}$. The best fit values prefer a slightly lighter DM particle than the back-of-the envelope estimates in in Table 4.2 due to the on-shell mediator smearing the b spectrum. The fits are flexible over the range of mediator masses within the kinematically accessible region, as seen in Fig. 4.5(b,c). We note that these plots assume the limit of vanishing SM coupling, $\lambda_{\text{SM}} \to 0$, so that the contribution to the γ-ray spectrum from $\chi\bar{\chi} \to b\bar{b}$ via s-channel, off-shell mediators is negligible. We explore the role of finite λ_{SM} in Sec. 4.4.1. We also note that the simplest models spin-1 mediators typically have universal couplings to all quark generations; we address this in Sec. 4.6.1 and display the modified results in Fig. 4.10.

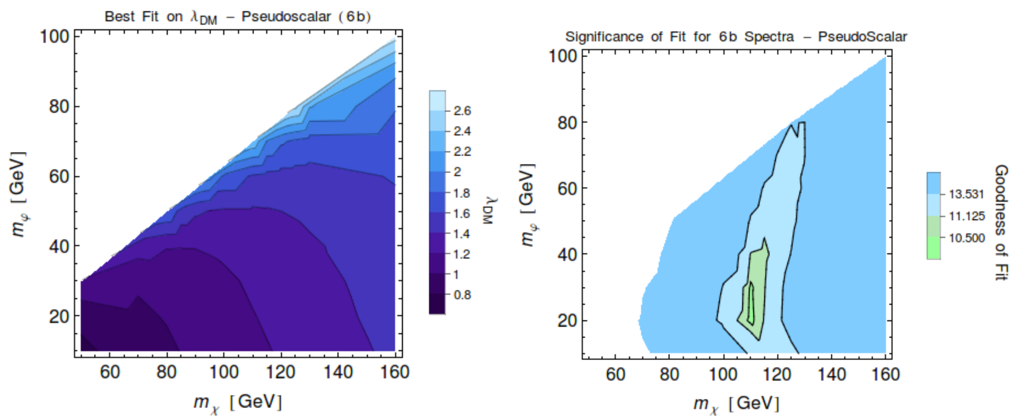

Figure 4.7: Fits for on-shell annihilation through spin-0 mediators. LEFT: best fit values of λ_{DM}. RIGHT: fit significance highlighting the best $(m_\chi, m_{\text{med.}})$ values. See text for details.

4.4 Experimental Bounds on the SM Coupling

One of the features of the on-shell mediator scenario is that the γ-ray excess annihilation mode is controlled by parameters that can be independent of the conventional experimental probes for DM–SM interactions. Following the complimentarity in Fig. 4.2, we examine the effect of non-negligible mediator coupling to the SM and determine the bounds on λ_{SM}.

In contrast to effective contact interactions or models with off-shell mediators, the the on-shell mediator scenario naturally includes the limit of extremely small SM coupling so that it is always possible to parametrically 'hide' from these bounds. In principle, one may invoke the morphology of the γ-ray excess to set a lower bound on the mediator coupling. For example, if the mediator decay were too suppressed, the observed γ-ray excess would have a spatial extent larger than the galactic center. In fact, the DM interpretations in [144, 150] found that the excess has a tighter profile ($\gamma > 1$) than the standard NFW DM density profile [217–219]. This lower bound on λ_{SM} is effectively irrelevant because of the astronomical distances associated with the galactic center.

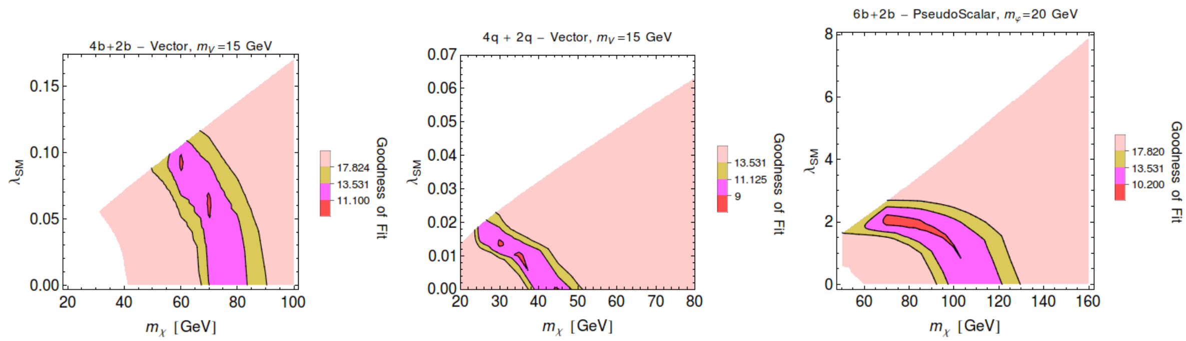

(a) (b) (c)

Figure 4.8: (a) Spin-1 (b-philic), (b) Spin-1 (q-democratic), (c) Spin-0. Fits including s-channel diagrams to the case of a (a) spin-1 mediator coupling only to b, (b) spin-1 mediator coupling to all quarks equally, and (c) pseudoscalar mediator. Plots assume that the s-channel diagrams are s-wave, see Tab. 4.2. Smaller values correspond to better fits, see (4.13).

4.4.1 Indirect Detection

In Sec. 4.3 we assumed that the contribution of s-channel diagrams to DM annihilation is negligible following (4.6 – 4.7). We can use the arbitrarily normalized goodness-of-fit measure (4.13) to assess the effect of these diagrams on the γ-ray excess fit as we parametrically increase λ_{SM}. We assume that the mediator couplings are such that the s-channel diagram supports s-wave annihilation, otherwise the contribution is negligible due to p-wave suppression by $\langle v^2 \rangle \sim 10^{-6}$. From Table 4.2, we see that non-negligible s-channel contributions may come from mediators with either pseudoscalar or vector coupling to the SM. For example, V could couple axially to both DM and the SM with a large s-channel contribution for finite λ_{SM}. On the other hand, if V couples axially to DM and vectorially to the SM, then there may be little modification to the annihilation spectrum from s-channel diagrams even for large values of λ_{SM}.

We scan over values of λ_{SM} that parametrically increases the relative fraction of s-channel off-shell DM annihilations to on-shell annihilations to mediators[5], allowing λ_{DM} and the mediator

[5] Note from (4.6 – 4.7) that the relative ratio of s-channel diagrams to on-shell mediator diagrams is determined not simply by λ_{SM}, but a ratio of λ_{SM} to a power of λ_{DM} depending on the type of mediator.

mass to float to a best-fit value. The results of the fit are shown in Fig. 4.8, where the best fit regions have smeared into lower DM masses compared to Fig. 4.6. The s-channel contribution produces γ-ray spectrum which is a poor fit due to the larger DM mass in the on-shell mediator limit. However, because the γ-ray spectrum is smeared out relative to the b spectrum, there are intermediate masses m_χ where the harder-than-usual s-channel diagram and the softer-than-usual on-shell mediator diagram average to yield good spectral fits. From the point of view of constructing DM models for the γ-ray excess, this shows that not only can the DM particle be as heavy as 80 or 120 GeV, as shown in Sec. 4.2, but it can take on intermediate values between these values and $m_\chi \approx 40$ GeV. We further generalize this in Appendix A where we find plausible fits with $m_\chi < 40$ GeV, and propose a simple mechanism to make $m_\chi > 120$ GeV.

We note that in this scenario, indirect detection bounds from cosmic antiprotons can constrain λ_{DM}. Current constraints from the PAMELA are not sensitive to the rates required in our model, though AMS-02 will access this region [227, 228][6].

4.4.2 Direct Detection

Unlike the other experimental options in Fig. 4.2, direct detection experiments probe WIMP–nucleon interactions at low transfer momentum, $q^2 \sim \mathcal{O}(10 \text{ MeV})$, and are accurately described in the contact interaction limit with corrections of order $\mathcal{O}(q^2/m_{\text{med}}^2) \ll 1$. The present experimental bounds on the spin-independent (SI) and spin-dependent (SD) interactions in the DM mass region of interest are set by the LUX [3] and XENON 100 [69] collaborations, respectively:

$$\sigma_{\text{SI}} \lesssim 10^{-45} \text{ cm}^2 \qquad\qquad \sigma_{\text{SD}} \lesssim 5 \times 10^{-40} \text{ cm}^2. \tag{4.14}$$

[6] We thank KC Kong for pointing this out. See Fig. 2 and Fig. 4 of [227] for the relevant bounds, recalling (4.10) for our model. Note, however the large propagation uncertainties in Fig. 2.

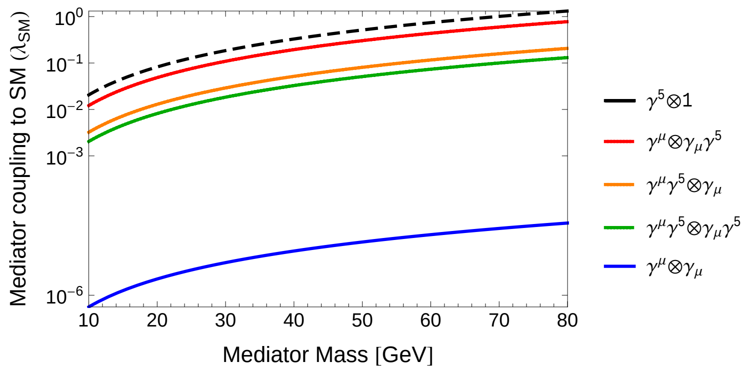

Figure 4.9: Estimated direct detection bounds on the mediator–SM coupling (λ_{SM}) for interactions $\mathcal{O}_\chi \otimes \mathcal{O}_q$ defined in (4.1). The dashed (solid) lines assume the benchmark value $m_\chi = 120$ (80) GeV for spin-0 (1) mediators and the median DM couplings in (4.11 –4.12).

In Fig. 4.9 we apply these bounds to the contact interactions in (4.1) with the identification $\Lambda^{-2} = \lambda_{\text{SM}}\lambda_{\text{DM}}/m^2_{\text{med.}}$. We use the benchmark parameters in Section 4.2.4 with the fact that the spin-0 mediator couple only to b quarks while the spin-1 mediator couples universally to all quarks.

In addition to the conventional spin-independent ($\gamma^\mu \otimes \gamma_\mu$) and spin-dependent ($\gamma^\mu\gamma^5 \otimes \gamma_\mu\gamma^5$) interactions, we present bounds on the axial–vector ($\gamma^\mu\gamma^5 \otimes \gamma_\mu$) and vector–axial ($\gamma^\mu \otimes \gamma_\mu\gamma^5$) interactions for a spin-1 mediator. These are suppressed by virtue of being higher order in the transfer momentum/DM velocity; we estimate these bounds following [67]. If the spin-1 mediator couples only to b quarks, the bound on λ_{SM} is weakened because interactions with target nucleons go through a b-quark loop that induces mixing between the mediator and the photon [208, 229].

As discussed in Sections 4.2.1 and 4.2.2, we only consider spin-0 mediators that couple as a pseudoscalar to DM. We do not include the $\gamma^5 \otimes \gamma^5$ operator since it is so suppressed by powers of the momentum transfer that the bounds on λ_{SM} are weaker than the perturbativity bound $\lambda_{\text{SM}} < \sqrt{4\pi}$. We evaluate momentum-dependent operators at $q^2 = 0.1$ GeV following [67]. These direct detection rates can be calculated in more detail using the nonrelativistic effective theory developed in [173, 175, 178]. Operator bounds in this formalism are presented in [89, 230] and *Mathematica* codes for these calculations are available in [89] and [174].

4.4.3 Collider bounds

The collider bounds for this class of models falls into two types: those based on processes where the mediator couples to both the SM and DM and those that only depend on the mediator's coupling to the SM.

The first type of collider bounds are epitomized by mono-object searchers with missing energy where the DM leaves the collider. These bounds are discussed extensively in the γ-ray [off-shell, s-channel] simplified models [150, 208]. We thus only highlight the most promising proposed bound, the 'mono-b' search [170]. Because of the requirement (4.5c) of on-shell annihilation into mediators, the class of models explored in this chapter typically falls in the range where the effective contact interaction description breaks down [23,49,54,181,182]. We leave a detailed simplified model study for future work, but instead translate the projected scalar–scalar ($\mathbb{1} \otimes \mathbb{1}$) contact interaction bounds in [170] as a conservative estimate for the reach of this search. Over the range of dark matter masses $m_\chi \lesssim 150$ GeV, the projected bound from 8 TeV LHC data is approximately

$$M_* > 100 \text{ GeV} \quad \Rightarrow \quad \lambda_{\text{SM}}^{\text{spin-0}} \lesssim 0.2, \qquad \lambda_{\text{SM}}^{\text{spin-1}} \lesssim 0.6, \tag{4.15}$$

where M_* parameterizes the scalar–scalar contact interaction,

$$\frac{m_q}{M_*^3} (\bar{\chi}\chi) (\bar{q}q) \,. \tag{4.16}$$

To estimate this bound, we have matched this to $\lambda_{\text{SM}}\lambda_{\text{DM}} s^{-1} (\bar{\chi}\chi) (\bar{q}q)$, where we have taken $s = 225$ GeV, the cut on the minimum missing energy in [170]. We have estimated that the spin-1 bound on M_* is identical and used the smaller λ_{DM} value (4.12). Note that at high energies the distinction between operators with and without a γ^5 in the parity basis is negligible. The bound (4.15) is thus fairly robust; unlike the direct detection bounds, a judicious choice of operator cannot avoid the constraints from this search.

A second class of collider bound comes from a search for the signatures of the mediator interacting only with the SM sector. The bounds from this type of search are relatively weak in the mediator mass range of interest (15 – 70 GeV) because of large QCD backgrounds in bump searches (dijet, $4b$); see, for example, [231]. Because our only requirement is that the mediator couple to b quarks (and other quarks as mandated by MFV, for example), a prototype for the mediator is a Z' that gauges baryon number $\mathrm{U}(1)_{\mathrm{B}}$. This has been examined originally in [101, 232] where the most stringent bounds come from the hadronic width of the Z which sets a relatively weak bound

$$\lambda_{\text{SM}} \lesssim 1. \tag{4.17}$$

This bound becomes stronger in the neighborhood of the Υ mass, but this is already at the edge of what is kinematically allowed for decay into b pairs (4.5d). See also [233] for a review including loop-level constraints from mixing and [234] for discussion of bounds combined with anomaly constraints. Another prototype for the spin-0 mediator is a gauge-phobic, leptophobic Higgs. There exist very few bounds for such an object in the mass range of interest. A preliminary estimate for the reach of a 'Higgs' diphoton search between 50 – 80 GeV ATLAS detector with 20/fb found weaker constraints than (4.17) [235].

4.5 Viability as a Thermal Relic

One of the appealing features of the simplest $\chi\bar{\chi} \to b\bar{b}$ mode is that the required annihilation cross section (4.8) is so close to the value required for a thermal relic. Due to the scaling in

(4.9), the s-wave annihilation cross section for the on-shell mediator scenario is a factor of n larger than the thermal value where $n = 2, 3$ is the number of mediators emitted, (4.10). This comes from a factor of n enhancement due to the number of $b\bar{b}$ final states and a factor of n^2 suppression coming from a decreased DM number density. We examine the extent to which our scenario may still furnish a standard thermal relic. Observe that this sector of the model no longer has free parameters since the γ-ray excess fixes both the dark matter mass m_χ and coupling λ_{DM}.

4.5.1 s-wave Cross Section

For simplicity, let us first assume that DM annihilation at freeze-out is dominated by the same diagrams that generate the galactic center γ-ray excess at the present time. We address s-channel and p-wave corrections below. The observed Dirac DM density $\Omega_\chi h^2$ is approximately[7] [237]

$$\Omega_\chi h^2 \approx \frac{6 \times 10^{-27}\ \text{cm}^3/s}{\langle\sigma v\rangle_{\text{ann.}}} \qquad \left(\Omega_\chi h^2\right)_{\text{obs.}} = 0.12 \quad [238\text{–}240] \tag{4.18}$$

where h is the Hubble constant in units of 100 km/(s $\cdot$ Mpc). From (4.10), the annihilation cross section is $\langle\sigma v\rangle_{\text{ann.}} \approx n(5 \times 10^{-26}\ \text{cm}^3/\text{s})$, where $n = 2$ or 3 depending on the mediator. At face value, this gives a relic abundance that is too small. One may not mitigate this by assuming another DM component since this, in turn, reduces the galactic center signal and hence requires one to increase the annihilation cross section further.

While the value of $\Omega_\chi h^2$ is well measured, the precise value of the annihilation cross section $\langle\sigma v\rangle_{\text{ann.}}$ at freeze-out carries uncertainties from early universe parameters such as the number of effective degrees of freedom. On top of this, there are further uncertainties in our approximation (4.10) coming from uncertainties in astrophysical parameters. For example,

[7] The thermal cross section for Dirac DM is a factor of 2 larger than Majorana DM [236].

the $\chi\bar{\chi} \to b\bar{b}$ annihilation cross section (4.8) depends on the fit to the dark matter density profile at the center of the galaxy [241]. The analysis in [150] found a tighter density profile for which $\langle\sigma v\rangle_{b\bar{b}} \approx 1.5 \times 10^{-26}$ cm$^3/c$. The value of $\langle\sigma v\rangle_{\text{ann.}}$ spin-1 mediators ($n = 2$) required for a thermal relic falls between these two estimates of $\langle\sigma v\rangle_{b\bar{b}}$. We may thus assume that it is consistent with the galactic center signal within the uncertainty of the DM morphology. In fact, when the boost from the on-shell mediator is taken into account, the best fit DM mass is slightly smaller than the assumed 80 GeV in our estimate. This can push the estimated relic abundance from $\Omega_\chi h^2 = 0.10$ to 0.12 so that the case of a spin-1 mediator may plausibly yield the correct thermal relic abundance. On the other hand, it is difficult for a spin-0 mediator to satisfy the observed DM relic abundance and seems to require additional mechanisms to produce $\Omega_\chi h^2$.

4.5.2 *s*-channel and *p*-wave Corrections

The corrections to the above estimates include *s*-channel $\chi\bar{\chi} \to b\bar{b}$ diagrams and *p*-wave corrections from additional on-shell mediator diagrams. The *s*-channel modes are parametrically suppressed by $\lambda_{\text{SM}}^2 \ll 1$ in the cross section and can be ignored.

Corrections from *p*-wave diagrams are negligible for present day annihilation in the galactic center due to a large velocity suppression. At the time of DM freeze-out, on the other hand, this velocity suppression is much weaker and one should check for *p*-wave corrections to the relic abundance. For spin-1 mediators there are no additional diagrams which are not suppressed relative to the $\chi\bar{\chi} \to VV$ *s*-wave diagram. For pseudoscalars mediators, on the other hand, the $\chi\bar{\chi} \to 2\varphi$ mode is *p*-wave but not parametrically suppressed by λ_{SM}. At freeze-out these diagrams may contribute appreciably to DM annihilation,

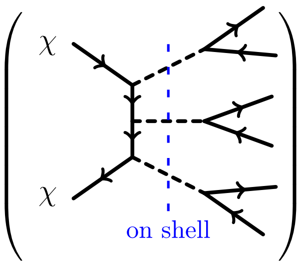

$$\sim \quad \frac{\lambda_{\rm DM}}{\sqrt{4\pi}}\sqrt{\frac{x_f}{3}} \qquad (4.19)$$

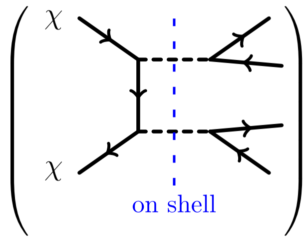

The prefactor accounts for the additional phase space and p-wave suppression. The ratio of the DM mass to the freeze-out temperature $x_f = m_\chi/T_f \approx 20$ appears when thermally averaging the annihilation cross section at freeze-out over a Maxwell–Bolztmann velocity distribution. This factor is not especially large and so one expects the pseudoscalar annihilation cross section at freeze-out to be even larger than approximated with only the s-wave piece. This further reinforces the observation that this class of mediator requires additional mechanisms to attain the observed DM relic density. See [13, 242–259] for a partial list of model-building tools for obtaining the correct relic abundance without the standard freeze-out mechanism.

4.5.3 MSPs Can Save Freeze-Out

As noted in the Introduction, [1, 144, 145, 148, 162, 260] have pointed out that an alternate source for the γ-ray excess is a population of hitherto unobserved millisecond pulsars (MSPs). As an estimate, a few thousand MSPs could generate the observed γ-ray flux [1]. A recent study of low-mass X-ray binaries (LMXB) may lend credence to this argument. It is thought that MSPs are old pulsars that have been spun up 'reborn' due to mass accretion from a binary companion and that LMXB are simply a different phase of the same binary system. During accretion, the system is X-ray luminous and is categorized as an LMXB. The X-ray flux drops when the accretion rate drops and the system is then observed as a MSP. One can thus attempt to use the spatial distribution of the LMXB as a proxy for that of MSPs. [261]

found that the spatial morphology of the LMXB in M31 is consistent with both the γ-ray excess and the DM interpretation—thus making it difficult to distinguish the two [163].

This, however, can be a boon for model-building within our DM framework. [144] noted that the degeneracy between the MSP and DM intepretations of the excess suggests that the excess may come from a combination of the two sources. In this way one may take the DM annihilation cross section to be that which is required for a thermal relic—thus undershooting the expected γ-ray flux—and then posit that a MSP population accounts for the remainder of the γ-ray excess.

4.5.4 Conditions for Thermal Equilibrium

In order for the thermal freeze-out calculation for χ to be valid, we must assume that the mediator is in thermal equilibrium when the DM freezes out. This imposes a lower bound on the coupling of the mediator to the SM. In principle one must solve the Boltzmann equation for the mediator, but to good approximation it is sufficient to impost $H \ll \Gamma(\text{med} \to b\bar{b})$. For the range of mediators that can give the γ-ray excess, this imposes a very modest lower bound $\lambda_{\text{SM}} \gtrsim 10^{-9}$.

4.6 Comments on UV Completions and Model Building

Simplified models, such as those presented here, are bridges between experimental data and explicit UV models. In this section we highlight connections between our on-shell simplified models and viable UV completions.

4.6.1 Minimal Flavor Violation

The simplified models constructed in Section 4.2 couple the mediator only to b quarks to fit to the galactic center extended γ-ray source. Assuming only this coupling violates flavor symmetry and can lead to strong constraints from flavor-changing neutral currents. A standard approach to this issue in models of new physics is to impose the minimal flavor violation (MFV) ansatz where the Yukawa matrices are the only flavor spurions in the new physics sector [61, 214–216]. This prescribes a set of relative couplings to the SM fermions up to overall prefactors. We assume that the dark sector is flavor neutral, see [160, 262, 263] for models with nontrivial flavor charge.

For the pseudoscalar mediator this is a small correction as can be seen by writing out the flavor indices in the spin-0 fermion bilinears (4.3) by which the pseudoscalar couples to the quarks. MFV mandates insertions of the Yukawa matrices between couplings of right- and left-handed fermions. After rotating to mass eigenstates this yields mediator–SM interactions

$$\mathcal{L}_{\varphi\text{-SM}} = \lambda_u \frac{m_{u_i}}{\Lambda}\varphi \bar{u}_{Li} u_{Ri} + \lambda_d \frac{m_{d_i}}{\Lambda}\varphi \bar{d}_{Li} d_{Ri} + \lambda_\ell \frac{m_{\ell_i}}{\Lambda}\varphi \bar{\ell}_{Li} \ell_{Ri}, \tag{4.20}$$

where $q_{L,R} = P_{L,R}q$, the $\lambda_{u,d,\ell}$ are overall prefactors, and Λ is a UV flavor scale. Assuming that the $\lambda_{u,d,\ell}$ are the same order naturally sets the dominant φ decay mode to be $b\bar{b}$ since the $t\bar{t}$ mode is kinematically inaccessible for the range of masses we consider. The simplified model coupling to b quarks is thus identified as

$$\lambda_{\text{SM}} = \lambda_d \frac{m_b}{\Lambda}. \tag{4.21}$$

The results of the simplified model above should be adjusted by including the effects of the other φ decay modes, though these effects are suppressed by the relative size of the other fermion masses to m_b. We remark that modest to large values of λ_u can lead to new signatures such as mediator emission off of a top quark at the LHC or gluon couplings through top loops.

The spin-1 mediators couple fermions of the same chirality, as demonstrated in (4.4). Promoting these interactions to an MFV-compliant coupling does not introduce additional factors of the Yukawa matrices since each term is a flavor singlet. Thus, unless the UV model is specifically constructed so that the spin-1 mediator couples preferentially to b quarks, the generic expectation is the spin-1 mediators have a universal coupling to each generation, for example

$$(\lambda_{\text{SM}})_d = (\lambda_{\text{SM}})_s = (\lambda_{\text{SM}})_b, \tag{4.22}$$

and similarly for the up-type quarks, leptons, and neutrinos. Unlike the case of the pseudoscalar mediator, this can lead to dramatic modifications since the light quarks produce a softer spectrum of secondary photons relative to the b. This is demonstrated in Fig. 4.10 which shows that the best fit spectrum is very different from that of the case where the spin-1 mediator only couples to the b: the best fit DM mass is ≈ 45 GeV rather than ≈ 75 GeV.

As a caveat, we note that for fitting the γ-ray excess with either spin-0 or spin-1 mediators, it is sufficient that λ_d is nonzero. Thus, in principle, one can set λ_u and λ_ℓ to vanish; the latter condition suppresses the leptonic signals for the mediator at colliders and skirts the most stringent constraints on bosons in the on-shell mediator mass range (4.5a – 4.5b).

4.6.2 Gauge symmetries

Gauge invariance also constrains UV completions of these simplified models. Because the SM fermions are chiral, the parity basis spin-0 interactions on the left-hand side of (4.3) are

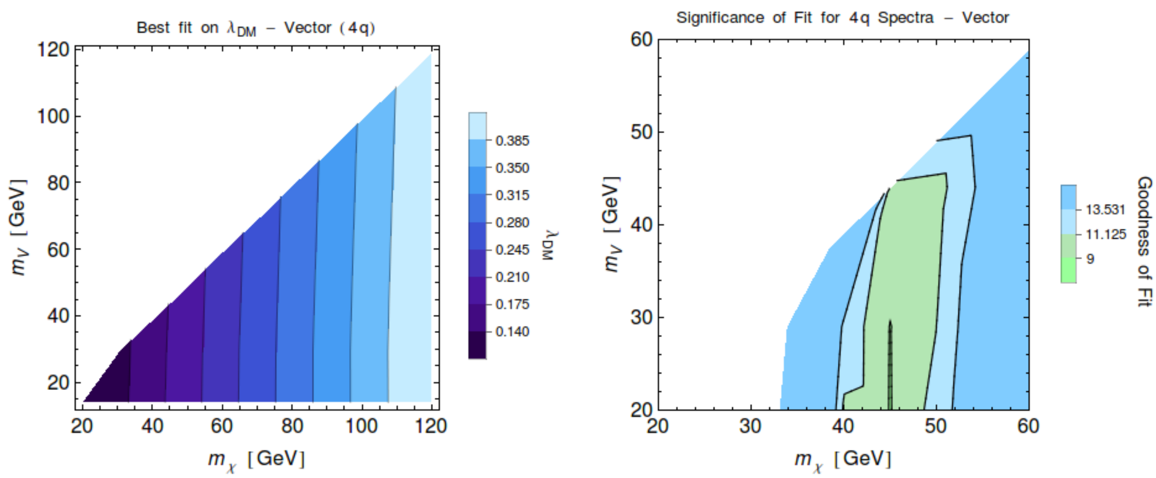

Figure 4.10: Fits for on-shell annihilation through spin-1 mediators assuming universal coupling to all quarks; compare to Fig. 4.6 which assumed a coupling to only b quarks. LEFT: best fit values of $\lambda_{\rm DM}$. RIGHT: fit significance highlighting the best $(m_\chi, m_{\rm med.})$ values. See Section 4.3.3 for details.

not $\mathrm{SU}(2)_\mathrm{L} \times \mathrm{U}(1)_\mathrm{Y}$ gauge invariant. The similarity of (4.20) to the Yukawa coupling gives a hint for how to make this interaction SM gauge invariant. The $m_b \bar{b}_R b_L$ term is implicitly $y_b(v/\sqrt{2})\bar{b}_R b_L$, where v is the Higgs vacuum expectation value. We may promote this to a gauge invariant coupling by restoring the Higgs doublet H so that (4.20) becomes

$$\mathcal{L}_{\varphi\text{-SM}} = \frac{\lambda_u y^u_{ij}}{\Lambda}\varphi H \cdot \bar{Q} u_R + \frac{\lambda_d y^d_{ij}}{\Lambda}\varphi \widetilde{H} \cdot \bar{Q} d_R + \frac{\lambda_\ell y^\ell_{ij}}{\Lambda}\varphi \widetilde{H} \cdot \bar{L} \ell_R, \tag{4.23}$$

where $\widetilde{H} = i\sigma^2 H^*$, Q and L are the left-handed SU(2) doublets.

UV models for the spin-1 mediators are also constrained by gauge invariance since these couplings can be assumed to be interactions of a spontaneously broken U(1) gauge symmetry. In a UV model one must be able to assign messenger charges to the SM fermions—or otherwise introduce new matter in the dark sector—to cancel all gauge anomalies with respect to the mediator gauge symmetry. The axial mediator case requires particular care since the global chiral symmetry of the SM is anomalous requiring, for example, a cancellation between the up-type and down-type quarks. See [234] for a recent analysis of anomaly constraints on the phenomenology of Z' bosons in the mass range and with the type of leptophobic/gauge-phobic couplings we consider for on-shell mediators for the γ-ray excess.

4.6.3 Renormalizability

Finally, one may push further and argue that a true 'simplified model' should depend only on renormalizable couplings; i.e. that it should be a UV complete theory. While the spin-1 couplings automatically satisfy this, the pseudoscalar couplings (4.23) are dimension-5. We would thus like to consider renormalizable operators that generate (4.23). Because the SM fermions are chiral, there are no renormalizable interactions with the SM singlet φ and the SM fermions. We thus left with interactions between the Higgs and the pseudoscalar,

$$\mathcal{L}_{\varphi\mathrm{H}} = |H|^2 \lambda_H \left(M\varphi + \varphi^2 \right) , \tag{4.24}$$

where M is a dimensionful coupling. These couplings are reminiscent of the Higgs portal framework [92,264] with the caveat that φ is now a mediator rather than the DM particle. At energies below m_h, (4.24) generates the couplings in (4.23) with the prediction $\lambda_u = \lambda_d = \lambda_\ell$. This is model dependent: In a two-Higgs doublet model such as the MSSM, one may have φ mix differently with the up- and down-type Higgses. These couplings introduce additional handles for dark sector bounds through the invisible width of the Higgs. See [265] for an explicit model for the γ-ray excess of this type.

4.6.4 Self-Interacting Dark Matter

The on-shell mediator scenario has nontrivial dynamics even in the limit of parametrically small coupling to the SM and may be a candidate for a model of self-interacting dark matter. However, the lower bound on the mediator mass (4.5d) is heavier than the typical scale required to address anomalies in small-scale structure [186, 188, 189, 194, 196–199, 202–204, 266, 267]. A complete study of DM self-interactions through a pseudoscalar has yet to be completed, though the first steps are presented in [45] and have indicated that resonance effects may be relevant even for $m_\varphi \gtrsim 10$ GeV. Alternately, in Appendix A we address alternate final states that may match the γ-ray excess. Of particular interest is a mediator which decays into gluons—say through a loop of heavy quarks—could be made light enough to plausibly be in the regime of interesting models for self-interaction. We leave a detailed exploration for future work.

4.6.5 Prototypes for UV models

We briefly comment on directions in specific models that may be adapted to the on-shell mediator scenario. The MSSM introduces an additional pseudoscalar state which can plausibly mix with the Higgs as in (4.24), but SUSY bounds tend to rule out the mass range of interest. Alternately, the singlet superfield of the NMSSM may be sufficiently unconstrained to furnish the required pseudoscalar. More generally, [265] recently proposed a complete non-supersymmetric UV model with two-Higgs doublets for the γ-ray excess.

A second alternate direction is to develop models with spin-1 mediators. We have shown that these typically are forced to have a constrained SM coupling if the mediator has a universal coupling to all generations, as one may generically expect for a gauged symmetry; see [268] for an explicit leptophilic model. While a Z' coupling to $\mathrm{U}(1)_\mathrm{B}$ and parametrically small coupling to the SM is a valid scenario within the on-shell mediator framework, one may also consider options where the spin-1 mediator does not have universal coupling, for example [269]. Inspiration for such a particle is motivated by Randall-Sundrum models [270] (gauge bosons with the 4D zero mode projected out, see e.g. [271, 272]) or their holographic duals (composite Higgs models with ρ-meson-like excitations) [273, 274].

4.6.6 Exceptions

Finally, we point out several exceptions to some of the 'generic' statements we have made in this chapter.

- In Sec. 4.1.2 we motivated the on-shell mediator scenario by exploiting how bounds on one operator 'generically' bound others. Some of these bounds are avoided when χ were a Majorana fermion since operators such as $\bar{\chi}\gamma^\mu\chi \equiv 0$. More generically one may also consider bosonic dark matter.
- In the MFV ansatz, we saw from the chiral structure that scalar couplings naturally follow the mass hierarchy while vector couplings tend to be universal. The latter condition is not necessary even within the MFV framework. For example, if the leading order spin-1 flavor spurion δ_{ij} were to vanish, the next-to-leading term is $y_i^\dagger y_j$ which has an even strongly hierarchical coupling to the third generation. Such a structure may be possible through models of partial compositeness [273, 274].
- We limited our analysis to a single class of mediator at a time. In the presence of multiple mediator fields, one can find processes that violate the relation between diagram topology and partial wave. For example, $\chi\bar{\chi} \to \varphi_1\varphi_2$ is s-wave for distinct spin-0 particles $\varphi_{1,2}$.

4.7 Conclusions and Outlook

We have presented a class of simplified models where dark matter annihilates into on-shell mediators which, in turn, decay into the SM with a typically suppressed width. This separates the sector of the model which can account for indirect detection signals—such as the FERMI galactic center γ-ray excess—and those which are bounded by direct detection and collider experiments. We have addressed γ-ray spectrum coming from these models and

Mediator	MASS [GeV] m_χ	$m_{\text{mes.}}$	INTERACTION DM	SM	COUPLING λ_{DM}	λ_{SM}	**Thermal Relic?**
spin-0	110	20	γ^5	$\mathbb{1}$	1.2	< 0.08	MSP?
"	"	"	γ^5	γ^5	"	$< 0.02^*$	"
spin-1	45	14	γ^μ	γ_μ	0.18	$< 10^{-6}$	$\gamma = 1.3$
"	"	"	$\gamma^\mu\gamma^5$	$\gamma_\mu\gamma^5$	"	< 0.004	"
"	"	"	$\gamma^\mu\gamma^5$	γ_μ	"	< 0.006	"
"	"	"	γ^μ	$\gamma_\mu\gamma^5$	"	< 0.02	"

Table 4.3: Best fit parameters assuming b-philic couplings for the spin-0 mediator and universal quark couplings for the spin-1 mediator. The upper bound for λ_{SM} for the $\gamma^5 \otimes \gamma^5$ is a conservative estimate for the 8 TeV mono-b reach at the LHC (see Section 4.4.3); the other bounds come from direct detection. In the last column, we indicate whether consistency with a thermal relic abundance suggests a tighter DM profile ($\gamma = 1.3$) or some population of millisecond pulsars (MSP), see Section 4.5.

have compared used the γ-ray excess to identify plausible regions of parameter space for a DM interpretation; the best fit parameters and bounds on the SM coupling are shown in Table 4.3. We have addressed the key points for UV model building and, in an appendix below, highlight further directions for modifying the γ-ray spectrum with more general SM final states.

This chapter shares significant overlap with Refs. [153, 212, 275]. [153, 212] has an explicit model for on-shell vector mediators. [212] differs from the $\chi\bar{\chi} \to VV$ mode in this work in that it examines a specific UV completion which includes semi-annihilations. Their 1σ contours also do not account for the systematic uncertainties discussed in Sec. 4.3.3. Ref. [275] was explores on-shell mediators with diverse SM final states and emphasizes the theme in our Figs. 4.10–4.8 and Appendix A that one need not focus only on bottom quark couplings and, further, that dark matter masses both above and below 40 GeV can yield the γ-ray excess.

Chapter 5

A 3.55 keV Line from Exciting Dark Matter without a Hidden Sector

Based on arXiv:1501.03496 [276]

5.1 Introduction

The nature of dark matter remains one of the most elusive and longstanding problems in physics today. As a consequence, much attention has been given to observational anomalies that can be plausibly interpreted in terms of dark matter interactions. One such signal is an approximately 3.55 keV X-ray line that has been observed from a number of galaxy clusters, as well as from the nearby Andromeda Galaxy.

The first reported evidence for the 3.55 keV line was found in data from the XMM-Newton satellite, from the directions of a stacked sample of 73 low redshift galaxy clusters [277]. Shortly thereafter, a similar line was reported from the directions of the Perseus Cluster and the Andromeda Galaxy [278]. A study of XMM-Newton data also suggests the existence of a 3.55 keV line from the direction of the Milky Way's center [279] (see also, however, Ref [280]).

More recently, the line was identified within Suzaku data from the Perseus Cluster [281].

A number of interpretations for these observations have been proposed. On the one hand, it has been suggested that atomic transitions (such as those associated with the chlorine or potassium ions, Cl-XVII and K-XVIII, for example [282]) might be responsible for the line, although the viability of this explanation is currently unclear [283–285]. Alternatively, decaying dark matter particles could generate such an X-ray line. Particularly well motivated is dark matter in the form of an approximately 7 keV sterile neutrino, which decays through a loop to a photon and an active neutrino. If one assumes that all of the dark matter consists of 7 keV sterile neutrinos, the observed X-ray line flux implies a mixing angle of $\sin^2(2\theta) \sim 7 \times 10^{-11}$. With such a small degree of mixing, however, the standard Dodelson-Widrow mechanism of production via the collision-dominated oscillation conversion of thermal active neutrinos [286] leads to an abundance of sterile neutrinos that corresponds to only a few percent of the total dark matter density, thus requiring additional resonant or otherwise enhanced production mechanisms. Alternatively, sterile neutrinos with a larger mixing angle of $\sin^2(2\theta) \sim 3 \times 10^{-10}$ could naturally constitute roughly 10% of the dark matter abundance, and decay at a rate that is sufficient to generate the observed line flux.

Interpretations of the X-ray line in terms of decaying dark matter are in considerable tension, however, with studies of galaxies using Chandra and XMM-Newton data [287] and dwarf spheroidal galaxies using XMM-Newton data [288], which do not detect a line at the level predicted by decaying dark matter scenarios. One way to potentially reconcile the intensity of the line observed from clusters with the null results from dwarfs and other smaller systems is to consider the class of scenarios known as eXciting Dark Matter (XDM) [289–292]. In such models, the collisions of dark matter particles can cause them to up-scatter into an excited state, $\chi_1\chi_1 \to \chi_2\chi_2$ or $\chi_1\chi_1 \to \chi_1\chi_2$. For a mass splitting of $m_{\chi_2} - m_{\chi_1} \simeq 3.55$ keV, the subsequent decays of the slightly heavier state can generate a 3.55 keV photon, $\chi_2 \to \chi_1\gamma$. Critical to the problem at hand are the kinematics of the XDM scenario, which introduce a velocity threshold for up-scattering, suppressing the X-ray flux from dwarf galaxies (and, to a lesser extent, from larger galaxies) [291, 293]. Within the paradigm of XDM, the observations of clusters, galaxies, and dwarf galaxies can be mutually consistent for dark matter masses between approximately 40 GeV and 10 TeV [293], covering the mass range generally associated with conventional WIMPs.

If up-scattering WIMPs are responsible for the 3.55 keV line, one might also imagine that the same dark matter species could generate the excess of GeV-scale gamma-rays observed from the region surrounding the Galactic Center [1, 139, 142, 143, 145, 147–150, 294]. This signal, identified within data from the Fermi Gamma-Ray Space Telescope, exhibits a spectrum and morphology that are in good agreement with that anticipated from dark matter annihilations. This data has been explored by several groups independently, including recently the Fermi Collaboration [295]. Assuming annihilations to $b\bar{b}$, for example, dark matter particles with a mass of $m_\chi \sim$ 35-65 GeV and a cross section of $\langle \sigma v \rangle \sim 10^{-26}$ cm^3/s provide a good fit to the observed excess [296].

The primary challenge in developing a viable XDM model for the 3.55 keV line is that the up-scattering rate must be very high, several orders of magnitude larger than the annihilation rate. One way to realize this is to consider dark matter that scatters through a light mediator and annihilates into pairs of the same mediator. This naturally leads to an up-scattering rate that is enhanced by a factor of $\sim (m_\chi/M_{\rm Med})^4$ relative to the annihilation rate. As this phenomenology can be realized without the dark matter or mediator possessing any sizable couplings to the Standard Model (SM), these scenarios are sometimes called "hidden sector" models. Examples of such proposals include models with a massive vector (hidden photon) or a massive scalar (hidden Higgs) that couples directly to the dark matter, but interacts with the SM only through a very small degree of kinetic or mass mixing. As a result, the dark sector and SM are effectively sequestered from one another. As this class of possibilities has been explored previously in some detail [291, 292, 297–299], we do not consider it here.

Instead, we explore models in which the dark matter annihilates directly into SM fermions (for an earlier investigation in this direction, see Ref. [300]). By introducing a resonant mediator with a hierarchy of couplings ($g_{\rm dark} >> g_{\rm SM}$), it is possible to accomplish similar phenomenology without a light mediator. We identify such a model that can simultaneously explain the 3.55 keV line from Galaxy Clusters and the Galactic Center gamma-ray excess. We find viable parameter space in our model that is consistent with all current collider, direct detection, and indirect detection constraints.

5.2 The Kinematics of eXciting Dark Matter

If the 3.55 keV signal is due to dark matter, the model responsible needs to address why this signal is not seen from dwarf galaxies (and, to a lesser extent, from larger galaxies). As the up-scattering rate in the XDM scenario depends strongly on the dark matter velocity dispersion in such systems, this framework provides a simple mechanism to suppress the line flux predicted from smaller halos.

The velocity averaged cross section for up-scattering is given by:

$$\langle \sigma v \rangle = \sigma_0 v_t \gamma, \tag{5.1}$$

where the normalization, σ_0, is taken to be a free parameter and γ accounts for the effect of the threshold velocity on the up-scattering rate:

$$\gamma = \left\langle \sqrt{v^2/v_t^2 - 1}\ \Theta\left(v - v_t\right) \right\rangle. \tag{5.2}$$

The quantity v_t is the threshold velocity, given by:

$$v_t = 2\sqrt{N\frac{\delta m_\chi}{m_\chi}}, \tag{5.3}$$

where δm_χ (taken to be $\simeq 3.55$ keV) is the mass splitting between χ_2 and χ_1 and $N = 1$ (2) for up-scattering to $\chi_1\chi_2$ ($\chi_2\chi_2$).

In the limit of $\delta m_\chi = 0$ (and $v_t = 0$), the standard $\langle \sigma v \rangle = \sigma_0 v$ is recovered. For larger mass splittings, however, the up-scattering rate and corresponding line flux will be suppressed in smaller systems, where typical velocities are lower.

To obtain up-scattering rates in dwarfs, galaxies, and clusters that are each compatible with the reported observations, Ref. [293] finds that a threshold velocity of $v_t \simeq 20 - 245$ km/s is required (at the $\delta\chi^2 < 3$ level, and assuming that the excited state decays promptly). Combining this with Eq. 5.3 (where $N = 2$), this implies $m_\chi \sim 40$ GeV-10 TeV. Annihilating dark matter particles near the low end of this mass range are also well suited to account for the Galactic Center gamma-ray excess.

5.3 Model Building

5.3.1 Up-scattering

There are two classes of scenarios in which an excited state could be presently decaying in order to generate the observed 3.55 keV line. First, if the excited state has a lifetime on the order of the age of the Universe or longer, a population of such particles could have been produced in the early universe. Primordial excitations, however, do not lead to a relative suppression in dwarf galaxies, and thus suffer from the same challenges in explaining the 3.55 keV line as ordinary decaying dark matter. Alternatively, if the excited state is short lived (millions of years or less) collisions between dark matter particles must lead to an up-scattering rate that is sufficient to perpetually populate these excitations in galaxy clusters. It is this second case that we consider here.

In order for XDM to generate the flux of 3.55 keV photons observed from galaxy clusters, very large cross sections for up-scattering are required, in the approximate range of $\sigma v\,(\chi_1\chi_1 \to \chi_2\chi_2) \sim (m_\chi/50\text{ GeV})^2 \times 10^{-18}$ cm^3/s. In addition to being very large in and of itself, this value for the up-scattering cross section is several orders of magnitude larger than the annihilation cross section needed to generate the Galactic Center gamma-ray excess, or to obtain a thermal relic abundance in agreement with the measured dark matter density.

In light of this, it is interesting to consider the upper limit imposed on dark matter scattering from the point of view of perturbativity and unitarity. In this chapter, we will focus on up-scattering through a resonant s-channel pseudoscalar, a (see Fig. 5.1). We will further assume that the dark matter and its excited state, $\chi_{1,2}$, are each Majorana fermions with nearly degenerate masses, $m_{\chi_1} \approx m_{\chi_2} \equiv m_\chi$ (collectively constituting a pseudo-Dirac fermion). The scalar ($J = 0$) bilinear involved in this interaction, $\bar{\chi} i\gamma^5\chi$, being even under charge, $\mathcal{C} = (-1)^{L+S}$, and odd under parity, $\mathcal{P} = (-1)^{L+1}$, implies that this operator only acts on incoming dark matter pairs with zero spin and orbital angular momentum, $J = S = L = 0$. As a result, scattering through an s-channel pseudoscalar is purely s-wave, and the unitarity bound (see *e.g.* Ref. [301]) on up-scattering is given by (assuming χ_2 is self-conjugate):

$$\sigma v \leq \frac{2\pi}{m_\chi^2 v} \approx \left(\frac{50\text{ GeV}}{m_\chi}\right)^2 \left(\frac{0.003}{v}\right) \times 10^{-17}\text{ cm}^3/\text{s}\ , \tag{5.4}$$

where $v \sim 0.003$ is the typical dark matter relative velocity in a galaxy cluster. For comparison, note that this upper limit is much stronger than that derived from self-scattering in objects such as the Bullet Cluster, $\sigma v \lesssim \left(\frac{m_\chi}{50\text{ GeV}}\right)\left(\frac{v}{0.003}\right) \times 10^{-14}$ cm^3/s [302].

A more explicit bound on the couplings of the theory arises if one parametrizes the La-

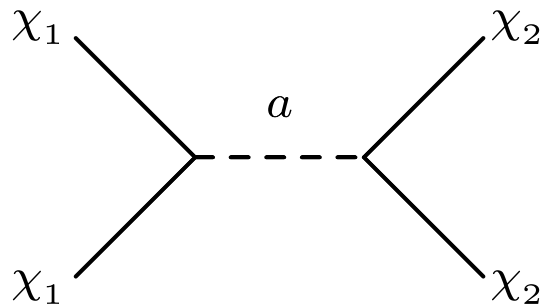

Figure 5.1: The dominant Feynman diagram for up-scattering in our model.

grangian responsible for up-scattering as follows:

$$\mathcal{L} \supset \lambda^a_{11} a \bar{\chi}_1 i\gamma^5 \chi_1 + \lambda^a_{22} a \bar{\chi}_2 i\gamma^5 \chi_2 + \lambda^a_{12} a \bar{\chi}_1 i\gamma^5 \chi_2. \tag{5.5}$$

If we assume that χ_1 and χ_2 couple to the pseudoscalar, a, with approximately equal strength, we can use Eq. 5.4 to deduce:

$$\lambda^a_{11,22} \leq \sqrt{2\pi} \left[\frac{\left(s - m_a^2\right)^2 + m_a^2 \Gamma_a^2}{s\left(s - 4m_\chi^2\right)} \right]^{1/4}, \tag{5.6}$$

where m_a and Γ_a are the mass and width of a, respectively. Therefore, perturbative unitarity of the theory in the non-relativistic and ultra-relativistic regimes requires:

$$\lambda^a_{11,22} \lesssim \begin{cases} 20 \times \left(\delta/0.1\right)^{1/2} \left(0.003/v\right)^{1/2}, & \sqrt{s} \approx 2m_\chi \\ 2.5, & \sqrt{s} \sim \infty, \end{cases} \tag{5.7}$$

where $\delta \equiv |1 - \left(m_a/2m_\chi\right)^2| \ll 1$. In the first line of Eq. 5.7, we have assumed that the width Γ_a is sufficiently small such that $\Gamma_a/m_a \ll \delta$. We will show later that these conditions will be satisfied within the most viable parameter space for generating a large cross section for up-scattering. We see that in the non-relativistic regime, the upper limit on $\lambda^a_{11,22}$ from perturbative unitarity is weaker than one generically expects from perturbativity of the theory, $\lambda^a_{11,22} \lesssim 4\pi$. Throughout our analysis, we will consider Yukawa couplings as large as $\lambda^a_{11,22} \sim 5$ in the non-relativistic regime. If $\chi_{1,2}$ only couple to a, then large values of $\lambda^a_{11,22}$ will contribute positively to its beta function and cause $\lambda^a_{11,22}$ to grow rapidly at higher energies. By considering such large values of this coupling, we implicitly require that new physics (such as couplings to new gauge bosons) come in at higher energies in order to stabilize $\lambda^a_{11,22} \lesssim 2.5$ in the high-energy limit.

In the low velocity limit, the cross section for $\chi_1\chi_1$ to become excited to $\chi_2\chi_2$ is given by:

$$\sigma v(\chi_1\chi_1 \to \chi_2\chi_2) \approx (v^2 - v_t^2)^{1/2} \times \frac{2m_\chi^2[\lambda^a_{11}\lambda^a_{22}]^2}{\pi[(4m_\chi^2 - m_a^2)^2 + m_a^2\Gamma_a^2]}, \tag{5.8}$$

where v_t is as defined in Eq. 5.3. The up-scattering of $\chi_1\chi_1$ into $\chi_1\chi_2$ is subdominant, but for a somewhat subtle reason. As we will see later in this chapter, after diagonalizing into mass eigenstates, one of the fields χ_1 or χ_2 generally has a mass term with the "wrong sign", requiring a transformation $\chi \to i\gamma^5\chi$. This leaves the $a\bar{\chi}_1 i\gamma^5\chi_1$ and $a\bar{\chi}_2 i\gamma^5\chi_2$ interaction terms as written in Eq. 5.5, but changes the mixed term into $a\bar{\chi}_1\chi_2$, resulting in the suppression of the corresponding up-scattering cross section by an additional factor of $(v^2 - v_t^2)$.

5.3.2 Annihilation and Coannihilation

In the previous subsection, we showed that the very large up-scattering rates required for the 3.55 keV line can be generated through the resonant exchange of a pseudoscalar, a, but at the cost of introducing $\mathcal{O}(1)$ Yukawa couplings into the dark matter sector. If χ_1 is to be populated thermally in the early universe, however, it must also have non-zero couplings to the SM. Furthermore, if the couplings of a to the SM are comparable to its couplings to the dark matter, then the annihilation cross section during freeze-out will be many orders of magnitude larger than that needed to generate a thermal relic abundance of χ_1 consistent with $\Omega_\chi h^2 \sim 0.12$. Instead, there must be a large hierarchy between the couplings of a with

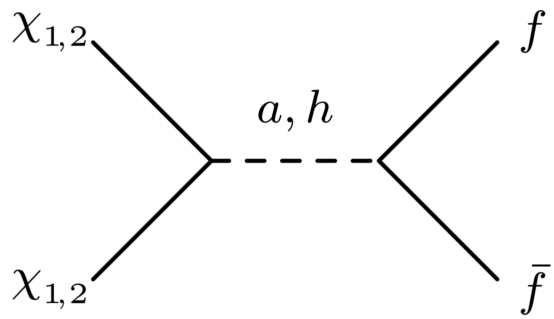

Figure 5.2: The dominant Feynman diagram for the annihilation or coannihilation of $\chi_1\chi_1$, $\chi_1\chi_2$, or $\chi_2\chi_2$.

the dark matter and with the SM.

One way to generate a very small coupling between the a and SM fermions is through mass-mixing with the heavy pseudoscalar in a two-Higgs doublet model (2HDM). Such a scenario has been discussed previously within the context of the Galactic Center gamma-ray excess [265]. The idea is to introduce a scalar potential involving a parity-odd singlet pseudoscalar, a_0, along with a second Higgs doublet in the framework of a Type-II 2HDM. The two Higgs doublets, each with hypercharge of $+1/2$, are denoted as $H_{d,u}$, and the corresponding pseudoscalar of the 2HDM sector is written as A_0. After a_0 and A_0 mix, the light and heavy mass eigenstates of the CP-odd sector will be written as a and A, respectively.

The Higgs portal between the dark matter and the SM emerges from the trilinear interaction of the scalar potential involving a_0, H_d, and H_u. More specifically, the terms of the scalar potential relevant for the annihilation and coannihiation of $\chi_{1,2}$ are given by:

$$V_{\text{scalar}} \supset V_{\text{2HDM}} + \frac{1}{2}m_{a_0}^2 a_0^2 + \left(iB_a a_0 H_d^\dagger H_u + \text{h.c.}\right), \tag{5.9}$$

where V_{2HDM} is the most general CP-conserving 2HDM potential corresponding to a Type-II 2HDM, and B_a is a dimensionful parameter governing the strength of mixing in the Higgs portal. In order to suppress flavor changing neutral currents at tree-level, Type-II 2HDMs involve a $\mathbb{Z}_2$ symmetry under which $H_d \to -H_d$ and $H_u \to H_u$. We have assumed that this symmetry is softly broken by dimensionful couplings, such as by the Higgs portal interaction involving B_a in Eq. 5.9, and similar terms within the 2HDM scalar potential. For simplicity, we assume that CP is conserved in the full potential of Eq. 5.9, which implies that B_a is real and that a_0 and A_0 do not develop vacuum expectation values. Once electroweak symmetry breaking is induced by $\langle H_{d,u}\rangle = v_{d,u}/\sqrt{2}$, H_d and H_u can be written in terms of the scalar mass eigenstates of the 2HDM potential:

$$\begin{aligned} H_d &= \frac{1}{\sqrt{2}}\begin{pmatrix} -\sqrt{2}\, s_\beta H^+ + \sqrt{2}\, c_\beta G^+ \\ v_d - s_\alpha h + c_\alpha H - i s_\beta A_0 + i c_\beta G \end{pmatrix} \,, \\ H_u &= \frac{1}{\sqrt{2}}\begin{pmatrix} \sqrt{2}\, c_\beta H^+ + \sqrt{2}\, s_\beta G^+ \\ v_d + c_\alpha h + s_\alpha H + i c_\beta A_0 + i s_\beta G \end{pmatrix} \,, \end{aligned} \tag{5.10}$$

where h, H are the light and heavy CP-even Higgs bosons, $H^\pm$ the charged Higgs, G and $G^\pm$ the neutral and charged Goldstones bosons, and A_0 is the pseudoscalar of the 2HDM sector. c_β and s_β are the cosine and sine of β, defined by $\tan\beta \equiv v_u/v_d$ and $\sqrt{v_d^2 + v_u^2} = v = 246$ GeV, and c_α and s_α are the cosine and sine of the mass mixing angle of the CP-even scalars, α. We will remove all dependence on α by choosing to work in the alignment limit throughout, where $\sin(\beta - \alpha) = 1$ and the h couplings are SM-like. We will further assume that the masses of A_0, H, and $H^\pm$ are decoupled, with values at a scale around 1 TeV.

Mass mixing between the pseudoscalars a_0 and A_0 is induced by the coupling B_a in Eq. 5.9. The mass-squared matrix of the CP-odd sector in the (a_0, A_0) basis is written as:

$$M^2_{\text{CP-odd}} = \begin{pmatrix} m^2_{a_0} & -B_a v \\ -B_a v & m^2_{A_0} \end{pmatrix} \,, \tag{5.11}$$

where m_{A_0} is the mass of the the pseudoscalar A_0 in the 2HDM potential. Diagonalizing

$M^2_{\text{CP-odd}}$ leads to the mass eigenstates a and A such that:

$$\begin{pmatrix} a_0 \\ A_0 \end{pmatrix} = \begin{pmatrix} \cos\theta & \sin\theta \\ -\sin\theta & \cos\theta \end{pmatrix} \begin{pmatrix} a \\ A \end{pmatrix}, \tag{5.12}$$
$$m^2_{a,A} = \frac{1}{2}\left[m^2_{A_0} + m^2_{a_0} \mp \sqrt{\left(m^2_{A_0} - m^2_{a_0}\right)^2 + 4B_a^2 v^2} \right],$$
$$\cos\theta = \frac{1}{\sqrt{2}} \left(1 + \frac{m^2_{A_0} - m^2_{a_0}}{\sqrt{\left(m^2_{A_0} - m^2_{a_0}\right)^2 + 4B_a^2 v^2}} \right)^{1/2}.$$

Throughout this chapter, we will consider values of $m_a \sim 100$ GeV, $m_A \sim m_H \sim m_{H^\pm} \sim 1$ TeV, and $\theta \sim 10^{-5}$. These choices of parameters uniquely determine $|B_a| \sim \mathcal{O}(0.1)$ GeV. Therefore, we will be working in the limit in which mixing is induced by small off-diagonal terms and $m_{a_0} \ll m_{A_0}$. As a result, the light pseudoscalar, a, is mostly singlet-like and the much heavier A is mostly 2HDM-like.

Stringent constraints on new scalars and pseudoscalars can be derived from the results of searches for MSSM Higgs bosons at colliders [303–305]. In particular, if a has some sizable branching ratio to SM fermions, then the production of a a in association with a b-jet can produce distinctive bbb and $b\tau\tau$ events. In our case, however, the a has suppressed couplings to quarks and leptons and very large couplings to dark matter, enabling collider searches for invisibly decaying light scalars and pseudoscalars to provide much stronger bounds [170, 306, 307]. Even these searches, however, yield extremely weak bounds for $\theta \lesssim 10^{-3}$ since the production of a depends on its suppressed couplings to SM quarks. In fact, for $m_a \sim 100$ GeV in the large $\tan\beta$ limit, the most stringent constraint comes from the contribution to $B_s \to \mu^+\mu^-$, which results in the approximate upper bound $\theta \lesssim 0.1$ [265].

Due to the small mass splitting between χ_1 and χ_2, both of these states can play an important role in determining the thermal relic abundance of dark matter in this model. Although we use the publicly available program micrOMEGAs [73] to calculate the relic abundance numerically, it is illustrative to consider analytic forms for the relevant cross sections in the low velocity limit (see Fig. 5.2):

$$\begin{aligned}
\sigma v(\chi_1\chi_1 \to f\bar{f}) &\approx \frac{2n_c}{\pi}\sqrt{1-\frac{m_f^2}{m_\chi^2}}\left[\frac{\lambda_{11}^a\lambda_f^a m_\chi}{4m_\chi^2-m_a^2}\right]^2, \\
\sigma v(\chi_2\chi_2 \to f\bar{f}) &\approx \frac{2n_c}{\pi}\sqrt{1-\frac{m_f^2}{m_\chi^2}}\left[\frac{\lambda_{22}^a\lambda_f^a m_\chi}{4m_\chi^2-m_a^2}\right]^2, \\
\sigma v(\chi_1\chi_2 \to f\bar{f}) &\approx \frac{n_c}{2\pi}\left(1-\frac{m_f^2}{m_\chi^2}\right)^{3/2}\left[\frac{\lambda_{12}^h\lambda_f^h m_\chi}{4m_\chi^2-m_h^2}\right]^2,
\end{aligned} \tag{5.13}$$

where $n_c = 3(1)$ for annihilation into quarks (leptons), and the widths of a and h should be included when near resonance. The first two of these processes are mediated by the exchange of the light pseudoscalar, a, which couples to the SM through mixing with the heavier pseudoscalar of the 2HDM, $\lambda_f^a = -\sin\theta\, m_f \cot\beta/v$ for up-type fermions and $\lambda_f^a = -\sin\theta\, m_f \tan\beta/v$ for down-type fermions. The last of these processes is mediated by the SM-like scalar Higgs boson. For reasons that are similar to those described in the previous subsection for the process $\chi_1\chi_1 \to \chi_1\chi_2$, this process is s-wave and contributes in the low velocity limit. Here, λ_{12}^h is the $\chi_1 - \chi_2 - h$ coupling (corresponding to the term $\lambda_{12}^h h\bar{\chi}_1\chi_2$ in the Lagrangian of Eq. B.1), and $\lambda_f^h = -m_f/v$ is the coupling between the light scalar Higgs boson and SM fermions.

The process of thermal freeze-out in this model depends on the hierarchy of the annihilation and coannihilation cross sections described in Eq. 5.13. If $\sigma v(\chi_1\chi_1 \to f\bar{f}), \sigma v(\chi_2\chi_2 \to f\bar{f}) \gg \sigma v(\chi_1\chi_2 \to f\bar{f})$, for example, each of the two species freeze-out largely independently of one another, followed by the decay $\chi_2 \to \chi_1\gamma$, which increases the final abundance of the χ_1 population. Alternatively, if $\sigma v(\chi_1\chi_2 \to f\bar{f})$ is not negligible, these coannihilations will deplete the abundances of both species, and the total resulting dark matter abundance. The dark matter's annihilation cross section in the universe today can vary significantly depending on which of these processes dominates. In the former case, we expect a comparatively large cross section, $\sigma v \sim (4-6)\times 10^{-26}$ cm^3/s, which is in tension with constraints from

Field	Charge	Spin
S_1	$(\mathbf{1},\mathbf{1},0)$	$1/2$
S_2	$(\mathbf{1},\mathbf{1},0)$	$1/2$
D_1	$(\mathbf{1},\mathbf{2},-1/2)$	$1/2$
D_2	$(\mathbf{1},\mathbf{2},+1/2)$	$1/2$
a_0	$(\mathbf{1},\mathbf{1},0)$	0
H_d	$(\mathbf{1},\mathbf{2},+1/2)$	0
H_u	$(\mathbf{1},\mathbf{2},+1/2)$	0

Table 5.1: The field content of the model described in this chapter. The charges correspond to $SU(3)c \times SU(2)_W \times U(1)_Y$.

gamma-ray observations of dwarf spheroidal galaxies (especially in the case in which $2m_\chi$ is near resonance, but slightly greater than m_a, for which the low velocity annihilation rate is further enhanced). If the cross section for $\chi_1\chi_2$ coannihilations is substantial, however, the self-annihilation cross section required to generate the appropriate thermal relic abundance will be reduced, allowing us to comfortably evade this constraint.

To summarize the major points of this section, if the s-channel exchange of the pseudoscalar, a, is to contribute to both the up-scattering and the annihilation of the dark matter, a must have both large couplings to the dark matter and very small couplings to the SM. In our model, these latter interactions arise from the mass-mixing of the a with the 2HDM pseudoscalar, A_0, allowing the corresponding coupling to be highly suppressed.

5.3.3 Decay and Mass Splitting

Up to this point, we have assumed that the dark matter and its excited state, $\chi_{1,2}$, are gauge singlets. While this is sufficient to obtain the desired rates for both up-scattering and annihilation, we must also require that the excited state, χ_2, decays with a lifetime that is much shorter than the age of the universe. This requires the dark sector to couple to a charged state appearing in the loop-diagram responsible for the decay $\chi_2 \to \chi_1\gamma$.

A cosmologically short lifetime for χ_2 can be easily accommodated by mixing a small $SU(2)_W$ doublet component into the dark sector, allowing $\chi_{1,2}$ to couple to the Higgs doublets, $H_{d,u}$, (and their associated $H^{\pm}$) as well as to $W^{\pm}$. Additionally, an active degree of freedom that is allowed to mix with $\chi_{1,2}$ generically introduces new charged states into the dark matter sector, analogous to charginos in the MSSM, that can enter into the loop-induced decay as well. The introduction of a small doublet component into the dark sector can also provide a natural explanation for the 3.55 keV mass splitting between the states χ_1 and χ_2.

In this regard, we follow closely the approach laid out in Ref. [308], wherein a vector-like pair of 2-component Weyl fermion SM gauge singlets, S_1 and S_2, and a vector-like pair of Weyl fermion $SU(2)_W$ doublets, D_1 and D_2, are introduced, the latter of which are assigned hypercharge $\mp 1/2$. Unlike in Ref. [308], however, which only considers long-lived primordial decays with mixing introduced by interactions with the SM Higgs doublet, we will consider interactions involving the two Higgs doublets and much shorter lifetimes for the excited state.

In addition to the bare mass terms, in general, the singlet and doublet degrees of freedom can couple via Yukawa terms to one or both of the Higgs doublets, $H_{d,u}$. We will assume that the dark matter sector respects the $\mathbb{Z}_2$ symmetry of the 2HDM potential, which we enlarge to include $S_{1,2} \to -S_{1,2}$ (in addition to the usual $H_{d,u} \to \mp H_{d,u}$). As a result, the dark matter can only directly couple to H_d. We summarize our model's particle content in Table 5.1. The dark sector Lagrangian contains the following terms:

$$
\begin{aligned}
-\mathcal{L} \supset\ & M_S S_1 S_2 + M_D D_1 D_2 + i y_S a_0 S_1 S_2 + i y_D a_0 D_1 D_2 \\
& + y_{11} S_1 D_1 H_d + y_{21} S_2 D_1 H_d \\
& + y_{22} S_2 H_d^\dagger \cdot D_2 + y_{12} S_1 H_d^\dagger \cdot D_2 + \text{h.c.},
\end{aligned}
\tag{5.14}
$$

where 2-component Weyl and $SU(2)_W$ indices are implied. For simplicity, we take all of the couplings in Eq. 5.14 to be real and introduce an additional $\mathbb{Z}_2$ symmetry on the dark sector

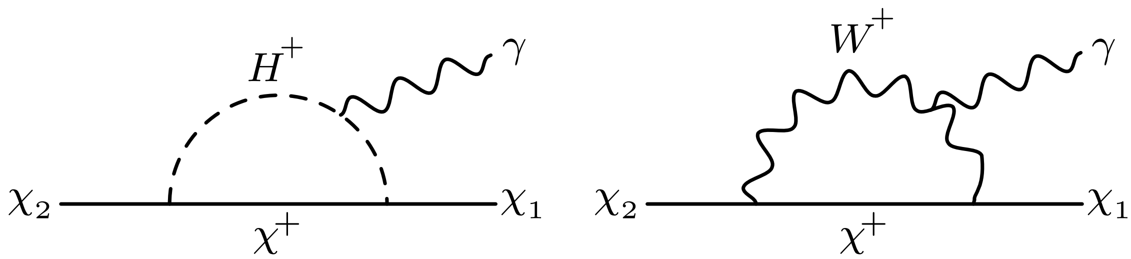

Figure 5.3: Feynman diagrams for the decay $\chi_2 \to \chi_1 \gamma$. Similar diagrams in which the photon is emitted off the χ^+ also contribute.

such that the lightest fermionic state is a stable dark matter candidate. For model building in a similar direction, see Ref. [309].

The dark matter $SU(2)_W$ doublets are parametrized as:

$$D_1 = \begin{pmatrix} \nu_1 \\ E_1 \end{pmatrix} , \; D_2 = \begin{pmatrix} -E_2 \\ \nu_2 \end{pmatrix} , \tag{5.15}$$

where $\nu_{1,2}$ and $E_{1,2}$ are the neutral and charged components of the doublets, respectively. E_1 and E_2 will mix to form an electrically charged Dirac fermion of mass M_D, which we will label as $\chi^{\pm}$. Since chargino searches at LEP generally exlude new charged fermions lighter than 100 GeV, we will take $M_D \gtrsim 100$ GeV. After elecroweak symmetry breaking, the neutral degrees of freedom, $S_{1,2}$ and $\nu_{1,2}$, will mix according to the following mass matrix (in the S_1-S_2-ν_1-ν_2 basis):

$$M_0 = \begin{pmatrix} 0 & M_S & \frac{1}{\sqrt{2}} y_{11} v_d & \frac{1}{\sqrt{2}} y_{12} v_d \\ M_S & 0 & \frac{1}{\sqrt{2}} y_{21} v_d & \frac{1}{\sqrt{2}} y_{22} v_d \\ \frac{1}{\sqrt{2}} y_{11} v_d & \frac{1}{\sqrt{2}} y_{21} v_d & 0 & M_D \\ \frac{1}{\sqrt{2}} y_{12} v_d & \frac{1}{\sqrt{2}} y_{22} v_d & M_D & 0 \end{pmatrix} . \tag{5.16}$$

The lightest mass eigenstate of M_0 will be the stable dark matter candidate, χ_1, and the second lightest mass eigenstate the excited state, χ_2. The gauge composition of $\chi_{1,2}$ can be written as:

$$\chi_{1,2} = N_{S_1}^{1,2} S_1 + N_{S_2}^{1,2} S_2 + N_{\nu_1}^{1,2} \nu_1 + N_{\nu_2}^{1,2} \nu_2 \ . \tag{5.17}$$

A large doublet component of $\chi_{1,2}$ is severely restricted by direct detection experiments because this usually introduces large couplings to the SM-like Higgs and to the Z. We therefore focus on the case in which χ_1 and χ_2 are largely singlet-like and $m_{\chi_1} \approx m_{\chi_2} \approx M_S \ll M_D$. In this small mixing limit, it is possible to derive approximate forms for the mixing angles:

$$\begin{aligned}
N_{S_1}^{1,2} &\approx \mp\frac{1}{\sqrt{2}} \ , \qquad N_{S_2}^{1,2} \approx -\frac{1}{\sqrt{2}} \\
N_{\nu_1}^{1,2} &\approx \frac{v_d}{2\,(M_D^2 - M_S^2)} \big[\,(y_{11} \pm y_{12})\,M_D \pm (y_{21} \pm y_{22})\,M_S\big] \\
N_{\nu_2}^{1,2} &\approx \frac{v_d}{2\,(M_D^2 - M_S^2)} \big[\,(y_{21} \pm y_{22})\,M_D \pm (y_{11} \pm y_{12})\,M_S\big] \ .
\end{aligned} \tag{5.18}$$

Furthermore, in this limit, the mass splitting, $\delta m_\chi \equiv m_{\chi_2} - m_{\chi_1}$, can be approximated as:

$$\delta m_\chi \approx \frac{v_d^2}{M_D^2 - M_S^2} \Big| \,(y_{11}y_{12} + y_{21}y_{22})\,M_D + (y_{11}y_{21} + y_{12}y_{22})\,M_S \Big| \ . \tag{5.19}$$

From Eq. 5.19 one can see that if either $y_{11} = y_{22} = 0$ or $y_{12} = y_{21} = 0$, then $\delta m_\chi = 0$. This can be understood from the symmetries of the Lagrangian of Eq. 5.14 as follows. The kinetic terms of S_1, S_2, D_1, D_2 possess a $U(1)^4$ symmetry. This is broken down to $U(1)_S \times U(1)_D$ by the bare masses M_S and M_D of Eq. 5.14. At this point, $U(1)_S \times U(1)_D$ guarantees that the mass eigenstates of M_0 in Eq. 5.16 will split into two separate degenerate pairs. Once the Yukawa couplings y_{11}, y_{12}, y_{21}, y_{22} are turned on, both of these $U(1)$'s are further broken. However, in the limit that either $y_{11} = y_{22} = 0$ or $y_{12} = y_{21} = 0$ holds, then $U(1)_S \times U(1)_D$ is restored, and the mass spectrum once again decouples to two pairs of mass degenerate states. This argument holds to all orders in perturbation theory.

To obtain a mass splitting as small as 3.55 keV, Yukawa couplings on the order of $y_{ij} \sim$

$10^{-2} \times (\tan\beta/50)(M_D/700\,\mathrm{GeV})^{1/2}$ are generally required. As we will see in the next section, however, order one values for these quantities are necessary if $\chi_1\chi_2$ coannihilations are to be efficient enough to obtain the desired thermal relic abundance without conflicting with constraints from gamma-ray observations of dwarf galaxies. This tension can be resolved if there is a cancellation in Eq. 5.19, such as arises for the choice $y_{11} \simeq y_{22} \simeq y_{21} \simeq -y_{12}$, with a small level of non-degeneracy needed for an $\mathcal{O}(\mathrm{keV})$ mass splitting. This is technically natural and can arise from symmetries in the ultraviolet, which are expected to be broken at the two-loop level (for a similar approach, see Ref. [308]).

After electroweak symmetry breaking, χ_1, χ_2, and $\chi^\pm$ couple to the charged bosons $H^\pm$ and $W^\pm$, and a mass splitting, δm_χ, is induced. As a result χ_2 can decay via a radiative 2-body process $\chi_2 \to \chi_1\gamma$ where $\chi^\pm$ and the charged bosons are exchanged in the loop (see Fig. 5.3). In the simple limit that $y_{11} = y_{22} = y_{21} = -y_{12} \equiv y$, $m_{H^\pm}, M_D \gg m_\chi$, and $\tan\beta \gg 1$, the $W^\pm$ loop contributes negligibly, and this decay width is given by:

$$\Gamma \approx \frac{e^2 y^4}{256\pi^5} \frac{(\delta m_\chi)^3 M_D^2}{(m_{H^\pm}^2 - M_D^2)^2} \left[1 - \frac{m_{H^\pm}^2}{m_{H^\pm}^2 - M_D^2} \ln\left(\frac{m_{H^\pm}^2}{M_D^2}\right)\right]^2. \tag{5.20}$$

A more general expression for this width is given in Appendix B.2. We find that the most viable parameter space leads to lifetimes for χ_2 that are on the order of an hour (see Fig. 5.4). Furthermore, the 3-body decay to neutrinos, $\chi_2 \to \chi_1\nu\nu$, remains kinematically open via an off-shell Z boson. This later process, however, remains subdominant since it is suppressed by two additional powers of δm_χ [308].

In the region of parameter space under consideration, our model is not significantly constrained by observations of the cosmic microwave background (CMB) or of the light element abundances. In particular, for χ_2 lifetimes less than 10^{12} s, the most stringent bounds from the CMB are on the $\chi_1\chi_1$ annihilation cross section, and are weaker than the values considered in our study [310]. Constraints from Big Bang Nucleosynthesis (BBN) are generally

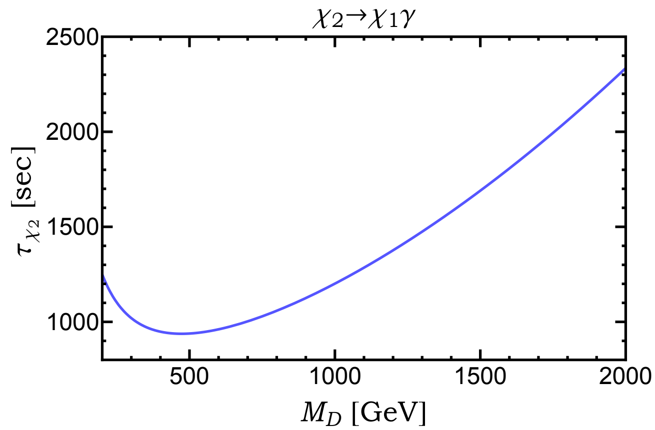

Figure 5.4: The lifetime for the decay $\chi_2 \to \chi_1\gamma$, for $\delta m_\chi = 3.55$ keV, $m_\chi \ll M_D, m_{H^\pm}$, $m_{H^\pm} = 1$ TeV, $\tan\beta \gg 1$, $y_{11} \approx y_{21} \approx y_{22} \approx -y_{12} \approx 2.5$.

expressed in terms of the rescaled electromagnetic energy released, as a function of the χ_2 lifetime. For lifetimes less than 10^6 s, the upper bound is derived from the measured deuterium abundance [250, 311]. Our model, however, predicts values for this quantity that are many orders of magnitude smaller than the existing upper limit.

5.4 Results

Due to the sizable number of free parameters in this model (M_S, M_D, y_{11}, y_{22}, y_{12}, y_{21}, y_D, y_S, α, β, m_{a_0}, m_{A_0}, B_a), a wide range of phenomenology can emerge. We will simplify this to some extent by focusing on the parameters which yield $\delta m_\chi \simeq 3.55$ keV and $m_\chi \simeq 60$ GeV, which are within the range capable of generating both the 3.55 keV line and the Galactic Center gamma-ray excess [296].

In Fig. 5.5, we show an example of a slice of the parameter space in this model. Here, we have adopted $|\lambda^a_{11,22}| = 6$, $y_D = 0$, $y_{11} = y_{21} = y_{22} = 2.5$, $y_{12} \approx -2.5$ (with y_{12} fixed to give $\delta m_\chi = 3.55$ keV throughout the $M_D - M_S$ plane shown), $\theta = 3 \times 10^{-5}$, $\tan\beta = 50$, $m_a = 120$ GeV, and $m_A = m_H = m_{H^\pm} = 1$ TeV. The region yielding a thermal relic abundance equal to the cosmological dark matter density (solid black line) passes through the region that can

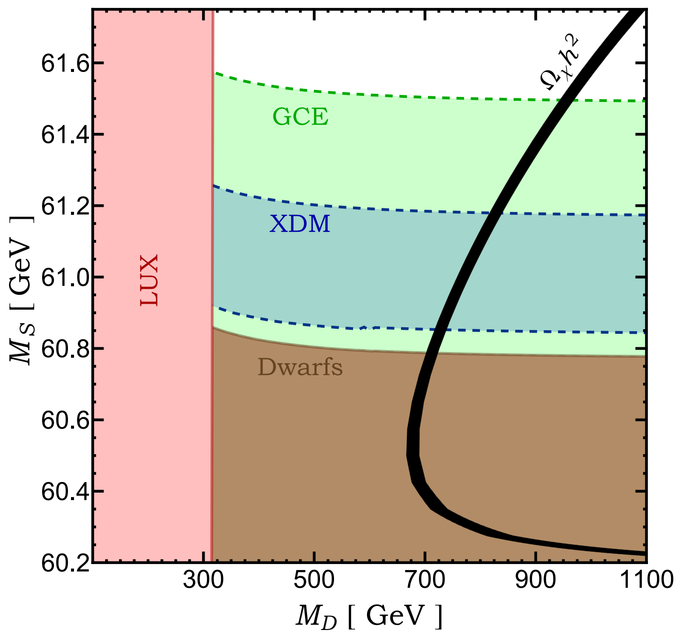

Figure 5.5: An example of the parameter space of our model, with $|\lambda^a_{11,22}| = 6$, $y_D = 0$, $y_{11} = y_{21} = y_{22} = 2.5$, $y_{12} \approx -2.5$, $\delta m_\chi = 3.55$ keV, $\theta = 3 \times 10^{-5}$, $\tan\beta = 50$, $m_a = 120$ GeV, and $m_A = m_H = m_{H^\pm} = 1$ TeV. The region yielding a thermal relic abundance equal to the cosmological dark matter density $\Omega_\chi h^2 = 0.1199 \pm 0.0027$ (solid black line) passes through the region that can generate the observed 3.55 keV signal (labelled "XDM") for values of $M_S \approx 61$ GeV (about 1 GeV above the a resonance). Also shown is the region capable of generating the Galactic Center gamma-ray excess (labelled "GCE", corresponding to $\sigma v = 5 \times 10^{-27}$ to 5×10^{-26} cm^3/s) and the regions that are excluded by gamma-ray observations of dwarf galaxies [2] or by LUX [3].

generate the observed 3.55 keV line (labelled "XDM") for values of $M_S \approx 61$ GeV (about 1 GeV above the a resonance). In particular, to provide an adequate fit to the 3.55 keV signal we demand that the up-scattering rate fits the measured fluxes within the $\delta\chi^2 < 3$ contour of Ref. [293] for promptly decaying excited states. Also shown is the region that is capable of generating the Galactic Center gamma-ray excess ($\sigma v = 5 \times 10^{-27}$ to 5×10^{-26} cm^3/s), as well as the regions that are excluded by gamma-ray observations of dwarf galaxies [2] or by direct detection experiments [3] (see Appendix B.3). Constraints from the invisible width of the Higgs do not restrict any of the parameter space shown.

The process of $\chi_1\chi_2$ coannihilation plays an important role in the determination of the thermal relic abundance in this region of parameter space. In particular, in the limit at hand, $\lambda^h_{12}/\lambda^h_{11} \sim 2M_D/M_S \gg 1$, large coannihilation rates are possible without large elastic scattering cross sections with nuclei (for details, see Appendices B.1 and B.3). In addition, resonant annihilation and coannihilation through the a and the SM-like Higgs significantly deplete the thermal abundance for $M_S \simeq 60$ GeV and 62.5 GeV, respectively. The relic abundance is relatively insensitive to the parameters scanned over in Fig. 5.5, and is within approximately an order of magnitude of the measured quantity over the entire plane shown. Lastly, we note that up-scattering and decay rates are insensitive to the parameter θ. If we had chosen to set this quantity to zero (decoupling a from the pseudoscalar of the 2HDM), we can still generate the 3.55 keV line, but without a mechanism to produce the Galactic Center gamma-ray excess and without constraints from gamma-ray observations of dwarf galaxies.

5.5 Summary and Conclusions

It has been previously proposed that dark matter scattering into an excited state (eXciting Dark Matter, or XDM) could be responsible for the 3.55 keV line observed from Galaxy Clusters without conflicting with the lack of such a signal from dwarf galaxies [291]. Such a model could also potentially generate Fermi's gamma-ray excess from the Galactic Center. Most of the XDM model building discussed in the literature has focused on scenarios in which the dark matter interacts through a light mediator, with no significant couplings between the dark sector and the Standard Model. Here, instead of hidden sector, we have considered a model in which the dark matter directly annihilates into Standard Model fermions through the near resonant exchange of a pseudoscalar, a, which also efficiently mediates the process of up-scattering, $\chi_1\chi_1 \to \chi_2\chi_2$. This pseudoscalar is a mixture of a Standard Model singlet and the pseudoscalar appearing from a two-Higgs doublet model. The dark matter itself is a mixture of two Standard Model gauge singlets and the neutral components of two $SU(2)_W$ doublets. This allows us to generate a 3.55 keV mass splitting between the two lightest mass eigenstates, and enables for the rapid decay of $\chi_2 \to \chi_1 \gamma$.

We have identified regions of parameter space in our model that can simultaneously generate the 3.55 keV line and the Galactic Center gamma-ray excess, while remaining consistent with all constraints from colliders, direct detection experiments, and gamma-ray observations of dwarf galaxies. Coannihilations between χ_1 and χ_2 can play an important role in determining the thermal relic abundance of dark matter in this model.

Chapter 6

Vector Dark Matter through a Radiative Higgs Portal

Based on arXiv:1512.06853 [312]

6.1 Introduction

As the only elementary scalar in the Standard Model (SM), the Higgs boson presents a unique opportunity as a window to physics beyond the Standard Model (SM). The operator $H^\dagger H$ is the lowest dimensional operator which is both a gauge and Lorentz singlet. As such, it occurs time and again as the means by which physics uncharged under the SM gauge symmetries communicates with the Standard Model. In particular, it is an effective mechanism by which scalar dark matter (DM) can talk to the ordinary matter [91], as is required if we wish to understand its abundance in the Universe today as the result of thermal processes acting in a standard cosmological history.

In the present chapter, we focus on the case in which the dark matter is a spin one vector boson. At first glance, it would appear that this case (much like scalar DM) offers a renormalizable connection between the dark matter and the Higgs [313, 314],

$$\mathcal{L} \supset \lambda \; H^\dagger H \; V_\mu V^\mu \;, \tag{6.1}$$

where V_μ is a massive vector field which plays the role of dark matter and λ is a dimensionless coupling. But this form, while invariant under the SM gauge symmetries, is misleading. Just like the SM W and Z bosons, a well-behaved UV description of V requires that it be associated with a gauge symmetry (the most simple construction of which would be an Abelian U(1)$'$, though one could also consider non-Abelian theories as well), spontaneously broken to give V a mass. The term in Eq. (6.1) violates the U(1)$'$, and must be engineered via its spontaneous breaking.

One tempting avenue would be to charge the Higgs itself under U(1)$'$. In that case the Higgs kinetic term $(D_\mu H)^\dagger (D^\mu H)$ contains Eq. (6.1), and the mass of V will arise as part of the vacuum expectation value (VEV) of H, naturally connecting the scale of the V mass to the electroweak scale. However, this construction contains other terms which mix V with the SM Z boson, with the result that V will inevitably end up unstable and contribute unacceptably to precision electroweak measurements unless it is very light (implying that it is very weakly coupled). This regime, though worth pursuing, is not very interesting for particle physics at the weak scale, and not very amenable to exploration through Higgs measurements at the LHC.

The situation is very different when the V mass is the result of a VEV living in a different scalar particle Φ which is a SM gauge singlet. In that case, there is no dangerous mixing with the SM Z boson, and the gauge coupling can be relatively large,

$$\mathcal{L} \quad \supset \quad -\frac{1}{4} V_{\mu\nu} V^{\mu\nu} + (D_\mu \Phi)^\dagger \, (D^\mu \Phi) - V(\Phi) + \lambda_P \; |H|^2 |\Phi|^2 \;, \tag{6.2}$$

where $D_\mu \Phi \equiv \partial_\mu \Phi - g Q_\Phi V_\mu \Phi$ is the usual covariant derivative for a particle of charge Q_Φ

and $V(\Phi)$ is a U(1)$'$-invariant potential designed to induce a VEV $\langle\Phi\rangle = v_\phi$, producing a mass for V,

$$m_V^2 \;\; = \;\; g^2 Q_\Phi^2 \, v_\phi^2 \; . \tag{6.3}$$

We have also included a scalar Higgs portal coupling λ_P, which leads to tree-level mixing between the SM Higgs boson and the Higgs mode of Φ, effectively implementing the Higgs portal. As a construction implementing the Higgs portal, it is well motivated and has been extensively explored in the literature[1] [153, 317–326].

However, it does not represent the *only* possible UV completion. In this chapter, we explore an alternative completion which realizes the Higgs portal as a consequence of additional heavy fermions which are charged under both U(1)$'$ and the SM gauge symmetries. At one loop, these fermions mediate an interaction between the Higgs and the DM somewhat in analogy with the effective Higgs-gluon vertex induced by the top quarks in the SM. This *radiative* UV completion leads to different phenomenology and singles out different interesting regions of parameter space.

This article is organized as follows. In Sec. 6.2, we discuss a simplified picture to illustrate the most important physics behind this concept, followed by the full matter content of the UV theory. In Sec. 6.3, we examine the phenomenology in light of experimental probes, such as direct detection, the invisible Higgs width, and relic abundance. We first focus on the case where the simplified picture is valid, with and without also considering mixing generated by a Scalar Higgs Portal. We then examine the effect of the full radiative portion of the UV theory. We reserve Sec. 6.4 for conclusions and summary.

[1] It also provides a mechanism to stabilize the Higgs potential [315] and/or generate a first order electroweak phase transition [316].

6.2 Radiative Higgs Portal for Vector Dark Matter

6.2.1 Particle Content and Structure

A radiative model often has multiple paths to the same low energy physics, since the mediating particles are not themselves involved in the initial and final states. Starting with the basic module of Eq. (6.2), we aim for a construction which adds fermions mediating an interaction of the form (6.1) such that:

- the vector particle V remains stable at the radiative level, which in particular requires that it does not kinetically mix with the SM electroweak interaction;
- the full gauge structure $\mathrm{SU}(3)_C\times\ \mathrm{SU}(2)_W\times\ \mathrm{U}(1)_Y\times\ \mathrm{U}(1)'$ remains free from gauge anomalies;
- there are no large contributions to the SM Higgs coupling to gluons or photons in contradiction with LHC measurements [327].

The first of these is the most subtle. Generically, communication between the SM Higgs and V requires that the mediator fermions be charged under both $\mathrm{U}(1)'$ and the Standard Model, which typically will induce processes involving an odd number of V's, resulting in their decay. The simplest example of such a process is the kinetic mixing between V and hypercharge. Such dangerous processes can be forbidden by a charge-conjugation symmetry, under which V is odd. In analogy with Furry's theorem of QED [328], this symmetry forbids processes involving an odd number of V's at energies below the masses of the mediator fermions.

Cancelling gauge anomalies further suggests that the additional fermions appear in vector-like pairs under both the SM and $\mathrm{U}(1)'$ gauge symmetries, whereas renormalizable coupling to the Higgs requires fields in $\mathrm{SU}(2)_W$ representations of size n and $n+1$ (and have hypercharges

Table 6.1: Charge assignments for fermions ψ, χ, and n and complex scalar Φ.

Field	($\mathrm{SU}(2)_W$, $\mathrm{U}(1)_Y$, $\mathrm{U}(1)'$)	Field	($\mathrm{SU}(2)_W$, $\mathrm{U}(1)_Y$, $\mathrm{U}(1)'$)
$\psi_{1\alpha}$	(2, 1/2, 1)	$\psi_{2\alpha}$	(2, 1/2, -1)
$\chi_{1\alpha}$	(2, -1/2, -1)	$\chi_{2\alpha}$	(2, -1/2, 1)
$n_{1\alpha}$	(1, 0, -1)	$n_{2\alpha}$	(1, 0, 1)
Φ	(1, 0, Q_Φ)		

differing by 1/2). A minimal set of particles satisfying these conditions is shown in Table 6.1, consisting of four $\mathrm{SU}(2)_W$ doublets and two singlets. (Different) pairs of the doublets are vector-like under both $\mathrm{U}(1)_Y$ and $\mathrm{U}(1)'$, cancelling gauge anomalies, and a $\mathrm{U}(1)'$ charge conjugation is implemented by $f_1 \leftrightarrow f_2$ (where $f = \psi, \chi, n$).

We have left the $\mathrm{U}(1)'$ charge of Φ as a free non-zero parameter which controls the dark matter mass as per Eq. (6.3). Choosing $Q_\Phi = \pm 1$ would allow the Φ VEV to mix the SM lepton doublets with the new fermions, which would be strongly constrained by precision measurements and ruin the $\mathrm{U}(1)'$ charge conjugation symmetry. Choosing $Q_\Phi = \pm 2$ would allow for Yukawa interactions of Φ with pairs of the new fermions, which would complicate the analysis of their mass eigenstates. We will restrict ourselves to other values for Q_Φ, which avoids these features, and serves simply to adjust the mass of V. It's worth pointing out that this implies that the lightest of the fermionic states is also stable, and will be present in the Universe to some degree as a second component of dark matter. However, provided its mass is much larger than m_V, fermion anti-fermion pairs will annihilate efficiently into weak bosons and V's, leaving it as a negligible fraction of the dark matter.

In 2-component Weyl notation, the Lagrangian contains mass terms and Yukawa interactions for the new fermions,

$$\begin{aligned} \mathcal{L} \supset & -m\, \epsilon^{ab} \left(\psi_{1a}\chi_{1b} + \psi_{2a}\chi_{2b}\right) - m_n\, n_1 n_2 \\ & - y_\psi\, \epsilon^{ab} \left(\psi_{1a} H_b n_1 + \psi_{2a} H_b n_2\right) - y_\chi \left(\chi_1 H^* n_2 + \chi_2 H^* n_1\right) + h.c. \end{aligned} \tag{6.4}$$

where a and b are $\mathrm{SU}(2)_W$ indices, the SM Higgs H is defined to transform as a (2, −1/2, 0), and spin indices have been suppressed. The U(1)$'$ charge conjugation symmetry, $f_1 \leftrightarrow f_2$ is manifest. After electroweak symmetry-breaking, the mass terms can be written as,

$$\mathcal{L}_m = -N^T M_n N' - E^T M_e E' + h.c. \tag{6.5}$$

where

$$N = \begin{bmatrix} \psi_{1n} \\ \chi_{2n} \\ n_2 \end{bmatrix}, \qquad N' = \begin{bmatrix} \psi_{2n} \\ \chi_{1n} \\ n_1 \end{bmatrix}, \qquad E = \begin{bmatrix} \psi_{1e} \\ \chi_{2e} \end{bmatrix}, \qquad E' = \begin{bmatrix} \chi_{1e} \\ \psi_{2e} \end{bmatrix}, \tag{6.6}$$

assemble collections of the electrically neutral (N and N') and charged (E and E') components of the fermions, and the mass matrices are given by,

$$M_n = \begin{bmatrix} 0 & -m & -y_\psi v/\sqrt{2} \\ -m & 0 & y_\chi v/\sqrt{2} \\ -y_\psi v/\sqrt{2} & y_\chi v/\sqrt{2} & m_n \end{bmatrix}, \qquad M_e = \begin{bmatrix} m & 0 \\ 0 & m \end{bmatrix}. \tag{6.7}$$

In the mass basis, there are three electrically neutral and two charged Dirac fermions, all of which interact with the dark matter V diagonally, since the states that mix all carry the same $U(1)'$ charge. Their coupling to the SM Higgs will involve the mixing matrices which transform from the gauge to the mass basis.

Note that by construction the electrically charged fermions receive no contributions from $\langle H \rangle$, implying that they do not interact with the Higgs boson and lead to no one-loop correction to its effective coupling to photons. Our choice to arrange N such that they also receive no contributions from Φ implies that the fermions do not renormalize the usual Higgs portal coupling λ_P of Eq. (6.2) at one-loop (starting at two loops, there are contributions mediated by a mixture of the fermions and V itself). In order to better extract the features of the radiative model, we self-consistently assume that λ_P is small enough to be subdominant

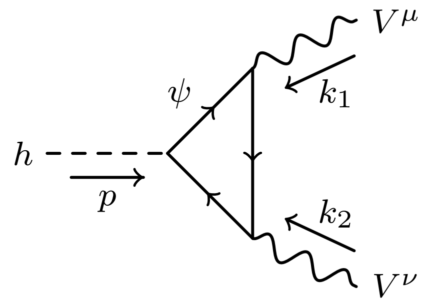

Figure 6.1: Representative triangle diagram contributing to the Higgs–dark matter interaction.

in the majority of the remainder of this chapter.

6.2.2 $\sigma_{\rm SI}$ and Higgs Invisible Width

Both the direct detection cross-section and the Higgs invisible decay width result from triangle diagrams (see Fig. 6.1). Integrating out the fermion ψ running in the loop, the $h-V-V$ interaction can be encoded by two form factors:

$$-\left(\frac{1}{4}A(p^2)\ h\ V^{\mu\nu}V_{\mu\nu}+\frac{1}{2}B(p^2)\ h\ V^{\mu}V_{\mu}\right) \tag{6.8}$$

with coefficients A and B which are (in the on-shell DM limit, $k_1^2 = k_2^2 = m_V^2$) functions of the fermion masses and mixings, m_V, and the momentum through the Higgs line, p^2. Reasonably compact analytic expressions for A and B are derived in Appendix C. We observe that $B(p^2) \to 0$ in the limit $m_V \to 0$ (i.e. when the $U(1)'$ symmetry is restored), as is required by gauge invariance, see Appendix C.

In terms of A and B, the cross section for non-relativistic scattering of V with a nucleon n is given by,

$$\sigma_{\rm SI} \quad = \quad \frac{1}{4\pi m_h^4}\left(\frac{f_n}{v}\right)^2\left(\frac{m_n^2}{m_n+m_V}\right)^2 |B(0)-A(0)\ m_V^2|^2 \tag{6.9}$$

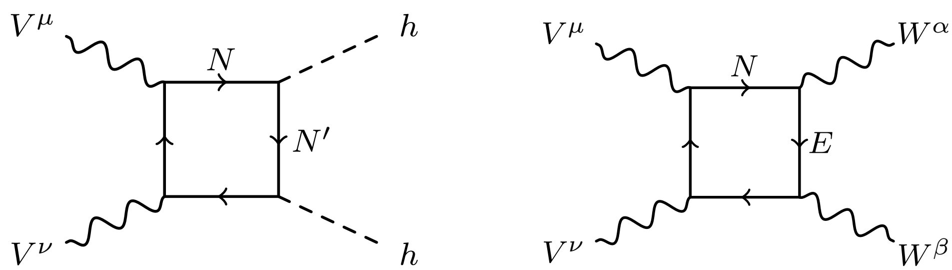

Figure 6.2: Representative box diagrams which contribute to DM annihilation into pairs of Higgs or electroweak bosons.

where the momentum transfer through the Higgs is approximated as $p^2 \approx 0$,

$$f_n = \sum_{q=u,d,s} f_{Tq}^{(n)} + \frac{2}{9} f_{TG}^{(n)}, \tag{6.10}$$

and we use the hadronic matrix elements f_{Tq}, from DarkSUSY [68]. Because of the tiny up and down Yukawa couplings, scattering mediated by a Higgs is to good approximation iso-symmetric.

The same three point vertex function also describes the invisible decay width of the Higgs boson,

$$\begin{aligned}\Gamma(h \to VV) \;\; = \;\; & \frac{1}{64\pi m_h}\sqrt{1-4\frac{m_V^2}{m_h^2}}\left[\left|A(m_h^2)\right|^2 m_h^4 \left(1-4\frac{m_V^2}{m_h^2}+6\frac{m_V^4}{m_h^4}\right)\right. \\ & +6\,\mathrm{Re}\left(A^*(m_h^2)B(m_h^2)\right) m_h^2 \left(1-2\frac{m_V^2}{m_h^2}\right) \\ & \left. +\frac{1}{2}\left|B(m_h^2)\right|^2 \frac{m_h^4}{m_V^4}\left(1-4\frac{m_V^2}{m_h^2}+12\frac{m_V^4}{m_h^4}\right)\right]\end{aligned} \tag{6.11}$$

where the Higgs is on-shell, $p^2 = m_h^2$. Note that because for small m_V the coefficient $B(p^2) \propto m_V^4$, this expression is finite in the limit $m_V \to 0$, as it should be.

6.2.3 Annihilation Cross Section and Relic Abundance

Pairs of dark matter can annihilate through the three point coupling of Fig. 6.1 through an (off- or on-shell) SM Higgs, leading to final states containing heavy quarks and/or weak bosons. These contributions exhibit a strong resonant behavior when $m_V \simeq m_h/2$. The gauge and Higgs boson final states also receive contributions at the same order from box diagrams (see Fig. 6.2), which contribute to processes including $VV \to hh, ZZ, WW, \gamma\gamma, hZ, Z\gamma$. These box diagrams are sensitive to more of the details of the UV theory, receiving contributions from the charged fermions as well as the neutral ones. As a result, simple analytic forms are not particularly illuminating, and we evaluate them using FeynArts [329], FormCalc, and LoopTools [330]. In the following section, we compute the full annihilation cross section including all of the accessible SM final states.

6.3 Experimental Constraints and Parameter Space

In this section, we examine the interesting parameter space, finding the regions consistent with the LUX limits on the spin independent DM-nucleon scattering cross-section [3]; and the invisible decay width of the Higgs produced via vector boson fusion (VBF) as constrained by CMS with 19.7 fb^{-1} at 8 TeV [331]. In the latter, we include the off-shell Higgs contribution following the technique presented in [332], simulating VBF Higgs production with HAWKv2.0 [333]. We also identify the regions leading to the correct thermal relic abundance for a standard cosmology, computing the loop diagrams with FeynArts [329], FormCalc, and LoopTools [330], which is then linked into micrOMEGAsV4.0 [73].

Because of the relatively large number of parameters, we build up insight into the phenomenology gradually by considering three different limits of the full theory. Initially in Sec. 6.3.1, we consider the limit in which one of the neutral fermions is much lighter than

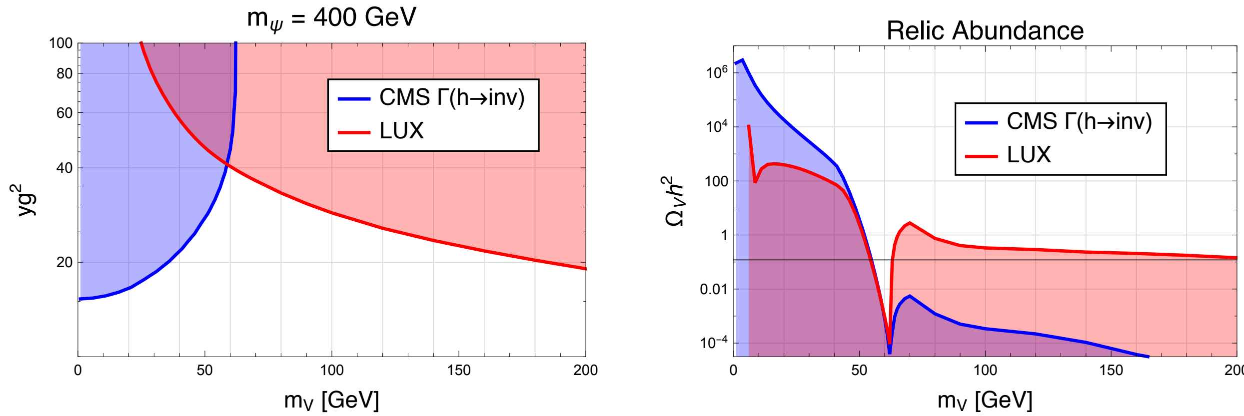

Figure 6.3: Left: Upper limits on yg^2 from VBF Higgs collider and direct detection constraints, with a fermion of mass 400 GeV. Right: The corresponding lower limit on the relic abundance for a standard cosmology.

both the other two neutral states and both of the charged ones, and the coupling λ_P is small enough to be neglected. We follow this in Sec. 6.3.2 by allowing λ_P to be large enough that there is relevant mixing between h and the Higgs mode of Φ. Finally, in Sec. 6.3.3 we switch off λ_P once more, but consider the case where all mediator fermions have comparable masses.

6.3.1 Single Fermion Limit

We begin with the case where the charged fermions and the two heavier neutral states are much heavier than the lightest neutral state, effectively decoupling from the phenomenology, and λ_P can be ignored. As before we assume the physical scalar contained in Φ is heavy enough to be ignored. In this limit, the relevant parameters are the $U(1)'$ gauge coupling g, Yukawa coupling to the light fermion y, light fermion mass m_ψ, and the vector dark matter mass m_V. As we will see below, the correct thermal relic density can only be achieved for annihilation in the Higgs funnel region, for which one can neglect the box diagram contributions. In that case, the gauge and Yukawa couplings always appear in the combination yg^2, leaving only three relevant parameter combinations.

Fig. 6.3, shows the collider and direct detection limits, plotted as the upper bound on yg^2

as a function of the dark matter mass, and the translation of those upper limits into a lower limit on the relic abundance, assuming a standard cosmology, for the case when the single relevant fermion has a mass of 400 GeV. Despite the fact that the limits on the couplings are relatively weak, the conclusion is nonetheless that aside from a narrow region in the Higgs funnel region, additional interactions would be required to deplete the dark matter relic density enough to saturate the observed relic density.

6.3.2 Single Fermion with Scalar Mixing

Building on the single fermion limit, we now allow for substantial λ_P such that the radial modes of H and Φ experience significant mixing, resulting in two CP even scalars we denote by h and h_2. Describing this limit requires three additional free parameters, which we take to be the mass of the second scalar m_{h_2}, $\langle\Phi\rangle = v_\phi$, and the Higgs-scalar mixing angle α.

For small α, the form factors of Eqn. (6.8) are shifted:

$$\begin{aligned} A(p^2) &\to \left(1 - \frac{\alpha^2}{2}\right) A(p^2) \\ B(p^2) &\to \left(1 - \frac{\alpha^2}{2}\right) B(p^2) - 2\alpha \frac{m_V^2}{v_\phi} \end{aligned} \tag{6.12}$$

where the additional contribution is the tree level contribution to $B(p^2)$ from the induced Φ component in h. In addition to the shift in the effective h-V-V coupling, the h_2 state acquires a coupling to the SM given by the corresponding SM Higgs coupling multiplied by α.

In Fig. 6.4, we indicate the bounds on yg^2 as a function of the vector mass for various benchmark values of the remaining free parameters as indicated, with shaded regions showing points excluded by the CMS invisible Higgs width bounds (green), and the LUX bounds on $\sigma_{\rm SI}$ (yellow). Note the appearance of “blind spots" in the direct detection plane coming from

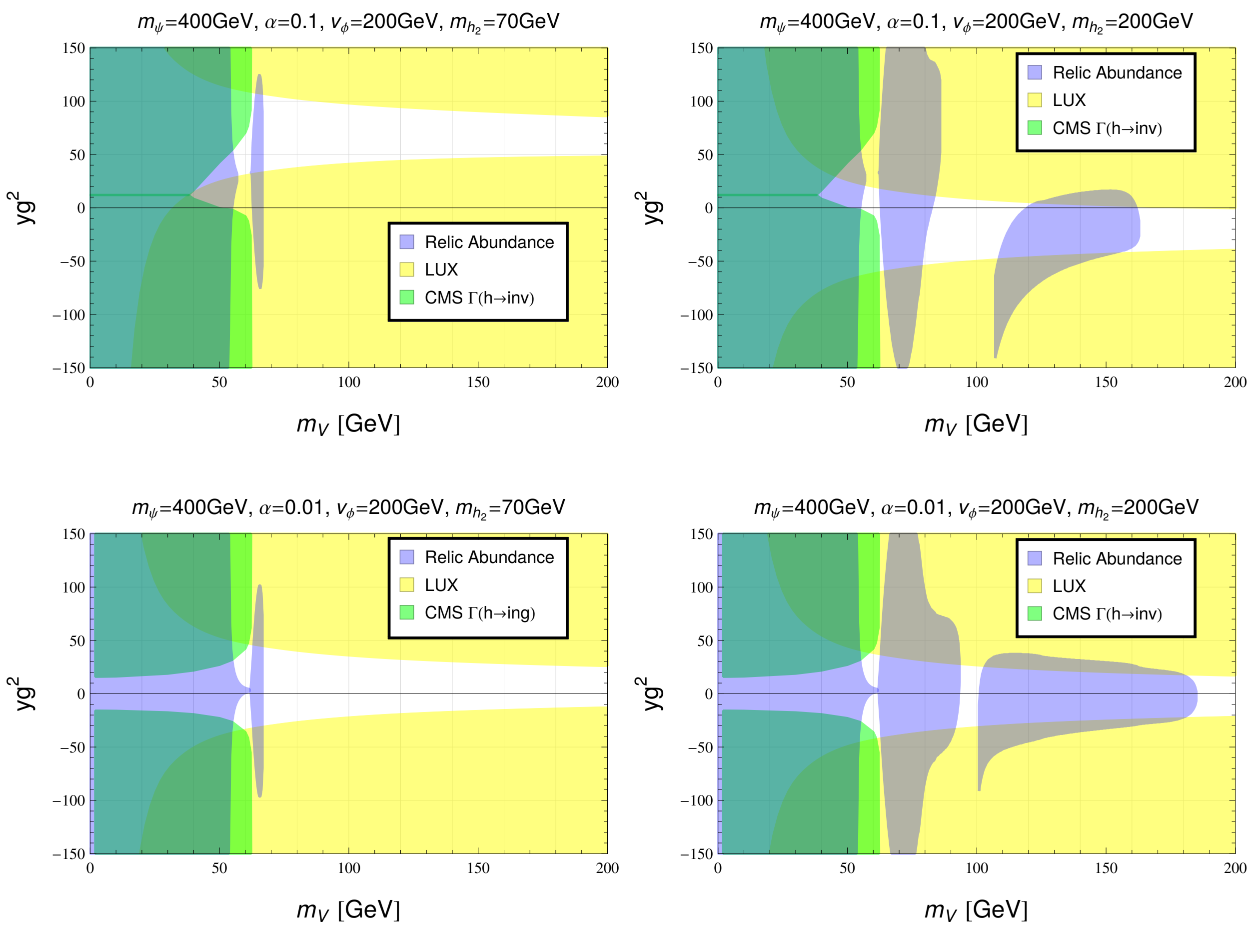

Figure 6.4: Exclusion regions on yg^2 for various parameters in the Higgs-Scalar mixing model. The left (right) two plots are for a scalar lighter (heavier) than the Higgs. The top (bottom) two plots are for a mixing angle of $\alpha = 0.1(0.01)$.

interference between loop- and tree-level contributions to the h-V-V vertex and/or between h and h_2 exchange [321]. Blue shading indicates regions where the dark matter is over-abundant in a standard cosmology. Unshaded regions are allowed by current data and do not over-close the Universe, with points close to the boundaries of the blue shading typically predicting a relic density close to the observed value. Such regions consistent with collider and direct searches are again typically in funnel regions for annihilation through h and h_2, when it is heavier than h itself. Additional parameter space also opens up for larger DM masses, where annihilation $VV \to h\ h_2$ becomes viable.

6.3.3 Full Matter Content

As our final limit, we return to $\lambda_P \ll 1$ but allow for all of the fermions to have comparable masses. We consider three benchmark sets of masses and Yukawa interactions summarized in Table 6.2, which contains the model parameters associated with the fermion sector, m, m_n, y_ψ, and y_χ, as well as the resulting spectrum of neutral state masses M_N and the coefficient of the h-$\bar{N}_i$-N_j coupling in the mass basis, Y_{ij}, with the mass eigenstates ordered as $M_{N_1} > M_{N_2} > M_{N_3}$. Table 6.3 and Eqn. 6.13, summarize the corresponding interaction of the gauge bosons with the new fermions. With these quantities fixed, we explore the plane of the U(1)$'$ gauge coupling g and the mass of the dark matter m_V.

The new electrically charged fermions may be pair produced or produced in association with a new neutral fermion at colliders. For the regime of interest, the charged fermions decay solely to one of the neutral fermions and a W boson. The charged states are sufficiently similar to charginos in the MSSM that chargino searches may be applied. LEP searches require the charged fermion to be heavier than 100 GeV [334–337]. LHC searches find similar bounds which strengthen as the charged state becomes very long lived [338,339]. The lightest charged state among our benchmarks is 300 GeV, which is safe from these constraints.

Table 6.2: Benchmark parameter sets, and resulting neutral fermion masses and Higgs couplings.

m	m_n	y_ψ	y_χ	M_N (GeV)	Y
800 GeV	250 GeV	1	-0.5	$\begin{bmatrix} 832 \\ 807 \\ 274 \end{bmatrix}$	$\begin{bmatrix} -0.25 & -0.04 & 0.71 \\ 0.04 & -0.06 & 0.26 \\ -0.71 & 0.26 & -0.19 \end{bmatrix}$
300 GeV	200 GeV	4	-2	$\begin{bmatrix} 848 \\ 810 \\ 238 \end{bmatrix}$	$\begin{bmatrix} -3.0 & -0.81 & -0.56 \\ 0.81 & -3.0 & -0.47 \\ 0.56 & -0.47 & -0.02 \end{bmatrix}$
500 GeV	1000 GeV	4	4	$\begin{bmatrix} 1770 \\ 500 \\ 265 \end{bmatrix}$	$\begin{bmatrix} -3.9 & 0 & 0.98 \\ 0 & 0 & 0 \\ -0.98 & 0 & -3.9 \end{bmatrix}$

Some couplings are taken to be quite large to help highlight the features of this model in observables. In choosing such large values for the gauge and yukawa couplings, one may be concerned that perturbativity breaks down or that higher order corrections should not be ignored. The latter case may even reduce the relic abundance when properly taken into account, which would open up available parameter space. Alternately, smaller couplings may be chosen which would reduce the range of viable dark matter masses. However, neither case appreciably alter our conclusions.

$$
\begin{aligned}
\mathcal{L}_{gauge} \;&= e\left(\bar{E}_1\gamma^\mu E_1 - \bar{E}_2\gamma^\mu E_2\right)\left(A_\mu + \tfrac{(1-2s_w^2)}{2c_w s_w} Z_\mu\right) \;+\; \tfrac{e}{2c_w s_w}\bar{N}_i\gamma^\mu\, G^Z_{ij}\, N_j\, Z_\mu \\
&+\tfrac{e}{\sqrt{2}s_w}\left[\left(\bar{E}_1\gamma^\mu\, G^{W1}_i\, N_i + \bar{N}_i\gamma^\mu\, G^{W2}_i\, E_2\right) W^+_\mu + h.c.\right] \\
&+g\left(\bar{E}_i\gamma^\mu E_i + \bar{N}_i\gamma^\mu N_i\right) V_\mu
\end{aligned} \tag{6.13}
$$

In Fig. 6.5, we show upper bounds on g as a function of the vector mass. We find that the collider and direct detection constraints are relatively weak, often less constraining than perturbativity. Despite the mass of the lightest neutral state being similar for all three

Table 6.3: Gauge couplings matrices defined in Eqn. 6.13 represented in fermion mass basis. With m and m_n in units of GeV.

m	m_n	y_ψ	y_χ	G^Z	G^{W1}	G^{W2}
800	250	1	−0.5	$\begin{bmatrix} 0.01\ \gamma^5 & -0.98 & -0.11 \\ -0.98 & 0.03\ \gamma^5 & -0.17\ \gamma^5 \\ -0.11 & -0.17\ \gamma^5 & -0.04\ \gamma^5 \end{bmatrix}$	$\begin{bmatrix} 0.70 \\ 0.70 - 0.01\ \gamma^5 \\ 0.08 + 0.12\ \gamma^5 \end{bmatrix}$	$\begin{bmatrix} 0.70 \\ -0.70 - 0.01\ \gamma^5 \\ -0.08 + 0.12\ \gamma^5 \end{bmatrix}$
300	200	4	−2	$\begin{bmatrix} 0.20\ \gamma^5 & -0.36 & 0.69 \\ -0.36 & 0.38\ \gamma^5 & -0.35\ \gamma^5 \\ 0.69 & -0.35\ \gamma^5 & -0.59\ \gamma^5 \end{bmatrix}$	$\begin{bmatrix} -0.56 + 0.09\ \gamma^5 \\ -0.26 + 0.36\ \gamma^5 \\ 0.65 + 0.23\ \gamma^5 \end{bmatrix}$	$\begin{bmatrix} -0.56 - 0.09\ \gamma^5 \\ 0.26 + 0.36\ \gamma^5 \\ -0.65 + 0.23\ \gamma^5 \end{bmatrix}$
500	1000	4	4	$\begin{bmatrix} 0 & -0.61 & 0 \\ -0.61 & 0 & 0.79\ \gamma^5 \\ 0 & 0.79\ \gamma^5 & 0 \end{bmatrix}$	$\begin{bmatrix} -0.43 \\ -0.71 \\ 0.56\ \gamma^5 \end{bmatrix}$	$\begin{bmatrix} 0.43 \\ -0.71 \\ -0.56\ \gamma^5 \end{bmatrix}$

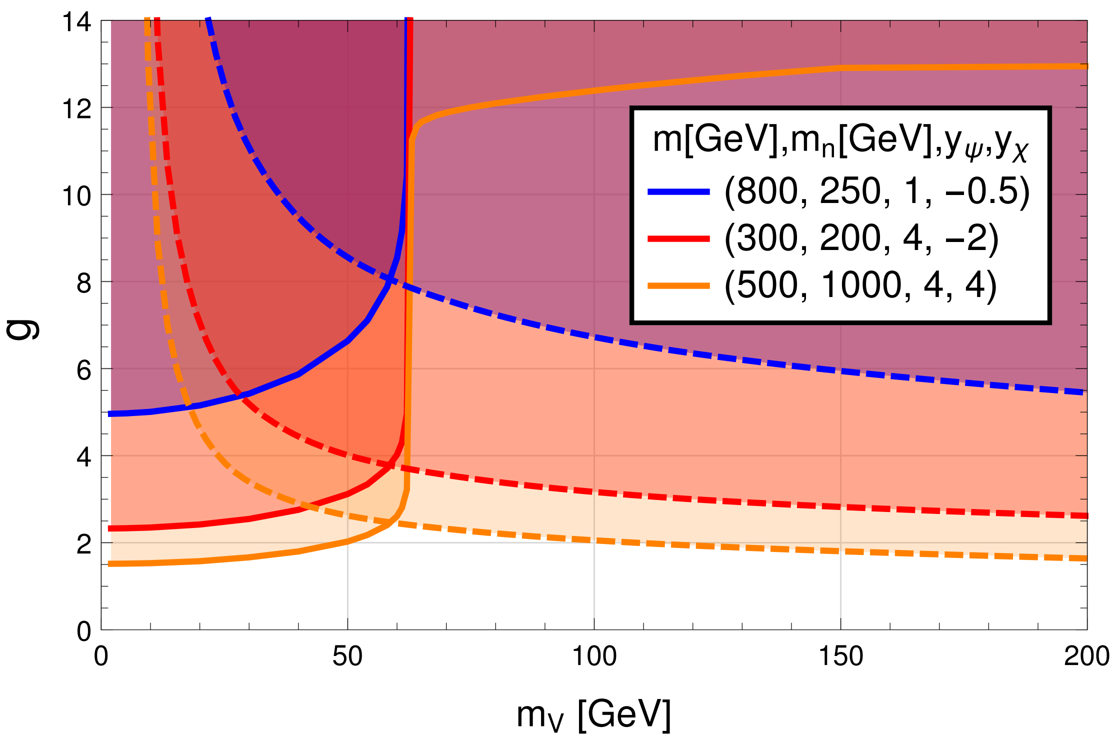

Figure 6.5: Upper bound on the gauge coupling, g, for the three benchmark parameters. VBF Higgs collider constraints are in solid and direct detection constraints are dashed lines. Note that for the direct detection constraints we assume the local abundance of DM is 0.3 GeV/cm^3 whereas the prediction from the model, for conventional thermal history, is often smaller, see Figure 6.6.

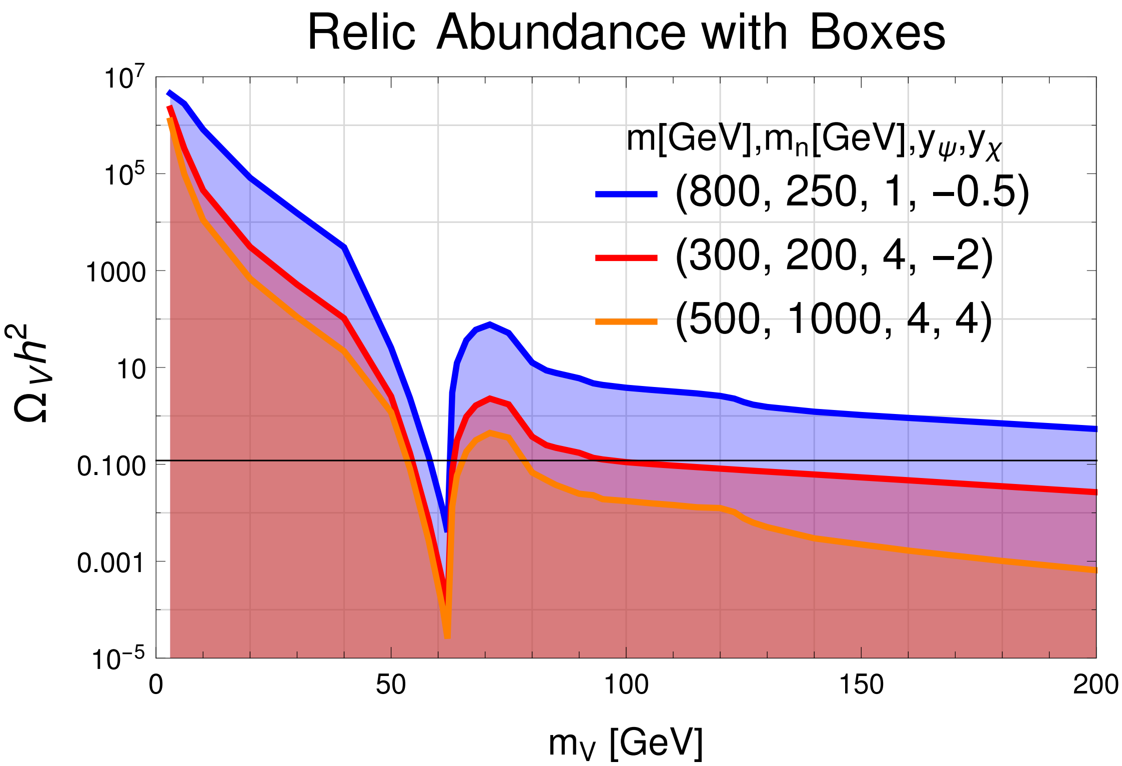

Figure 6.6: The vector relic abundance for the three benchmark parameters. The gauge coupling here is chosen to be $g = 3.5$.

benchmarks, constraints are significantly stronger for the second and third cases, where the Yukawa couplings are stronger. In terms of the dominant contribution to the effective h-V-V coupling, in the first and third models, the lightest neutral state is the dominant contribution, whereas in the second benchmark model the lightest state has a small Yukawa coupling and is less important than the second lightest state, which has a much larger coupling.

In Fig. 6.6, we plot the relic abundance for the benchmark parameters with a large, fixed gauge coupling of $g = 3.5$, to make comparisons between the benchmarks more apparent. Note that for our second and third benchmark models, this value is mildly excluded by limits on the invisible width of the Higgs for $m_V \leq 60$ GeV. All benchmarks can be thermal relics when the vector can resonantly annihilate through a Higgs, causing the sharp dip at $m_V \sim m_h/2$. We also find that the second benchmark can attain a thermal relic for vector masses above 100 GeV, and third may be a thermal relic above 80 GeV. The success at larger DM masses is due to annihilation channels with two bosons in the final state. Of the three benchmarks, the second has the lightest charged states. This allows efficient annihilation through loops involving the charged fermions, such as those which result in the WW and ZZ final states. The third benchmark, also benefits from this with slightly heavier charged states. However, this case also has large Yukawas causing a marked drop in the relic abundance when DM is heavy enough to annihilate to two Higgs bosons.

6.4 Conclusion

We have explored a simplified model in which the dark matter is a spin one vector particle which interacts with the Standard Model predominantly through Higgs exchange. Unlike the more usually considered Higgs portal based on the quartic interaction λ_P, we mediate the interaction radiatively, via a loop of heavy fermions charged under both the dark $\mathrm{U}(1)'$ as well as the SM electroweak interaction. By construction, the theory is anomaly free, has a heavy vector particle which is effectively stable, and leads to no large deviations in the properties of the SM Higgs. This last feature, together with the possibility to completely decouple the $\mathrm{U}(1)'$-breaking Higgs Φ from the SM are the primary features which distinguish the radiative model from the quartic-induced Higgs portal as far as dark matter phenomenology is concerned.

Of course, the UV structure of the radiative model is also far richer, with a family of electroweakly charged particles whose decays produce gauge bosons and missing momentum, a signature already under study in the context of the neutralinos and charginos of a supersymmetric theory. These states are the true avatars of the radiative Higgs portal. The thermal relic density suggests that their masses are at most around TeV, raising the hope that they could be found at the LHC run II or a future high energy collider.

Chapter 7

Searching for MeV-Scale Gauge Bosons with IceCube

Based on arXiv:1507.03015 [340]

7.1 Introduction

In addition to providing a new window into the origin of the cosmic ray spectrum, the observation of astrophysical neutrinos allows us to probe fundamental physics. More specifically, IceCube's recent detection of high-energy astrophysical neutrinos enables us to study and constrain a range of phenomena at higher energies and over longer baselines than can currently be tested in laboratory environments. The flavor ratios of high-energy astrophysical neutrinos can be used to constrain a variety of new phenomena, including neutrino decay and Lorentz violation [341–358]. Alternatively, a few PeV neutrino interacting with a nucleon at rest has a center-of-mass energy of a few TeV, enabling high energy neutrino telescopes to constrain a range of TeV-scale physics scenarios, including TeV-scale gravity models [359–363], and models featuring TeV-scale leptoquarks [364, 365]. These observations also make it possible to study interactions between high-energy neutrinos and the cosmic ray neutrino background (CνB). In particular, scenarios featuring a light gauge boson have received some recent attention within this context [366–374].

A new gauge boson with couplings to Standard Model neutrinos will induce a scattering resonance with the CνB at an energy given by:

$$E_\nu^{\rm res} \approx \frac{m_{Z'}^2}{2m_\nu} \approx 1\,\mathrm{PeV} \times \left(\frac{m_{Z'}}{10\,\mathrm{MeV}}\right)^2 \left(\frac{0.05\,\mathrm{eV}}{m_\nu}\right). \tag{7.1}$$

For even very small couplings, such a resonance can lead to the efficient absorption of high-energy neutrinos over cosmological distances.

In this chapter, we revisit the possibility of using IceCube (or future high-energy neutrino telescopes) to search for the effects of an MeV-scale gauge boson on the high-energy cosmic neutrino spectrum. In doing so, we consider the impact on both the shape of the neutrino spectrum, as well as on the ratio of flavors that reach the Earth. In the window of parameter space that is capable of explaining the measured value of the muon's anomalous magnetic moment, significant effects can result from such a Z'.

In the following two sections, we review IceCube's discovery of high-energy astrophysical neutrinos, and summarize the motivations for a model with an MeV-scale Z' with couplings to Standard Model neutrinos. In Sec. 7.4, we describe the interactions mediated by such a Z' between high-energy neutrinos and the cosmic neutrino background. The impact of such interactions on the spectrum and the flavor ratios of the high-energy astrophysical neutrino flux is discussed in Sec. 7.5. In Sec. 7.6, we summarize our results and conclusions.

7.2 IceCube's Observation of High-Energy Astrophysical Neutrinos

Recently, the IceCube Collaboration has reported the observation of a diffuse flux of high-energy extraterrestrial neutrinos, consisting of 37 neutrino candidate events with energies ranging from 30 TeV to 2 PeV [375–377]. Although the origin of these neutrinos is currently unknown, they appear to be approximately isotropically distributed across the sky [377], suggesting an extragalactic origin (see, however, Refs. [378–384]). The spectrum of these particles is well fit by a power-law with an index of $\gamma = -2.6$ [385].

Several features of this neutrino population are suggestive of a connection with the cosmic ray spectrum. In particular, the generation of the observed neutrino flux requires that $\sim$20% of the PeV-EeV protons accelerated by cosmic ray sources undergo photo-meson interactions; a fraction that could easily be accommodated in realistic astrophysical environments [386]. Stated another way, the observed neutrino flux is below, but not very far below, what is known as the "Waxman-Bahcall bound" [387, 388]. Furthermore, the numbers of showers and muon track events observed at IceCube is consistent with a flavor ratio of $\nu_e : \nu_\mu : \nu_\tau = 1 : 1 : 1$ (although with large error bars) [385,389], consistent with that predicted from photo-meson interactions after accounting for oscillations. Several plausible classes of sources have been proposed for these neutrinos, including active galactic nuclei [386, 390, 390–393], starburst or star-forming galaxies [394–397], and low-luminosity gamma-ray bursts [386,398–400]. In addition to these more conventional astrophysical source classes, exotic origins for IceCube's neutrinos have also been considered, such as the decays or annihilations of long-lived superheavy particles [401–410]. In this chapter, we remain agnostic as to the specific origin of these neutrinos, assuming only that they originate from extragalactic sources.

7.3 A Light Z' with Couplings to Neutrinos

New gauge bosons appear within many new physics scenarios [100]. For example, additional broken Abelian $U(1)$ gauge symmetries and the Z' bosons that accompany them are predicted by many Grand Unified Theories (GUTs), including those based on the groups $SO(10)$ and E_6 [411, 412]. New massive gauge bosons also appear within the context of many string inspired models [413–421], little Higgs theories [422–425], dynamical symmetry breaking scenarios [426–428], models with extra spatial dimensions [429–432], and many other proposed extensions of the Standard Model [433–435].

In this chapter, we are primarily interested in light gauge bosons ($m_{Z'} < 1$ GeV) with nonzero couplings to Standard Model neutrinos. Constraints on such a particle's couplings to electron neutrinos are quite stringent, however, motivating us to focus on models in which the Z' couples only to 2nd and/or 3rd generation leptons.

If the couplings of a Z' are assigned arbitrarily, anomalies are generally introduced, violating the principle of gauge invariance. To construct a self-consistent theory, care must be taken to ensure that all such anomalies cancel. A well-known example of an anomaly-free Z' is that arising from the gauge group $U(1)_{\mu-\tau}$. This is the only anomaly-free $U(1)$ group with nonzero charge assignments to Standard Model neutrinos that can lead to an experimentally viable MeV-scale Z' without requiring the addition of any exotic fermions. A $U(1)$ group charged under only muon or tau number is also a possibility, although new chiral fermions must be introduced in these cases, charged under both $SU(2)_W$ and $U(1)_Y$, as well as under the new $U(1)_\mu$ or $U(1)_\tau$ group.

A light Z' with couplings to the muon can be motivated by the measurement of the muon's anomalous magnetic moment, which currently differs from the value predicted by the Standard Model with a significance of approximately 3.6σ [97]. With efforts currently underway to improve this measurement [436, 437] and to reduce the related theoretical uncertainties [438–443], it should become clear within the next several years whether or not this is an authentic sign of new physics. Among other possibilities (see, for example, Refs. [444–449]), an MeV-scale Z' with small couplings to the muon could plausibly account for this measurement.

A Z' with a vector coupling to muons, g_μ, leads to the following contribution to the muon's magnetic moment [450, 451]:

$$\Delta a_\mu = \frac{g_\mu^2 m_\mu^2}{4\pi^2 m_{Z'}^2} \int_0^1 dx \frac{x^2(1-x)}{1-x+(m_\mu^2/m_{Z'}^2)x^2}. \tag{7.2}$$

For $m_{Z'} \ll m_\mu$, the measured value can be accommodated for $g_\mu \sim (3-6)\times 10^{-4}$, whereas for $m_{Z'} \simeq 1$ GeV, couplings an order of magnitude larger are required. Although this parameter space is in conflict with measurements of muon pair production in muon neutrino-nucleus scattering for $m_{Z'} \gtrsim 500$ MeV [367, 452], lower values of $m_{Z'}$ remain viable (below 1 MeV, constraints from big bang nuclosynthesis and the cosmic microwave background can also be relevant [368, 453–455]).

As stated above, a Z' resulting from the $U(1)_\mu$ or $U(1)_\tau$ groups requires the introduction of new chiral fermions charged under $SU(2)_W$ and $U(1)_Y$ in order to cancel anomalies. Furthermore, the masses of these exotics are bounded by the requirement of perturbativity, which requires [234]:

$$m_{\text{exotic}} \lesssim 108\,\text{GeV} \times \left(\frac{m_{Z'}}{10\,\text{MeV}}\right)\left(\frac{0.0005}{g_{Z'}}\right)\left(\frac{1}{z_\varphi}\right), \tag{7.3}$$

where z_φ is the charge assignment for the scalar whose VEV breaks the $U(1)$ responsible for the Z'. From this, we learn that the required exotics must be rather light, and will be subject to constraints from accelerators.

7.4 High Energy Neutrino Interactions with the Cosmic Neutrino Background

In generality, a Z' boson will couple to Standard Model neutrinos through the following interaction:

$$\mathcal{L}_{Z'\nu} = g_{Z'} Q_{\alpha\beta} Z'_\mu \overline{\nu}_\alpha \gamma^\mu P_L \nu_\beta \tag{7.4}$$

$$= g_{Z'} Q'_{ij} Z'_\mu \overline{\nu}_i \gamma^\mu P_L \nu_j, \tag{7.5}$$

where neutrinos with Greek (Latin) indices refer to the flavor (mass) basis. The $U(1)'$ gauge coupling is $g_{Z'}$ and the charge assignments are contained in the matrix, $Q_{\alpha\beta}$. For example, the charge matrix for $U(1)_{\mu-\tau}$ is given by $Q_{\alpha\beta} = \mathrm{diag}(0, 1, -1)$. In the mass basis, the charge matrix is represented as $Q'_{ij} = U^\dagger_{\alpha i} Q_{\alpha\beta} U_{\beta j}$. Where $U_{\alpha i}$ is the Pontecorvo–Maki–Nakagawa–Sakata (PMNS) matrix which rotates from the mass to the flavor basis. Here we have assumed that the charged leptons do not mix, such that the neutrino mixing matrix is entirely determined by the PMNS matrix. While this is a convention in the Standard Model, deviating from this assumption does lead to observable effects in models with gauged lepton numbers [456].

This interaction results in $\nu_i - \nu_j$ scattering, with the following cross section:

$$\sigma(\nu_i \nu_j \to \nu\nu) = \sum_{k\ell} Q'^2_{k\ell} \frac{g^4_{Z'} Q'^2_{ij}}{3\pi} \frac{s}{(s - m^2_{Z'})^2 + m^2_{Z'} \Gamma^2_{Z'}}, \tag{7.6}$$

where the sum is over the final neutrino states, k and ℓ. For example, $\sum_{k\ell} Q'^2_{k\ell} = 2$ for the $U(1)_{\mu-\tau}$ case. The t-channel contribution to the cross section is ignored, as it is highly suppressed relative to the s-channel resonance. The width of the Z' into neutrinos is given by $\Gamma_{Z'} = \sum_{ij} Q'^2_{ij} g^2_{Z'} m_{Z'}/24\pi$. In the parameter space of interest to IceCube, the mass of the Z' is less than $2m_\mu$, allowing us to safely neglect decays to muons or taus.

To calculate the spectrum of neutrinos at Earth, we solve the following coupled set of integro-differential equations [368, 369, 457]:

$$\begin{aligned} -(1+z)\frac{H(z)}{c}\,\frac{d\widetilde{n}_i}{dz} &= J_i(E_0,z) - \widetilde{n}_i \sum_j \langle n_{\nu j}(z)\ \sigma_{ij}(E_0,z)\rangle \\ &+ P_i \int_{E_0}^{\infty} dE' \sum_{j,k} \widetilde{n}_k \left\langle n_{\nu j}(z)\ \frac{d\sigma_{kj}}{dE_0}(E',z)\right\rangle, \end{aligned} \tag{7.7}$$

where

$$\begin{aligned} \widetilde{n}_i &\equiv \frac{dN_i}{dE}(E_0,z), \\ P_i &\equiv \sum_\ell Br(Z' \to \nu_\ell \nu_i). \end{aligned}$$

Here, $H(z)$ is the Hubble parameter as a function of redshift, E_0 is the neutrino energy as measured at Earth, and $n_\nu(z)$ is the proper number density of neutrinos in the $C\nu B$. The first term on the right-hand side accounts for the source spectral and density evolution through cosmology. The second term accounts for neutrinos of state i, scattering off a thermal distribution of $C\nu B$ neutrinos of state j, thereby attenuating the neutrino flux. The last term accounts for the regeneration of the scattering products from the process described in the second term. Here a neutrino of state k, with energy E', scatters with the $C\nu B$ to produce two neutrinos, one of which is of state i with energy E_0. Since this process is s-channel, the differential cross section can be broken into the total cross section and a distribution function in the outgoing neutrino energy space:

$$\frac{d\sigma_{kj}}{dE_0}(E',z) = \sigma_{kj}(E',z) f(E',E_0), \tag{7.8}$$

where

$$f(E',E_0) = \frac{3}{E'}\left[\left(\frac{E_0}{E'}\right)^2 + \left(1-\frac{E_0}{E'}\right)^2\right]\Theta(E'-E_0).$$

Note that this differential cross section accounts for both outgoing neutrinos, such that $\int dE_0 f(E', E_0) = 2$. Expressing the differential cross section in this way simplifies the numerical implementation of Eqn. 7.7.

The thermal averaging in the second term of Eqn. 7.7, and analogously in the third term, is given by:

$$\begin{aligned} \langle n_{\nu j}(z)\sigma_{ij}\rangle &\equiv \int \frac{d^3\mathbf{p}}{(2\pi)^3} \frac{\sigma_{ij}(E_0, z, \mathbf{p})}{e^{|\mathbf{p}|/T_0(1+z)}+1} \\ &\xrightarrow{m_j \gg T} n_{\nu j}(z)\ \sigma_{ij}(E_0, z), \end{aligned} \tag{7.9}$$

where the momentum dependence of the scattering cross section can be accounted for by evaluating Eqn. 7.6 with $s = 2E_0(1+z)\big(\sqrt{m_j^2+p^2} - |p|\cos\theta\big)$. In the limit that the neutrinos are much heavier than the effective temperature, the usual form is recovered. We take the effective temperature of the $C\nu B$ at $z = 0$ to be $T_0 = 1.7 \times 10^{-4}$ eV.

While an absorption resonance is predicted for each neutrino mass eigenstate, very light neutrinos (with masses comparable to or less than the effective temperature the thermal distribution of the $C\nu B$) will lead to broad spectral features. In scenarios in which the lightest neutrino is nearly massless, the energy of the resonance is determined by the energy (and therefore the temperature) of the neutrino, rather than by its mass. One then expects scattering to be most relevant at $E_\nu \sim m_{Z'}^2/2T_0$. [1]

Throughout this chapter, we adopt values for the neutrino mass splittings and mixing angles as presented in Ref. [458], with the exception of the CP violating angle which we take to be δ=0 (which is well within 2σ of the central value). For the cosmological parameters H_0, Ω_m, and Ω_λ, and for the upper limit on the sum of the neutrino masses, we adopt the values presented by the Planck Collaboration [12].

[1] More precisely, one expects the cross section to peak at $E_\nu \sim m_{Z'}^2/2\langle p\rangle$, with $\langle p\rangle = \frac{7\pi^4 T}{180\zeta(3)} \approx 3.15\,T$.

7.5 The Impact of a Light Z' on the Spectrum and Flavor Ratios of the High-Energy Neutrino Flux

7.5.1 Main Results

In this section, we present the results of our calculations. As our primary model of interest, we consider a Z' associated with the gauge group $U(1)_{\mu-\tau}$. For each value of $m_{Z'}$, the coupling $g_{Z'}$ is chosen to match the measured value of the muon's magnetic moment, Δa_μ:

$$g_{Z'} \approx \begin{cases} 4 \times 10^{-4} & \text{for } m_{Z'} = 1 \text{ MeV} \\ 5 \times 10^{-4} & \text{for } m_{Z'} = 10 \text{ MeV} \\ 8 \times 10^{-4} & \text{for } m_{Z'} = 100 \text{ MeV}. \end{cases} \tag{7.10}$$

For simplicity, we first consider the case in which all of the neutrino sources are located at a redshift of $z = 1$, and which emit a spectra characterized by a power-law of index $\gamma = -2.6$:

$$J(E_\nu, z) = A\, E_\nu^\gamma\, \delta(z-1), \tag{7.11}$$

where the normalization, A, is chosen to fit the IceCube data. We adopt an initial flavor ratio of $\nu_e : \nu_\mu : \nu_\tau = 1 : 2 : 0$ (as predicted from pion decay), which rapidly evolves to approximately $1 : 1 : 1$ via oscillations.

In Fig. 7.1, we plot the neutrino spectrum at Earth, including the effects of a Z'. Results are shown for three choices of $m_{Z'}$, and for both normal and inverted hierarchies, as well as maximal and minimal values for the sum of the neutrino masses. For each hierarchy, we take $\sum m_\nu$=0.23 eV to be the maximal value allowed by cosmological constraints [12]. For the minimal sum of masses, we adopt 0.058 eV and 0.10 eV for the normal and inverted

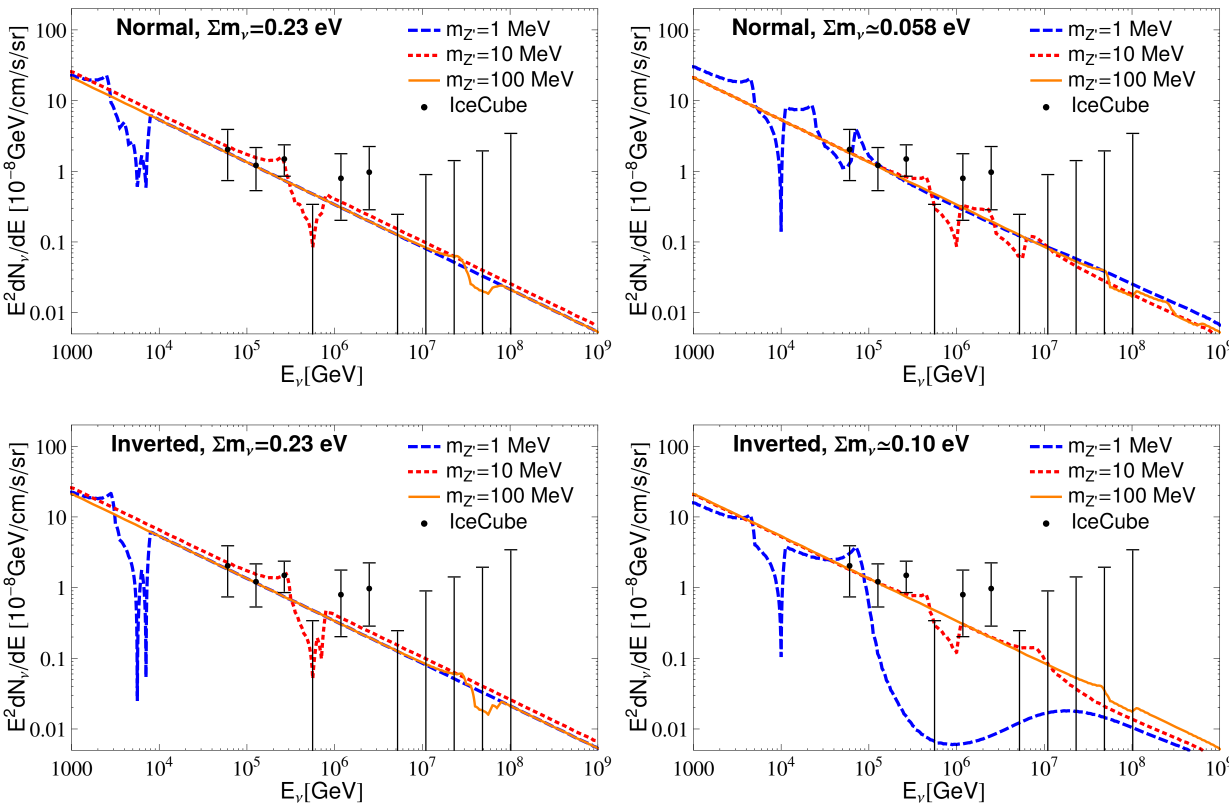

Figure 7.1: The spectrum of neutrinos at Earth, after including the effects of a Z' associated with the gauge group $U(1)_{\mu-\tau}$. The coupling of the Z' has been chosen in each case to accommodate the measured value of the muon's anomalous magnetic moment ($g_{Z'} = 4\times10^{-4}$, 5×10^{-4} and 8×10^{-4} for $m_{Z'} = 1$, 10 and 100 MeV, respectively). Here, we have assumed a population of sources at $z = 1$ which inject neutrinos with a power-law spectrum of index of -2.6, and with an initial flavor ratio of $\nu_e : \nu_\mu : \nu_\tau = 1 : 2 : 0$ (as predicted from pion decay). We show results for the normal and inverted hierarchies, and for maximal and minimal values of the sum of the neutrino masses.

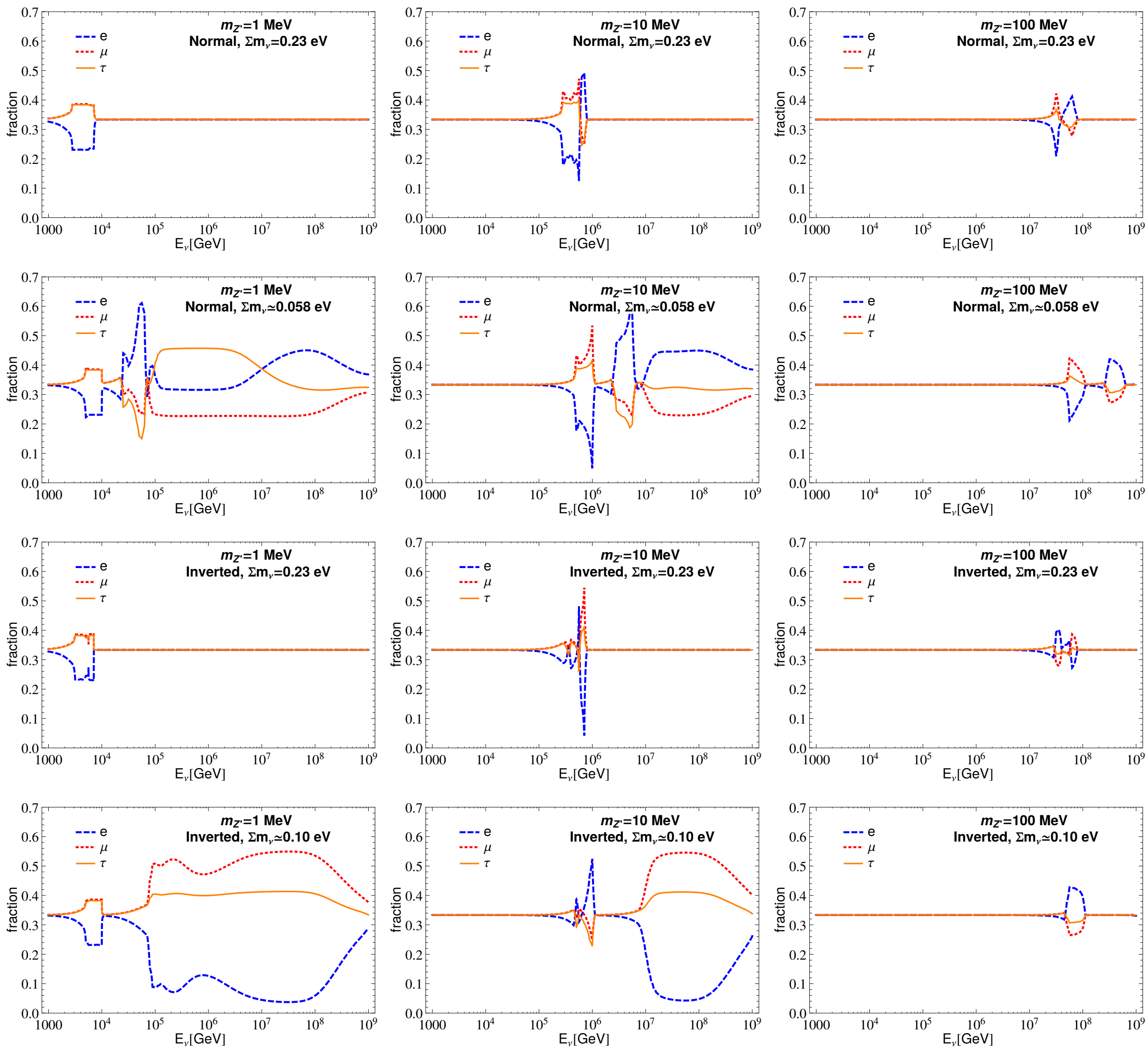

Figure 7.2: The fractions of neutrinos of each flavor at Earth, including the effects of a Z'. The models and other assumptions are the same as adopted in Fig. 7.1.

hierarchies, respectively.

In each case, the neutrino spectrum is altered by the interactions of the Z', although in ways that vary considerably depending on the mass of the Z' and on the hierarchy and the masses of the neutrinos. In the case of the normal hierarchy with $\sum m_\nu$=0.23 eV, for example, an absorption feature appears at $E_\nu \simeq 5\,\text{TeV} \times (m_{Z'}/\text{MeV})^2$. This feature results from the scattering with all three neutrino mass eigenstates, and the individual resonances cannot be easily distinguished. In the normal hierarchy with the minimal sum of masses, two features are visible: one at $E_\nu \simeq 10$ TeV $\times$ $(m_{Z'}/\text{MeV})^2$ from scattering with the heaviest mass eigenstate, and another at $E_\nu \simeq 50$ TeV $\times$ $(m_{Z'}/\text{MeV})^2$ resulting from the combination of the two lighter mass eigenstates.

The results are somewhat different in the case of the inverted hierarchy. As found for the normal hierarchy, an absorption feature appears at $E_\nu \simeq 5 - 10$ TeV $\times$ $(m_{Z'}/\text{MeV})^2$. In the case of $\sum m_\nu$=0.23 eV, this is the collective consequence of all three mass eigenstates. For $\sum m_\nu$=0.10 eV, however, this feature is induced only through scattering with the heaviest two eigenstates. In this case, the lightest neutrino leads instead to a very broad and potentially deep spectral feature, covering a range of energies between $E_\nu \sim$ 0.1–10 PeV $\times$ $(m_{Z'}/\text{MeV})^2$. This broad absorption feature is most clearly visible in the case of $m_{Z'} = 1$ MeV. In this case, the spectrum reported by the IceCube Collaboration (shown as error bars) is incompatible with a Z' lighter than a few MeV. Note that this feature does not appear in the case of the normal hierarchy because the lightest neutrino is largely of ν_e flavor, and thus does not couple to the Z' under consideration. In contrast, the lightest mass eigenstate in the inverted hierarchy is primarily composed of ν_μ and ν_τ.

In addition to the impact on the high-energy neutrino spectrum, a light Z' can alter the ratio of neutrino flavors that reach Earth. In Fig. 7.2, we plot these ratios for the same range of scenarios considered in Fig. 7.1. Similar to the spectrum, the most significant effects are seen in the case of the inverted hierarchy with a sum of neutrino masses near the minimal value.

In this case, the relative flux of electron (muon) neutrinos is suppressed (enhanced) over a wide range of energies, especially for the case of $m_{Z'} \lesssim 10$ MeV. Such an extreme departure from astrophysical expectations could plausibly be tested in the future by IceCube.

Constraints on the flavor ratios of IceCube's neutrinos have been placed by comparing the distribution of muon track events (generated in charged current interactions of ν_μ and $\bar{\nu}_\mu$) to the distribution of showers (generated most efficiently in charged current interactions of ν_e, $\bar{\nu}_e$, ν_τ and $\bar{\nu}_\tau$, as well as in neutral current interactions of all flavors). The results of this comparison have thus far been compatible with a ratio of $\nu_e : \nu_\mu : \nu_\tau = 1 : 1 : 1$, although with large error bars [385]. More specifically, extreme ratios of $\nu_e : \nu_\mu : \nu_\tau = 0 : 1 : 0$ and $\nu_e : \nu_\mu : \nu_\tau = 1 : 0 : 0$ have been excluded at the level of 3.3σ and 2.3σ significance, respectively.

Future flavor ratio measurements by IceCube are expected to be strengthened by improvements in veto techniques, and by searches for events unique to tau neutrinos.[2] Showers generated via the Glashow resonance (at $E_{\bar{\nu}_e} = m_W^2/2m_e \approx 6.3$ TeV) also provide an opportunity to constrain the electron antineutrino fraction at very high energies.

7.5.2 Alternative Gauge Groups

Thus far, we have restricted our calculations to the case of a Z' associated with the gauge group $U(1)_{\mu-\tau}$. As discussed in Sec. 7.3, however, one could also consider mediators arising from other gauge groups, such as $U(1)_\mu$ or $U(1)_\tau$. In Fig. 7.3 we compare the neutrino spectrum predicted for each of these three choices, for the case of the inverted hierarchy with $\sum m_\nu{\approx}0.10$ eV and $m_{Z'}{=}1$ MeV. From this comparison, we find that the $U(1)_{\mu-\tau}$ model results in a somewhat smaller degree of absorption at very high energies, despite the

[2] At energies above a few PeV, tau neutrinos and antineutrinos can generate a tau lepton that travels an observable distance before decaying; the mean distance traveled is $R_\tau = E_\tau c\tau_\tau/m_\tau \simeq 50\,\mathrm{m} \times E_\tau/(1\,\mathrm{PeV})$. As a result, very high-energy tau neutrinos can yield events with two showers (double bang events) [459,460], as well as events with one observed shower followed by or preceded by a tau-induced track (lollipop events) [342].

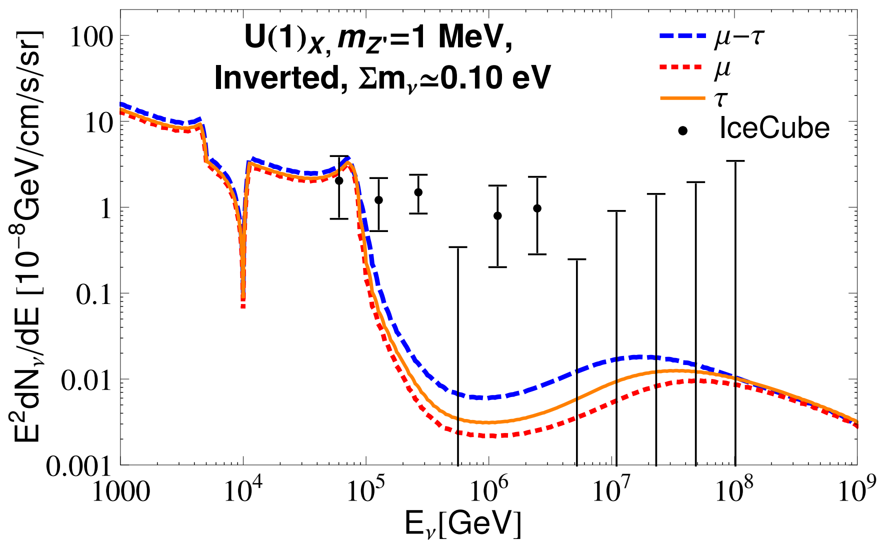

Figure 7.3: A comparison of the neutrino spectra predicted for a Z' associated with the $U(1)_{\mu-\tau}$ (blue), $U(1)_\mu$ (red), and $U(1)_\tau$ gauge groups. Results are shown for the case of an inverted hierarchy, $\sum m_\nu \approx 0.10$ eV, and $m_{Z'}$=1 MeV.

fact that more neutrino flavors participate in the scattering. This somewhat counterintuitive result is due to a cancellation between the μ and τ contributions to Q'_{33}. In Fig 7.4, we plot the flavor ratios in each of these scenarios. Here, the magnitude of the impact of the Z' is lessened relative to that predicted in the $U(1)_{\mu-\tau}$ case (see Fig. 7.2).

7.5.3 Source Distributions

Up to this point, our calculations have taken all of the neutrino sources to reside at a distance of $z = 1$. This distribution was adopted for simplicity, and reflects a plausible average for the distance traveled by a neutrino detected by IceCube. In this subsection, we consider more realistic redshift distributions for the sources of the high-energy neutrinos observed by IceCube.

The first possibility we consider is a distribution with a constant comoving number density

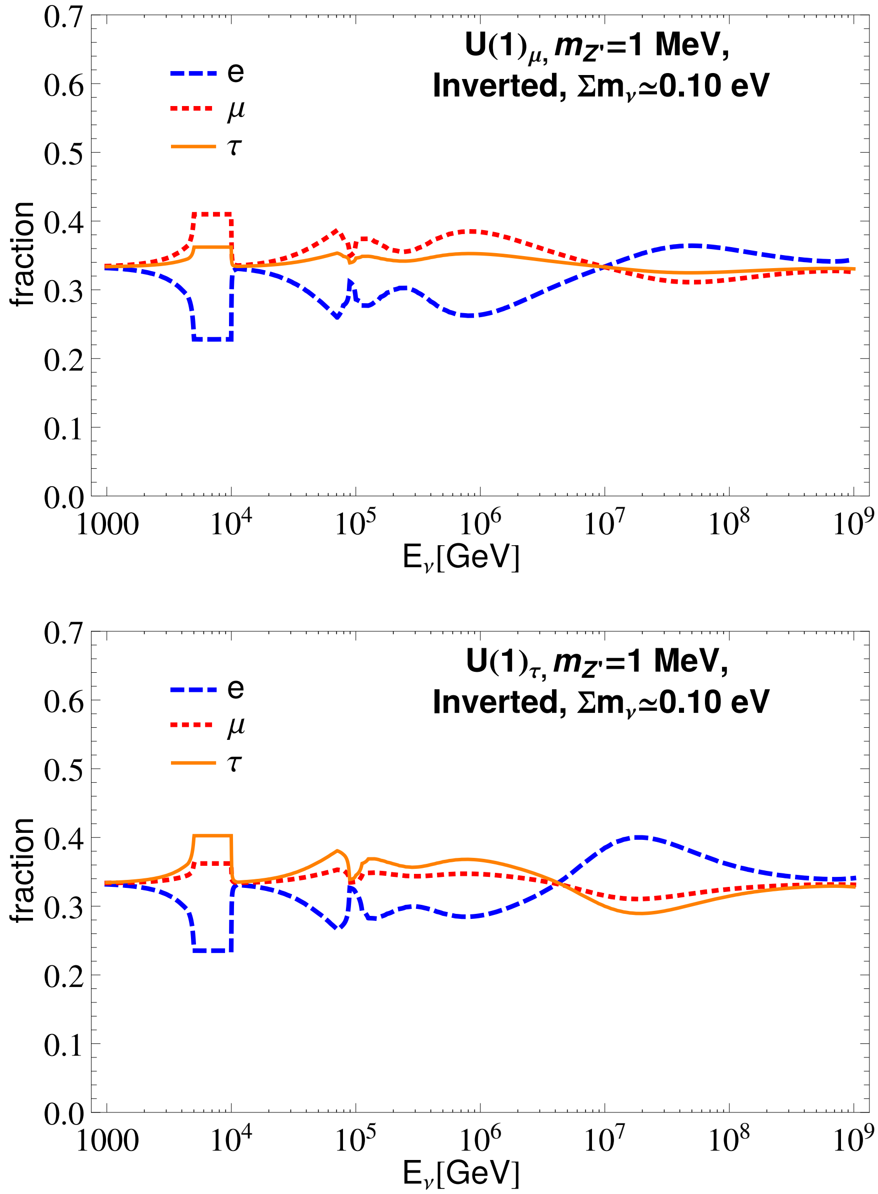

Figure 7.4: The fractions of neutrinos of each flavor predicted for a Z' associated with the $U(1)_\mu$ (upper frame) and $U(1)_\tau$ (lower frame) gauge groups. Results are shown for the case of an inverted hierarchy, $\sum m_\nu \approx 0.10$ eV, and $m_{Z'}$=1 MeV.

out to $z_{\max}$, beyond which no sources exist:

$$J_{\text{comoving}}(E_\nu, z) = A\, E_\nu^\gamma (1+z)^3\ \Theta(z_{\max} - z), \tag{7.12}$$

where again we take $\gamma = -2.6$. The second distribution that we consider follows the star formation rate [461]:

$$J_{SFR}(E_\nu, z) \ \ = A\, E_\nu^\gamma (1+z)^3 f_{SFR}(z), \tag{7.13}$$

where

$$f_{SFR}(z) \ \ \equiv \begin{cases} (1+z)^{3.4} & z \leq 1 \\ 2^{3.7}\,(1+z)^{-0.3} & 1 < z < 4 \\ 2^{3.7}\,5^{3.2}\,(1+z)^{-3.5} & z \geq 4. \end{cases} \tag{7.14}$$

For sources distributed according to the star formation rate, we consider redshifts up to $z = 7$, beyond which contributions to the final spectra are negligible. The neutrino spectra predicted from these distributions are compared in Fig. 7.5, as are their flavor ratios in Fig. 7.6. From these figures, we see that our results are qualitatively insensitive to the precise choice of redshift evolution.

7.6 Summary and Conclusions

IceCube's recent detection of high-energy astrophysical neutrinos provides us with an opportunity to study the interactions of these particles at higher energies and over longer baselines than are currently possible in laboratory environments. In this chapter, we have considered how light (∼1–100 MeV) gauge bosons, with couplings to Standard Model neutrinos, could

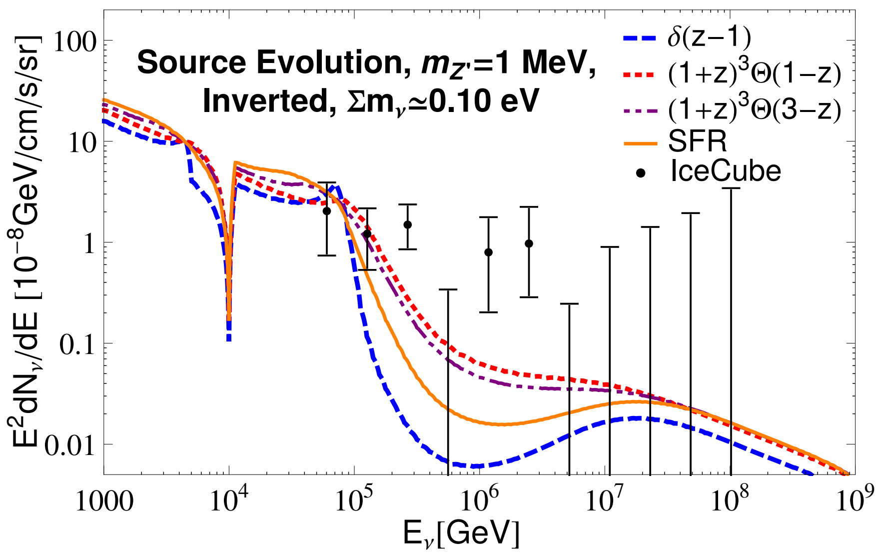

Figure 7.5: A comparison of the neutrino spectra predicted for four source distribution models: all sources at $z = 1$ (dashed blue), sources with a constant comoving number density out to $z_{\max} = 1$ (short dashed red), $z_{\max} = 3$ (dot-dashed purple), and a distribution of sources that follows the star formation rate (solid orange). Results are shown for the case of an inverted hierarchy, $\sum m_\nu \approx 0.10$ eV, and $m_{Z'}$=1 MeV.

impact the spectrum and flavors of the neutrinos observed by IceCube.

New gauge bosons are predicted within a variety of extensions of the Standard Model. Of particular interest is the Z' that arises from the anomaly-free $U(1)_{\mu-\tau}$ gauge group. For masses in the range of $m_{Z'} \sim 1 - 500$ MeV and a coupling of $g_{Z'} \sim 10^{-3}$, such a particle can explain the measured value of the muon's anomalous magnetic moment, without conflicting with constraints from accelerators or cosmology. For this range of masses and couplings, high-energy astrophysical neutrinos can scatter resonantly with the cosmic neutrino background, leading to absorption features in the spectrum observed at Earth. By measuring the spectrum and the flavor ratios of the extragalactic neutrino flux, IceCube can constrain or provide evidence for such models.

We found the most dramatic effects in models with a very light Z' ($m_{Z'} \lesssim 10$ MeV), which induces a significant absorption feature at $E_\nu \simeq 5 - 10$ TeV $\times (m_{Z'}/\text{MeV})^2$. Although not currently constrained, such a feature could plausibly be measured by IceCube or by next

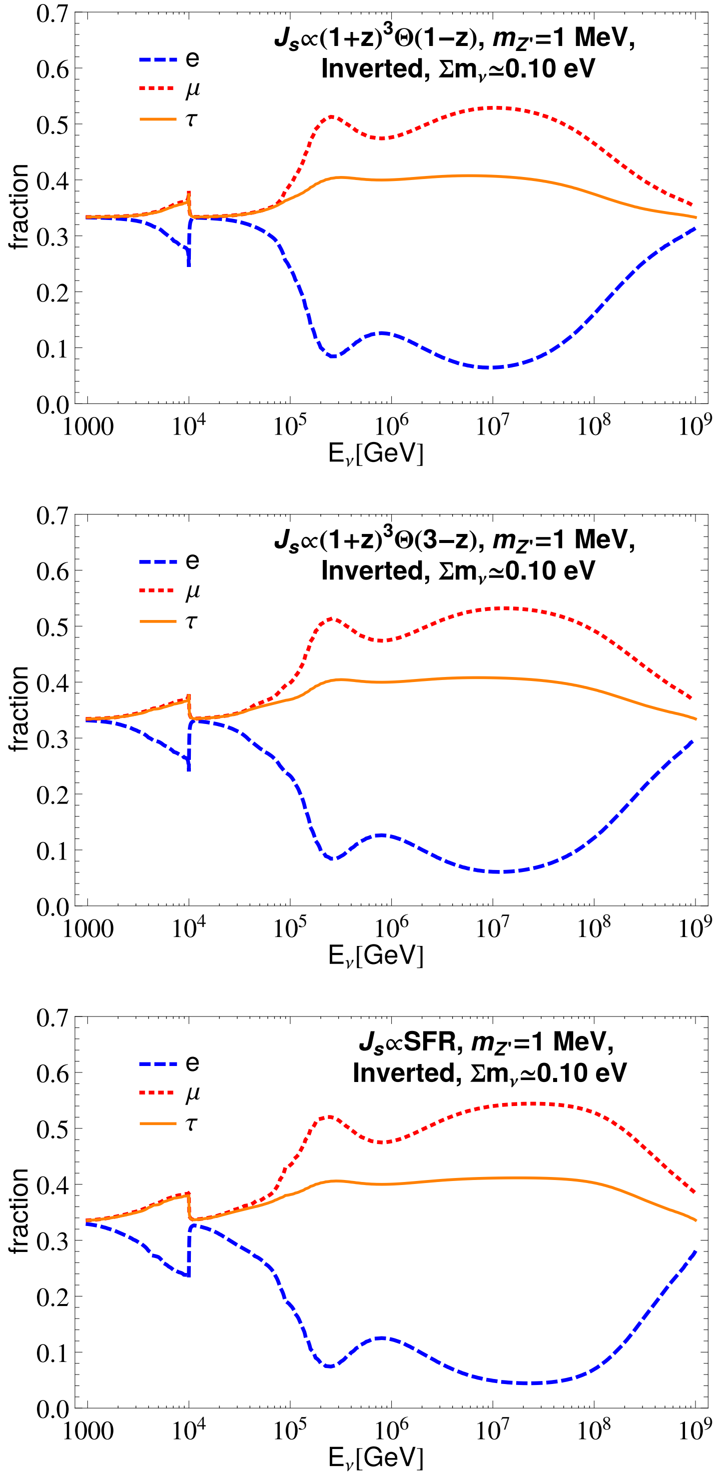

Figure 7.6: The fraction of neutrinos of each flavor predicted for three source distribution models: sources with a constant comoving number density out to $z_{\max} = 1$ (upper frame), $z_{\max} = 3$ (middle frame), and a distribution of sources that follows the star formation rate (lower frame). Results are shown for the case of an inverted hierarchy, $\sum m_\nu \approx 0.10$ eV, and $m_{Z'}$=1 MeV.

generation neutrino telescopes. Furthermore, in the case of the inverted hierarchy with the lightest neutrino lighter than $\sim 10^{-3}$ eV, such a Z' can lead to a very broad and deep spectral feature, covering a range of energies between ~ 0.1–10 PeV $\times (m_{Z'}/\text{MeV})^2$. Current IceCube data already excludes this case for a Z' lighter than a few MeV.

We also emphasize that a Z' can alter the ratios of the neutrino flavors that reach Earth, leading to a different distribution of muon tracks, showers, and tau-unique events at IceCube. Combining this information with measurements of the neutrino spectrum can significantly extend IceCube's sensitivity to Z' models and to other exotic physics scenarios.

IceCube's discovery has opened a new window into the interactions of neutrinos at high-energies and over very long baselines. As IceCube and other neutrino telescopes continue to refine their measurements of this population of extragalactic neutrinos, this data will become increasingly sensitive to physics beyond the reach of laboratory experiments. As we have shown, IceCube's current data already excludes a small range of the Z' models considered here. As more data is collected, the range of models within the reach of neutrino telescopes will increase, allowing us to explore a significant fraction of remaining allowed parameter space.

Chapter 8

Conclusion

Dark matter is one of the most compelling mysteries in physics today. Despite the collaborative effort of particle physicists, astrophysicists, and cosmologists for over 80 years, a discovery is still lacking. There is still great hope as the community refines possibilities and generates new search strategies.

This work has attempted to motivate a place for Simplified Models in the phenomenologist's toolbox. In particular, the usefulness and applications of Simplified model in the context of dark matter model building has been explored.

The possibility that dark matter interacts with quarks and new colored scalar is proposed in Ch.2. The three possibilities for this scalar are tested using LHC dijet searches, direct detection constraints, and the dark matter's viability as a thermal relic.

Models where dark matter can be produced at colliders in association with a Higgs boson is explored in Ch.3. A series of Simplified and Effective models are used to examine current and future sensitivity to such searches. While mono-jet searches tend to be more constraining, this avenue will help to scrutinize future dark matter signals in a complementary fashion.

When analyzing the Galactic Center GeV Excess, a single topology for dark matter annihilation is used. In Ch.4, alternate annihilation topologies are motivated in the context of light SM–dark matter mediators. The effect these plausible annihilation channels have on the fit and interpretation of the spectra is analyzed. The excess is reinterpreted with these plausible annihilation channels, ultimately changing the expected dark matter mass and annihilation cross-section. Such a model easily accommodates direct detection and collider limits without impacting the fit to this excess.

The 3.55 keV line is another exciting astrophysical excess which is considered in Ch.5. Dark matter can up-scatter to a nearly degenerate field which subsequently decays radiatively to produce the 3.55 keV line. It can further annihilate through different mediators to simultaneously generate the Galactic Center Excess. The proposed model further resolves conflicting measurements of the 3.55 keV line from different astrophysical bodies based on their individual velocity dispersions.

A UV complete model of spin-1 dark matter whose primary SM interactions are through the Higgs is detailed in Ch.6. This model allows the dark matter to be stable, is free of gauge anomalies, and prevents contributions to SM Higgs decay channels. This model also requires a rich phenomenology with new fermionic degrees of freedom. While they are assumed to be heavy in this analysis, they may be detectable at colliders.

Outside of dark matter another exciting source of new physics lies in the neutrino sector. In Ch.7, a search for neutrino–neutrino interactions using IceCube is proposed. A mediator of mass $1 - 500$ MeV could generate resonant scattering of high energy astrophysical neutrinos with the Cosmic Neutrino Background and may be visible at IceCube. Further, if cast in terms of $U(1)_{\mu-\tau}$ gauge boson, IceCube can probe parts of parameter space not yet available to other lab experiments and simultaneously explain the muon's anomalous magnetic moment.

These works have relied heavily on complementarity by maintaining predictiveness across many different experiments. This increases the value of our experiments by allowing us to make deeper statements about classes of models, even without a discovery. Run-II of the LHC is underway, soon to give us unprecedented energy scales to study. Direct Detection experiments are further improving their bounds. Data from Fermi-LAT and DES are paving the way to understanding the Galactic Center, dwarfs, and clusters. As we better understand these objects, discrepancies and prospective DM signals will become clearer. DM N-body simulations are becoming better understood with increasing agreement within the community. This will help us discern how different galaxies attain different DM halos and further elucidate DM properties at smaller scales. As these each of these fronts improve, model building will become increasingly important as evading bounds becomes more difficult forcing us to form a clearer picture of dark matter.

Bibliography

[1] K. N. Abazajian, N. Canac, S. Horiuchi, and M. Kaplinghat, "Astrophysical and Dark Matter Interpretations of Extended Gamma Ray Emission from the Galactic Center," `arXiv:1402.4090 [astro-ph.HE]`.

[2] **Fermi-LAT Collaboration** Collaboration, B. Anderson *Talk given at the 2014 Fermi Symposium, Nagoya, Japan, October 20-24* (2014) .

[3] **LUX Collaboration** Collaboration, D. Akerib *et al.*, "First results from the LUX dark matter experiment at the Sanford Underground Research Facility," `arXiv:1310.8214 [astro-ph.CO]`.

[4] J. Goodman, M. Ibe, A. Rajaraman, W. Shepherd, T. M. P. Tait, and H.-B. Yu, "Constraints on Dark Matter from Colliders," *Phys. Rev.* **D82** (2010) 116010, `arXiv:1008.1783 [hep-ph]`.

[5] A. Alves, S. Profumo, F. S. Queiroz, and W. Shepherd, "The Effective Hooperon," `arXiv:1403.5027 [hep-ph]`.

[6] J. Kumar and D. Marfatia, "Matrix Element Analyses of Dark Matter Scattering and Annihilation," *Phys.Rev.* **D88** (2013) 014035, `arXiv:1305.1611 [hep-ph]`.

[7] F. Zwicky, "Spectral displacement of extra galactic nebulae," *Helv. Phys. Acta* **6** (1933) 110–127.

[8] V. C. Rubin and W. K. Ford, Jr., "Rotation of the Andromeda Nebula from a Spectroscopic Survey of Emission Regions," *Astrophys. J.* **159** (1970) 379–403.

[9] H. Hoekstra, H. Yee, and M. Gladders, "Current status of weak gravitational lensing," *New Astron. Rev.* **46** (2002) 767–781, `arXiv:astro-ph/0205205 [astro-ph]`.

[10] D. Clowe, M. Bradac, A. H. Gonzalez, M. Markevitch, S. W. Randall, C. Jones, and D. Zaritsky, "A direct empirical proof of the existence of dark matter," *Astrophys. J.* **648** (2006) L109–L113, `arXiv:astro-ph/0608407 [astro-ph]`.

[11] E. L. Wright *et al.*, "Preliminary spectral observations of the Galaxy with a 7 deg beam by the Cosmic Background Explorer (COBE)," *Astrophys. J.* **381** (1991) 200–209.

[12] **Planck** Collaboration, P. Ade *et al.*, "Planck 2015 results. XIII. Cosmological parameters," arXiv:1502.01589 [astro-ph.CO].

[13] L. J. Hall, K. Jedamzik, J. March-Russell, and S. M. West, "Freeze-In Production of Fimp Dark Matter," *JHEP* **1003** (2010) 080, arXiv:0911.1120 [hep-ph].

[14] S. P. Martin, "A Supersymmetry primer," arXiv:hep-ph/9709356 [hep-ph]. [Adv. Ser. Direct. High Energy Phys.18,1(1998)].

[15] C. Csáki and P. Tanedo, "Beyond the Standard Model," in *Proceedings, 2013 European School of High-Energy Physics (ESHEP 2013): Paradfurdo, Hungary, June 5-18, 2013*, pp. 169–268. 2015. arXiv:1602.04228 [hep-ph]. https://inspirehep.net/record/1422131/files/arXiv:1602.04228.pdf.

[16] A. DiFranzo, K. I. Nagao, A. Rajaraman, and T. M. P. Tait, "Simplified Models for Dark Matter Interacting with Quarks," *JHEP* **1311** (2013) 014, arXiv:1308.2679 [hep-ph].

[17] **Snowmass 2013 Cosmic Frontier Working Groups 1-4** Collaboration, D. Bauer *et al.*, "Dark Matter in the Coming Decade: Complementary Paths to Discovery and Beyond," vol. 7-8, pp. 16–23. 2015. arXiv:1305.1605 [hep-ph]. http://lss.fnal.gov/archive/2013/conf/fermilab-conf-13-166-a-ae.pdf.

[18] M. Cahill-Rowley, R. Cotta, A. Drlica-Wagner, S. Funk, J. Hewett, A. Ismail, T. Rizzo, and M. Wood, "Complementarity and Searches for Dark Matter in the pMSSM," in *Community Summer Study 2013: Snowmass on the Mississippi (CSS2013) Minneapolis, MN, USA, July 29-August 6, 2013*. 2013. arXiv:1305.6921 [hep-ph]. http://inspirehep.net/record/1236121/files/arXiv:1305.6921.pdf.

[19] **LHC New Physics Working Group** Collaboration, D. Alves, "Simplified Models for LHC New Physics Searches," *J. Phys.* **G39** (2012) 105005, arXiv:1105.2838 [hep-ph].

[20] M. Beltran, D. Hooper, E. W. Kolb, Z. A. C. Krusberg, and T. M. P. Tait, "Maverick dark matter at colliders," *JHEP* **09** (2010) 037, arXiv:1002.4137 [hep-ph].

[21] Q.-H. Cao, C.-R. Chen, C. S. Li, and H. Zhang, "Effective Dark Matter Model: Relic density, CDMS II, Fermi LAT and LHC," *JHEP* **08** (2011) 018, arXiv:0912.4511 [hep-ph].

[22] J. Goodman, M. Ibe, A. Rajaraman, W. Shepherd, T. M. P. Tait, and H.-B. Yu, "Constraints on Light Majorana dark Matter from Colliders," *Phys. Lett.* **B695** (2011) 185–188, arXiv:1005.1286 [hep-ph].

[23] Y. Bai, P. J. Fox, and R. Harnik, "The Tevatron at the Frontier of Dark Matter Direct Detection," *JHEP* **12** (2010) 048, arXiv:1005.3797 [hep-ph].

[24] P. J. Fox, R. Harnik, J. Kopp, and Y. Tsai, "LEP Shines Light on Dark Matter," *Phys. Rev.* **D84** (2011) 014028, arXiv:1103.0240 [hep-ph].

[25] A. Rajaraman, W. Shepherd, T. M. P. Tait, and A. M. Wijangco, "LHC Bounds on Interactions of Dark Matter," *Phys. Rev.* **D84** (2011) 095013, arXiv:1108.1196 [hep-ph].

[26] P. J. Fox, R. Harnik, J. Kopp, and Y. Tsai, "Missing Energy Signatures of Dark Matter at the LHC," *Phys. Rev.* **D85** (2012) 056011, arXiv:1109.4398 [hep-ph].

[27] P. J. Fox, R. Harnik, R. Primulando, and C.-T. Yu, "Taking a Razor to Dark Matter Parameter Space at the LHC," *Phys. Rev.* **D86** (2012) 015010, arXiv:1203.1662 [hep-ph].

[28] J.-F. Fortin and T. M. P. Tait, "Collider Constraints on Dipole-Interacting Dark Matter," *Phys. Rev.* **D85** (2012) 063506, arXiv:1103.3289 [hep-ph].

[29] Y. Bai and T. M. P. Tait, "Searches with Mono-Leptons," *Phys. Lett.* **B723** (2013) 384–387, arXiv:1208.4361 [hep-ph].

[30] R. Ding and Y. Liao, "Spin 3/2 Particle as a Dark Matter Candidate: an Effective Field Theory Approach," *JHEP* **04** (2012) 054, arXiv:1201.0506 [hep-ph].

[31] R. C. Cotta, J. L. Hewett, M. P. Le, and T. G. Rizzo, "Bounds on Dark Matter Interactions with Electroweak Gauge Bosons," *Phys. Rev.* **D88** (2013) 116009, arXiv:1210.0525 [hep-ph].

[32] H. Dreiner, D. Schmeier, and J. Tattersall, "Contact Interactions Probe Effective Dark Matter Models at the LHC," *Europhys. Lett.* **102** (2013) 51001, arXiv:1303.3348 [hep-ph].

[33] L. M. Carpenter, A. Nelson, C. Shimmin, T. M. P. Tait, and D. Whiteson, "Collider searches for dark matter in events with a Z boson and missing energy," *Phys. Rev.* **D87** (2013) no. 7, 074005, arXiv:1212.3352 [hep-ex].

[34] Z.-H. Yu, Q.-S. Yan, and P.-F. Yin, "Detecting interactions between dark matter and photons at high energy e^+e^- colliders," *Phys. Rev.* **D88** (2013) no. 7, 075015, arXiv:1307.5740 [hep-ph].

[35] M. Beltran, D. Hooper, E. W. Kolb, and Z. C. Krusberg, "Deducing the Nature of Dark Matter from Direct and Indirect Detection Experiments in the Absence of Collider Signatures of New Physics," *Phys.Rev.* **D80** (2009) 043509, arXiv:0808.3384 [hep-ph].

[36] A. Kurylov and M. Kamionkowski, "Generalized Analysis of Weakly Interacting Massive Particle Searches," *Phys.Rev.* **D69** (2004) 063503, arXiv:hep-ph/0307185 [hep-ph].

[37] K. Cheung, P.-Y. Tseng, Y.-L. S. Tsai, and T.-C. Yuan, "Global Constraints on Effective Dark Matter Interactions: Relic Density, Direct Detection, Indirect Detection, and Collider," *JCAP* **1205** (2012) 001, arXiv:1201.3402 [hep-ph].

[38] J. Goodman, M. Ibe, A. Rajaraman, W. Shepherd, T. M. Tait, *et al.*, "Gamma Ray Line Constraints on Effective Theories of Dark Matter," *Nucl.Phys.* **B844** (2011) 55–68, arXiv:1009.0008 [hep-ph].

[39] K. Cheung, P.-Y. Tseng, and T.-C. Yuan, "Cosmic Antiproton Constraints on Effective Interactions of the Dark Matter," *JCAP* **1101** (2011) 004, arXiv:1011.2310 [hep-ph].

[40] K. Cheung, P.-Y. Tseng, and T.-C. Yuan, "Gamma-Ray Constraints on Effective Interactions of the Dark Matter," *JCAP* **1106** (2011) 023, arXiv:1104.5329 [hep-ph].

[41] A. Rajaraman, T. M. Tait, and D. Whiteson, "Two Lines Or Not Two Lines? That is the Question of Gamma Ray Spectra," *JCAP* **1209** (2012) 003, arXiv:1205.4723 [hep-ph].

[42] A. Rajaraman, T. M. Tait, and A. M. Wijangco, "Effective Theories of Gamma-Ray Lines from Dark Matter Annihilation," *Phys.Dark Univ.* **2** (2013) 17–21, arXiv:1211.7061 [hep-ph].

[43] A. De Simone, A. Monin, A. Thamm, and A. Urbano, "On the Effective Operators for Dark Matter Annihilations," *JCAP* **1302** (2013) 039, arXiv:1301.1486 [hep-ph].

[44] J.-M. Zheng, Z.-H. Yu, J.-W. Shao, X.-J. Bi, Z. Li, *et al.*, "Constraining the Interaction Strength Between Dark Matter and Visible Matter: I. Fermionic Dark Matter," *Nucl.Phys.* **B854** (2012) 350–374, arXiv:1012.2022 [hep-ph].

[45] B. Bellazzini, M. Cliche, and P. Tanedo, "The Effective Theory of Self-Interacting Dark Matter," *Phys.Rev.* **D88** (2013) 083506, arXiv:1307.1129.

[46] I. M. Shoemaker, "Constraints on Dark Matter Protohalos in Effective Theories and Neutrinophilic Dark Matter," *Phys.Dark Univ.* **2** (2013) no. 3, 157–162, arXiv:1305.1936 [hep-ph].

[47] P. Gondolo, J. Hisano, and K. Kadota, "The Effect of Quark Interactions on Dark Matter Kinetic Decoupling and the Mass of the Smallest Dark Halos," *Phys.Rev.* **D86** (2012) 083523, arXiv:1205.1914 [hep-ph].

[48] J. M. Cornell, S. Profumo, and W. Shepherd, "Kinetic Decoupling and Small-Scale Structure in Effective Theories of Dark Matter," *Phys.Rev.* **D88** (2013) 015027, arXiv:1305.4676 [hep-ph].

[49] J. Goodman and W. Shepherd, "LHC Bounds on UV-Complete Models of Dark Matter," arXiv:1111.2359 [hep-ph].

[50] M. T. Frandsen, F. Kahlhoefer, S. Sarkar, and K. Schmidt-Hoberg, "Direct Detection of Dark Matter in Models with a Light Z'," *JHEP* **1109** (2011) 128, arXiv:1107.2118 [hep-ph].

[51] I. M. Shoemaker and L. Vecchi, "Unitarity and Monojet Bounds on Models for Dama, Cogent, and Cresst-Ii," *Phys.Rev.* **D86** (2012) 015023, arXiv:1112.5457 [hep-ph].

[52] H. An, X. Ji, and L.-T. Wang, "Light Dark Matter and Z' Dark Force at Colliders," *JHEP* **1207** (2012) 182, arXiv:1202.2894 [hep-ph].

[53] M. T. Frandsen, F. Kahlhoefer, A. Preston, S. Sarkar, and K. Schmidt-Hoberg, "Lhc and Tevatron Bounds on the Dark Matter Direct Detection Cross-Section for Vector Mediators," *JHEP* **1207** (2012) 123, arXiv:1204.3839 [hep-ph].

[54] G. Busoni, A. De Simone, E. Morgante, and A. Riotto, "On the Validity of the Effective Field Theory for Dark Matter Searches at the Lhc," *Phys.Lett.* **B728** (2014) 412–421, arXiv:1307.2253 [hep-ph].

[55] R. C. Cotta, A. Rajaraman, T. M. P. Tait, and A. M. Wijangco, "Particle Physics Implications and Constraints on Dark Matter Interpretations of the CDMS Signal," *Phys. Rev.* **D90** (2014) no. 1, 013020, arXiv:1305.6609 [hep-ph].

[56] S. Profumo, W. Shepherd, and T. Tait, "The Pitfalls of Dark Crossings," arXiv:1307.6277 [hep-ph].

[57] Y. Gershtein, F. Petriello, S. Quackenbush, and K. M. Zurek, "Discovering Hidden Sectors with Mono-Photon Z' Searches," *Phys.Rev.* **D78** (2008) 095002, arXiv:0809.2849 [hep-ph].

[58] F. J. Petriello, S. Quackenbush, and K. M. Zurek, "The Invisible Z' at the CERN LHC," *Phys.Rev.* **D77** (2008) 115020, arXiv:0803.4005 [hep-ph].

[59] P. Agrawal, Z. Chacko, C. Kilic, and R. K. Mishra, "A Classification of Dark Matter Candidates with Primarily Spin-Dependent Interactions with Matter," arXiv:1003.1912 [hep-ph].

[60] M. Garny, A. Ibarra, M. Pato, and S. Vogl, "Closing in on Mass-Degenerate Dark Matter Scenarios with Antiprotons and Direct Detection," *JCAP* **1211** (2012) 017, arXiv:1207.1431 [hep-ph].

[61] G. D'Ambrosio, G. F. Giudice, G. Isidori, and A. Strumia, "Minimal flavor violation: An Effective field theory approach," *Nucl. Phys.* **B645** (2002) 155–187, arXiv:hep-ph/0207036 [hep-ph].

[62] **CMS** Collaboration, "Search for supersymmetry in final states with missing transverse energy and 0, 1, 2, 3, or at least 4 b-quark jets in 8 TeV pp collisions using the variable AlphaT,".

[63] J. Alwall, M. Herquet, F. Maltoni, O. Mattelaer, and T. Stelzer, "MadGraph 5 : Going Beyond," *JHEP* **06** (2011) 128, `arXiv:1106.0522 [hep-ph]`.

[64] N. D. Christensen and C. Duhr, "FeynRules - Feynman rules made easy," *Comput. Phys. Commun.* **180** (2009) 1614–1641, `arXiv:0806.4194 [hep-ph]`.

[65] W. Beenakker, R. Hopker, and M. Spira, "PROSPINO: A Program for the production of supersymmetric particles in next-to-leading order QCD," `arXiv:hep-ph/9611232 [hep-ph]`.

[66] J. F. Nieves and P. B. Pal, "Generalized Fierz identities," *Am. J. Phys.* **72** (2004) 1100–1108, `arXiv:hep-ph/0306087 [hep-ph]`.

[67] M. Freytsis and Z. Ligeti, "On dark matter models with uniquely spin-dependent detection possibilities," *Phys. Rev.* **D83** (2011) 115009, `arXiv:1012.5317 [hep-ph]`.

[68] P. Gondolo, J. Edsjo, P. Ullio, L. Bergstrom, M. Schelke, and E. A. Baltz, "DarkSUSY: Computing supersymmetric dark matter properties numerically," *JCAP* **0407** (2004) 008, `arXiv:astro-ph/0406204 [astro-ph]`.

[69] **XENON100** Collaboration, E. Aprile *et al.*, "Dark Matter Results from 225 Live Days of XENON100 Data," *Phys. Rev. Lett.* **109** (2012) 181301, `arXiv:1207.5988 [astro-ph.CO]`.

[70] **XENON10** Collaboration, J. Angle *et al.*, "A search for light dark matter in XENON10 data," *Phys. Rev. Lett.* **107** (2011) 051301, `arXiv:1104.3088 [astro-ph.CO]`. [Erratum: Phys. Rev. Lett.110,249901(2013)].

[71] **XENON100** Collaboration, E. Aprile *et al.*, "Limits on spin-dependent WIMP-nucleon cross sections from 225 live days of XENON100 data," *Phys. Rev. Lett.* **111** (2013) no. 2, 021301, `arXiv:1301.6620 [astro-ph.CO]`.

[72] **PICASSO** Collaboration, S. Archambault *et al.*, "Constraints on Low-Mass WIMP Interactions on ^{19}F from PICASSO," *Phys. Lett.* **B711** (2012) 153–161, `arXiv:1202.1240 [hep-ex]`.

[73] G. Belanger, F. Boudjema, A. Pukhov, and A. Semenov, "micrOMEGAs_3: A program for calculating dark matter observables," *Comput. Phys. Commun.* **185** (2014) 960–985, `arXiv:1305.0237 [hep-ph]`.

[74] S. Chang, R. Edezhath, J. Hutchinson, and M. Luty, "Effective WIMPs," *Phys. Rev.* **D89** (2014) no. 1, 015011, `arXiv:1307.8120 [hep-ph]`.

[75] H. An, L.-T. Wang, and H. Zhang, "Dark matter with t-channel mediator: a simple step beyond contact interaction," *Phys. Rev.* **D89** (2014) no. 11, 115014, `arXiv:1308.0592 [hep-ph]`.

[76] Y. Bai and J. Berger, "Fermion Portal Dark Matter," *JHEP* **11** (2013) 171, `arXiv:1308.0612 [hep-ph]`.

[77] L. Carpenter, A. DiFranzo, M. Mulhearn, C. Shimmin, S. Tulin, *et al.*, "Mono-Higgs: a New Collider Probe of Dark Matter," `arXiv:1312.2592 [hep-ph]`.

[78] G. Jungman, M. Kamionkowski, and K. Griest, "Supersymmetric dark matter," *Phys.Rept.* **267** (1996) 195–373, `arXiv:hep-ph/9506380 [hep-ph]`.

[79] G. Bertone, D. Hooper, and J. Silk, "Particle dark matter: Evidence, candidates and constraints," *Phys.Rept.* **405** (2005) 279–390, `arXiv:hep-ph/0404175 [hep-ph]`.

[80] R. J. Scherrer and M. S. Turner, "On the Relic, Cosmic Abundance of Stable Weakly Interacting Massive Particles," *Phys.Rev.* **D33** (1986) 1585.

[81] **ATLAS Collaboration** Collaboration, G. Aad *et al.*, "Observation of a new particle in the search for the Standard Model Higgs boson with the ATLAS detector at the LHC," *Phys.Lett.* **B716** (2012) 1–29, `arXiv:1207.7214 [hep-ex]`.

[82] **CMS Collaboration** Collaboration, S. Chatrchyan *et al.*, "Observation of a new boson at a mass of 125 GeV with the CMS experiment at the LHC," *Phys.Lett.* **B716** (2012) 30–61, `arXiv:1207.7235 [hep-ex]`.

[83] G. Belanger, B. Dumont, U. Ellwanger, J. Gunion, and S. Kraml, "Status of invisible Higgs decays," *Phys.Lett.* **B723** (2013) 340–347, `arXiv:1302.5694 [hep-ph]`.

[84] **ATLAS Collaboration** Collaboration, G. Aad *et al.*, "Search for dark matter in events with a hadronically decaying W or Z boson and missing transverse momentum in pp collisions at $\sqrt{s}$=8 TeV with the ATLAS detector," `arXiv:1309.4017 [hep-ex]`.

[85] **CMS Collaboration** Collaboration, S. Chatrchyan *et al.*, "Search for dark matter and large extra dimensions in monojet events in pp collisions at $\sqrt{s} = 7$ TeV," *JHEP* **1209** (2012) 094, `arXiv:1206.5663 [hep-ex]`.

[86] **ATLAS Collaboration** Collaboration, G. Aad *et al.*, "Search for new phenomena with the monojet and missing transverse momentum signature using the ATLAS detector in $\sqrt{s} = 7$ TeV proton-proton collisions," *Phys.Lett.* **B705** (2011) 294–312, `arXiv:1106.5327 [hep-ex]`.

[87] **ATLAS Collaboration** Collaboration, G. Aad *et al.*, "Search for dark matter candidates and large extra dimensions in events with a photon and missing transverse momentum in pp collision data at $\sqrt{s} = 7$ TeV with the ATLAS detector," *Phys.Rev.Lett.* **110** (2013) 011802, `arXiv:1209.4625 [hep-ex]`.

[88] **CMS Collaboration** Collaboration, S. Chatrchyan *et al.*, "Search for Dark Matter and Large Extra Dimensions in pp Collisions Yielding a Photon and Missing Transverse Energy," *Phys.Rev.Lett.* **108** (2012) 261803, `arXiv:1204.0821 [hep-ex]`.

[89] M. Cirelli, E. Del Nobile, and P. Panci, "Tools for model-independent bounds in direct dark matter searches," *JCAP* **1310** (2013) 019, `arXiv:1307.5955 [hep-ph]`.

[90] J. McDonald, "Gauge singlet scalars as cold dark matter," *Phys.Rev.* **D50** (1994) 3637–3649, arXiv:hep-ph/0702143 [HEP-PH].

[91] C. Burgess, M. Pospelov, and T. ter Veldhuis, "The Minimal model of nonbaryonic dark matter: A Singlet scalar," *Nucl.Phys.* **B619** (2001) 709–728, arXiv:hep-ph/0011335 [hep-ph].

[92] B. Patt and F. Wilczek, "Higgs-field portal into hidden sectors," arXiv:hep-ph/0605188 [hep-ph].

[93] Y. G. Kim and K. Y. Lee, "The Minimal model of fermionic dark matter," *Phys.Rev.* **D75** (2007) 115012, arXiv:hep-ph/0611069 [hep-ph].

[94] J. March-Russell, S. M. West, D. Cumberbatch, and D. Hooper, "Heavy Dark Matter Through the Higgs Portal," *JHEP* **0807** (2008) 058, arXiv:0801.3440 [hep-ph].

[95] I. Low, P. Schwaller, G. Shaughnessy, and C. E. Wagner, "The dark side of the Higgs boson," *Phys.Rev.* **D85** (2012) 015009, arXiv:1110.4405 [hep-ph].

[96] L. Lopez-Honorez, T. Schwetz, and J. Zupan, "Higgs portal, fermionic dark matter, and a Standard Model like Higgs at 125 GeV," *Phys.Lett.* **B716** (2012) 179–185, arXiv:1203.2064 [hep-ph].

[97] **Particle Data Group** Collaboration, J. Beringer *et al.*, "Review of Particle Physics (RPP)," *Phys.Rev.* **D86** (2012) 010001.

[98] J.-Y. Chen, E. W. Kolb, and L.-T. Wang, "Dark matter coupling to electroweak gauge and Higgs bosons: an effective field theory approach," arXiv:1305.0021 [hep-ph].

[99] M. A. Fedderke, E. W. Kolb, T. Lin, and L.-T. Wang, "Gamma-ray constraints on dark-matter annihilation to electroweak gauge and Higgs bosons," arXiv:1310.6047 [hep-ph].

[100] P. Langacker, "The Physics of Heavy Z' Gauge Bosons," *Rev.Mod.Phys.* **81** (2009) 1199–1228, arXiv:0801.1345 [hep-ph].

[101] C. D. Carone and H. Murayama, "Possible light U(1) gauge boson coupled to baryon number," *Phys.Rev.Lett.* **74** (1995) 3122–3125, arXiv:hep-ph/9411256 [hep-ph].

[102] K. Agashe and G. Servant, "Warped unification, proton stability and dark matter," *Phys.Rev.Lett.* **93** (2004) 231805, arXiv:hep-ph/0403143 [hep-ph].

[103] P. Fileviez Perez and M. B. Wise, "Baryon and lepton number as local gauge symmetries," *Phys.Rev.* **D82** (2010) 011901, arXiv:1002.1754 [hep-ph].

[104] F. del Aguila, G. A. Blair, M. Daniel, and G. G. Ross, "Superstring Inspired Models," *Nucl.Phys.* **B272** (1986) 413.

[105] W.-F. Chang, J. N. Ng, and J. M. Wu, "A Very Narrow Shadow Extra Z-boson at Colliders," *Phys.Rev.* **D74** (2006) 095005, arXiv:hep-ph/0608068 [hep-ph].

[106] M. Pospelov, A. Ritz, and M. B. Voloshin, "Secluded WIMP Dark Matter," *Phys.Lett.* **B662** (2008) 53–61, `arXiv:0711.4866 [hep-ph]`.

[107] D. Feldman, Z. Liu, and P. Nath, "The Stueckelberg Z-prime Extension with Kinetic Mixing and Milli-Charged Dark Matter From the Hidden Sector," *Phys.Rev.* **D75** (2007) 115001, `arXiv:hep-ph/0702123 [HEP-PH]`.

[108] J. L. Feng, H. Tu, and H.-B. Yu, "Thermal Relics in Hidden Sectors," *JCAP* **0810** (2008) 043, `arXiv:0808.2318 [hep-ph]`.

[109] S. Gopalakrishna, S. Jung, and J. D. Wells, "Higgs boson decays to four fermions through an abelian hidden sector," *Phys.Rev.* **D78** (2008) 055002, `arXiv:0801.3456 [hep-ph]`.

[110] B. Holdom, "Two U(1)'s and Epsilon Charge Shifts," *Phys.Lett.* **B166** (1986) 196.

[111] K. Babu, C. F. Kolda, and J. March-Russell, "Implications of generalized Z - Z-prime mixing," *Phys.Rev.* **D57** (1998) 6788–6792, `arXiv:hep-ph/9710441 [hep-ph]`.

[112] D. O'Connell, M. J. Ramsey-Musolf, and M. B. Wise, "Minimal Extension of the Standard Model Scalar Sector," *Phys.Rev.* **D75** (2007) 037701, `arXiv:hep-ph/0611014 [hep-ph]`.

[113] A. Falkowski, F. Riva, and A. Urbano, "Higgs At Last," `arXiv:1303.1812 [hep-ph]`.

[114] A. Djouadi and G. Moreau, "The couplings of the Higgs boson and its CP properties from fits of the signal strengths and their ratios at the 7+8 TeV LHC," `arXiv:1303.6591 [hep-ph]`.

[115] P. P. Giardino, K. Kannike, I. Masina, M. Raidal, and A. Strumia, "The universal Higgs fit," `arXiv:1303.3570 [hep-ph]`.

[116] J. Ellis and T. You, "Updated Global Analysis of Higgs Couplings," *JHEP* **1306** (2013) 103, `arXiv:1303.3879 [hep-ph]`.

[117] U. Haisch, F. Kahlhoefer, and J. Unwin, "The impact of heavy-quark loops on LHC dark matter searches," *JHEP* **1307** (2013) 125, `arXiv:1208.4605 [hep-ph]`.

[118] J. Alwall, M. Herquet, F. Maltoni, O. Mattelaer, and T. Stelzer, "MadGraph 5 : Going Beyond," *JHEP* **1106** (2011) 128, `arXiv:1106.0522 [hep-ph]`.

[119] T. Sjostrand, S. Mrenna, and P. Z. Skands, "PYTHIA 6.4 Physics and Manual," *JHEP* **0605** (2006) 026, `arXiv:hep-ph/0603175 [hep-ph]`.

[120] S. Ovyn, X. Rouby, and V. Lemaitre, "DELPHES, a framework for fast simulation of a generic collider experiment," `arXiv:0903.2225 [hep-ph]`.

[121] **LHC Higgs Cross Section Working Group** Collaboration, S. Heinemeyer *et al.*, "Handbook of LHC Higgs Cross Sections: 3. Higgs Properties," `arXiv:1307.1347 [hep-ph]`.

[122] G. Bozzi, F. Campanario, M. Rauch, and D. Zeppenfeld, "Z$\gamma\gamma$ production with leptonic decays and triple photon production at NLO QCD," *Phys.Rev.* **D84** (2011) 074028, arXiv:1107.3149 [hep-ph].

[123] **ATLAS Collaboration** Collaboration, G. Aad *et al.*, "Measurement of the isolated di-photon cross-section in pp collisions at $\sqrt{s} = 7$ TeV with the ATLAS detector," *Phys.Rev.* **D85** (2012) 012003, arXiv:1107.0581 [hep-ex].

[124] G. Cowan, K. Cranmer, E. Gross, and O. Vitells, "Asymptotic formulae for likelihood-based tests of new physics," *Eur.Phys.J.* **C71** (2011) 1554, arXiv:1007.1727 [physics.data-an].

[125] **ATLAS Collaboration** Collaboration, G. Aad *et al.*, "Measurements of Higgs boson production and couplings in diboson final states with the {ATLAS} detector at the {LHC}," *Phys.Lett.* **B726** (2013) 88–119, arXiv:1307.1427 [hep-ex].

[126] M. Czakon, P. Fiedler, and A. Mitov, "The total top quark pair production cross-section at hadron colliders through $O(alpha_S^4)$," *Phys.Rev.Lett.* **110** (2013) 252004, arXiv:1303.6254 [hep-ph].

[127] F. Febres Cordero, L. Reina, and D. Wackeroth, "NLO QCD corrections to $Zb\bar{b}$ production with massive bottom quarks at the Fermilab Tevatron," *Phys.Rev.* **D78** (2008) 074014, arXiv:0806.0808 [hep-ph].

[128] F. Febres Cordero, L. Reina, and D. Wackeroth, "W- and Z-boson production with a massive bottom-quark pair at the Large Hadron Collider," *Phys.Rev.* **D80** (2009) 034015, arXiv:0906.1923 [hep-ph].

[129] A. Banfi, G. P. Salam, and G. Zanderighi, "Accurate QCD predictions for heavy-quark jets at the Tevatron and LHC," *JHEP* **0707** (2007) 026, arXiv:0704.2999 [hep-ph].

[130] D. Tucker-Smith and N. Weiner, "Inelastic dark matter," *Phys.Rev.* **D64** (2001) 043502, arXiv:hep-ph/0101138 [hep-ph].

[131] D. A. Dicus, C. Kao, and S. S. Willenbrock, "Higgs Boson Pair Production From Gluon Fusion," *Phys.Lett.* **B203** (1988) 457.

[132] S. Dawson, S. Dittmaier, and M. Spira, "Neutral Higgs boson pair production at hadron colliders: QCD corrections," *Phys.Rev.* **D58** (1998) 115012, arXiv:hep-ph/9805244 [hep-ph].

[133] V. Barger, L. L. Everett, C. Jackson, and G. Shaughnessy, "Higgs-Pair Production and Measurement of the Triscalar Coupling at LHC(8,14)," arXiv:1311.2931 [hep-ph].

[134] X.-G. He and J. Tandean, "Low-Mass Dark-Matter Hint from CDMS II, Higgs Boson at the LHC, and Darkon Models," *Phys.Rev.* **D88** (2013) 013020, arXiv:1304.6058 [hep-ph].

[135] A. A. Petrov and W. Shepherd, "Searching for dark matter at LHC with Mono-Higgs production," `arXiv:1311.1511 [hep-ph]`.

[136] **CMS Collaboration** Collaboration, S. Chatrchyan *et al.*, "Search for the standard model Higgs boson produced in association with a W or a Z boson and decaying to bottom quarks," `arXiv:1310.3687 [hep-ex]`.

[137] M. Abdullah, A. DiFranzo, A. Rajaraman, T. M. P. Tait, P. Tanedo, *et al.*, "Hidden On-Shell Mediators for the Galactic Center Gamma-Ray Excess," `arXiv:1404.6528 [hep-ph]`.

[138] S. Arrenberg, H. Baer, V. Barger, L. Baudis, D. Bauer, *et al.*, "Dark Matter in the Coming Decade: Complementary Paths to Discovery and Beyond," `arXiv:1310.8621 [hep-ph]`.

[139] D. Hooper and T. R. Slatyer, "Two Emission Mechanisms in the Fermi Bubbles: a Possible Signal of Annihilating Dark Matter," *Phys.Dark Univ.* **2** (2013) 118–138, `arXiv:1302.6589 [astro-ph.HE]`.

[140] N. Okada and O. Seto, "Gamma Ray Emission in Fermi Bubbles and Higgs Portal Dark Matter," `arXiv:1310.5991 [hep-ph]`.

[141] W.-C. Huang, A. Urbano, and W. Xue, "Fermi Bubbles Under Dark Matter Scrutiny. Part I: Astrophysical Analysis," `arXiv:1307.6862 [hep-ph]`.

[142] L. Goodenough and D. Hooper, "Possible Evidence for Dark Matter Annihilation in the Inner Milky Way from the Fermi Gamma Ray Space Telescope," `arXiv:0910.2998 [hep-ph]`.

[143] D. Hooper and L. Goodenough, "Dark Matter Annihilation in the Galactic Center as Seen by the Fermi Gamma Ray Space Telescope," *Phys.Lett.* **B697** (2011) 412–428, `arXiv:1010.2752 [hep-ph]`.

[144] K. N. Abazajian, "The Consistency of Fermi-Lat Observations of the Galactic Center with a Millisecond Pulsar Population in the Central Stellar Cluster," *JCAP* **1103** (2011) 010, `arXiv:1011.4275 [astro-ph.HE]`.

[145] K. N. Abazajian and M. Kaplinghat, "Detection of a Gamma-Ray Source in the Galactic Center Consistent with Extended Emission from Dark Matter Annihilation and Concentrated Astrophysical Emission," *Phys.Rev.* **D86** (2012) 083511, `arXiv:1207.6047 [astro-ph.HE]`.

[146] A. Boyarsky, D. Malyshev, and O. Ruchayskiy, "A Comment on the Emission from the Galactic Center as Seen by the Fermi Telescope," *Phys.Lett.* **B705** (2011) 165–169, `arXiv:1012.5839 [hep-ph]`.

[147] D. Hooper and T. Linden, "On the Origin of the Gamma Rays from the Galactic Center," *Phys.Rev.* **D84** (2011) 123005, `arXiv:1110.0006 [astro-ph.HE]`.

[148] C. Gordon and O. Macías, “Dark Matter and Pulsar Model Constraints from Galactic Center Fermi-Lat Gamma Ray Observations,” *Phys.Rev.* **D88** (2013) 083521, arXiv:1306.5725 [astro-ph.HE].

[149] O. Macias and C. Gordon, “The Contribution of Cosmic Rays Interacting with Molecular Clouds to the Galactic Center Gamma-Ray Excess,” arXiv:1312.6671 [astro-ph.HE].

[150] T. Daylan, D. P. Finkbeiner, D. Hooper, T. Linden, S. K. N. Portillo, *et al.*, “The Characterization of the Gamma-Ray Signal from the Central Milky Way: a Compelling Case for Annihilating Dark Matter,” arXiv:1402.6703 [astro-ph.HE].

[151] K. P. Modak, D. Majumdar, and S. Rakshit, “A Possible Explanation of Low Energy Γ-Ray Excess from Galactic Centre and Fermi Bubble by a Dark Matter Model with Two Real Scalars,” arXiv:1312.7488 [hep-ph].

[152] L. A. Anchordoqui and B. J. Vlcek, “W-Wimp Annihilation as a Source of the Fermi Bubbles,” *Phys.Rev.* **D88** (2013) 043513, arXiv:1305.4625 [hep-ph].

[153] P. Ko, W.-I. Park, and Y. Tang, “Higgs Portal Vector Dark Matter for GeV Scale γ-Ray Excess from Galactic Center,” arXiv:1404.5257 [hep-ph].

[154] M. R. Buckley, D. Hooper, and J. L. Rosner, “A Leptophobic Z’ and Dark Matter from Grand Unification,” *Phys.Lett.* **B703** (2011) 343–347, arXiv:1106.3583 [hep-ph].

[155] M. Boucenna and S. Profumo, “Direct and Indirect Singlet Scalar Dark Matter Detection in the Lepton-Specific Two-Higgs-Doublet Model,” *Phys.Rev.* **D84** (2011) 055011, arXiv:1106.3368 [hep-ph].

[156] G. Zhu, “Wimpless Dark Matter and the Excess Gamma Rays from the Galactic Center,” *Phys.Rev.* **D83** (2011) 076011, arXiv:1101.4387 [hep-ph].

[157] B. Kyae and J.-C. Park, “Light Dark Matter for Fermi-Lat and Cdms Observations,” *Phys.Lett.* **B732** (2014) 373–379, arXiv:1310.2284 [hep-ph].

[158] G. Marshall and R. Primulando, “The Galactic Center Region Gamma Ray Excess from a Supersymmetric Leptophilic Higgs Model,” *JHEP* **1105** (2011) 026, arXiv:1102.0492 [hep-ph].

[159] D. Cerdeno, M. Peiro, and S. Robles, “Low-Mass Right-Handed Sneutrino Dark Matter: Supercdms and Lux Constraints and the Galactic Centre Gamma-Ray Excess,” arXiv:1404.2572 [hep-ph].

[160] P. Agrawal, B. Batell, D. Hooper, and T. Lin, “Flavored Dark Matter and the Galactic Center Gamma-Ray Excess,” arXiv:1404.1373 [hep-ph].

[161] D. Hooper, I. Cholis, T. Linden, J. Siegal-Gaskins, and T. Slatyer, “Millisecond Pulsars Cannot Account for the Inner Galaxy’s GeV Excess,” *Phys.Rev.* **D88** (2013) 083009, arXiv:1305.0830 [astro-ph.HE].

[162] Q. Yuan and B. Zhang, "Millisecond Pulsar Interpretation of the Galactic Center Gamma-Ray Excess," arXiv:1404.2318 [astro-ph.HE].

[163] K. N. Abazajian, N. Canac, S. Horiuchi, M. Kaplinghat, and A. Kwa, "Discovery of a New Galactic Center Excess Consistent with Upscattered Starlight," *JCAP* **1507** (2015) no. 07, 013, arXiv:1410.6168 [astro-ph.HE].

[164] K. Hagiwara, S. Mukhopadhyay, and J. Nakamura, "10 GeV Neutralino Dark Matter and Light Stau in the MSSM," *Phys.Rev.* **D89** (2014) 015023, arXiv:1308.6738 [hep-ph].

[165] M. R. Buckley, D. Hooper, and J. Kumar, "Phenomenology of Dirac Neutralino Dark Matter," *Phys.Rev.* **D88** (2013) 063532, arXiv:1307.3561.

[166] H. E. Logan, "Dark Matter Annihilation Through a Lepton-Specific Higgs Boson," *Phys.Rev.* **D83** (2011) 035022, arXiv:1010.4214 [hep-ph].

[167] T. Lacroix, C. Boehm, and J. Silk, "Fitting the Fermi-Lat GeV Excess: on the Importance of Including the Propagation of Electrons from Dark Matter," arXiv:1403.1987 [astro-ph.HE].

[168] N. F. Bell, J. B. Dent, A. J. Galea, T. D. Jacques, L. M. Krauss, *et al.*, "Searching for Dark Matter at the Lhc with a Mono-Z," *Phys.Rev.* **D86** (2012) 096011, arXiv:1209.0231 [hep-ph].

[169] N. Zhou, D. Berge, and D. Whiteson, "Mono-Everything: Combined Limits on Dark Matter Production at Colliders from Multiple Final States," *Phys.Rev.* **D87** (2013) no. 9, 095013, arXiv:1302.3619 [hep-ex].

[170] T. Lin, E. W. Kolb, and L.-T. Wang, "Probing Dark Matter Couplings to Top and Bottom at the Lhc," *Phys.Rev.* **D88** (2013) 063510, arXiv:1303.6638 [hep-ph].

[171] A. Berlin, T. Lin, and L.-T. Wang, "Mono-Higgs Detection of Dark Matter at the Lhc," arXiv:1402.7074 [hep-ph].

[172] G. Belanger, F. Boudjema, A. Pukhov, and A. Semenov, "Dark Matter Direct Detection Rate in a Generic Model with Micromegas 2.2," *Comput.Phys.Commun.* **180** (2009) 747–767, arXiv:0803.2360 [hep-ph].

[173] A. L. Fitzpatrick, W. Haxton, E. Katz, N. Lubbers, and Y. Xu, "Model Independent Direct Detection Analyses," arXiv:1211.2818 [hep-ph].

[174] N. Anand, A. L. Fitzpatrick, and W. Haxton, "Model-Independent WIMP Scattering Responses and Event Rates: a Mathematica Package for Experimental Analysis," arXiv:1308.6288 [hep-ph].

[175] J. Fan, M. Reece, and L.-T. Wang, "Non-Relativistic Effective Theory of Dark Matter Direct Detection," *JCAP* **1011** (2010) 042, arXiv:1008.1591 [hep-ph].

[176] T. Cohen, D. J. Phalen, and A. Pierce, "On the Correlation Between the Spin-Independent and Spin-Dependent Direct Detection of Dark Matter," *Phys.Rev.* **D81** (2010) 116001, arXiv:1001.3408 [hep-ph].

[177] M. I. Gresham and K. M. Zurek, "On the Effect of Nuclear Response Functions in Dark Matter Direct Detection," arXiv:1401.3739 [hep-ph].

[178] A. L. Fitzpatrick, W. Haxton, E. Katz, N. Lubbers, and Y. Xu, "The Effective Field Theory of Dark Matter Direct Detection," *JCAP* **1302** (2013) 004, arXiv:1203.3542 [hep-ph].

[179] Y. Hochberg, E. Kuflik, T. Volansky, and J. G. Wacker, "The Simp Miracle," arXiv:1402.5143 [hep-ph].

[180] D. Curtin, Z. Surujon, and Y. Tsai, "Direct Detection with Dark Mediators," arXiv:1312.2618 [hep-ph].

[181] M. Papucci, A. Vichi, and K. M. Zurek, "Monojet Versus Rest of the World I: T-Channel Models," arXiv:1402.2285 [hep-ph].

[182] O. Buchmueller, M. J. Dolan, and C. McCabe, "Beyond Effective Field Theory for Dark Matter Searches at the Lhc," *JHEP* **1401** (2014) 025, arXiv:1308.6799 [hep-ph].

[183] P. J. Fox and C. Williams, "Next-To-Leading Order Predictions for Dark Matter Production at Hadron Colliders," *Phys.Rev.* **D87** (2013) no. 5, 054030, arXiv:1211.6390 [hep-ph].

[184] A. Friedland, M. L. Graesser, I. M. Shoemaker, and L. Vecchi, "Probing Nonstandard Standard Model Backgrounds with Lhc Monojets," *Phys.Lett.* **B714** (2012) 267–275, arXiv:1111.5331 [hep-ph].

[185] M. L. Graesser, I. M. Shoemaker, and L. Vecchi, "A Dark Force for Baryons," arXiv:1107.2666 [hep-ph].

[186] M. Kaplinghat, S. Tulin, and H.-B. Yu, "Self-interacting Dark Matter Benchmarks," arXiv:1308.0618 [hep-ph].

[187] J. Fan, A. Katz, L. Randall, and M. Reece, "Double-Disk Dark Matter," *Phys.Dark Univ.* **2** (2013) 139–156, arXiv:1303.1521 [astro-ph.CO].

[188] S. Tulin, H.-B. Yu, and K. M. Zurek, "Beyond Collisionless Dark Matter: Particle Physics Dynamics for Dark Matter Halo Structure," *Phys.Rev.* **D87** (2013) no. 11, 115007, arXiv:1302.3898 [hep-ph].

[189] S. Tulin, H.-B. Yu, and K. M. Zurek, "Resonant Dark Forces and Small Scale Structure," *Phys.Rev.Lett.* **110** (2013) no. 11, 111301, arXiv:1210.0900 [hep-ph].

[190] F.-Y. Cyr-Racine and K. Sigurdson, "Cosmology of Atomic Dark Matter," *Phys.Rev.* **D87** (2013) no. 10, 103515, arXiv:1209.5752 [astro-ph.CO].

[191] R. Foot, "Implications of Mirror Dark Matter Kinetic Mixing for Cmb Anisotropies," *Phys.Lett.* **B718** (2013) 745–751, arXiv:1208.6022 [astro-ph.CO].

[192] S. Tulin, H.-B. Yu, and K. M. Zurek, "Three Exceptions for Thermal Dark Matter with Enhanced Annihilation to $\Gamma\Gamma$," *Phys.Rev.* **D87** (2013) 036011, arXiv:1208.0009 [hep-ph].

[193] D. E. Kaplan, G. Z. Krnjaic, K. R. Rehermann, and C. M. Wells, "Dark Atoms: Asymmetry and Direct Detection," *JCAP* **1110** (2011) 011, arXiv:1105.2073 [hep-ph].

[194] A. Loeb and N. Weiner, "Cores in Dwarf Galaxies from Dark Matter with a Yukawa Potential," *Phys.Rev.Lett.* **106** (2011) 171302, arXiv:1011.6374 [astro-ph.CO].

[195] H. An, S.-L. Chen, R. N. Mohapatra, and Y. Zhang, "Leptogenesis as a Common Origin for Matter and Dark Matter," *JHEP* **1003** (2010) 124, arXiv:0911.4463 [hep-ph].

[196] M. R. Buckley and P. J. Fox, "Dark Matter Self-Interactions and Light Force Carriers," *Phys.Rev.* **D81** (2010) 083522, arXiv:0911.3898 [hep-ph].

[197] J. L. Feng, M. Kaplinghat, and H.-B. Yu, "Halo Shape and Relic Density Exclusions of Sommerfeld-Enhanced Dark Matter Explanations of Cosmic Ray Excesses," *Phys.Rev.Lett.* **104** (2010) 151301, arXiv:0911.0422 [hep-ph].

[198] J. L. Feng, M. Kaplinghat, H. Tu, and H.-B. Yu, "Hidden Charged Dark Matter," *JCAP* **0907** (2009) 004, arXiv:0905.3039 [hep-ph].

[199] M. Pospelov and A. Ritz, "Astrophysical Signatures of Secluded Dark Matter," *Phys.Lett.* **B671** (2009) 391–397, arXiv:0810.1502 [hep-ph].

[200] N. Arkani-Hamed, D. P. Finkbeiner, T. R. Slatyer, and N. Weiner, "A Theory of Dark Matter," *Phys.Rev.* **D79** (2009) 015014, arXiv:0810.0713 [hep-ph].

[201] M. Kesden and M. Kamionkowski, "Galilean Equivalence for Galactic Dark Matter," *Phys.Rev.Lett.* **97** (2006) 131303, arXiv:astro-ph/0606566 [astro-ph].

[202] R. Foot, "Mirror Matter-Type Dark Matter," *Int.J.Mod.Phys.* **D13** (2004) 2161–2192, arXiv:astro-ph/0407623 [astro-ph].

[203] R. Mohapatra, S. Nussinov, and V. Teplitz, "Mirror Matter as Selfinteracting Dark Matter," *Phys.Rev.* **D66** (2002) 063002, arXiv:hep-ph/0111381 [hep-ph].

[204] D. N. Spergel and P. J. Steinhardt, "Observational Evidence for Selfinteracting Cold Dark Matter," *Phys.Rev.Lett.* **84** (2000) 3760–3763, arXiv:astro-ph/9909386 [astro-ph].

[205] **ATLAS Collaboration** Collaboration, "Search for New Phenomena in Monojet plus Missing Transverse Momentum Final States using 10fb^{-1} of pp Collisions at $\sqrt{s} = 8$ TeV with the ATLAS detector at the LHC," Tech. Rep. ATLAS-CONF-2012-147, CERN, Geneva, Nov, 2012.

[206] W.-C. Huang, A. Urbano, and W. Xue, "Fermi Bubbles Under Dark Matter Scrutiny Part Ii: Particle Physics Analysis," `arXiv:1310.7609 [hep-ph]`.

[207] A. Berlin, D. Hooper, and S. D. McDermott, "Simplified Dark Matter Models for the Galactic Center Gamma-Ray Excess," `arXiv:1404.0022 [hep-ph]`.

[208] E. Izaguirre, G. Krnjaic, and B. Shuve, "The Galactic Center Excess from the Bottom Up," `arXiv:1404.2018 [hep-ph]`.

[209] C. Boehm, M. J. Dolan, C. McCabe, M. Spannowsky, and C. J. Wallace, "Extended Gamma-Ray Emission from Coy Dark Matter," `arXiv:1401.6458 [hep-ph]`.

[210] A. Hektor and L. Marzola, "Coy Dark Matter and the Anomalous Magnetic Moment," `arXiv:1403.3401 [hep-ph]`.

[211] F. D'Eramo and J. Thaler, "Semi-annihilation of Dark Matter," *JHEP* **06** (2010) 109, `arXiv:1003.5912 [hep-ph]`.

[212] C. Boehm, M. J. Dolan, and C. McCabe, "A Weighty Interpretation of the Galactic Centre Excess," `arXiv:1404.4977 [hep-ph]`.

[213] H. K. Dreiner, H. E. Haber, and S. P. Martin, "Two-Component Spinor Techniques and Feynman Rules for Quantum Field Theory and Supersymmetry," *Phys.Rept.* **494** (2010) 1–196, `arXiv:0812.1594 [hep-ph]`.

[214] L. Hall and L. Randall, "Weak Scale Effective Supersymmetry," *Phys.Rev.Lett.* **65** (1990) 2939–2942.

[215] R. S. Chivukula and H. Georgi, "Composite Technicolor Standard Model," *Phys.Lett.* **B188** (1987) 99.

[216] A. Buras, P. Gambino, M. Gorbahn, S. Jager, and L. Silvestrini, "Universal Unitarity Triangle and Physics Beyond the Standard Model," *Phys.Lett.* **B500** (2001) 161–167, `arXiv:hep-ph/0007085 [hep-ph]`.

[217] J. F. Navarro, C. S. Frenk, and S. D. White, "The Structure of Cold Dark Matter Halos," *Astrophys.J.* **462** (1996) 563–575, `arXiv:astro-ph/9508025 [astro-ph]`.

[218] J. F. Navarro, C. S. Frenk, and S. D. White, "A Universal Density Profile from Hierarchical Clustering," *Astrophys.J.* **490** (1997) 493–508, `arXiv:astro-ph/9611107 [astro-ph]`.

[219] A. Klypin, H. Zhao, and R. S. Somerville, "Lambda Cdm-Based Models for the Milky Way and M31 I: Dynamical Models," *Astrophys.J.* **573** (2002) 597–613, `arXiv:astro-ph/0110390 [astro-ph]`.

[220] J. Mardon, Y. Nomura, D. Stolarski, and J. Thaler, "Dark Matter Signals from Cascade Annihilations," *JCAP* **0905** (2009) 016, arXiv:0901.2926 [hep-ph].

[221] A. Ibarra, S. Lopez Gehler, and M. Pato, "Dark Matter Constraints from Box-Shaped Gamma-Ray Features," *JCAP* **1207** (2012) 043, arXiv:1205.0007 [hep-ph].

[222] M. Cirelli, "PPPC 4 DM ID - A Poor Particle Physicist Cookbook for Dark Matter Indirect Detection," December, 2013.
http://www.marcocirelli.net/PPPC4DMID.html.

[223] M. Cirelli, G. Corcella, A. Hektor, G. Hutsi, M. Kadastik, *et al.*, "PPPC 4 DM ID: a Poor Particle Physicist Cookbook for Dark Matter Indirect Detection," *JCAP* **1103** (2011) 051, arXiv:1012.4515 [hep-ph].

[224] P. Ciafaloni, D. Comelli, A. Riotto, F. Sala, A. Strumia, *et al.*, "Weak Corrections are Relevant for Dark Matter Indirect Detection," *JCAP* **1103** (2011) 019, arXiv:1009.0224 [hep-ph].

[225] Wolfram Research, Inc., *Mathematica, Version 8.0.* Champaign, Illinois, 2010.

[226] T. Sjostrand, S. Mrenna, and P. Z. Skands, "A Brief Introduction to Pythia 8.1," *Comput.Phys.Commun.* **178** (2008) 852–867, arXiv:0710.3820 [hep-ph].

[227] M. Cirelli and G. Giesen, "Antiprotons from Dark Matter: Current Constraints and Future Sensitivities," *JCAP* **1304** (2013) 015, arXiv:1301.7079 [hep-ph].

[228] K. Kong and J.-C. Park, "Bounds on Dark Matter Interpretation of Fermi-Lat GeV Excess," arXiv:1404.3741 [hep-ph].

[229] J. Kopp, V. Niro, T. Schwetz, and J. Zupan, "Dama/Libra and Leptonically Interacting Dark Matter," *Phys.Rev.* **D80** (2009) 083502, arXiv:0907.3159 [hep-ph].

[230] M. I. Gresham and K. M. Zurek, "Light Dark Matter Anomalies After Lux," *Phys.Rev.* **D89** (2014) 016017, arXiv:1311.2082 [hep-ph].

[231] B. A. Dobrescu and F. Yu, "Coupling-Mass Mapping of Dijet Peak Searches," *Phys.Rev.* **D88** (2013) no. 3, 035021, arXiv:1306.2629 [hep-ph].

[232] C. D. Carone and H. Murayama, "Realistic Models with a Light U(1) Gauge Boson Coupled to Baryon Number," *Phys.Rev.* **D52** (1995) 484–493, arXiv:hep-ph/9501220 [hep-ph].

[233] M. Williams, C. Burgess, A. Maharana, and F. Quevedo, "New Constraints (And Motivations) for Abelian Gauge Bosons in the Mev-Tev Mass Range," *JHEP* **1108** (2011) 106, arXiv:1103.4556 [hep-ph].

[234] B. A. Dobrescu and C. Frugiuele, "Hidden Gev-Scale Interactions of Quarks," arXiv:1404.3947 [hep-ph].

[235] D. Whiteson, et al. Private Communication.

[236] M. Srednicki, R. Watkins, and K. A. Olive, "Calculations of Relic Densities in the Early Universe," *Nucl. Phys.* **B310** (1988) 693.

[237] E. Kolb and M. Turner, *The Early Universe*. Westview Press, 1994.

[238] **WMAP Collaboration** Collaboration, J. Dunkley *et al.*, "Five-Year Wilkinson Microwave Anisotropy Probe (Wmap) Observations: Likelihoods and Parameters from the WMAP Data," *Astrophys.J.Suppl.* **180** (2009) 306–329, `arXiv:0803.0586 [astro-ph]`.

[239] **WMAP Collaboration** Collaboration, E. Komatsu *et al.*, "Five-Year Wilkinson Microwave Anisotropy Probe (Wmap) Observations: Cosmological Interpretation," *Astrophys.J.Suppl.* **180** (2009) 330–376, `arXiv:0803.0547 [astro-ph]`.

[240] **Planck Collaboration** Collaboration, P. Ade *et al.*, "Planck 2013 results. I. Overview of products and scientific results," `arXiv:1303.5062 [astro-ph.CO]`.

[241] M. Pierre, J. M. Siegal-Gaskins, and P. Scott, "Sensitivity of Cta to Dark Matter Signals from the Galactic Center," `arXiv:1401.7330 [astro-ph.HE]`.

[242] K. M. Zurek, "Asymmetric Dark Matter: Theories, Signatures, and Constraints," *Phys.Rept.* **537** (2014) 91–121, `arXiv:1308.0338 [hep-ph]`.

[243] R. Easther, R. Galvez, O. Ozsoy, and S. Watson, "Supersymmetry, Nonthermal Dark Matter and Precision Cosmology," *Phys.Rev.* **D89** (2014) 023522, `arXiv:1307.2453 [hep-ph]`.

[244] K. Petraki and R. R. Volkas, "Review of Asymmetric Dark Matter," *Int.J.Mod.Phys.* **A28** (2013) 1330028, `arXiv:1305.4939 [hep-ph]`.

[245] J. McDonald, "Comment on the 'Freeze-In' Mechanism of Dark Matter Production," `arXiv:1112.1501 [hep-ph]`.

[246] G. Arcadi and P. Ullio, "Accurate Estimate of the Relic Density and the Kinetic Decoupling in Non-Thermal Dark Matter Models," *Phys.Rev.* **D84** (2011) 043520, `arXiv:1104.3591 [hep-ph]`.

[247] P. Sandick and S. Watson, "Constraints on a Non-Thermal History from Galactic Dark Matter Spikes," *Phys.Rev.* **D84** (2011) 023507, `arXiv:1102.2897 [astro-ph.CO]`.

[248] R. Aloisio, V. Berezinsky, and M. Kachelriess, "On the Status of Superheavy Dark Matter," *Phys.Rev.* **D74** (2006) 023516, `arXiv:astro-ph/0604311 [astro-ph]`.

[249] J. L. Feng, S.-f. Su, and F. Takayama, "Superwimp Gravitino Dark Matter from Slepton and Sneutrino Decays," *Phys.Rev.* **D70** (2004) 063514, `arXiv:hep-ph/0404198 [hep-ph]`.

[250] J. L. Feng, A. Rajaraman, and F. Takayama, "Superwimp Dark Matter Signals from the Early Universe," *Phys.Rev.* **D68** (2003) 063504, `arXiv:hep-ph/0306024 [hep-ph]`.

[251] J. L. Feng, A. Rajaraman, and F. Takayama, "Superweakly Interacting Massive Particles," *Phys.Rev.Lett.* **91** (2003) 011302, `arXiv:hep-ph/0302215 [hep-ph]`.

[252] E. A. Baltz and H. Murayama, "Gravitino Warm Dark Matter with Entropy Production," *JHEP* **0305** (2003) 067, `arXiv:astro-ph/0108172 [astro-ph]`.

[253] J. McDonald, "Thermally Generated Gauge Singlet Scalars as Selfinteracting Dark Matter," *Phys.Rev.Lett.* **88** (2002) 091304, `arXiv:hep-ph/0106249 [hep-ph]`.

[254] E. W. Kolb, D. J. Chung, and A. Riotto, "Wimpzillas!," `arXiv:hep-ph/9810361 [hep-ph]`.

[255] D. J. Chung, E. W. Kolb, and A. Riotto, "Production of Massive Particles during Reheating," *Phys.Rev.* **D60** (1999) 063504, `arXiv:hep-ph/9809453 [hep-ph]`.

[256] D. J. Chung, E. W. Kolb, and A. Riotto, "Superheavy Dark Matter," *Phys.Rev.* **D59** (1999) 023501, `arXiv:hep-ph/9802238 [hep-ph]`.

[257] L. Kofman, A. D. Linde, and A. A. Starobinsky, "Reheating After Inflation," *Phys.Rev.Lett.* **73** (1994) 3195–3198, `arXiv:hep-th/9405187 [hep-th]`.

[258] J. R. Ellis, G. Gelmini, J. L. Lopez, D. V. Nanopoulos, and S. Sarkar, "Astrophysical Constraints on Massive Unstable Neutral Relic Particles," *Nucl.Phys.* **B373** (1992) 399–437.

[259] J. R. Ellis, D. V. Nanopoulos, and S. Sarkar, "The Cosmology of Decaying Gravitinos," *Nucl.Phys.* **B259** (1985) 175.

[260] N. Mirabal, "Dark Matter Vs. Pulsars: Catching the Impostor," `arXiv:1309.3428 [astro-ph.HE]`.

[261] R. Voss and M. Gilfanov, "Dynamical Formation of X-Ray Binaries in the Inner Bulge of M31," `arXiv:astro-ph/0702580 [ASTRO-PH]`.

[262] B. Batell, J. Pradler, and M. Spannowsky, "Dark Matter from Minimal Flavor Violation," *JHEP* **1108** (2011) 038, `arXiv:1105.1781 [hep-ph]`.

[263] P. Agrawal, M. Blanke, and K. Gemmler, "Flavored dark matter beyond Minimal Flavor Violation," *JHEP* **10** (2014) 72, `arXiv:1405.6709 [hep-ph]`.

[264] V. Silveira and A. Zee, "Scalar Phantoms," *Phys.Lett.* **B161** (1985) 136.

[265] S. Ipek, D. McKeen, and A. E. Nelson, "A Renormalizable Model for the Galactic Center Gamma Ray Excess from Dark Matter Annihilation," `arXiv:1404.3716 [hep-ph]`.

[266] S. Tulin, "New Weakly-Coupled Forces Hidden in Low-Energy QCD," arXiv:1404.4370 [hep-ph].

[267] M. Kaplinghat, S. Tulin, and H.-B. Yu, "Direct Detection Portals for Self-Interacting Dark Matter," *Phys.Rev.* **D89** (2014) 035009, arXiv:1310.7945 [hep-ph].

[268] D. Hooper, N. Weiner, and W. Xue, "Dark Forces and Light Dark Matter," *Phys.Rev.* **D86** (2012) 056009, arXiv:1206.2929 [hep-ph].

[269] C. D. Carone, "Flavor-Nonuniversal Dark Gauge Bosons and the Muon G-2," *Phys.Lett.* **B721** (2013) 118–122, arXiv:1301.2027 [hep-ph].

[270] L. Randall and R. Sundrum, "A Large Mass Hierarchy from a Small Extra Dimension," *Phys.Rev.Lett.* **83** (1999) 3370–3373, arXiv:hep-ph/9905221 [hep-ph].

[271] L. Randall and M. D. Schwartz, "Quantum Field Theory and Unification in AdS5," *JHEP* **0111** (2001) 003, arXiv:hep-th/0108114 [hep-th].

[272] C. Csaki, J. Erlich, and J. Terning, "The Effective Lagrangian in the Randall-Sundrum Model and Electroweak Physics," *Phys.Rev.* **D66** (2002) 064021, arXiv:hep-ph/0203034 [hep-ph].

[273] R. Contino, D. Marzocca, D. Pappadopulo, and R. Rattazzi, "On the Effect of Resonances in Composite Higgs Phenomenology," *JHEP* **1110** (2011) 081, arXiv:1109.1570 [hep-ph].

[274] B. Bellazzini, C. Csaki, J. Hubisz, J. Serra, and J. Terning, "Composite Higgs Sketch," *JHEP* **1211** (2012) 003, arXiv:1205.4032 [hep-ph].

[275] A. Martin, J. Shelton, and J. Unwin, "Fitting the Galactic Center Gamma-Ray Excess with Cascade Annihilations," arXiv:1405.0272 [hep-ph].

[276] A. Berlin, A. DiFranzo, and D. Hooper, "3.55 keV line from exciting dark matter without a hidden sector," *Phys. Rev.* **D91** (2015) no. 7, 075018, arXiv:1501.03496 [hep-ph].

[277] E. Bulbul, M. Markevitch, A. Foster, R. K. Smith, M. Loewenstein, and S. W. Randall, "Detection of An Unidentified Emission Line in the Stacked X-ray spectrum of Galaxy Clusters," *Astrophys. J.* **789** (2014) 13, arXiv:1402.2301 [astro-ph.CO].

[278] A. Boyarsky, O. Ruchayskiy, D. Iakubovskyi, and J. Franse, "Unidentified Line in X-Ray Spectra of the Andromeda Galaxy and Perseus Galaxy Cluster," *Phys. Rev. Lett.* **113** (2014) 251301, arXiv:1402.4119 [astro-ph.CO].

[279] A. Boyarsky, J. Franse, D. Iakubovskyi, and O. Ruchayskiy, "Checking the Dark Matter Origin of a 3.53 keV Line with the Milky Way Center," *Phys. Rev. Lett.* **115** (2015) 161301, arXiv:1408.2503 [astro-ph.CO].

[280] S. Riemer-Sorensen, "Questioning a 3.5 keV dark matter emission line," arXiv:1405.7943 [astro-ph.CO].

[281] O. Urban, N. Werner, S. W. Allen, A. Simionescu, J. S. Kaastra, and L. E. Strigari, "A Suzaku Search for Dark Matter Emission Lines in the X-ray Brightest Galaxy Clusters," *Mon. Not. Roy. Astron. Soc.* **451** (2015) no. 3, 2447–2461, arXiv:1411.0050 [astro-ph.CO].

[282] T. E. Jeltema and S. Profumo, "Discovery of a 3.5 keV line in the Galactic Centre and a critical look at the origin of the line across astronomical targets," *Mon. Not. Roy. Astron. Soc.* **450** (2015) no. 2, 2143–2152, arXiv:1408.1699 [astro-ph.HE].

[283] E. Bulbul, M. Markevitch, A. R. Foster, R. K. Smith, M. Loewenstein, and S. W. Randall, "Comment on "Dark matter searches going bananas: the contribution of Potassium (and Chlorine) to the 3.5 keV line"," arXiv:1409.4143 [astro-ph.HE].

[284] A. Boyarsky, J. Franse, D. Iakubovskyi, and O. Ruchayskiy, "Comment on the paper "Dark matter searches going bananas: the contribution of Potassium (and Chlorine) to the 3.5 keV line" by T. Jeltema and S. Profumo," arXiv:1408.4388 [astro-ph.CO].

[285] T. Jeltema and S. Profumo, "Reply to Two Comments on "Dark matter searches going bananas the contribution of Potassium (and Chlorine) to the 3.5 keV line"," arXiv:1411.1759 [astro-ph.HE].

[286] S. Dodelson and L. M. Widrow, "Sterile-neutrinos as dark matter," *Phys. Rev. Lett.* **72** (1994) 17–20, arXiv:hep-ph/9303287 [hep-ph].

[287] M. E. Anderson, E. Churazov, and J. N. Bregman, "Non-Detection of X-Ray Emission From Sterile Neutrinos in Stacked Galaxy Spectra," *Mon. Not. Roy. Astron. Soc.* **452** (2015) no. 4, 3905–3923, arXiv:1408.4115 [astro-ph.HE].

[288] D. Malyshev, A. Neronov, and D. Eckert, "Constraints on 3.55 keV line emission from stacked observations of dwarf spheroidal galaxies," *Phys. Rev.* **D90** (2014) 103506, arXiv:1408.3531 [astro-ph.HE].

[289] D. P. Finkbeiner and N. Weiner, "Exciting Dark Matter and the INTEGRAL/SPI 511 keV signal," *Phys. Rev.* **D76** (2007) 083519, arXiv:astro-ph/0702587 [astro-ph].

[290] M. Pospelov and A. Ritz, "The galactic 511 keV line from electroweak scale WIMPs," *Phys. Lett.* **B651** (2007) 208–215, arXiv:hep-ph/0703128 [HEP-PH].

[291] D. P. Finkbeiner and N. Weiner, "An X-Ray Line from eXciting Dark Matter," arXiv:1402.6671 [hep-ph].

[292] M. T. Frandsen, F. Sannino, I. M. Shoemaker, and O. Svendsen, "X-ray Lines from Dark Matter: The Good, The Bad, and The Unlikely," *JCAP* **1405** (2014) 033, arXiv:1403.1570 [hep-ph].

[293] J. M. Cline and A. R. Frey, "Consistency of dark matter interpretations of the 3.5 keV x-ray line," *Phys. Rev.* **D90** (2014) no. 12, 123537, arXiv:1410.7766 [astro-ph.CO].

[294] F. Calore, I. Cholis, and C. Weniger, "Background model systematics for the Fermi GeV excess," *JCAP* **1503** (2015) 038, `arXiv:1409.0042 [astro-ph.CO]`.

[295] **Fermi-LAT** Collaboration, M. Ajello *et al.*, "Fermi-LAT Observations of High-Energy γ-Ray Emission Toward the Galactic Center," *Astrophys. J.* **819** (2016) no. 1, 44, `arXiv:1511.02938 [astro-ph.HE]`.

[296] F. Calore, I. Cholis, C. McCabe, and C. Weniger, "A Tale of Tails: Dark Matter Interpretations of the Fermi GeV Excess in Light of Background Model Systematics," *Phys. Rev.* **D91** (2015) no. 6, 063003, `arXiv:1411.4647 [hep-ph]`.

[297] J. M. Cline and A. R. Frey, "Nonabelian dark matter models for 3.5 keV X-rays," *JCAP* **1410** (2014) 013, `arXiv:1408.0233 [hep-ph]`.

[298] K. Cheung, W.-C. Huang, and Y.-L. S. Tsai, "Non-abelian Dark Matter Solutions for Galactic Gamma-ray Excess and Perseus 3.5 keV X-ray Line," *JCAP* **1505** (2015) no. 05, 053, `arXiv:1411.2619 [hep-ph]`.

[299] J. M. Cline, Y. Farzan, Z. Liu, G. D. Moore, and W. Xue, "3.5 keV x rays as the "21 cm line" of dark atoms, and a link to light sterile neutrinos," *Phys. Rev.* **D89** (2014) 121302, `arXiv:1404.3729 [hep-ph]`.

[300] H. Okada and T. Toma, "3.55 keV X-ray Line Signal from Excited Dark Matter in Radiative Neutrino Model," *Phys. Lett.* **B737** (2014) 162–166, `arXiv:1404.4795 [hep-ph]`.

[301] K. Griest and M. Kamionkowski, "Unitarity Limits on the Mass and Radius of Dark Matter Particles," *Phys.Rev.Lett.* **64** (1990) 615.

[302] D. H. Weinberg, J. S. Bullock, F. Governato, R. K. de Naray, and A. H. G. Peter, "Cold dark matter: controversies on small scales," in *Sackler Colloquium: Dark Matter Universe: On the Threshhold of Discovery Irvine, USA, October 18-20, 2012*. 2013. `arXiv:1306.0913 [astro-ph.CO]`. `https://inspirehep.net/record/1237028/files/arXiv:1306.0913.pdf`.

[303] **CMS Collaboration** Collaboration, S. Chatrchyan *et al.*, "Search for a Higgs Boson Decaying into a B-Quark Pair and Produced in Association with B Quarks in Proton-Proton Collisions at 7 TeV," *Phys.Lett.* **B722** (2013) 207–232, `arXiv:1302.2892 [hep-ex]`.

[304] **ATLAS** Collaboration, G. Aad *et al.*, "Search for neutral Higgs bosons of the minimal supersymmetric standard model in pp collisions at $\sqrt{s} = 8$ TeV with the ATLAS detector," *JHEP* **11** (2014) 056, `arXiv:1409.6064 [hep-ex]`.

[305] **CMS** Collaboration, V. Khachatryan *et al.*, "Search for neutral MSSM Higgs bosons decaying to a pair of tau leptons in pp collisions," *JHEP* **10** (2014) 160, `arXiv:1408.3316 [hep-ex]`.

[306] N. Zhou, Z. Khechadoorian, D. Whiteson, and T. M. P. Tait, "Bounds on Invisible Higgs boson Decays from $t\bar{t}H$ Production," *Phys. Rev. Lett.* **113** (2014) 151801, arXiv:1408.0011 [hep-ph]. [Erratum: Phys. Rev. Lett.114,no.22,229901(2015)].

[307] **ATLAS** Collaboration, G. Aad *et al.*, "Search for dark matter in events with heavy quarks and missing transverse momentum in pp collisions with the ATLAS detector," *Eur. Phys. J.* **C75** (2015) no. 2, 92, arXiv:1410.4031 [hep-ex].

[308] A. Falkowski, Y. Hochberg, and J. T. Ruderman, "Displaced Vertices from X-ray Lines," *JHEP* **11** (2014) 140, arXiv:1409.2872 [hep-ph].

[309] A. Berlin, S. Gori, T. Lin, and L.-T. Wang, "Pseudoscalar Portal Dark Matter," *Phys. Rev.* **D92** (2015) 015005, arXiv:1502.06000 [hep-ph].

[310] S. G. P. Collaboration) Talk given at Planck 2014, Ferrara, Italy, December 1-5(2014).

[311] R. H. Cyburt, J. R. Ellis, B. D. Fields, and K. A. Olive, "Updated nucleosynthesis constraints on unstable relic particles," *Phys. Rev.* **D67** (2003) 103521, arXiv:astro-ph/0211258 [astro-ph].

[312] A. DiFranzo, P. J. Fox, and T. M. P. Tait, "Vector Dark Matter through a Radiative Higgs Portal," *JHEP* **04** (2016) 135, arXiv:1512.06853 [hep-ph].

[313] A. Djouadi, O. Lebedev, Y. Mambrini, and J. Quevillon, "Implications of LHC searches for Higgs–portal dark matter," *Phys.Lett.* **B709** (2012) 65–69, arXiv:1112.3299 [hep-ph].

[314] O. Lebedev, H. M. Lee, and Y. Mambrini, "Vector Higgs-portal dark matter and the invisible Higgs," *Phys. Lett.* **B707** (2012) 570–576, arXiv:1111.4482 [hep-ph].

[315] M. Duch, B. Grzadkowski, and M. McGarrie, "A stable Higgs portal with vector dark matter," *JHEP* **09** (2015) 162, arXiv:1506.08805 [hep-ph].

[316] W. Chao, "First order electroweak phase transition triggered by the Higgs portal vector dark matter," arXiv:1412.3823 [hep-ph].

[317] T. Hambye, "Hidden vector dark matter," *JHEP* **01** (2009) 028, arXiv:0811.0172 [hep-ph].

[318] Y. Farzan and A. R. Akbarieh, "VDM: A model for Vector Dark Matter," *JCAP* **1210** (2012) 026, arXiv:1207.4272 [hep-ph].

[319] S. Baek, P. Ko, W.-I. Park, and E. Senaha, "Higgs Portal Vector Dark Matter : Revisited," *JHEP* **05** (2013) 036, arXiv:1212.2131 [hep-ph].

[320] S. Baek, P. Ko, and W.-I. Park, "Singlet Portal Extensions of the Standard Seesaw Models to a Dark Sector with Local Dark Symmetry," *JHEP* **07** (2013) 013, arXiv:1303.4280 [hep-ph].

[321] S. Baek, P. Ko, and W.-I. Park, "Invisible Higgs Decay Width vs. Dark Matter Direct Detection Cross Section in Higgs Portal Dark Matter Models," *Phys.Rev.* **D90** (2014) no. 5, 055014, `arXiv:1405.3530 [hep-ph]`.

[322] S. Baek, P. Ko, W.-I. Park, and Y. Tang, "Indirect and direct signatures of Higgs portal decaying vector dark matter for positron excess in cosmic rays," *JCAP* **1406** (2014) 046, `arXiv:1402.2115 [hep-ph]`.

[323] C. Gross, O. Lebedev, and Y. Mambrini, "Non-Abelian gauge fields as dark matter," *JHEP* **08** (2015) 158, `arXiv:1505.07480 [hep-ph]`.

[324] S. Di Chiara and K. Tuominen, "A minimal model for SU(N) vector dark matter," *JHEP* **11** (2015) 188, `arXiv:1506.03285 [hep-ph]`.

[325] C.-H. Chen and T. Nomura, "Searching for Vector Dark Matter by Higgs Portal at the LHC," `arXiv:1507.00886 [hep-ph]`.

[326] J. S. Kim, O. Lebedev, and D. Schmeier, "Higgsophilic gauge bosons and monojets at the LHC," `arXiv:1507.08673 [hep-ph]`.

[327] **ATLAS, CMS** Collaboration, M. Flechl, "Higgs physics: Review of recent results and prospects from ATLAS and CMS," *J. Phys. Conf. Ser.* **631** (2015) no. 1, 012028, `arXiv:1503.00632 [hep-ex]`.

[328] W. H. Furry, "A Symmetry Theorem in the Positron Theory," *Phys. Rev.* **51** (1937) 125–129.

[329] T. Hahn, "Generating Feynman diagrams and amplitudes with FeynArts 3," *Comput. Phys. Commun.* **140** (2001) 418–431, `arXiv:hep-ph/0012260 [hep-ph]`.

[330] T. Hahn and M. Perez-Victoria, "Automatized one loop calculations in four-dimensions and D-dimensions," *Comput. Phys. Commun.* **118** (1999) 153–165, `arXiv:hep-ph/9807565 [hep-ph]`.

[331] **CMS** Collaboration, S. Chatrchyan *et al.*, "Search for invisible decays of Higgs bosons in the vector boson fusion and associated ZH production modes," *Eur. Phys. J.* **C74** (2014) 2980, `arXiv:1404.1344 [hep-ex]`.

[332] M. Endo and Y. Takaesu, "Heavy WIMP through Higgs portal at the LHC," *Phys. Lett.* **B743** (2015) 228–234, `arXiv:1407.6882 [hep-ph]`.

[333] A. Denner, S. Dittmaier, S. Kallweit, and A. Muck, "Electroweak corrections to Higgs-strahlung off W/Z bosons at the Tevatron and the LHC with HAWK," *JHEP* **03** (2012) 075, `arXiv:1112.5142 [hep-ph]`.

[334] **ALEPH** Collaboration, A. Heister *et al.*, "Search for charginos nearly mass degenerate with the lightest neutralino in e+ e- collisions at center-of-mass energies up to 209-GeV," *Phys. Lett.* **B533** (2002) 223–236, `arXiv:hep-ex/0203020 [hep-ex]`.

[335] **DELPHI** Collaboration, J. Abdallah *et al.*, "Search for SUSY in the AMSB scenario with the DELPHI detector," *Eur. Phys. J.* **C34** (2004) 145–156, `arXiv:hep-ex/0403047 [hep-ex]`.

[336] **L3** Collaboration, M. Acciarri *et al.*, "Search for charginos with a small mass difference with the lightest supersymmetric particle at $\sqrt{S} = 189$-GeV," *Phys. Lett.* **B482** (2000) 31–42, `arXiv:hep-ex/0002043 [hep-ex]`.

[337] **OPAL** Collaboration, G. Abbiendi *et al.*, "Search for nearly mass degenerate charginos and neutralinos at LEP," *Eur. Phys. J.* **C29** (2003) 479–489, `arXiv:hep-ex/0210043 [hep-ex]`.

[338] **ATLAS** Collaboration, G. Aad *et al.*, "Search for direct production of charginos, neutralinos and sleptons in final states with two leptons and missing transverse momentum in pp collisions at $\sqrt{s} = 8$ TeV with the ATLAS detector," *JHEP* **05** (2014) 071, `arXiv:1403.5294 [hep-ex]`.

[339] **CMS** Collaboration, V. Khachatryan *et al.*, "Searches for electroweak neutralino and chargino production in channels with Higgs, Z, and W bosons in pp collisions at 8 TeV," *Phys. Rev.* **D90** (2014) no. 9, 092007, `arXiv:1409.3168 [hep-ex]`.

[340] A. DiFranzo and D. Hooper, "Searching for MeV-Scale Gauge Bosons with IceCube," *Phys. Rev.* **D92** (2015) no. 9, 095007, `arXiv:1507.03015 [hep-ph]`.

[341] J. F. Beacom, N. F. Bell, D. Hooper, S. Pakvasa, and T. J. Weiler, "Decay of high-energy astrophysical neutrinos," *Phys.Rev.Lett.* **90** (2003) 181301, `arXiv:hep-ph/0211305 [hep-ph]`.

[342] J. F. Beacom, N. F. Bell, D. Hooper, S. Pakvasa, and T. J. Weiler, "Measuring flavor ratios of high-energy astrophysical neutrinos," *Phys.Rev.* **D68** (2003) 093005, `arXiv:hep-ph/0307025 [hep-ph]`.

[343] J. F. Beacom, N. F. Bell, D. Hooper, J. G. Learned, S. Pakvasa, *et al.*, "PseudoDirac neutrinos: A Challenge for neutrino telescopes," *Phys.Rev.Lett.* **92** (2004) 011101, `arXiv:hep-ph/0307151 [hep-ph]`.

[344] J. F. Beacom, N. F. Bell, D. Hooper, S. Pakvasa, and T. J. Weiler, "Sensitivity to theta(13) and delta in the decaying astrophysical neutrino scenario," *Phys.Rev.* **D69** (2004) 017303, `arXiv:hep-ph/0309267 [hep-ph]`.

[345] G. Pagliaroli, A. Palladino, F. Vissani, and F. Villante, "Testing neutrino decay scenarios with IceCube data," `arXiv:1506.02624 [hep-ph]`.

[346] M. Bustamante, J. F. Beacom, and W. Winter, "Theoretically palatable flavor combinations of astrophysical neutrinos," `arXiv:1506.02645 [astro-ph.HE]`.

[347] E. Aeikens, H. Päs, S. Pakvasa, and P. Sicking, "Flavor ratios of extragalactical neutrinos and neutrino shortcuts in extra dimensions," `arXiv:1410.0408 [hep-ph]`.

[348] D. Hollander, “Astrophysical neutrino flavor ratios in the presence of sterile neutrinos,” arXiv:1301.5313 [hep-ph].

[349] L. Fu, C. M. Ho, and T. J. Weiler, “Cosmic Neutrino Flavor Ratios with Broken $\nu_\mu - \nu_\tau$ Symmetry,” *Phys.Lett.* **B718** (2012) 558–565, arXiv:1209.5382 [hep-ph].

[350] A. Bhattacharya, S. Choubey, R. Gandhi, and A. Watanabe, “Ultra-high neutrino fluxes as a probe for non-standard physics,” *JCAP* **1009** (2010) 009, arXiv:1006.3082 [hep-ph].

[351] M. Bustamante, A. Gago, and C. Pena-Garay, “Energy-independent new physics in the flavour ratios of high-energy astrophysical neutrinos,” *JHEP* **1004** (2010) 066, arXiv:1001.4878 [hep-ph].

[352] A. Bhattacharya, S. Choubey, R. Gandhi, and A. Watanabe, “Diffuse Ultra-High Energy Neutrino Fluxes and Physics Beyond the Standard Model,” *Phys.Lett.* **B690** (2010) 42–47, arXiv:0910.4396 [hep-ph].

[353] Z.-z. Xing and S. Zhou, “Implications of Leptonic Unitarity Violation at Neutrino Telescopes,” *Phys.Lett.* **B666** (2008) 166–172, arXiv:0804.3512 [hep-ph].

[354] D. Hooper, D. Morgan, and E. Winstanley, “Lorentz and CPT invariance violation in high-energy neutrinos,” *Phys.Rev.* **D72** (2005) 065009, arXiv:hep-ph/0506091 [hep-ph].

[355] D. Hooper, D. Morgan, and E. Winstanley, “Probing quantum decoherence with high-energy neutrinos,” *Phys.Lett.* **B609** (2005) 206–211, arXiv:hep-ph/0410094 [hep-ph].

[356] C. A. ArgÃijelles, T. Katori, and J. Salvado, “New Physics in Astrophysical Neutrino Flavor,” arXiv:1506.02043 [hep-ph].

[357] Y. Farzan and S. Palomares-Ruiz, “Dips in the Diffuse Supernova Neutrino Background,” *JCAP* **1406** (2014) 014, arXiv:1401.7019 [hep-ph].

[358] A. Chatterjee, M. M. Devi, M. Ghosh, R. Moharana, and S. K. Raut, “Probing CP violation with the first three years of ultrahigh energy neutrinos from IceCube,” *Phys. Rev.* **D90** (2014) no. 7, 073003, arXiv:1312.6593 [hep-ph].

[359] J. I. Illana, M. Masip, and D. Meloni, “A new physics interpretation of the IceCube data,” *Astropart.Phys.* **65** (2015) 64–68, arXiv:1410.3208 [hep-ph].

[360] J. Alvarez-Muniz, J. L. Feng, F. Halzen, T. Han, and D. Hooper, “Detecting microscopic black holes with neutrino telescopes,” *Phys.Rev.* **D65** (2002) 124015, arXiv:hep-ph/0202081 [hep-ph].

[361] J. Alvarez-Muniz, F. Halzen, T. Han, and D. Hooper, “Phenomenology of high-energy neutrinos in low scale quantum gravity models,” *Phys.Rev.Lett.* **88** (2002) 021301, arXiv:hep-ph/0107057 [hep-ph].

[362] J. J. Friess, T. Han, and D. Hooper, "TeV string state excitation via high-energy cosmic neutrinos," *Phys.Lett.* **B547** (2002) 31–36, arXiv:hep-ph/0204112 [hep-ph].

[363] T. Han and D. Hooper, "The Particle physics reach of high-energy neutrino astronomy," *New J.Phys.* **6** (2004) 150, arXiv:hep-ph/0408348 [hep-ph].

[364] B. Dutta, Y. Gao, T. Li, C. Rott, and L. E. Strigari, "The Leptoquark Implication from the CMS and IceCube Experiments," arXiv:1505.00028 [hep-ph].

[365] U. K. Dey and S. Mohanty, "Constraints on Leptoquark Models from IceCube Data," arXiv:1505.01037 [hep-ph].

[366] D. Hooper, "Detecting MeV gauge bosons with high-energy neutrino telescopes," *Phys.Rev.* **D75** (2007) 123001, arXiv:hep-ph/0701194 [hep-ph].

[367] T. Araki, F. Kaneko, Y. Konishi, T. Ota, J. Sato, *et al.*, "Cosmic neutrino spectrum and the muon anomalous magnetic moment in the gauged $L - L$ model," *Phys.Rev.* **D91** (2015) no. 3, 037301, arXiv:1409.4180 [hep-ph].

[368] K. C. Y. Ng and J. F. Beacom, "Cosmic neutrino cascades from secret neutrino interactions," *Phys.Rev.* **D90** (2014) no. 6, 065035, arXiv:1404.2288 [astro-ph.HE].

[369] T. Araki, F. Kaneko, Y. Konishi, T. Ota, J. Sato, *et al.*, "Mind the Gap on IceCube: Cosmic neutrino spectrum and muon anomalous magnetic moment," arXiv:1505.01284 [hep-ph].

[370] A. Kamada and H.-B. Yu, "Coherent Propagation of PeV Neutrinos and the Dip in the Neutrino Spectrum at IceCube," arXiv:1504.00711 [hep-ph].

[371] M. Ibe and K. Kaneta, "Cosmic neutrino background absorption line in the neutrino spectrum at IceCube," *Phys.Rev.* **D90** (2014) no. 5, 053011, arXiv:1407.2848 [hep-ph].

[372] K. Ioka and K. Murase, "IceCube PeV-EeV neutrinos and secret interactions of neutrinos," *PTEP* **2014** (2014) no. 6, 061E01, arXiv:1404.2279 [astro-ph.HE].

[373] Y. Farzan, "A model for large non-standard interactions of neutrinos leading to the LMA-Dark solution," arXiv:1505.06906 [hep-ph].

[374] J. F. Cherry, A. Friedland, and I. M. Shoemaker, "Neutrino Portal Dark Matter: From Dwarf Galaxies to IceCube," arXiv:1411.1071 [hep-ph].

[375] **IceCube** Collaboration, M. Aartsen *et al.*, "First observation of PeV-energy neutrinos with IceCube," *Phys.Rev.Lett.* **111** (2013) 021103, arXiv:1304.5356 [astro-ph.HE].

[376] **IceCube** Collaboration, M. Aartsen *et al.*, "Evidence for High-Energy Extraterrestrial Neutrinos at the IceCube Detector," *Science* **342** (2013) 1242856, arXiv:1311.5238 [astro-ph.HE].

[377] **IceCube** Collaboration, M. Aartsen *et al.*, "Observation of High-Energy Astrophysical Neutrinos in Three Years of IceCube Data," *Phys.Rev.Lett.* **113** (2014) 101101, arXiv:1405.5303 [astro-ph.HE].

[378] M. Ahlers, Y. Bai, V. Barger, and R. Lu, "Galactic TeV-PeV Neutrinos," arXiv:1505.03156 [hep-ph].

[379] A. Neronov, D. Semikoz, and C. Tchernin, "PeV neutrinos from interactions of cosmic rays with the interstellar medium in the Galaxy," *Phys.Rev.* **D89** (2014) no. 10, 103002, arXiv:1307.2158 [astro-ph.HE].

[380] M. Ahlers and K. Murase, "Probing the Galactic Origin of the IceCube Excess with Gamma-Rays," *Phys.Rev.* **D90** (2014) no. 2, 023010, arXiv:1309.4077 [astro-ph.HE].

[381] N. Gupta, "Galactic PeV Neutrinos," *Astropart.Phys.* **48** (2013) 75–77, arXiv:1305.4123 [astro-ph.HE].

[382] C. Lunardini, S. Razzaque, K. T. Theodoseau, and L. Yang, "Neutrino Events at IceCube and the Fermi Bubbles," *Phys.Rev.* **D90** (2014) no. 2, 023016, arXiv:1311.7188 [astro-ph.HE].

[383] J. C. Joshi, W. Winter, and N. Gupta, "How Many of the Observed Neutrino Events Can Be Described by Cosmic Ray Interactions in the Milky Way?," *Mon.Not.Roy.Astron.Soc.* **439** (2014) no. 4, 3414–3419, arXiv:1310.5123 [astro-ph.HE].

[384] A. M. Taylor, S. Gabici, and F. Aharonian, "Galactic halo origin of the neutrinos detected by IceCube," *Phys.Rev.* **D89** (2014) no. 10, 103003, arXiv:1403.3206 [astro-ph.HE].

[385] **IceCube** Collaboration, M. Aartsen *et al.*, "Flavor Ratio of Astrophysical Neutrinos above 35 TeV in IceCube," *Phys.Rev.Lett.* **114** (2015) no. 17, 171102, arXiv:1502.03376 [astro-ph.HE].

[386] I. Cholis and D. Hooper, "On The Origin of IceCube's PeV Neutrinos," *JCAP* **1306** (2013) 030, arXiv:1211.1974 [astro-ph.HE].

[387] E. Waxman and J. N. Bahcall, "High-energy neutrinos from astrophysical sources: An Upper bound," *Phys.Rev.* **D59** (1998) 023002, arXiv:hep-ph/9807282 [hep-ph].

[388] J. N. Bahcall and E. Waxman, "High-energy astrophysical neutrinos: The Upper bound is robust," *Phys.Rev.* **D64** (2001) 023002, arXiv:hep-ph/9902383 [hep-ph].

[389] O. Mena, S. Palomares-Ruiz, and A. C. Vincent, "Flavor Composition of the High-Energy Neutrino Events in IceCube," *Phys.Rev.Lett.* **113** (2014) 091103, arXiv:1404.0017 [astro-ph.HE].

[390] K. Murase, Y. Inoue, and C. D. Dermer, "Diffuse Neutrino Intensity from the Inner Jets of Active Galactic Nuclei: Impacts of External Photon Fields and the Blazar Sequence," *Phys.Rev.* **D90** (2014) no. 2, 023007, arXiv:1403.4089 [astro-ph.HE].

[391] C. D. Dermer, K. Murase, and Y. Inoue, "Photopion Production in Black-Hole Jets and Flat-Spectrum Radio Quasars as PeV Neutrino Sources," *JHEAp* **3-4** (2014) 29–40, arXiv:1406.2633 [astro-ph.HE].

[392] F. W. Stecker, "PeV neutrinos observed by IceCube from cores of active galactic nuclei," *Phys.Rev.* **D88** (2013) no. 4, 047301, arXiv:1305.7404 [astro-ph.HE].

[393] B. Wang and Z. Li, "Can FSRQs produce the IceCube detected diffuse neutrino emission?," arXiv:1505.04418 [astro-ph.HE].

[394] R.-Y. Liu, X.-Y. Wang, S. Inoue, R. Crocker, and F. Aharonian, "Diffuse PeV neutrinos from EeV cosmic ray sources: Semirelativistic hypernova remnants in star-forming galaxies," *Phys.Rev.* **D89** (2014) no. 8, 083004, arXiv:1310.1263 [astro-ph.HE].

[395] H.-N. He, T. Wang, Y.-Z. Fan, S.-M. Liu, and D.-M. Wei, "Diffuse PeV neutrino emission from ultraluminous infrared galaxies," *Phys.Rev.* **D87** (2013) no. 6, 063011, arXiv:1303.1253 [astro-ph.HE].

[396] B. Wang, X.-H. Zhao, and Z. Li, "Implications of Fermi-LAT observations on the origin of IceCube neutrinos," *JCAP* **1411** (2014) no. 11, 028, arXiv:1407.2536 [astro-ph.HE].

[397] I. Tamborra, S. Ando, and K. Murase, "Star-forming galaxies as the origin of diffuse high-energy backgrounds: Gamma-ray and neutrino connections, and implications for starburst history," *JCAP* **1409** (2014) no. 09, 043, arXiv:1404.1189 [astro-ph.HE].

[398] R.-Y. Liu and X.-Y. Wang, "Diffuse PeV neutrinos from gamma-ray bursts," *Astrophys.J.* **766** (2013) 73, arXiv:1212.1260 [astro-ph.HE].

[399] K. Murase and K. Ioka, "TeV-PeV Neutrinos from Low-Power Gamma-Ray Burst Jets inside Stars," *Phys.Rev.Lett.* **111** (2013) no. 12, 121102, arXiv:1306.2274 [astro-ph.HE].

[400] D. Xiao and Z. Dai, "TeV-PeV Neutrino Oscillation of Low-luminosity Gamma-ray Bursts," arXiv:1504.01603 [astro-ph.HE].

[401] K. Murase, R. Laha, S. Ando, and M. Ahlers, "Testing the Dark Matter Scenario for PeV Neutrinos Observed in IceCube," arXiv:1503.04663 [hep-ph].

[402] J. Kopp, J. Liu, and X.-P. Wang, "Boosted Dark Matter in IceCube and at the Galactic Center," *JHEP* **1504** (2015) 105, arXiv:1503.02669 [hep-ph].

[403] Y. Daikoku and H. Okada, "PeV Scale Right Handed Neutrino Dark Matter in S_4 Flavor Symmetric extra U(1) model," *Phys.Rev.* **D91** (2015) no. 7, 075009, arXiv:1502.07032 [hep-ph].

[404] C. S. Fong, H. Minakata, B. Panes, and R. Z. Funchal, "Possible Interpretations of IceCube High-Energy Neutrino Events," *JHEP* **1502** (2015) 189, arXiv:1411.5318 [hep-ph].

[405] A. Esmaili, S. K. Kang, and P. D. Serpico, "IceCube events and decaying dark matter: hints and constraints," *JCAP* **1412** (2014) no. 12, 054, arXiv:1410.5979 [hep-ph].

[406] C. Rott, K. Kohri, and S. C. Park, "Superheavy dark matter and IceCube neutrino signals:bounds on decaying dark matter," arXiv:1408.4575 [hep-ph].

[407] Y. Ema, R. Jinno, and T. Moroi, "Cosmological Implications of High-Energy Neutrino Emission from the Decay of Long-Lived Particle," *JHEP* **1410** (2014) 150, arXiv:1408.1745 [hep-ph].

[408] A. Bhattacharya, R. Gandhi, and A. Gupta, "The Direct Detection of Boosted Dark Matter at High Energies and PeV events at IceCube," *JCAP* **1503** (2015) no. 03, 027, arXiv:1407.3280 [hep-ph].

[409] J. Zavala, "Galactic PeV neutrinos from dark matter annihilation," *Phys.Rev.* **D89** (2014) no. 12, 123516, arXiv:1404.2932 [astro-ph.HE].

[410] S. M. Boucenna, M. Chianese, G. Mangano, G. Miele, S. Morisi, O. Pisanti, and E. Vitagliano, "Decaying Leptophilic Dark Matter at IceCube," arXiv:1507.01000 [hep-ph].

[411] D. London and J. L. Rosner, "Extra Gauge Bosons in E(6)," *Phys. Rev.* **D34** (1986) 1530.

[412] J. L. Hewett and T. G. Rizzo, "Low-Energy Phenomenology of Superstring Inspired E(6) Models," *Phys. Rept.* **183** (1989) 193.

[413] V. Braun, Y.-H. He, B. A. Ovrut, and T. Pantev, "A Standard model from the E(8) x E(8) heterotic superstring," *JHEP* **0506** (2005) 039, arXiv:hep-th/0502155 [hep-th].

[414] G. Cleaver, M. Cvetič, J. Espinosa, L. Everett, P. Langacker, *et al.*, "Physics implications of flat directions in free fermionic superstring models 1. Mass spectrum and couplings," *Phys.Rev.* **D59** (1999) 055005, arXiv:hep-ph/9807479 [hep-ph].

[415] C. Coriano, A. E. Faraggi, and M. Guzzi, "A Novel string derived Z-prime with stable proton, light-neutrinos and R-parity violation," *Eur.Phys.J.* **C53** (2008) 421–428, arXiv:0704.1256 [hep-ph].

[416] A. E. Faraggi and D. V. Nanopoulos, "A SUPERSTRING Z' AT O (1-TeV) ?," *Mod.Phys.Lett. A* **06** (1991) 61–68.

[417] J. Giedt, "Completion of standard model like embeddings," *Annals Phys.* **289** (2001) 251, `arXiv:hep-th/0009104 [hep-th]`.

[418] O. Lebedev, H. P. Nilles, S. Raby, S. Ramos-Sanchez, M. Ratz, *et al.*, "The Heterotic Road to the MSSM with R parity," *Phys.Rev.* **D77** (2008) 046013, `arXiv:0708.2691 [hep-th]`.

[419] P. Anastasopoulos, M. Bianchi, E. Dudas, and E. Kiritsis, "Anomalies, anomalous U(1)'s and generalized Chern-Simons terms," *JHEP* **0611** (2006) 057, `arXiv:hep-th/0605225 [hep-th]`.

[420] A. E. Faraggi, "Yukawa couplings in superstring derived standard like models," *Phys.Rev.* **D47** (1993) 5021–5028.

[421] M. Cvetič, G. Shiu, and A. M. Uranga, "Chiral four-dimensional N=1 supersymmetric type 2A orientifolds from intersecting D6 branes," *Nucl.Phys.* **B615** (2001) 3–32, `arXiv:hep-th/0107166 [hep-th]`.

[422] N. Arkani-Hamed, A. G. Cohen, and H. Georgi, "Anomalies on orbifolds," *Phys.Lett.* **B516** (2001) 395–402, `arXiv:hep-th/0103135 [hep-th]`.

[423] N. Arkani-Hamed *et al.*, "The Minimal Moose for a Little Higgs," *JHEP* **08** (2002) 021, `arXiv:hep-ph/0206020`.

[424] T. Han, H. E. Logan, B. McElrath, and L.-T. Wang, "Phenomenology of the little Higgs model," *Phys.Rev.* **D67** (2003) 095004, `arXiv:hep-ph/0301040 [hep-ph]`.

[425] M. Perelstein, "Little Higgs models and their phenomenology," *Prog.Part.Nucl.Phys.* **58** (2007) 247–291, `arXiv:hep-ph/0512128 [hep-ph]`.

[426] C. T. Hill and E. H. Simmons, "Strong dynamics and electroweak symmetry breaking," *Phys.Rept.* **381** (2003) 235–402, `arXiv:hep-ph/0203079 [hep-ph]`.

[427] R. S. Chivukula, H.-J. He, J. Howard, and E. H. Simmons, "The Structure of electroweak corrections due to extended gauge symmetries," *Phys.Rev.* **D69** (2004) 015009, `arXiv:hep-ph/0307209 [hep-ph]`.

[428] R. Chivukula and E. H. Simmons, "Electroweak limits on nonuniversal Z-prime bosons," *Phys.Rev.* **D66** (2002) 015006, `arXiv:hep-ph/0205064 [hep-ph]`.

[429] K. Agashe, A. Delgado, M. J. May, and R. Sundrum, "RS1, custodial isospin and precision tests," *JHEP* **0308** (2003) 050, `arXiv:hep-ph/0308036 [hep-ph]`.

[430] K. Agashe, H. Davoudiasl, S. Gopalakrishna, T. Han, G.-Y. Huang, *et al.*, "LHC Signals for Warped Electroweak Neutral Gauge Bosons," *Phys.Rev.* **D76** (2007) 115015, `arXiv:0709.0007 [hep-ph]`.

[431] M. S. Carena, A. Delgado, E. Ponton, T. M. Tait, and C. Wagner, "Precision electroweak data and unification of couplings in warped extra dimensions," *Phys.Rev.* **D68** (2003) 035010, `arXiv:hep-ph/0305188 [hep-ph]`.

[432] J. Hewett, F. Petriello, and T. Rizzo, "Precision measurements and fermion geography in the Randall-Sundrum model revisited," *JHEP* **0209** (2002) 030, `arXiv:hep-ph/0203091 [hep-ph]`.

[433] N. Arkani-Hamed, A. G. Cohen, and H. Georgi, "Electroweak symmetry breaking from dimensional deconstruction," *Phys. Lett.* **B513** (2001) 232–240, `arXiv:hep-ph/0105239`.

[434] M. Cvetič, D. A. Demir, J. R. Espinosa, L. L. Everett, and P. Langacker, "Electroweak breaking and the mu problem in supergravity models with an additional U(1)," *Phys. Rev.* **D56** (1997) 2861, `arXiv:hep-ph/9703317`.

[435] P. Langacker, N. Polonsky, and J. Wang, "A low-energy solution to the mu-problem in gauge mediation," *Phys. Rev.* **D60** (1999) 115005, `arXiv:hep-ph/9905252`.

[436] R. Carey, K. Lynch, J. Miller, B. Roberts, W. Morse, *et al.*, "The New (g-2) Experiment: A proposal to measure the muon anomalous magnetic moment to +-0.14 ppm precision,".

[437] A. S. Kronfeld, R. S. Tschirhart, U. Al-Binni, W. Altmannshofer, C. Ankenbrandt, *et al.*, "Project X: Physics Opportunities," `arXiv:1306.5009 [hep-ex]`.

[438] C. Aubin, T. Blum, M. Golterman, and S. Peris, "Model-independent parametrization of the hadronic vacuum polarization and g-2 for the muon on the lattice," *Phys.Rev.* **D86** (2012) 054509, `arXiv:1205.3695 [hep-lat]`.

[439] C. Aubin, T. Blum, M. Golterman, and S. Peris, "Hadronic vacuum polarization with twisted boundary conditions," *Phys.Rev.* **D88** (2013) no. 7, 074505, `arXiv:1307.4701 [hep-lat]`.

[440] C. Aubin, T. Blum, M. Golterman, K. Maltman, and S. Peris, "The muon anomalous magnetic moment, a view from the lattice," *Int.J.Mod.Phys.Conf.Ser.* **35** (2014) 1460418, `arXiv:1311.5504 [hep-lat]`.

[441] T. Blum, A. Denig, I. Logashenko, E. de Rafael, B. Lee Roberts, *et al.*, "The Muon (g-2) Theory Value: Present and Future," `arXiv:1311.2198 [hep-ph]`.

[442] M. Golterman, K. Maltman, and S. Peris, "Tests of hadronic vacuum polarization fits for the muon anomalous magnetic moment," *PoS* **LATTICE2013** (2014) 300, `arXiv:1310.5928 [hep-lat]`.

[443] A. Nyffeler, "Status of hadronic light-by-light scattering in the muon $g - 2$," *Nuovo Cim.* **C037** (2014) no. 02, 173–178, `arXiv:1312.4804 [hep-ph]`.

[444] M. Endo, K. Hamaguchi, T. Kitahara, and T. Yoshinaga, "Probing Bino contribution to muon $g-2$," *JHEP* **1311** (2013) 013, arXiv:1309.3065 [hep-ph].

[445] M. Ibe, T. T. Yanagida, and N. Yokozaki, "Muon g-2 and 125 GeV Higgs in Split-Family Supersymmetry," *JHEP* **1308** (2013) 067, arXiv:1303.6995 [hep-ph].

[446] H. Davoudiasl, H.-S. Lee, and W. J. Marciano, "Muon $g2$, rare kaon decays, and parity violation from dark bosons," *Phys.Rev.* **D89** (2014) no. 9, 095006, arXiv:1402.3620 [hep-ph].

[447] P. Agrawal, Z. Chacko, and C. B. Verhaaren, "Leptophilic Dark Matter and the Anomalous Magnetic Moment of the Muon," *JHEP* **1408** (2014) 147, arXiv:1402.7369 [hep-ph].

[448] M. A. Ajaib, I. Gogoladze, Q. Shafi, and C. S. ÃIJn, "Split sfermion families, Yukawa unification and muon $g-2$," *JHEP* **1405** (2014) 079, arXiv:1402.4918 [hep-ph].

[449] D. McKeen, "Contributions to the Muon's Anomalous Magnetic Moment from a Hidden Sector," *Annals Phys.* **326** (2011) 1501–1514, arXiv:0912.1076 [hep-ph].

[450] F. Jegerlehner and A. Nyffeler, "The Muon g-2," *Phys.Rept.* **477** (2009) 1–110, arXiv:0902.3360 [hep-ph].

[451] F. S. Queiroz and W. Shepherd, "New Physics Contributions to the Muon Anomalous Magnetic Moment," arXiv:1403.2309 [hep-ph].

[452] W. Altmannshofer, S. Gori, M. Pospelov, and I. Yavin, "Neutrino Trident Production: A Powerful Probe of New Physics with Neutrino Beams," *Phys.Rev.Lett.* **113** (2014) 091801, arXiv:1406.2332 [hep-ph].

[453] B. Ahlgren, T. Ohlsson, and S. Zhou, "Comment on "Is Dark Matter with Long-Range Interactions a Solution to All Small-Scale Problems of Λ Cold Dark Matter Cosmology?"," *Phys.Rev.Lett.* **111** (2013) no. 19, 199001, arXiv:1309.0991 [hep-ph].

[454] F.-Y. Cyr-Racine and K. Sigurdson, "Limits on Neutrino-Neutrino Scattering in the Early Universe," *Phys.Rev.* **D90** (2014) no. 12, 123533, arXiv:1306.1536 [astro-ph.CO].

[455] M. Archidiacono and S. Hannestad, "Updated constraints on non-standard neutrino interactions from Planck," *JCAP* **1407** (2014) 046, arXiv:1311.3873 [astro-ph.CO].

[456] J. Heeck and W. Rodejohann, "Gauged L_μ - L_τ Symmetry at the Electroweak Scale," *Phys. Rev.* **D84** (2011) 075007, arXiv:1107.5238 [hep-ph].

[457] K. Blum, A. Hook, and K. Murase, "High energy neutrino telescopes as a probe of the neutrino mass mechanism," arXiv:1408.3799 [hep-ph].

[458] D. Forero, M. Tortola, and J. Valle, "Neutrino oscillations refitted," *Phys.Rev.* **D90** (2014) no. 9, 093006, `arXiv:1405.7540 [hep-ph]`.

[459] J. G. Learned and S. Pakvasa, "Detecting tau-neutrino oscillations at PeV energies," *Astropart.Phys.* **3** (1995) 267–274, `arXiv:hep-ph/9405296 [hep-ph]`.

[460] H. Athar, G. Parente, and E. Zas, "Prospects for observations of high-energy cosmic tau neutrinos," *Phys.Rev.* **D62** (2000) 093010, `arXiv:hep-ph/0006123 [hep-ph]`.

[461] H. Yuksel, M. D. Kistler, J. F. Beacom, and A. M. Hopkins, "Revealing the High-Redshift Star Formation Rate with Gamma-Ray Bursts," *Astrophys.J.* **683** (2008) L5–L8, `arXiv:0804.4008 [astro-ph]`.

[462] **PAMELA Collaboration** Collaboration, O. Adriani *et al.*, "An Anomalous Positron Abundance in Cosmic Rays with Energies 1.5-100 GeV," *Nature* **458** (2009) 607–609, `arXiv:0810.4995 [astro-ph]`.

[463] H. E. Haber and D. Wyler, "RADIATIVE NEUTRALINO DECAY," *Nucl. Phys.* **B323** (1989) 267–310.

[464] G. Passarino and M. J. G. Veltman, "One Loop Corrections for e+ e- Annihilation Into mu+ mu- in the Weinberg Model," *Nucl. Phys.* **B160** (1979) 151.

Appendix A

The Spectrum of Spectra

In Ch. 4 we have shown how the conventional 40 GeV DM model for the γ-ray excess can be converted into a heavier DM model ($m_\chi = 80$, 120 GeV) by taking the limit where annihilation to on-shell mediators dominates. We further showed that one can interpolate the DM masses between $m_\chi = 40$GeV and 80, 120 GeV by parametrically increasing the SM coupling and increasing the fraction annihilations through an off-shell mediator. In this appendix we briefly demonstrate nonstandard (i.e. beyond $b\bar{b}$ and $\tau\bar{\tau}$) spectra that may also fit the γ-ray excess in the regimes $m_\chi < 40$ GeV and $m_\chi > 80$, 120 GeV. We use PPPC as described in Sec. 4.3.2 and our fits are subject to the caveats described in Sec. 4.3.3. For simplicity and consistency when comparing to other plots in Ch. 4, we plot the data fit to the $b\bar{b}$ template from Fig. 8 of [1].

Fig. A.1 shows sample spectra that show the range of behavior when considering different final states both for off-shell s-channel processes and for those with on-shell mediators. In each of these cases, we note that by considering either admixtures of different final states or on-shell mediator annihilation into different species, one can find viable DM models for the γ-ray excess where the DM mass is less than the 40 GeV value typically considered in the

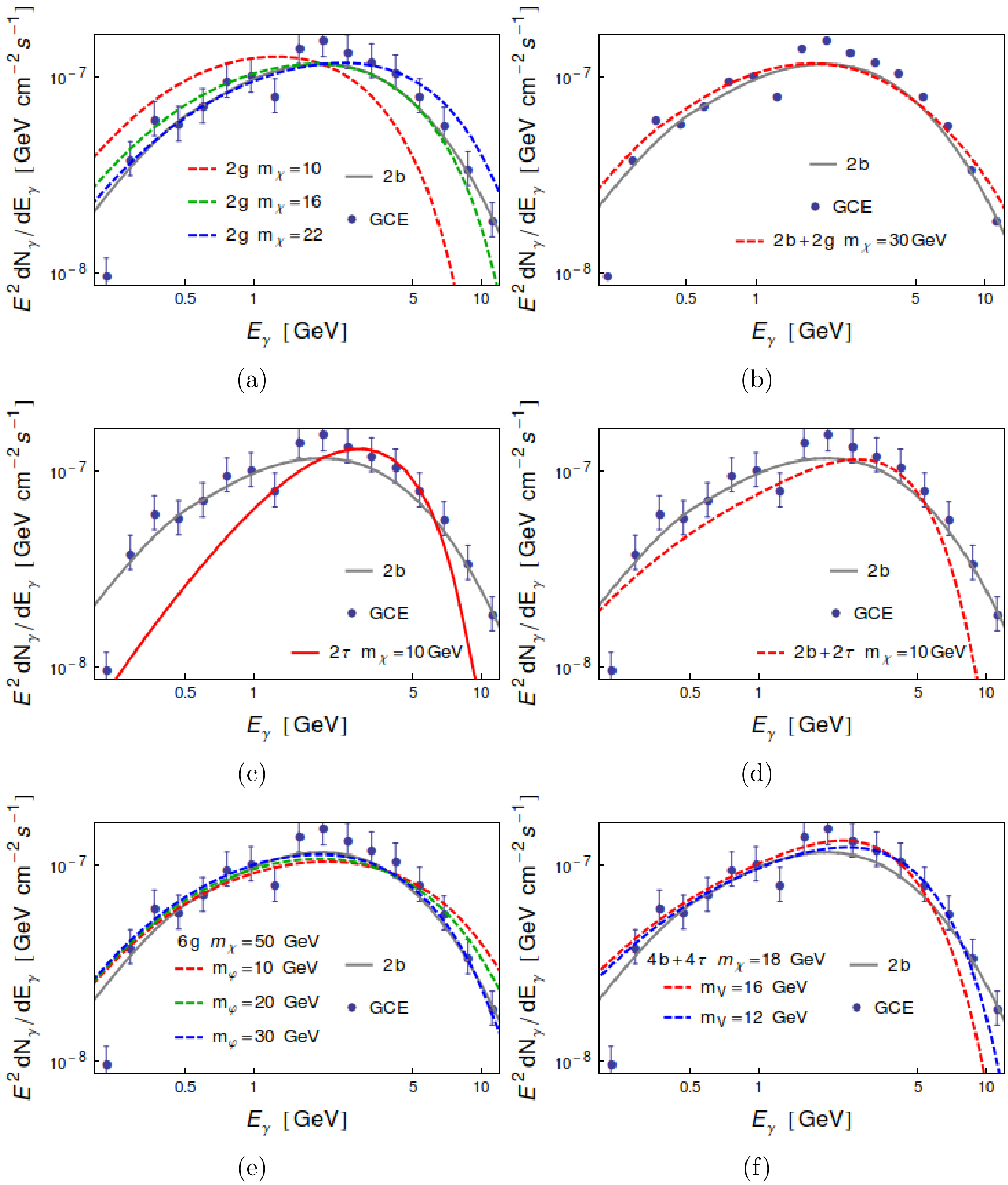

Figure A.1: (a) $\chi\bar{\chi} \to gg$, (b) $\chi\bar{\chi} \to gg$ (67%) or $b\bar{b}$ (33%), (c) $\chi\bar{\chi} \to \tau\bar{\tau}$, (d) $\chi\bar{\chi} \to \tau\bar{\tau}$ (85%) or $b\bar{b}$ (15%), (e) $\chi\bar{\chi} \to 6g$, (f) $\chi\bar{\chi} \to 2 \times \left[\tau\bar{\tau}\ (85\%) \text{ or } b\bar{b}\ (15\%)\right]$. Spectra for various final states, including branching ratios to different final states. 4-(6-)body final states originate from on-shell mediators with masses m_V (m_φ) shown. For visual comparison with plots in Ch. 4, the gray $2b$ line is the $\chi\bar{\chi} \to b\bar{b}$ best fit spectrum and dots are the measured galactic center γ-ray excess spectrum (GCE) assuming a $b\bar{b}$ signal template from [1]. Bars demonstrate an arbitrary measure of goodness-of-fit with respect to this spectrum. Note that the γ-ray excess data depends on the template used for the DM γ-ray spectrum so these data points are mainly for comparative purposes and are not necessarily representative of the goodness-of-fit to the γ-ray excess. See Sec. 4.3.3 for details.

literature.

For example, we point out in (a) and (b) that gluons can give a reasonable fit to the spectrum. While the photon spectrum from monochromatic gluons takes a slightly different shape than that of the b—presumably part of the reason why gg final states were not proposed for the γ-ray excess fit—they are reasonably close to the data given the implicit systematic uncertainties. This fit is improved significantly if the [off-shell, s-channel] mediator is allowed to decay to both gluons or $b\bar{b}$ pairs. Shown in (b) is the fit for a mediator that decays to either gluons or $b\bar{b}$ pairs, with

$$\text{Br}(\text{mediator} \to gg) \approx 2\,\text{Br}(\text{mediator} \to b\bar{b}). \tag{A.1}$$

The gluon mode is especially amenable to lighter dark matter masses since the final state is massless. Couplings to a spin-0 mediator can be generated through, for example, loops of third generation quarks.

Similarly, in Fig. A.1(c) we show what appears to be a poor fit to 10 GeV $\tau\bar{\tau}$ pairs. This, however, is a consequence of comparing the γ-ray spectrum from $\tau\bar{\tau}$ to the γ-ray excess fit assuming a $b\bar{b}$ DM template. It is indeed well known that DM annihilating into 10 GeV τs fits the excess well; this should be taken as a reminder of the systematic uncertainties implicit with the γ-ray fits. It also serves to highlight that for a specific model, a proper assessment of the fit to the γ ray excess requires a full astrophysical fit to the specific annihilation mode (along the lines of [144] and [150]) where both the model parameters and background parameters are fit simultaneously. For our purposes here, we only highlight the change in the spectrum from (c) to (d) where we introduce a 15% branching ratio of the mediator going to $b\bar{b}$—the fit has interpolated between the two spectra and gives an intuitive handle for how to generate hybrid spectra. A similar hybrid spectrum was explored in Fig. 6 of [149].

In Fig. A.1(e, f) we demonstrate the range of behavior for annihilation to on-shell mediators that each decay to either gluons or $\tau\bar{\tau}/b\bar{b}$. Note that an on-shell vector mediator cannot decay into two gluons by the Landau-Yang theorem so that one is forced to consider either $\chi\bar{\chi} \to 2 \times (V \to ggg)$ or $\chi\bar{\chi} \to 3 \times (\phi \to gg)$, each with six final state gluons. We plot the latter case in (e). In (f) we see an example of an on-shell vector mediator that decays to $\tau\bar{\tau}$ 85% of the time and $b\bar{b}$ the remainder. This spectrum fits the γ-ray excess spectrum for a $b\bar{b}$ template with $m_V \approx 12$ GeV.

Finally, we propose a simple extension where the DM mass can be made heavier than the region considered in the primary text. We saw that the on-shell mediator scenario raised the DM mass by having DM annihilation go into more final state primaries (b quarks). By extending the mediator sector to include additional on-shell states between the DM and SM sectors in Fig. 4.3, one may force larger dark matter masses. For example, [220] explored the cascade where $\chi\bar{\chi} \to 2\phi_1$ with $\phi_i \to 2\phi_{i+1}$ for the PAMELA positron excess [462]. See the appendix in that paper for analytical results for the generalization of the box spectrum to a higher polynomial spectrum where the degree of the polynomial is set by the number of on-shell mediator sectors. Additionally, as we mentioned above, one may use the Landau-Yang theorem to force $V_1 \to 3g$ decays at the end of the cascade or use mediator sectors where symmetries force $\phi_i \to n\phi_{i+1}$ with $n > 2$. We remember from our analysis in Sec. 4.5, however, that increasing the number of on-shell mediators per annihilation while maintaining the γ-ray excess signal also increases the annihilation cross section beyond what is expected from a simple thermal relic.

Appendix B

Exciting Dark Matter Formulae

B.1 Higgs and Gauge Couplings

In this appendix, we provide analytic forms for the couplings of $\chi_1\chi_1$, $\chi_2\chi_2$, and $\chi_1\chi_2$ to the light Higgs bosons (a, h) and to the Z. These couplings are defined according to the following terms in the Lagrangian:

$$\begin{aligned} \mathcal{L} &\supset \lambda^a_{11} a\bar{\chi}_1 i\gamma^5\chi_1 + \lambda^a_{22} a\bar{\chi}_2 i\gamma^5\chi_2 + \lambda^a_{12} a\bar{\chi}_1 i\gamma^5\chi_2 + \lambda^h_{11} h\bar{\chi}_1\chi_1 + \lambda^h_{22} h\bar{\chi}_2\chi_2 + \lambda^h_{12} h\bar{\chi}_1\chi_2 \\ &+ g_{11} Z_\mu\bar{\chi}_1\gamma^\mu\gamma^5\chi_1 + g_{22} Z_\mu\bar{\chi}_2\gamma^\mu\gamma^5\chi_2 + g_{12} Z_\mu\bar{\chi}_1\gamma^\mu\gamma^5\chi_2. \end{aligned} \tag{B.1}$$

As discussed in Ch. 5, the field χ_2 requires a transformation of the form $\chi_2 \to i\gamma^5\chi_2$ in order to ensure a positive value for its mass term. After this field redefinition, the above Lagrangian appears as follows:

$$\begin{aligned} \mathcal{L} &\supset \lambda^a_{11} a\bar{\chi}_1 i\gamma^5\chi_1 - \lambda^a_{22} a\bar{\chi}_2 i\gamma^5\chi_2 - \lambda^a_{12} a\bar{\chi}_1\chi_2 + \lambda^h_{11} h\bar{\chi}_1\chi_1 - \lambda^h_{22} h\bar{\chi}_2\chi_2 + \lambda^h_{12} h\bar{\chi}_1 i\gamma^5\chi_2 \\ &+ g_{11} Z_\mu\bar{\chi}_1\gamma^\mu\gamma^5\chi_1 + g_{22} Z_\mu\bar{\chi}_2\gamma^\mu\gamma^5\chi_2 + i g_{12} Z_\mu\bar{\chi}_1\gamma^\mu\chi_2. \end{aligned} \tag{B.2}$$

The couplings are given by:

$$\begin{aligned}
\lambda^a_{11} &= \frac{\sin\theta\sin\beta}{\sqrt{2}}\left[y_{11}N^1_{S_1}N^1_{\nu_1} + y_{21}N^1_{S_2}N^1_{\nu_1} - y_{22}N^1_{S_2}N^1_{\nu_2} - y_{12}N^1_{S_1}N^1_{\nu_2}\right] \\
&+ \cos\theta\left[y_S N^1_{S_1}N^1_{S_2} + y_D N^1_{\nu_1}N^1_{\nu_2}\right] \\
\lambda^a_{22} &= \frac{\sin\theta\sin\beta}{\sqrt{2}}\left[y_{11}N^2_{S_1}N^2_{\nu_1} + y_{21}N^2_{S_2}N^2_{\nu_1} - y_{22}N^2_{S_2}N^2_{\nu_2} - y_{12}N^2_{S_1}N^2_{\nu_2}\right] \\
&+ \cos\theta\left[y_S N^2_{S_1}N^2_{S_2} + y_D N^2_{\nu_1}N^2_{\nu_2}\right] \\
\lambda^a_{12} &= \cos\theta\left[y_S(N^1_{S_1}N^2_{S_2} + N^2_{S_1}N^1_{S_2}) + y_D(N^1_{\nu_1}N^2_{\nu_2} + N^2_{\nu_1}N^1_{\nu_2})\right] \\
&+ \frac{\sin\theta\sin\beta}{\sqrt{2}}\Big[y_{11}(N^1_{S_1}N^2_{\nu_1} + N^2_{S_1}N^1_{\nu_1}) + y_{21}(N^1_{S_2}N^2_{\nu_1} + N^2_{S_2}N^1_{\nu_1}) \\
&\quad - y_{22}(N^1_{S_2}N^2_{\nu_2} + N^2_{S_2}N^1_{\nu_2}) - y_{12}(N^1_{S_1}N^2_{\nu_2} + N^2_{S_1}N^1_{\nu_2})\Big] \\
\lambda^h_{11} &= -\frac{\cos\beta}{\sqrt{2}}\left[y_{11}N^1_{S_1}N^1_{\nu_1} + y_{21}N^1_{S_2}N^1_{\nu_1} + y_{22}N^1_{S_2}N^1_{\nu_2} + y_{12}N^1_{S_1}N^1_{\nu_2}\right] \\
\lambda^h_{22} &= -\frac{\cos\beta}{\sqrt{2}}\left[y_{11}N^2_{S_1}N^2_{\nu_1} + y_{21}N^2_{S_2}N^2_{\nu_1} + y_{22}N^2_{S_2}N^2_{\nu_2} + y_{12}N^2_{S_1}N^2_{\nu_2}\right] \\
\lambda^h_{12} &= -\frac{\cos\beta}{\sqrt{2}}\Big[y_{11}(N^1_{S_1}N^2_{\nu_1} + N^2_{S_1}N^1_{\nu_1}) + y_{21}(N^1_{S_2}N^2_{\nu_1} + N^2_{S_2}N^1_{\nu_1}) \\
&\quad + y_{22}(N^1_{S_2}N^2_{\nu_2} + N^2_{S_2}N^1_{\nu_2}) + y_{12}(N^1_{S_1}N^2_{\nu_2} + N^2_{S_1}N^1_{\nu_2})\Big] \\
g_{11} &= -\frac{g}{4c_W}\left[(N^1_{\nu_1})^2 - (N^1_{\nu_2})^2\right] \\
g_{22} &= -\frac{g}{4c_W}\left[(N^2_{\nu_1})^2 - (N^2_{\nu_2})^2\right] \\
g_{12} &= -\frac{g}{2c_W}\left[N^1_{\nu_1}N^2_{\nu_1} - N^1_{\nu_2}N^2_{\nu_2}\right],
\end{aligned} \tag{B.3}$$

where the mixing angles are defined in Eq. 5.17, and g and c_W are the $SU(2)_W$ coupling constant and cosine of the Weinberg angle, respectively. Note that in the limit of small a_0-A_0 mixing, $\lambda^a_{11,22} \approx \pm y_S\cos\theta/2$.

B.2 Decay

In this appendix, we provide formulae describing the decay $\chi_2 \to \chi_1\gamma$. We note that a convenient gauge choice is *non-linear R gauge* due to the vanishing of the $\gamma W^+ G^-$ vertex (see e.g. Ref. [463]). The width for this process is given by:

$$\Gamma(\chi_2 \to \chi_1\gamma) = \frac{g_{\text{eff}}^2}{8\pi}\left(\frac{\Delta}{m_{\chi_2}}\right)^3, \tag{B.4}$$

where $\Delta \equiv m_{\chi_2}^2 - m_{\chi_1}^2$. The effective coupling in this expression is given by:

$$\begin{aligned} g_{\text{eff}} &= \frac{e\epsilon_1}{8\pi^2}\bigg[- 2M_D(\epsilon_1 g_{1L}g_{2R} - \epsilon_2 g_{1R}g_{2L})J_g \\ &- (\epsilon_1\epsilon_2 g_{1L}g_{2L} - g_{1R}g_{2R})[\epsilon_2 m_{\chi_2}(I_{g2} - J_g - K_g) + \epsilon_1 m_{\chi_1}(J_g - K_g)] \\ &+ \frac{1}{4}(\lambda_{1L}\lambda_{2L} - \epsilon_1\epsilon_2\lambda_{1R}\lambda_{2R})[\epsilon_2 m_{\chi_2}(I_{s2} - K_s) - \epsilon_1 m_{\chi_1}K_s] \\ &+ \frac{1}{4}(\lambda_{1L}^G\lambda_{2L}^G - \epsilon_1\epsilon_2\lambda_{1R}^G\lambda_{2R}^G)[\epsilon_2 m_{\chi_2}(I_{g2} - K_g) - \epsilon_1 m_{\chi_1}K_g] \\ &+ \frac{1}{4}M_D[I_g(\epsilon_2\lambda_{1L}^G\lambda_{2R}^G - \epsilon_1\lambda_{1R}^G\lambda_{2L}^G) + I_s(\epsilon_2\lambda_{1L}\lambda_{2R} - \epsilon_1\lambda_{1R}\lambda_{2L})]\bigg], \end{aligned} \tag{B.5}$$

where ϵ_1 and ϵ_2 are the signs of the first two eigenvalues of the mass matrix, M_0, as given in Eq. 5.16. The couplings in the above expression are given by:

$$g_{1L} \equiv -\frac{g}{\sqrt{2}}N_{\nu_2}^1, \qquad g_{1R} \equiv -\frac{g}{\sqrt{2}}N_{\nu_1}^1, \qquad g_{2L} \equiv -\frac{g}{\sqrt{2}}N_{\nu_2}^2, \qquad g_{2R} \equiv -\frac{g}{\sqrt{2}}N_{\nu_1}^2, \tag{B.6}$$

$$\lambda_{1L} \equiv -\sin\beta\,(y_{22}N_{S_2}^1 + y_{12}N_{S_1}^1), \qquad \lambda_{2L} \equiv -\sin\beta\,(y_{22}N_{S_2}^2 + y_{12}N_{S_1}^2),$$

$$\lambda_{1R} \equiv -\sin\beta\,(y_{11}N_{S_1}^1 + y_{21}N_{S_2}^1), \qquad \lambda_{2R} \equiv -\sin\beta\,(y_{11}N_{S_1}^2 + y_{21}N_{S_2}^2),$$

$$\lambda_{1L}^G \equiv \cos\beta\,(y_{22}N_{S_2}^1 + y_{12}N_{S_1}^1), \qquad \lambda_{2L}^G \equiv \cos\beta\,(y_{22}N_{S_2}^2 + y_{12}N_{S_1}^2),$$

$$\lambda_{1R}^G \equiv \cos\beta\,(y_{11}N_{S_1}^1 + y_{21}N_{S_2}^1), \qquad \lambda_{2R}^G \equiv \cos\beta\,(y_{11}N_{S_1}^2 + y_{21}N_{S_2}^2).$$

Lastly, Eq. B.6 contains a number of integrals, defined as follows:

$$\begin{aligned}
I_g &\equiv \frac{1}{\Delta}\int_0^1 \frac{dx}{1-x}\log X_g, \\
I_{g2} &\equiv \frac{1}{\Delta}\int_0^1 dx\log X_g, \\
J_g &\equiv \frac{1}{\Delta}\int_0^1 \frac{dx}{1-x}\log X'_g, \\
I_s &\equiv \frac{1}{\Delta}\int_0^1 \frac{dx}{1-x}\log X_s, \\
I_{s2} &\equiv \frac{1}{\Delta}\int_0^1 dx\log X_s, \\
J_s &\equiv \frac{1}{\Delta}\int_0^1 \frac{dx}{1-x}\log X'_s, \\
K_g &\equiv -\frac{1}{\Delta}(1+M_D^2 I_g + m_W^2 J_g - m_{\chi_2}^2 I_{g2}), \\
K_s &\equiv -\frac{1}{\Delta}(1+M_D^2 I_s + m_{H^\pm}^2 J_s - m_{\chi_2}^2 I_{s2}),
\end{aligned} \tag{B.7}$$

where

$$\begin{aligned}
X_g &\equiv \frac{M_D^2 x + m_W^2(1-x) - m_{\chi_2}^2 x(1-x)}{M_D^2 x + m_W^2(1-x) - m_{\chi_1}^2 x(1-x)}, \\
X'_g &\equiv \frac{m_W^2 x + M_D^2(1-x) - m_{\chi_2}^2 x(1-x)}{m_W^2 x + M_D^2(1-x) - m_{\chi_1}^2 x(1-x)}, \\
X_s &\equiv \frac{M_D^2 x + m_{H^\pm}^2(1-x) - m_{\chi_2}^2 x(1-x)}{M_D^2 x + m_{H^\pm}^2(1-x) - m_{\chi_1}^2 x(1-x)} \\
X'_s &\equiv \frac{m_{H^\pm}^2 x + M_D^2(1-x) - m_{\chi_2}^2 x(1-x)}{m_{H^\pm}^2 x + M_D^2(1-x) - m_{\chi_1}^2 x(1-x)}.
\end{aligned} \tag{B.8}$$

B.3 Direct Detection

The elastic scattering cross section between the dark matter, χ_1, and a nucleus with atomic number Z and atomic mass A is given by:

$$\sigma_0^{\text{elastic}} = \frac{4\mu_{\chi,N}^2}{\pi}\left[Zf_p + (A-Z)f_n\right]^2, \tag{B.9}$$

where $\mu_{\chi,N}$ is the reduced mass of the system and the nucleon level couplings are given by:

$$f_{p,n} = m_{p,n}\left[\sum_{q=u,d,s}\frac{a_q}{m_q}f_{T_q}^{(p,n)} + \frac{2}{27}f_{TG}^{(p,n)}\sum_{q=c,b,t}\frac{a_q}{m_q}\right], \tag{B.10}$$

and

$$\frac{a_q}{m_q} = \frac{1}{v}\left[-\frac{\lambda_{11}^h}{m_h^2} + \frac{\lambda_{11}^H q_\beta}{m_H^2}\right], \tag{B.11}$$

where $q_\beta = \cot\beta$ $(-\tan\beta)$ for up-type (down-type) quarks.

In addition, direct detection experiments can also detect inelastic events, $\chi_1 N \to \chi_2 N$. For $\delta m_\chi \lesssim v^2\mu_{\chi,N}/2$, the dark matter particles typically possess enough kinetic energy to scatter into the excited state. The cross section for inelastic scattering is given by:

$$\sigma_0^{\text{inelastic}} = \frac{\mu_{\chi,N}^2}{\pi}\,F\left[Zf_p + (A-Z)f_n\right]^2, \tag{B.12}$$

where in this case,

$$\begin{aligned} f_p &= \frac{g\sin\theta_W g_{12}}{4m_Z^2}\left(\cot\theta_W - 3\tan\theta_W\right) \\ f_n &= -\frac{g\sin\theta_W g_{12}}{4m_Z^2}\left(\cot\theta_W + \tan\theta_W\right), \end{aligned} \tag{B.13}$$

and the following factor accounts for the kinematic suppression associated with inelastic scattering:

$$F = \left[\frac{s^2 - 2(m_{\chi_2}^2 + m_N^2)s + (m_{\chi_2}^2 - m_N^2)^2}{s^2 - 2(m_{\chi_1}^2 + m_N^2)s + (m_{\chi_1}^2 - m_N^2)^2}\right]^{1/2}, \tag{B.14}$$

and

$$\sqrt{s} \approx m_N\left[1 + \frac{1}{2}\left(\frac{\mu_{\chi,N}v}{m_N}\right)^2\right] + m_{\chi_1}\left[1 + \frac{1}{2}\left(\frac{\mu_{\chi,N}v}{m_{\chi_1}}\right)^2\right], \tag{B.15}$$

where $v \sim 10^{-3}$. Note that $F \to 0$ in the limit of $v \to v_{\min} = \sqrt{2\delta m_\chi/\mu_{\chi,N}}$, below which inelastic scattering is not possible. In contrast, for the mass splitting and masses under consideration in Ch. 5 (and for typical dark matter velocities in the local Milky Way), $v \gg v_{\min}$ and $F \sim 1$.

Appendix C

h-V-V Effective Vertex at One Loop

Here we outline the details of the triangle loop calculation. The following results are for a single fermion species running in the loop. While the Higgs has off-diagonal couplings with the three neutral fermions in the mass basis, the vector only has diagonal couplings and thus only the diagonal Higgs interactions appear in the triangle diagrams. As a result, the functions A and B of Eq. (6.8) are the sum of the contributions from each individual fermion species.

Momenta are defined as in Fig. 6.1, with k_1 and k_2 the two (on-shell) vector momenta coming into the diagram, and $p = -(k_1 + k_2)$ the momentum incoming through the Higgs line. In addition to the diagram shown explicitly in Fig. 6.1, there is a second contribution related to it by $k_1 \leftrightarrow k_2$, $\mu \leftrightarrow \nu$.

The contribution to the matrix element from a single fermion of mass m and Yukawa coupling y is given by:

$$\mathcal{M} = g^2 \frac{y}{\sqrt{2}} \frac{i\pi^2 8m}{(2\pi)^4} \times \mathcal{I}^{\mu\nu}(k_1, k_2) \times \epsilon_\mu(k_1)\epsilon_\nu(k_2) \tag{C.1}$$

where,

$$\mathcal{I}^{\mu\nu}(k_1,k_2) = \frac{1}{8m}\int \frac{d^dk}{i\pi^2}\frac{\mathrm{Tr}\left[(\not{k}+m)\gamma^\nu(\not{k}+\not{k}_2+m)(\not{k}-\not{k}_1+m)\gamma^\mu\right]}{(k^2-m^2)((k-k_1)^2-m^2)((k+k_2)^2-m^2)} + (k_1,\mu\leftrightarrow k_2,\nu). \tag{C.2}$$

Evaluating the trace in the numerator and making use of the fact that $k_1\cdot\epsilon(k_1) = k_2\cdot\epsilon(k_2) = 0$ for on-shell vectors results in,

$$\mathrm{Tr}[...] = 4m\left(g^{\mu\nu}(m^2 - k_1\cdot k_2 - k^2) + 4k^\mu k^\nu + k_1^\nu k_2^\mu\right)\ . \tag{C.3}$$

After Passarino–Veltman decomposition [464] we find,

$$\mathcal{I}^{\mu\nu}(k_1,k_2) = \Big\{g^{\mu\nu}\Big[(4-d)C_{00} + m^2C_0 + k_1\cdot k_2(2C_{12}-C_0) - m_V^2(C_{11}+C_{22})\Big] + k_1^\nu k_2^\mu\Big[C_0 - 4C_{12}\Big]\Big\}, \tag{C.4}$$

where the arguments of the C functions are (uniformly) $C_0(k_1,k_2;m,m,m)$, etc.

Reducing to scalar functions results in a finite expression of the form,

$$\mathcal{I}^{\mu\nu} = F_1(p^2,m)\ (k_1\cdot k_2 g^{\mu\nu} - k_1^\nu k_2^\mu) + F_2(p^2,m)\ g^{\mu\nu} \tag{C.5}$$

corresponding to an effective three-point vertex described by

$$-\left(\frac{g^2ym}{2\sqrt{2}\pi^2}\right)\left(\frac{1}{4}F_1(p^2,m)\ hV^{\mu\nu}V_{\mu\nu} + \frac{1}{2}F_2(p^2,m)\ hV^\mu V_\mu\right) \tag{C.6}$$

where the form factors F_1 and F_2 are given by,

$$\begin{aligned}
F_1(p^2,m) &= \frac{1}{2bm^2(b-4a)^2}\Big\{2m^2(b-2a)\Big[4a(a-1)+b(1+6a-b)\Big]C_0 \\
&\qquad -2a(2a+b)\Delta B_0+(b-2a)(b-4a)\Big\} \qquad \text{(C.7)}\\
F_2(p^2,m) &= \frac{4a^2}{b(b-4a)^2}\Big\{2(b-a)\Delta B_0-2m^2\Big[4a(a-1)+b(1-2a+b)\Big]C_0+4a-b\Big\}
\end{aligned}$$

with,

$$a \equiv \frac{m_V^2}{4m^2}, \qquad b \equiv \frac{p^2}{4m^2}. \qquad \text{(C.8)}$$

The scalar integrals C_0 and ΔB_0 can be expressed analytically as,

$$\begin{aligned}
C_0 &= \frac{1}{4m^2 b\beta}\sum_{j,k=1}^{2}\left[2\mathrm{Li}_2\left(\frac{1+(-1)^j\beta}{1+(-1)^k\mathrm{X}\beta}\right)-\mathrm{Li}_2\left(\frac{(1+(-1)^j\beta)^2}{1+(-1)^k 2\mathrm{Y}\beta+\beta^2}\right)\right]\;, \\
\Delta B_0 &\equiv B_0(m_V^2;m,m)-B_0(p^2;m,m) \qquad \text{(C.9)}\\
&= 2\sqrt{\frac{1-b}{b}}\arctan\left[\sqrt{\frac{b}{1-b}}\right]-2\sqrt{\frac{1-a}{a}}\arctan\left[\sqrt{\frac{a}{1-a}}\right].
\end{aligned}$$

with

$$\beta \equiv \sqrt{1-4\frac{a}{b}}, \quad \mathrm{X} \equiv \sqrt{1-\frac{1}{a}}, \quad \mathrm{Y} \equiv \sqrt{1-\frac{1}{b}}\;. \qquad \text{(C.10)}$$

As mentioned above, the coefficients A and B in Eq. (6.8) are given by the sum over the contributions from all three neutral mediator fermions,

$$\begin{aligned}
A(p^2) &= \sum_i \left(\frac{g^2 y_i m_i}{2\sqrt{2}\pi^2}\right) F_1(p^2,m_i), \\
B(p^2) &= \sum_i \left(\frac{g^2 y_i m_i}{2\sqrt{2}\pi^2}\right) F_2(p^2,m_i).
\end{aligned} \qquad \text{(C.11)}$$

In the $m_V \to 0$ limit the two form factors become,

$$F_1 = \frac{1}{2b\,m^2}\left(1+\frac{b-1}{2b}\left[\mathrm{Li}_2\left(\frac{2\sqrt{b}}{\sqrt{b}-\sqrt{b-1}}\right)+\mathrm{Li}_2\left(\frac{2\sqrt{b}}{\sqrt{b}+\sqrt{b-1}}\right)\right]\right) + \mathcal{O}(m_V^2)\ , \tag{C.12}$$

$$F_2 = \frac{m_V^4}{4b^2 m^4}\left(-5+\frac{1+b}{2b}\left[\mathrm{Li}_2\left(\frac{2\sqrt{b}}{\sqrt{b}-\sqrt{b-1}}\right)+\mathrm{Li}_2\left(\frac{2\sqrt{b}}{\sqrt{b}+\sqrt{b-1}}\right)\right] + 4\sqrt{\frac{1-b}{b}}\arctan\sqrt{\frac{b}{1-b}}\right) + \mathcal{O}(m_V^6)\ . \tag{C.13}$$